TECHNICAL REPORT ARCCB-TR-93009

BLAST FIELD CONTOURING USING UPSTREAM VENTING

G.C. CAROFANO

MARCH 1993

US ARMY ARMAMENT RESEARCH,
DEVELOPMENT AND ENGINEERING CENTER
CLOSE COMBAT ARMAMENTS CENTER
BENÉT LABORATORIES
WATERVLIET, N.Y. 12189-4050

APPROVED FOR PUBLIC RELEASE; DISTRIBUTION UNLIMITED

DISCLAIMER

The findings in this report are not to be construed as an official Department of the Army position unless so designated by other authorized documents.

The use of trade name(s) and/or manufacturer(s) does not constitute an official indorsement or approval.

DESTRUCTION NOTICE

For classified documents, follow the procedures in DoD 5200.22-M, Industrial Security Manual, Section II-19 or DoD 5200.1-R, Information Security Program Regulation, Chapter IX.

For unclassified, limited documents, destroy by any method that will prevent disclosure of contents or reconstruction of the document.

For unclassified, unlimited documents, destroy when the report is no longer needed. Do not return it to the originator.

DISCLAIMER NOTICE

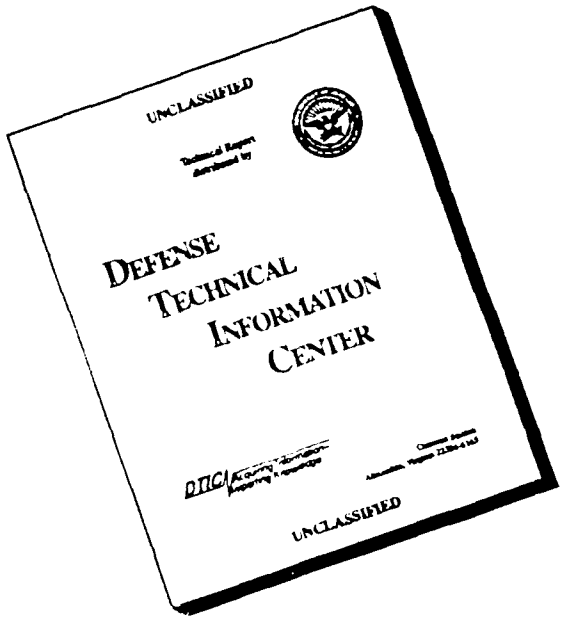

THIS DOCUMENT IS BEST QUALITY AVAILABLE. THE COPY FURNISHED TO DTIC CONTAINED A SIGNIFICANT NUMBER OF PAGES WHICH DO NOT REPRODUCE LEGIBLY.

REPORT DOCUMENTATION PAGE

Form Approved
OMB No. 0704-0188

1. AGENCY USE ONLY (Leave blank)	2. REPORT DATE	3. REPORT TYPE AND DATES COVERED
	March 1993	Final

4. TITLE AND SUBTITLE
BLAST FIELD CONTOURING USING UPSTREAM VENTING

5. FUNDING NUMBERS
PRON: 1A13Z1CANMBJ
AMCMS: 6111.02.H610.0

6. AUTHOR(S)
G.C. Carofano

7. PERFORMING ORGANIZATION NAME(S) AND ADDRESS(ES)
U.S. Army ARDEC
Benet Laboratories, SMCAR-CCB-TL
Watervliet, NY 12189-4050

8. PERFORMING ORGANIZATION REPORT NUMBER
ARCCB-TR-93009

9. SPONSORING / MONITORING AGENCY NAME(S) AND ADDRESS(ES)
U.S. Army ARDEC
Close Combat Armaments Center
Picatinny Arsenal, NJ 07806-5000

10. SPONSORING / MONITORING AGENCY REPORT NUMBER

11. SUPPLEMENTARY NOTES

12a. DISTRIBUTION / AVAILABILITY STATEMENT
Approved for public release; distribution unlimited

12b. DISTRIBUTION CODE

13. ABSTRACT *(Maximum 200 words)*

Modern cannon often employ vents in the tube wall near the muzzle as a lightweight brake. While all brakes reduce weapon impulse at the expense of increasing blast upstream, this type affords some opportunity to contour the blast field. Normally, the vents are clustered at the muzzle, but calculations indicated that relocating some upstream could reduce blast levels near the breech without compromising weapon impulse or projectile velocity. Laboratory experiments using a 20-mm cannon showed a reduction of 4 to 5 dB, as predicted. However, field experiments with a 105-mm cannon showed no beneficial effect of upstream venting. The presence of the ground plane in the latter is believed to be the reason.

14. SUBJECT TERMS	15. NUMBER OF PAGES
Muzzle Blast, Muzzle Brake, Perforated Muzzle Brake, Brake Efficiency	170
	16. PRICE CODE

17. SECURITY CLASSIFICATION OF REPORT	18. SECURITY CLASSIFICATION OF THIS PAGE	19. SECURITY CLASSIFICATION OF ABSTRACT	20. LIMITATION OF ABSTRACT
UNCLASSIFIED	UNCLASSIFIED	UNCLASSIFIED	UL

TABLE OF CONTENTS

Tables

List of Illustrations

ACKNOWLEDGEMENTS

The author would like to thank Mr. Larry Rusch of Benet Laboratories for making the preparations for the experiments and Mr. Doug Savick of the Ballistic Research Laboratory for conducting the experiments and reducing the data. Gratitude is also expressed to Mr. Mick Cipollo of Benet Laboratories for setting up the graphics program to do the surface plots. Funding for the experiments was provided by the Project Manager of Tank Main Armaments Systems (PM-TMAS), Picatinny Arsenal, NJ.

INTRODUCTION

Historically, muzzle brakes have consisted of one or more baffles placed a few calibers downstream of the muzzle to deflect a portion of the propellant gas radially. The resulting force on the brake surface reduces the impulse transferred to the gun mount, but the redirected exhaust considerably increases the blast levels in the breech area where troops and sensitive equipment are likely to be located. Today, designers often replace this heavy device with vents machined directly into the tube wall (see Figure 1). The vents are placed near the muzzle to minimize their effect on the ballistics, but the question arises, "Could another arrangement meet the same impulse and projectile velocity requirements but produce lower blast levels in the critical breech area?" Several patterns were considered using the blast model developed by Carofano (refs 1-5). The most successful involved moving two rows of vents upstream while leaving the rest near the muzzle. In this report, the model is briefly described and the predictions are compared with 20-mm test results obtained at a Ballistic Research Laboratory (BRL) firing range. Finally, the results from a field experiment using a 105-mm cannon are presented.

THE BLAST MODEL

The model is based upon the unsteady Euler equations and is developed in detail in References 2 through 4. An overview is given here.

The pressure histories at various locations are needed for comparison with the experiments. To obtain a reasonable time sample, the blast field must be computed to distances considerably beyond the weapon. This severely limits the fineness of the grid that can be used. Conversely, the flow through the vents is three-dimensional and requires a much finer grid. Fortunately, the problem contains some features that permit the two flows to be solved separately.

First, the tube blowdown process is gradual, and the three-dimensional flow through each vent can be treated as quasi-steady. Secondly, at the brake entrance, the flow is supersonic and continues to expand downstream due to venting. Also, because of the high tube pressures, the gas leaves each vent at near sonic or supersonic velocity over most of the exit area. Experience with the code has shown that the flow is rather insensitive to the outflow boundary condition over the remaining subsonic portion. For the Euler equations, then, it can be shown (refs 2-4) that the flow at a particular vent location is completely described by its geometry and the Mach number and thermodynamic properties of the gas just ahead of the vent. One solution with these parameters specified is valid for all upstream pressures and densities. A few solutions suffice to describe the entire blowdown process.

Data from these solutions are used to obtain average values of density and pressure along with the mass and momentum fluxes at the vent exit. The averages are dimensionless functions of the parameters that appear in the three-dimensional solution and are used to couple the transient interior and exterior flows.

The flow inside of the tube is calculated using the one-dimensional Euler equations with a source term included to represent the venting at the tube wall. This is constructed from the mass flux function and the local conditions prevailing in the tube at a given instant.

The flow outside of the tube is treated as axisymmetric. The large number of vents and their symmetrical placement around the tube makes this feasible. However, since the area of each vent represents only a portion of the local tube area, the averaged variables at the vent exit have to be adjusted to provide an appropriate boundary condition for the axisymmetric equations. A control volume approach to achieve this is described in Reference 4. The quantities at the vent exit are related to the interior flow through the averaged functions described above. Because the vent exit flow is supersonic, the exterior boundary condition is completely determined by the local conditions in the tube.

The code uses the Abel equation of state (ref 6) to more adequately represent the gases at the pressure levels that prevail in large caliber cannon. Harten's Total Variation Diminishing scheme (ref 7) is used in conjunction with a time-splitting algorithm to solve the Euler equations. The projectile equation of motion is also solved.

A uniform grid is employed over a rectangular region extending 50 calibers upstream and downstream from the muzzle and 60 calibers radially outward from the tube axis. Beyond this region, a gradually expanding grid is used to limit memory requirements while still permitting the calculation to continue. Four cells are used across the tube radius--950 in the axial direction and 550 in the radial direction.

INITIAL CONDITIONS

As the projectile accelerates in the tube from rest, a shock wave forms ahead of it. The column of air set into motion by the shock is called the precursor flow and is included in the calculation because it disturbs the quiescent environment for a considerable distance from the muzzle prior to projectile exit. The specification of the state of the propellant gas behind the projectile is delayed until its base reaches the end of the 20-mm barrel (without an extension). This is called the projectile base position in Table 1. The base pressure and projectile velocity are known at this instant from earlier experiments (ref 8). The flow variables behind the projectile are then calculated from the Pidduck-Kent limiting solution for an Abel gas (refs 3,6). In this manner, essentially all of the information relating to the combustion, friction, and heat transfer processes is included in the starting data behind the projectile. Prior to this time, an analytical representation of the velocity and position time histories is used to advance the projectile. The numerical calculation of the precursor flow remains one-dimensional until the shock reaches the muzzle in the bare muzzle case or the first row of vents when a brake is used, as shown in Figure 2.

Table 1. Starting Data for Solution

Projectile base position, cm	143.00
Projectile velocity, m/sec	1045.0
Projectile base pressure, atm	287.0
Propellant mass, kg	0.0389
Projectile mass, kg	0.0980
Bore diameter, cm	2.0
Gun chamber volume, cm^3	41.7
Specific heat ratio	1.25
Molecular weight	22.8
Covolume, cm^3/kg	982.0

THE LABORATORY EXPERIMENT

To verify the concept, the decision was made to start with the 20-mm cannon facility at BRL rather than a full-scale field test. In the laboratory, shadowgraphs can be taken to help interpret the limited number of pressure histories that can be obtained in an experiment. Also, because the cannon can be located away from reflecting surfaces, the flow remains axisymmetric for some distance which facilitates comparison with the model. Finally, the cannon can be allowed to recoil freely for a period of time which permits an accurate determination of the impulse from simple velocity and mass measurements. Impulse measurements in a full-scale experiment are much less precise.

The 20-mm cannon is threaded at the muzzle to accept the three extensions shown schematically in Figure 1 (scaled drawings may be found in Appendix A). The bare muzzle extension is used as a reference. The standard brake has twelve rows of vents located near the muzzle. Each row has twelve vents uniformly spaced around the tube. The split brake has nine rows of vents near the muzzle and two rows upstream at 7.6 and 9.1 calibers, respectively, from the muzzle. Although this brake has one less row of vents than the standard brake, it was predicted to have nearly the same gasdynamic efficiency. The upstream vents see a higher tube pressure and generate greater loads.

The extensions have the same length. In practice, vented tubes have to be somewhat longer to produce the desired projectile velocity. However, for the 20-mm cannon, the addition was only a few centimeters and was omitted to facilitate comparison of the three blast fields.

THE FLOW FIELDS

Surface plots of the pressure fields are shown in Figures 3 through 5. The long rectangle at the left represents the tube; the small rectangle at the right is the projectile. The planar surface surrounding the disturbance represents atmospheric pressure. To avoid a large spike at the muzzle, the maximum pressure plotted was limited to four atmospheres. This accounts for the flat spot just downstream of the muzzle. The pressure spike at the right is due partly to the bluntness of the projectile used in the computer model. The tube and projectile are drawn with a 'height' of one atmosphere above atmospheric pressure to serve as a reference.

The asterisks in these plots indicate the pressure transducer locations in the laboratory experiments. They provide a convenient reference for the discussion. Seven transducers were used for each shot, placed at angles of 15, 30, 60, 90, 120, 150, and 165 degrees with respect to the line of fire. Data were taken at radii of 30, 40, and 50 calibers from the muzzle. Shown in the figures are the locations at 30 calibers and a few farther downstream.

For the bare muzzle case in Figure 3, the flow upstream consists of the precursor shock 'ps' and the main blast wave 'mb', both of which are followed by mild expansions. Downstream, the flow has more structure and includes the interaction between the main blast wave and the projectile bow shock 'pbs'. The 'shock bottle', which extends from the muzzle exit to the Mach disk 'md' and is enclosed by the barrel shock 'bs', contains the strong muzzle expansion 'me'. The highest and lowest pressures in the exterior flow are found in this small region.

With respect to the brake flow fields in Figures 4 and 5, venting reduces the muzzle exit pressure, so the extent and structure of the flow downstream differ somewhat from the bare muzzle case. Upstream, the internal structure of the vent flows contract to a very narrow region. Apparently, the gas expands primarily in the circumferential direction as the flow volume increases with the square of the radial dimension. Note, too, that although the vents are perpendicular to the tube axis, the flow develops in the direction of 110 degrees. This occurs because much of the gas leaving the vents is directed slightly upstream, not because it is deflected by the muzzle flow (refs 2,4).

A shadowgraph was taken for most of the rounds fired. The spark light source was triggered, after a preset time delay, by the arrival of the precursor shock at a microphone placed near the muzzle. After passing through the disturbance, the light was diffracted by a Fresnel lens into the camera. The lens had a diameter of 80 cm and was placed in a vertical plane 30 calibers from the tube axis. All of the shadowgraphs are given in Appendix B. A few are shown here to aid in the discussion.

The shadowgraph in Figure 6 was taken as the projectile base was emerging from the bare muzzle extension. Most of the disturbance in this picture is the precursor flow. The precursor shock is seen to be considerably weaker upstream after diffracting around the muzzle. Following projectile exit, the propellant gas flow commences and drives the main blast wave which, at this instant, is just starting to form near the muzzle. The solid object below the tube is the trigger microphone. Also visible are the circular striations of the Fresnel lens and a few scratches that can be identified by their repetition in the other shadowgraphs.

The flow field produced by the standard brake is shown in Figure 7. The nose of the projectile is just barely visible in the remnants of the precursor flow at the right of the picture. The disturbance is bounded by the precursor shocks formed by the air flowing from the vents and the muzzle. The dark plume on the left is the propellant gas flowing from the vents; the plume on the right is the muzzle flow. Both generate strong shock waves that interact near the muzzle exit plane. The resulting structure is called the main blast wave.

The split brake flow field is shown in Figure 8. The plume on the left is associated with the propellant gas flowing from the upstream vents. The center plume is produced by the vents near the muzzle. The precursor shock extends the width of the picture.

A shadowgraph of the upstream half of the bare muzzle flow field at a later instant is shown in Figure 9. The semicircular objects at the left are the pressure transducer fixtures at 150 and 165 degrees and 30 calibers. The precursor shock is barely visible. Note that the main blast wave, which intersects the tube just upstream of the transition in diameter, is weakest near the barrel and gets progressively stronger toward the muzzle. This contrasts sharply with the more uniform strength of the main blast wave for the standard brake in Figure 10.

The split brake generates the pair of disturbances shown in Figure 11. The shock at the left is associated with the upstream vents. The disturbance produced by the muzzle vents is composed of a set of wavelets near the tube that coalesce to form a single shock farther away. This is interesting because, prior to interacting with the upstream vent plumes, this disturbance was a more impressive set of shocks (see Figure 8).

The computed flow for the standard brake differs in one important respect from the experiment. In the shadowgraph of Figure 8, the main blast wave appears to be driven along the tube as a normal shock. In the computed flow of Figure 4, this wave appears to form near the head of the vent plume and then travel inward toward the tube surface. In the process, the wave strengthens somewhat due to the decreasing volume of gas processed by the shock and finally reflects off the tube to produce a short Mach stem and a weak reflected wave. The difference may represent a limitation of the axisymmetric assumption. In the laboratory, the individual jets do not necessarily merge in the circumferential direction to form an annular flow as they are assumed to do in the model.

For the split brake, the main blast wave in the computed flow of Figure 5 has the same general appearance as its counterpart in the shadowgraph of Figure 11. However, the disturbance produced by the muzzle vents appears to be a strong shock near the tube rather than a set of wavelets, as in the shadowgraph. Away from the tube, the two flows show better agreement. Once again, the difference may be the result of the axisymmetric assumption in the model.

FREE-FIELD OVERPRESSURE DATA

Seven pressure histories were recorded for each shot. All of the data are given in Appendix B. In this section, representative cases are compared with the computed histories.

A set of histories for each extension at 30, 40, and 50 calibers is given in Figures 12 through 20. Zero time corresponds approximately to the instant the projectile leaves the barrel. The computed traces, shown at the right, are plotted such that the arrival time of the disturbance at the 30-degree position coincides with the experimental trace. In this way, the arrival times at the other positions can be compared for accuracy.

The ordinate of each sub-grid represents overpressure (pressure above atmospheric pressure), measured in atmospheres. It was varied from trace to trace to better display the data. Also indicated are the transducer location and maximum pressure of the main blast wave for each trace.

In analyzing the pressure histories, there is always some difficulty in interpreting waves that arrive after the main blast wave. The three sets of surface plots in Figures 21 through 23 permit most of the waves in the computed traces to be identified. The times indicated correlate with the time scale in the computed traces.

The primary thrust of this study is to determine the effect of the vent pattern on the blast levels near the tube. The composite plot in Figure 24 shows the pressure histories at the 150- and 165-degree transducer locations along the 30-caliber radius for the three extensions. The data were taken from Figures 12, 13, and 14. The traces start with the arrival of the weak precursor shock 'ps'. This is followed by the main blast wave 'mb' and an expansion wave 'ew', which reduces the pressure to sub-atmospheric levels. The precursor shock is quickly overtaken by the main blast wave in the brake cases, as shown by the shadowgraphs and pressure surface plots.

The standard brake considerably strengthens the main blast wave relative to the bare muzzle case. When the vent pattern is split, the small number of upstream vents produces a weaker main blast wave, and equally important, the interaction with their plume reduces the disturbance from the muzzle vents to a perturbation 'pt' in the succeeding expansion wave. Similar results are obtained at 40 and 50 calibers (see Figures 15 through 20). By moving the right number of vents the correct distance from the muzzle, the strength of the blast wave and the perturbation can be made equal. It is interesting that this worked out for both the computed and the experimental results.

Another prominent feature in Figure 24 is the arrival of a significant disturbance 'sd' within two milliseconds of the main blast wave. A subsequent experiment revealed that it is the reflection of the main blast wave off the Fresnel lens used in the optical setup. The gage fixtures were located above the tube in a plane parallel to the lens. The sensitive elements of the transducers faced away from the lens so the wave had to diffract around the fixture giving the disturbance a somewhat rounded appearance in several of the traces. The data are representative of an axisymmetric flow field until the arrival of this wave.

Similar disturbances are present in the computed traces and their source is readily discernible in the pressure plots of Figures 21, 22, and 23. For the bare muzzle case, they originate at the muzzle plume and travel upstream. Additional waves are generated by the vent plumes in the brake cases. The solution at these late times seems questionable and is discussed in a separate report for the bare muzzle case (ref 9). The comparisons in Figures 12 through 20 show that the solution at earlier times is satisfactory.

SUMMARY OF OVERPRESSURE DATA

The peak overpressure data of the main blast wave are summarized in Figure 25. The data at each transducer location are averages of the information in Appendix B. The principal effect of venting is seen to be the generation of a more uniform blast field around the cannon. The disturbance is diminished somewhat downstream of the muzzle but considerably strengthened upstream. Both brakes produce essentially the same results except at the 150- and 165-degree positions where the effect of the upstream vents is apparent.

The brake data are replotted in Figure 26 using the decibel scale. The ordinate represents the increase in overpressure relative to the bare muzzle case, or

$$decibel\ increase = 20 \log_{10}[(P_{brk}-P_o)/(P_{brm}-P_o)] \quad (1)$$

where P_o is atmospheric pressure. The quantities $(P_{brk}-P_o)$ and $(P_{brm}-P_o)$ are the measured overpressures for the brake and bare muzzle cases, respectively. At a distance of 40 to 50 calibers upstream from the muzzle, the increase is over 10 decibels for the standard brake. The split brake reduces this by 4 to 5 decibels near the tube.

In Figures 27, 28, and 29, the computed results (solid lines) are compared with the experimental data at radii of 30, 40, and 50 calibers, respectively. The symbols represent the average peak overpressure of the main blast wave at each location. The minimum and maximum values are indicated by the flags through the symbol in those cases where the data spread exceeds the size of the symbol. The reproducibility of the experimental data is seen to be good.

The model predictions show satisfactory agreement with the data, particularly upstream where they are of greatest interest. However, the results near the line of fire require further discussion. The experimental data exhibit a maximum at the 15-degree position in every plot, while the calculations generally place the maximum at 30 degrees. This can be explained using the pressure surface plots in Figures 3, 4, and 5. Note that the 15-degree position is near the point where the projectile bow wave intersects the main blast wave and that the pressure falls off rapidly between this point and the center line. In the bare muzzle case at 30 calibers, the main blast wave passes over the 15-degree position, producing a maximum there. For the remaining cases, however, the weaker bow wave structure passes over this position, shifting the maximum to 30 degrees. The blunt projectile used in the model may be responsible by producing a somewhat broader disturbance than would result with an aerodynamically-shaped nose. It can also be observed from the shadowgraphs that the fixtures holding the transducers were quite sizable and may have altered the flow field somewhat in the experiment.

VELOCITY AND IMPULSE DATA

The weapon impulse and projectile velocity were measured for each shot. The data are tabulated in Appendix C and summarized here. Each measured value in Table 2 is the average of ten or more rounds. The projectile velocity was measured by a pair of light stations placed downstream that produced an average value 4.6 m from the muzzle. The computed values refer to the muzzle exit and should be somewhat higher.

Table 2. Velocity and Impulse Data

Extension	Velocity (m/sec)		Impulse (nt-sec)	
	Measured	Computed	Measured	Computed
Bare muzzle	1059	1065	150.4	146.8
Standard brake	1060	1064	121.4	121.4
Split brake	1058	1063	121.6	121.7

Since each extension was the same length, the projectile velocities for the brakes should be lower than the bare muzzle value because less work can be done on the projectile by the gas as it expands to lower pressures in the vented region. Further, the split brake should have the lowest velocity because venting starts farther upstream. This pattern is followed by the computed velocities in Table 2 but not by the measured values. However, the round-to-round variation was found to be plus or minus 10 m/sec (see Appendix C), so the fact that the measured velocity for the standard brake slightly exceeds the bare muzzle value is not especially disturbing. The velocity loss due to venting is surprisingly modest based on either set of values.

The gasdynamic efficiency, β, of a brake is defined as

$$\beta = (I_{wo} - I_w)/(I_{wo} - M \cdot V_p) \qquad (2)$$

where I_w and I_{wo} are the weapon impulses with and without a brake, respectively, M is the projectile mass, and V_p is the bare muzzle velocity. The computed efficiencies are somewhat below the measured values given in Table 3. The discrepancy is due primarily to the difference in the bare muzzle impulse values, I_{wo}, in Table 2. Note that the split brake has nearly the same efficiency as the standard brake based on either set of values.

Table 3. Gasdynamic Efficiency (%)

	Measured	Computed
Standard brake	62.1	59.8
Split brake	61.6	59.0

THE 105-MM FIELD EXPERIMENT

Encouraged by the laboratory results, it was decided to test the scheme in the field using a 105-mm cannon. Two series of tests were run using the same cannon. In the first series, the cannon had a brake with twelve rows of vents at the muzzle, geometrically similar to the standard brake used in the 20-mm experiments and shown in Figure 1. In the second series, the three rows of vents nearest the breech were covered with a collar, and two rows of vents were added upstream about ten calibers from the muzzle, as shown in Figure 30. This pattern was chosen because calculations indicated it would produce somewhat lower blast levels near the breech than a design geometrically similar to the 20-mm split brake shown in Figure 1. The cannon axis was 17.4 calibers above the ground plane during the tests.

Overpressure data were taken at angles of 90, 120, 150, 165, and 175 degrees from the line of fire along radii 30 and 60 calibers from the muzzle exit plane. The sensitive elements of the transducers were located in the horizontal plane containing the tube axis. Four or five rounds of M490 and M735 ammunition were fired at each radius. The pressure histories are given in Appendix D.

Interpreting the pressure histories from the 20-mm experiments was greatly simplified because the flow was axisymmetric and the shadowgraphs were available. Neither aid is present in the field experiments and there is the added complexity of reflected waves from the ground plane. This is demonstrated in Figure 31 which shows the pressure histories at 60 calibers for both brakes using M490 ammunition. Consider the data at the 165-degree position. For the standard brake, the main blast wave 'mb' is always followed by what is assumed to be the reflection of this wave 'rw' off the ground plane. For the split brake, the first wave 'mb' is obviously associated with the upstream vents. However, an intermediate wave 'iw' also appears and is assumed to be the reflection of the first wave off the ground plane. The final wave 'fw' is associated with the disturbance produced by the muzzle vents, as in the laboratory experiments. The expansion process that follows the main blast wave is interrupted by the arrival of the intermediate wave. As a result, when the disturbance from the muzzle vents arrives, it raises the overpressure to a level that is generally higher than the main blast wave. This appears to be the principal difference between the laboratory and field experiments.

The peak overpressure data for the 105-mm experiments are summarized in Figures 32 through 35. Each figure contains three plots--two showing the data for each brake expressed in atmospheres, and one showing the numerical difference between the split and standard brakes expressed in decibels. Two sets of data are given on each plot. The solid line represents the maximum overpressure of the pressure trace, while the dashed line gives the magnitude of the first wave or main blast wave. The latter is what might be expected if the experiment was axisymmetric or, equivalently, if ground reflection was unimportant. The data in the figures indicate that, at least for this configuration, there is no beneficial effect of upstream venting when the ground plane is present, i.e., in the real case, and only modest benefit in the absence of the ground plane. Other configurations may produce more favorable results.

Unfortunately, this means that the axisymmetric computer program has only limited value in determining the optimum placement of the upstream vents when the ground plane is present, assuming an optimum exists. The only practical alternative is to do a parametric study in the laboratory with a simulated ground plane. This is a more delicate experiment to perform because the sensitive element of the pressure transducer must be placed such that it is simultaneously perpendicular to waves reflected off the ground plane and to the waves arriving from the muzzle region. Examination of the shadowgraphs presented earlier shows that this is not always feasible, particularly when a brake is employed.

CONCLUSIONS

Calculations and laboratory experiments having axial symmetry showed upstream venting to be a promising method of reducing blast levels in the breech area while maintaining specified values of projectile velocity and weapon impulse. However, field experiments with a 105-mm cannon showed that the ground plane nullified any possible benefits of the scheme, at least for the configuration tested. Since three-dimensional calculations of this extent are not practical, more costly laboratory experiments with a simulated ground plane would be needed to determine if the scheme has practical value. For further discussion of the effect of the ground plane on blast, see Reference 10.

REFERENCES

1. G.C. Carofano, "Blast Computation Using Harten's Total Variation Diminishing Scheme," Technical Report ARLCB-TR-84029, Benet Weapons Laboratory, Watervliet, NY, October 1984.

2. H.T. Nagamatsu, K.Y. Choi, R.E. Duffy, and G.C. Carofano, "An Experimental and Numerical Study of the Flow Through a Vent Hole in a Perforated Muzzle Brake," Technical Report ARCCB-TR-87016, Benet Laboratories, Watervliet, NY, June 1987.

3. G.C. Carofano, "The Gasdynamics of Perforated Muzzle Brakes," Technical Report ARCCB-TR-88006, Benet Laboratories, Watervliet, NY, February 1988.

4. G.C. Carofano, "The Blast Field Produced by a Cannon Having a Perforated Muzzle Brake," Technical Report ARCCB-TR-88043, Benet Laboratories, Watervliet, NY, December 1988.

5. G.C. Carofano, "A Comparison of Experimental and Numerical Blast Data for Perforated Muzzle Brakes," Technical Report ARCCB-TR-90034, Benet Laboratories, Watervliet, NY, December 1990.

6. J. Corner, *Theory of the Interior Ballistics of Guns*, John Wiley and Sons, NY, 1950.

7. A. Harten, "High Resolution Schemes for Hyperbolic Conservation Laws," *J. Computational Physics*, Vol. 49, 1983, p. 357.

8. R.E. Dillon, Jr., "A Parametric Study of Perforated Muzzle Brakes," Technical Report ARLCB-TR-84015, Benet Weapons Laboratory, Watervliet, NY, May 1984.

9. G.C. Carofano, "A Note on the Blast Signature of a Cannon," Technical Report ARCCB-TR-92014, Benet Laboratories, Watervliet, NY, March 1992.

10. G.C. Carofano, "Perforated Brake Efficiency Measurements Using a 20-mm Cannon," Technical Report ARCCB-TR-93010, Benet Laboratories, Watervliet, NY, March 1993.

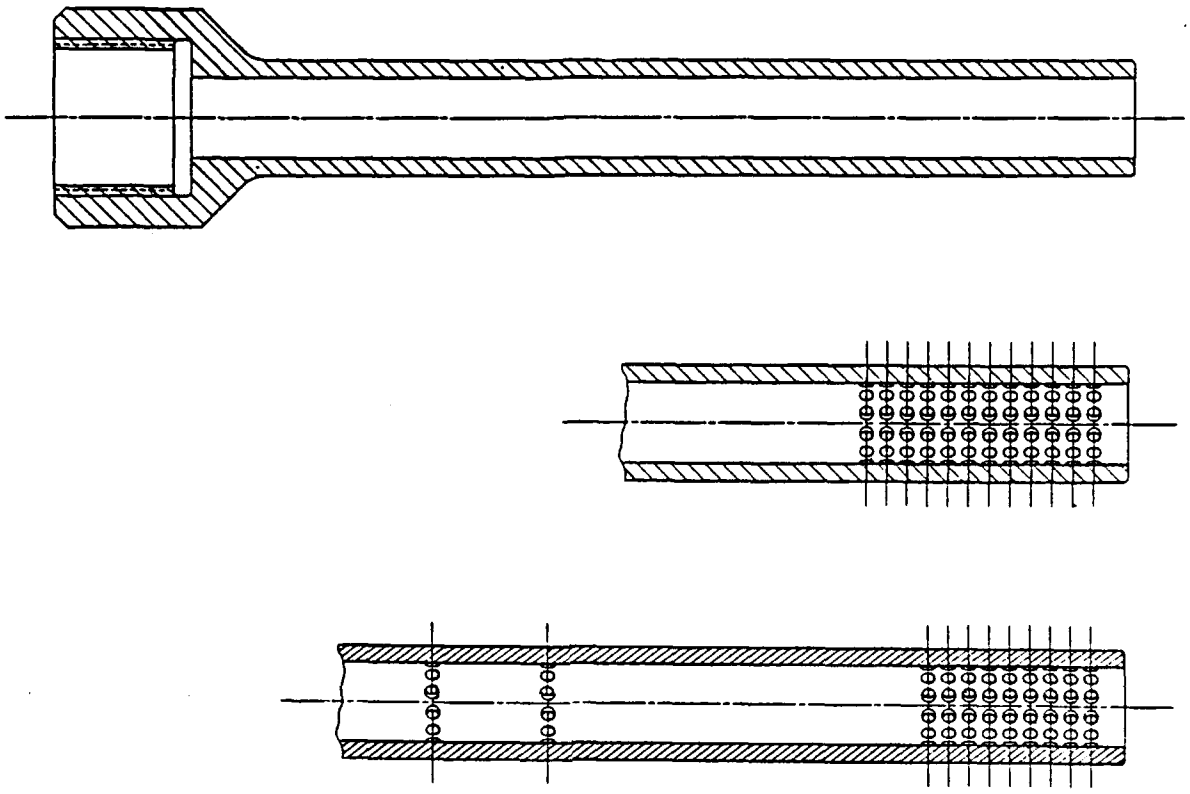

Figure 1. Sketch of the three extensions used in the experiments: bare muzzle (top), standard brake (middle), split brake (bottom).

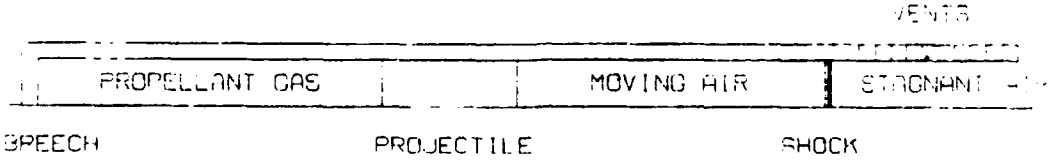

Figure 2. The starting configuration for the calculations.

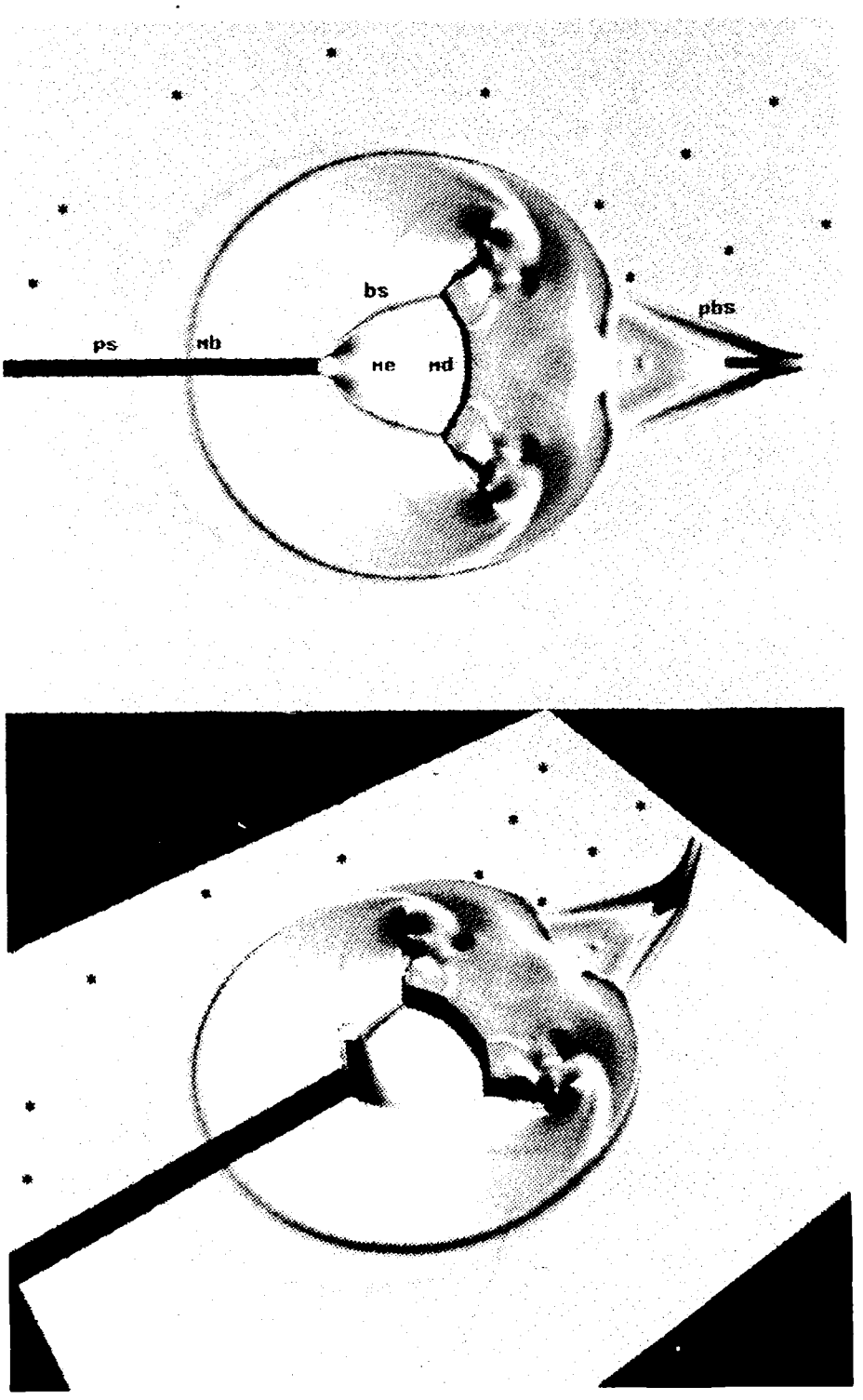

Figure 3. Surface plots of the computed pressure field for the bare muzzle case.

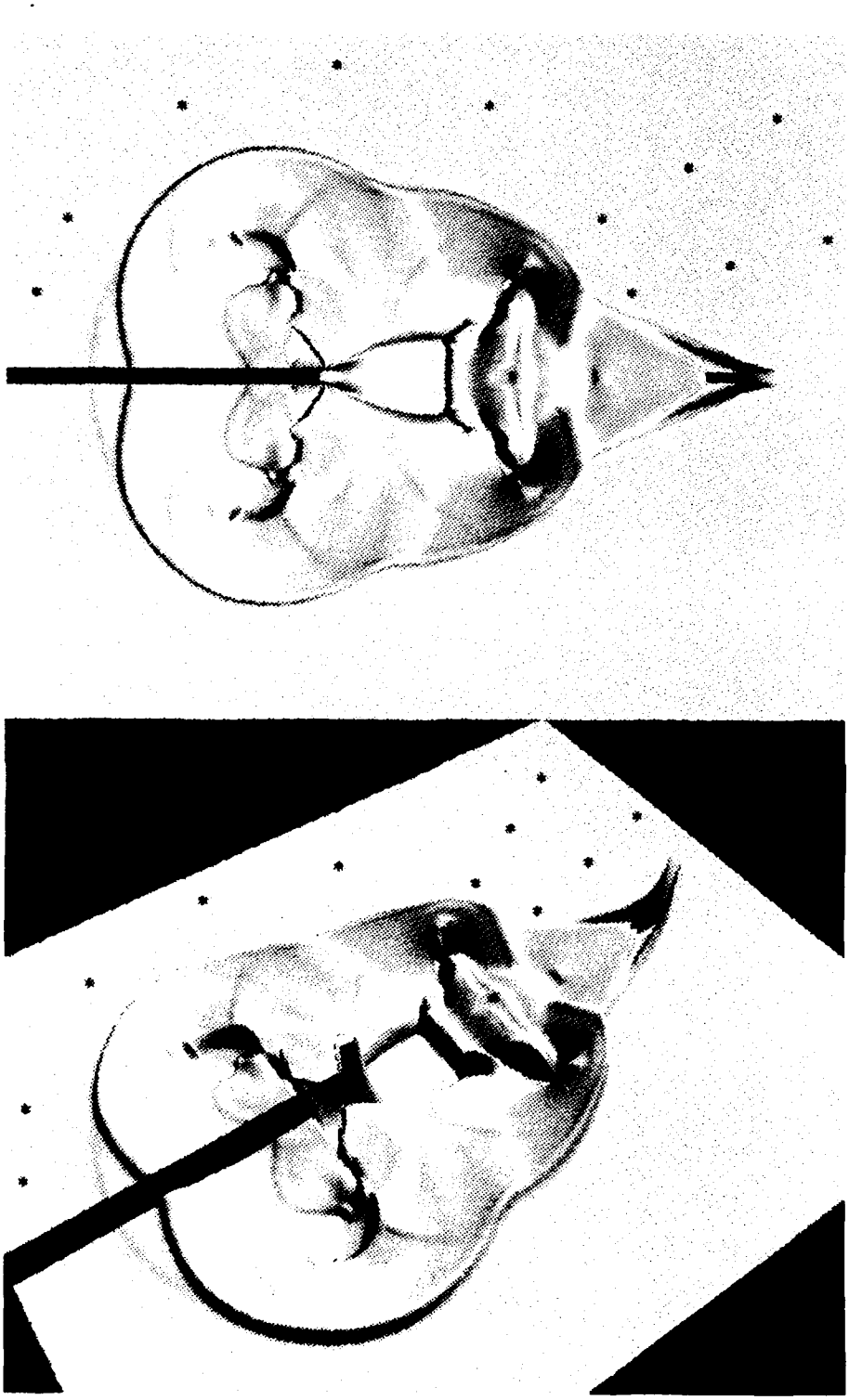

Figure 4. Surface plots of the computed pressure field for the standard brake case.

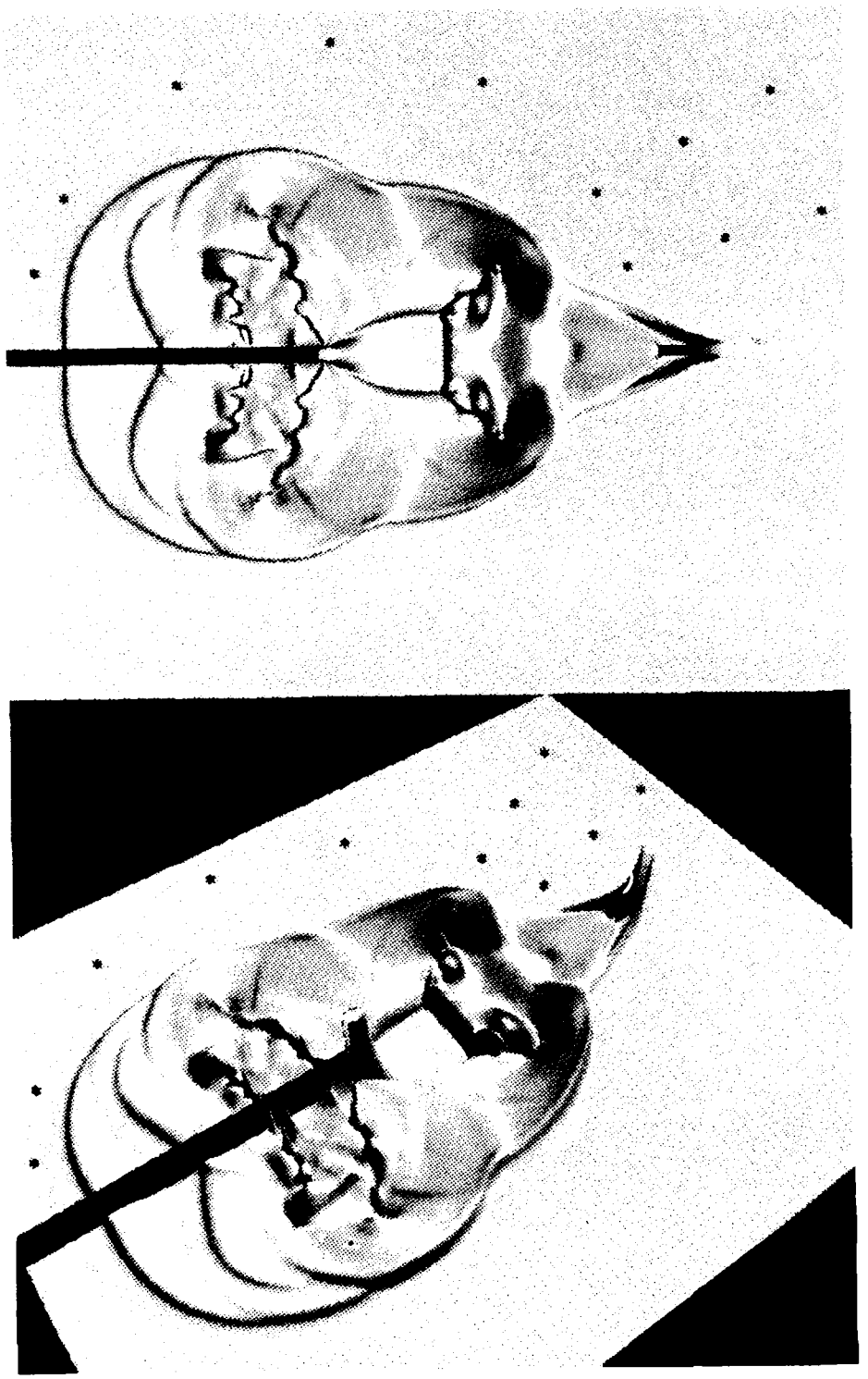

Figure 5. Surface plots of the computed pressure field for the split brake case.

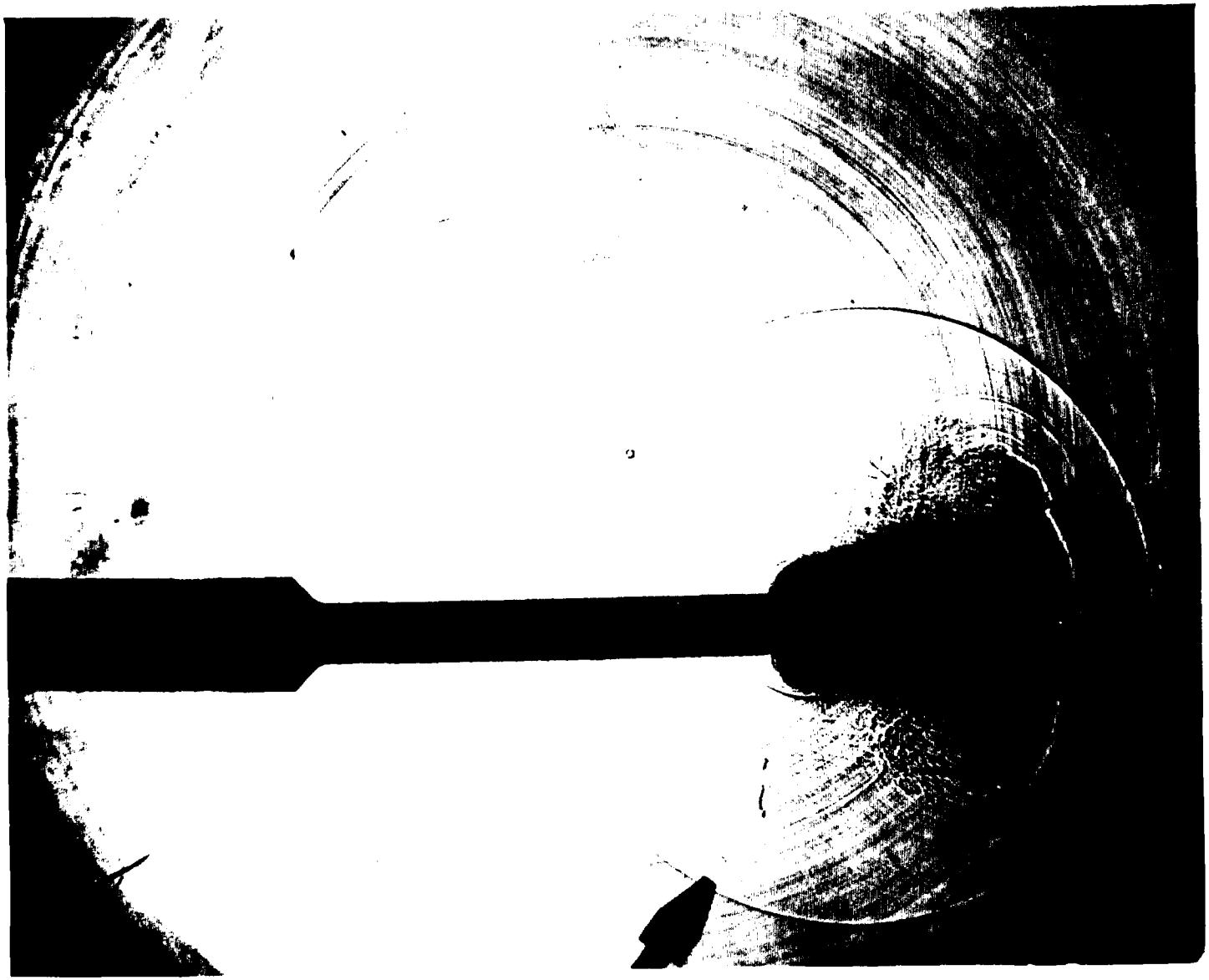

Figure 6. Shadowgraph of the bare muzzle flow field taken with no time delay (round 19531, Appendix B).

Figure 7. Shadowgraph of the standard brake flow field taken with a 150-microsecond time delay (round 19544, Appendix B).

Figure 8. Shadowgraph of the split brake flow field taken with a 150-microsecond time delay (round 19550, Appendix B).

Figure 9. Shadowgraph of the bare muzzle flow field taken with a 750-microsecond time delay (round 19556, Appendix B).

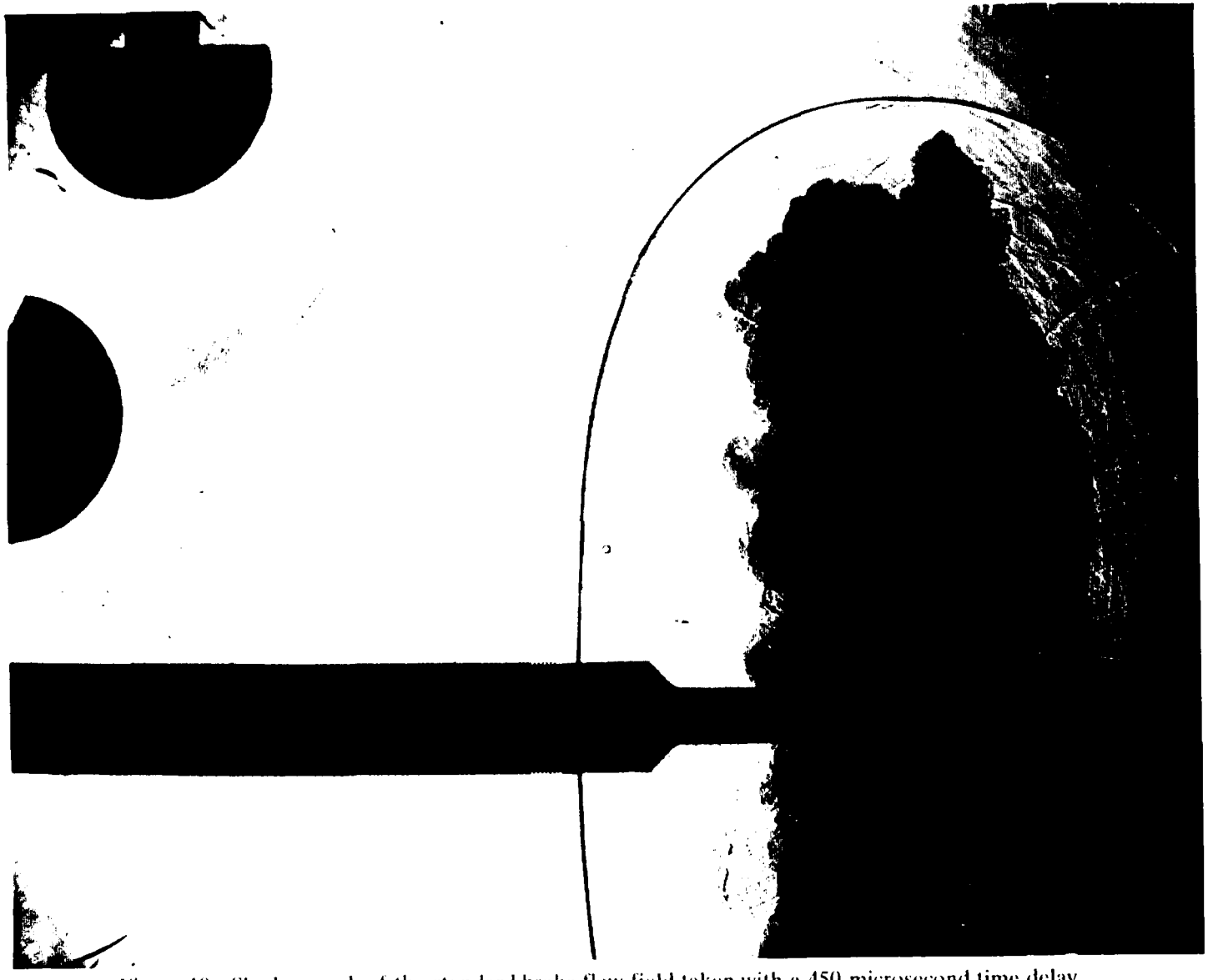

Figure 10. Shadowgraph of the standard brake flow field taken with a 450-microsecond time delay (round 19566, Appendix B).

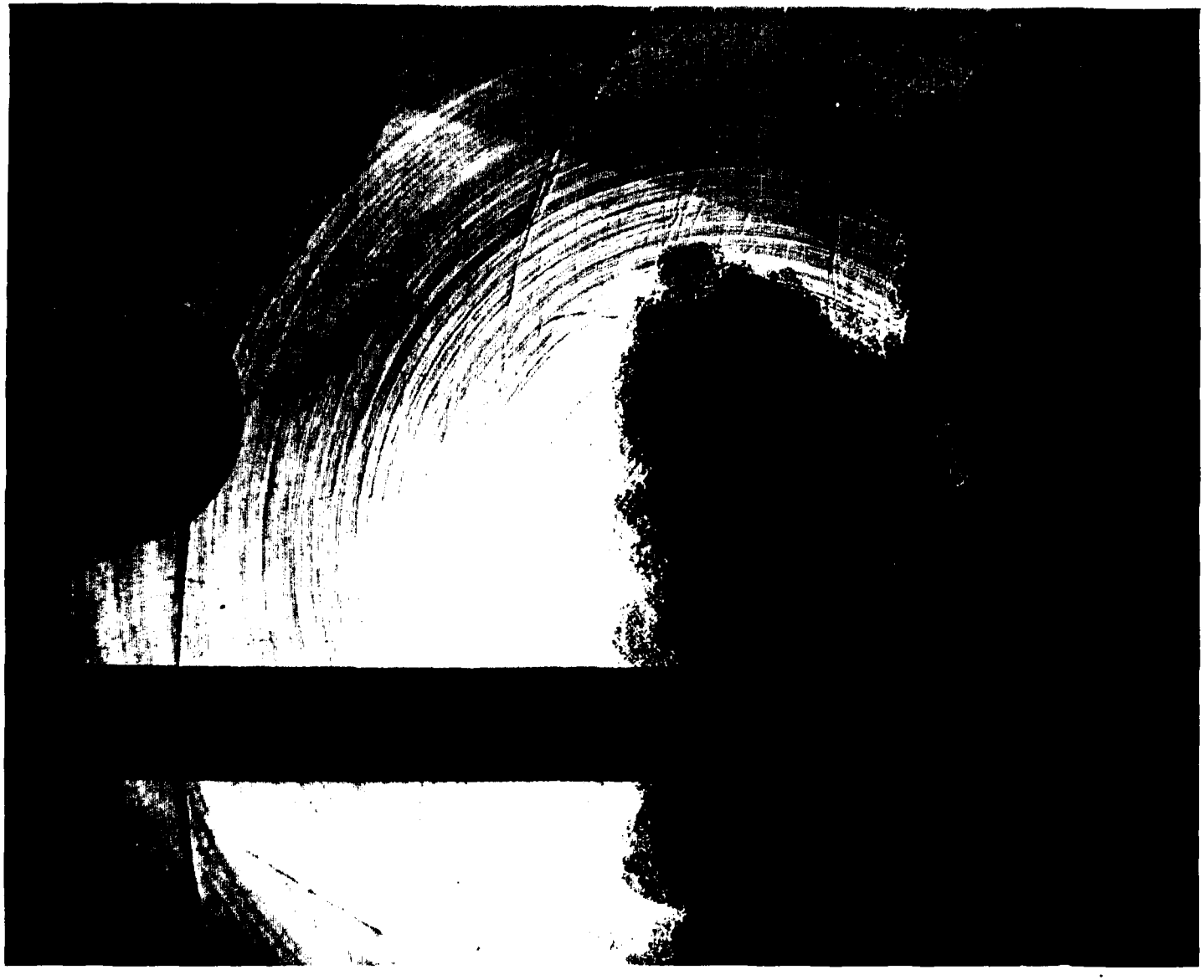

Figure 11. Shadowgraph of the split brake flow field taken with a 750-microsecond time delay (round 19575, Appendix B).

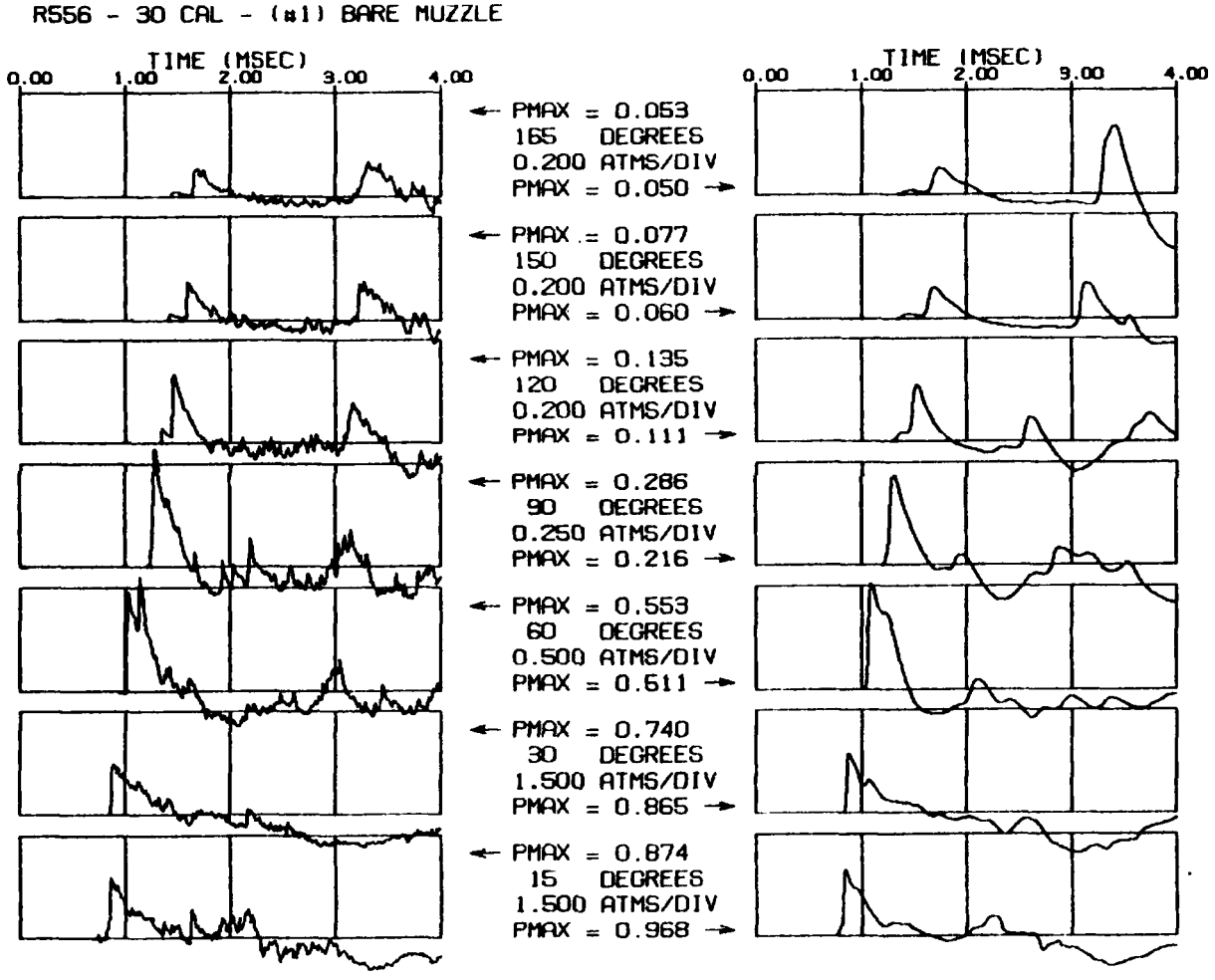

Figure 12. Pressure-time histories for the bare muzzle case at 30 calibers (round 19556, Appendix B).

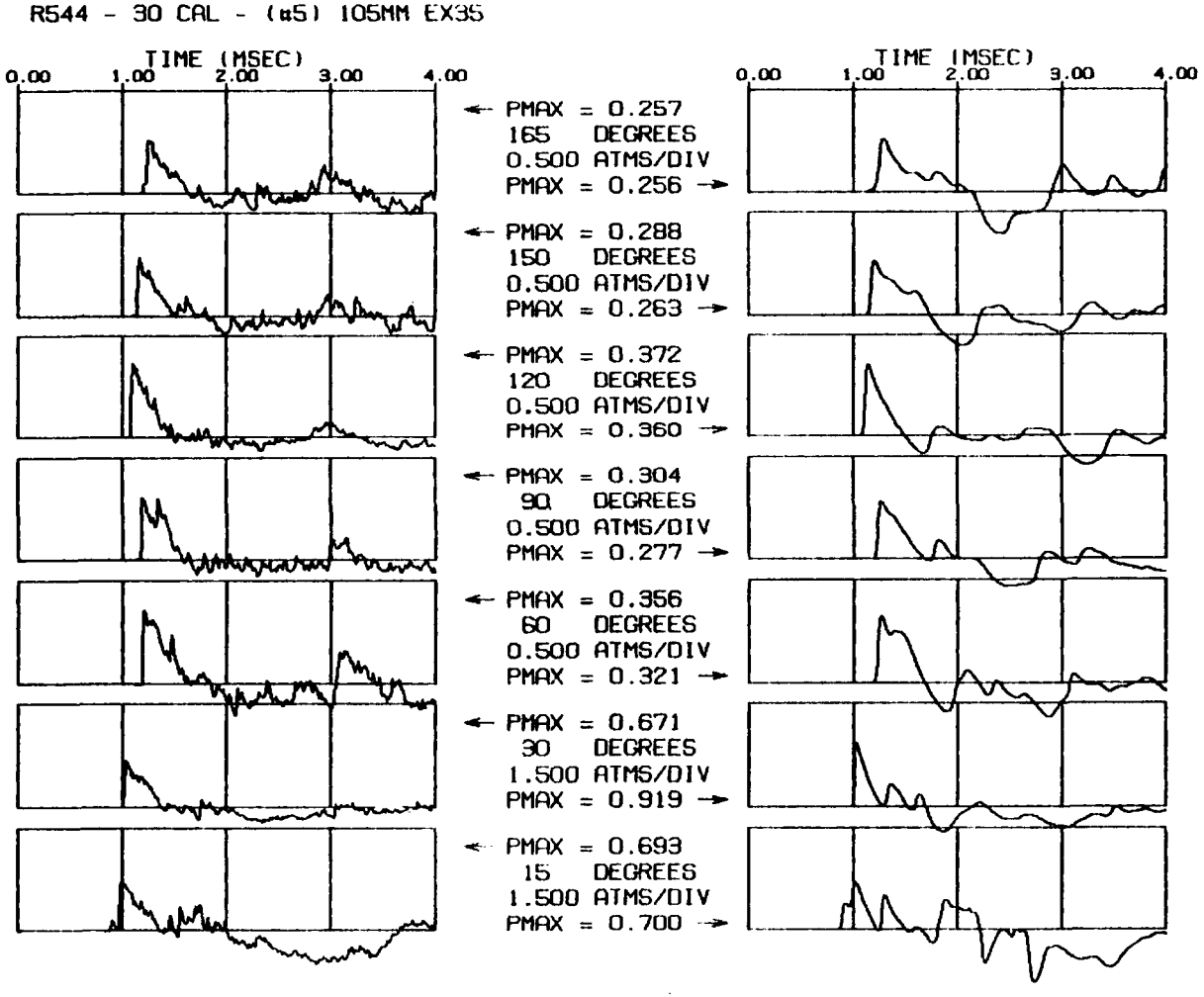

Figure 13. Pressure-time histories for the standard brake at 30 calibers (round 19544, Appendix B).

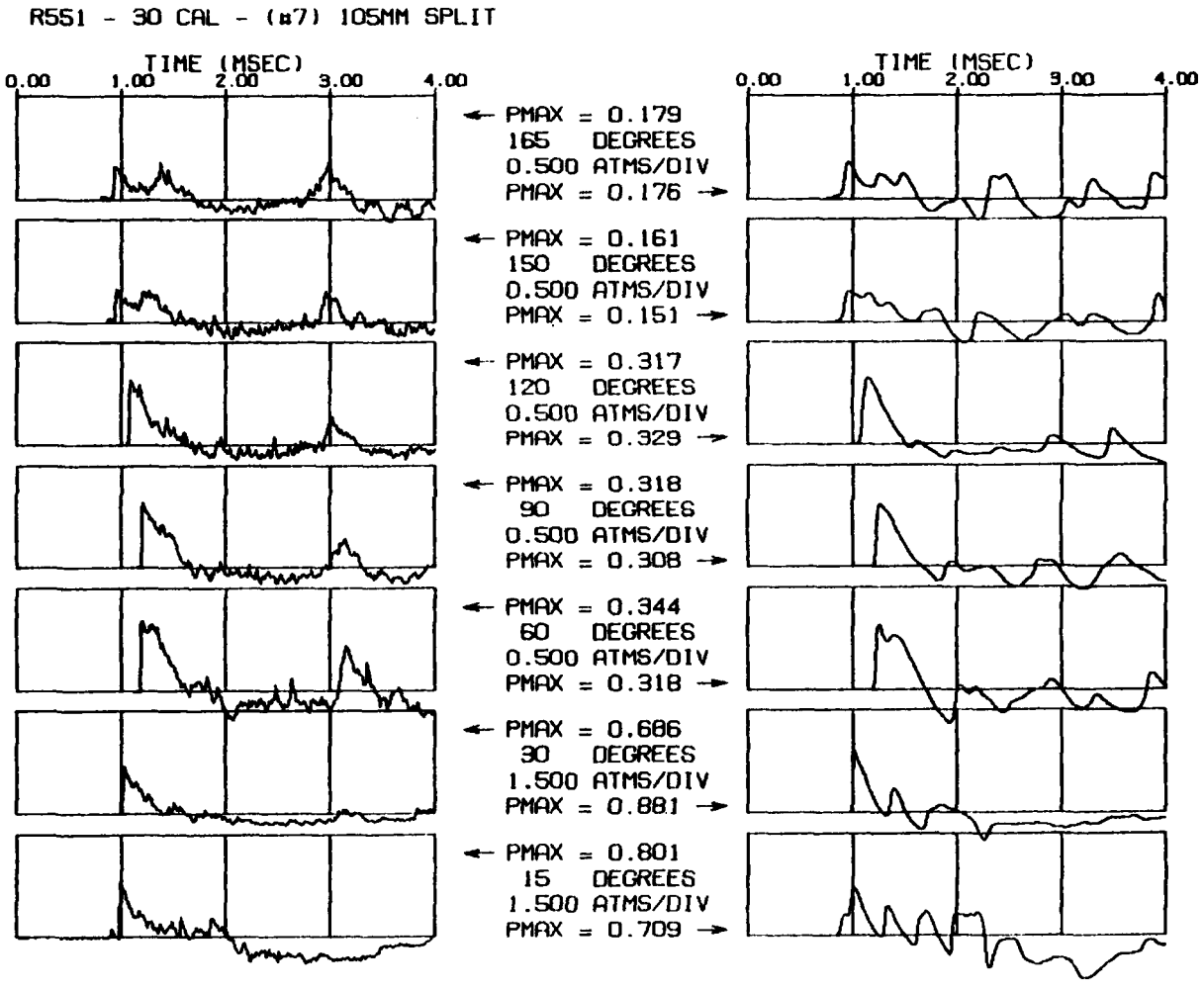

Figure 14. Pressure-time histories for the split brake at 30 calibers (round 19551, Appendix B).

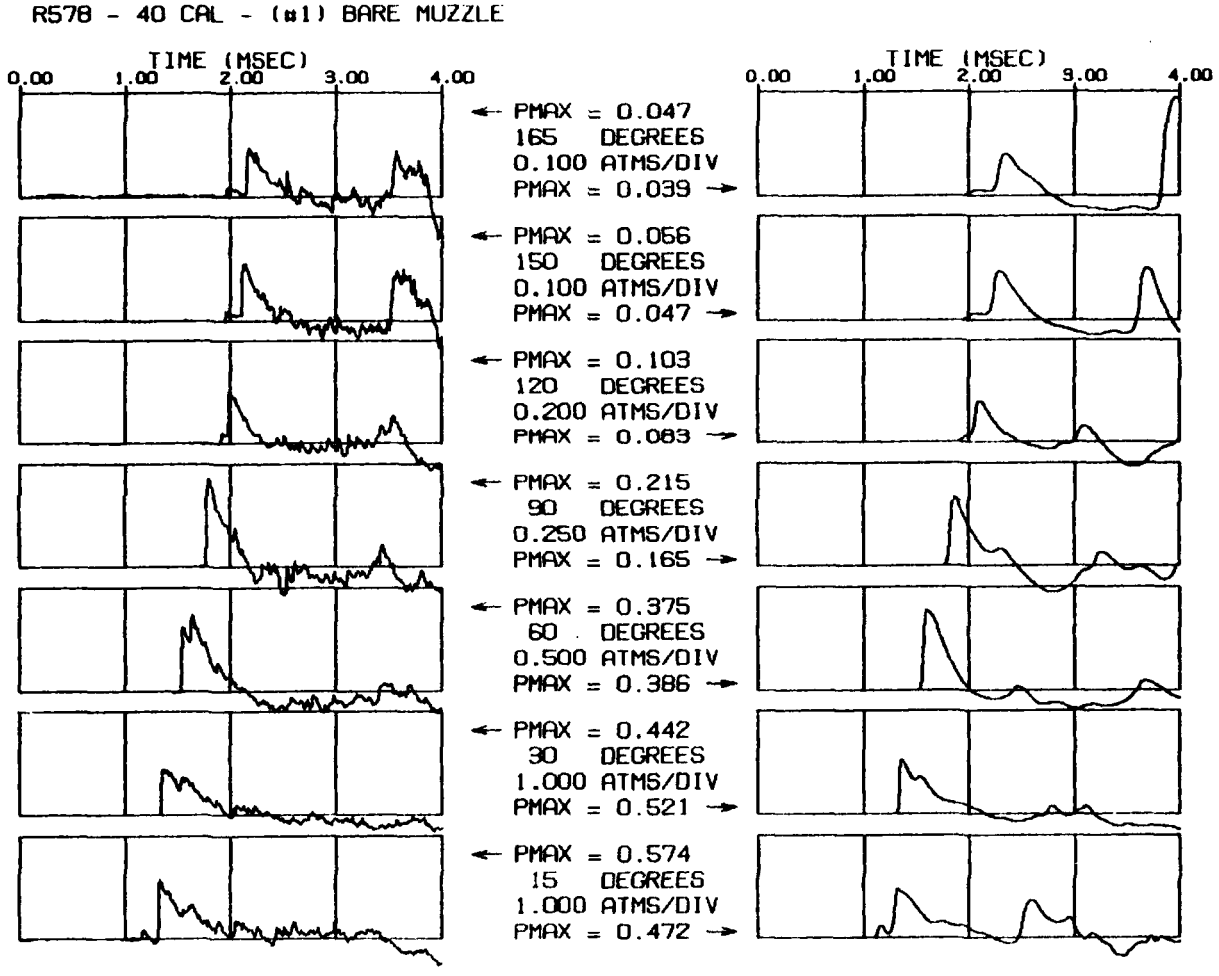

Figure 15. Pressure-time histories for the bare muzzle case at 40 calibers (round 19578, Appendix B).

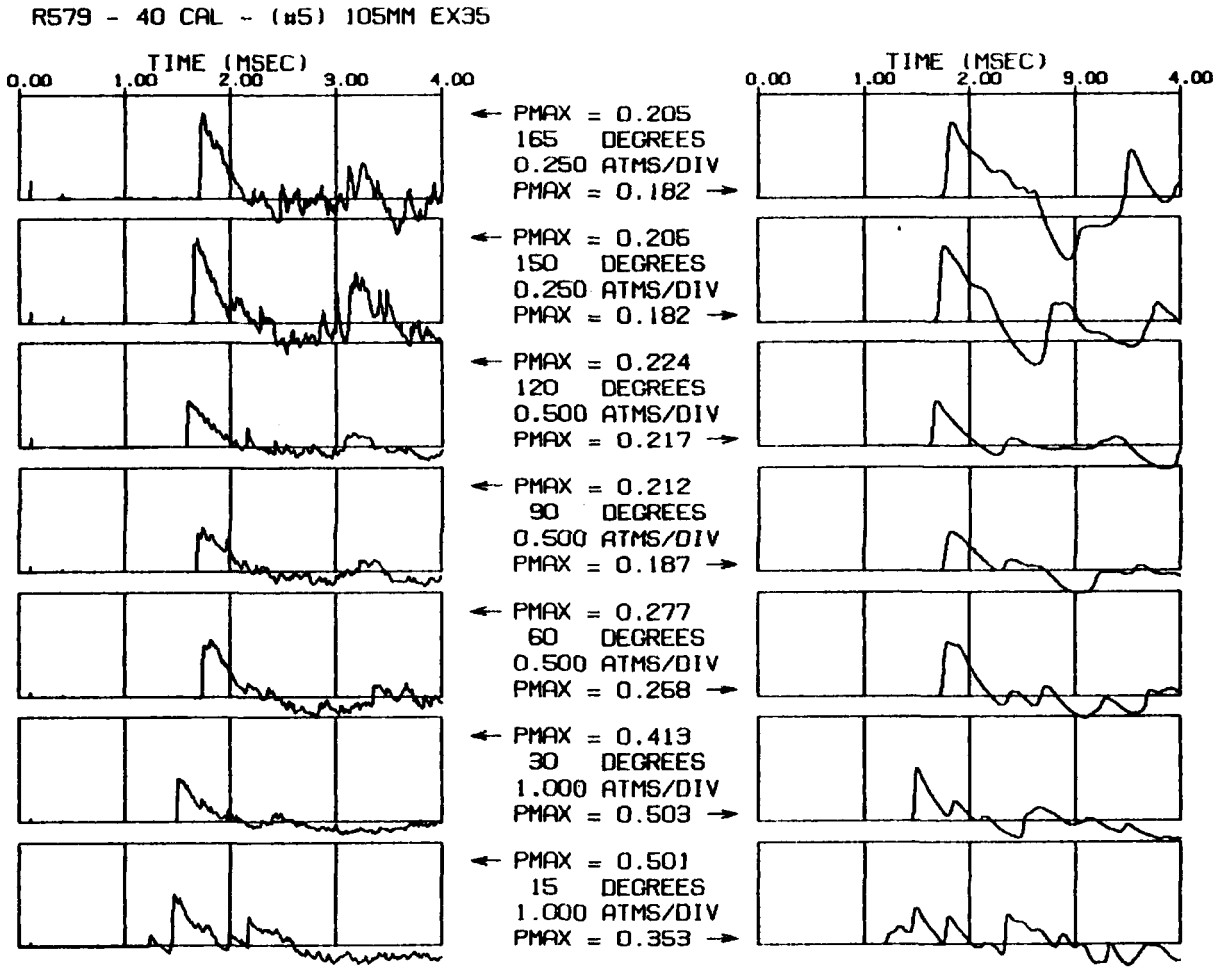

Figure 16. Pressure-time histories for the standard brake at 40 calibers (round 19579, Appendix B).

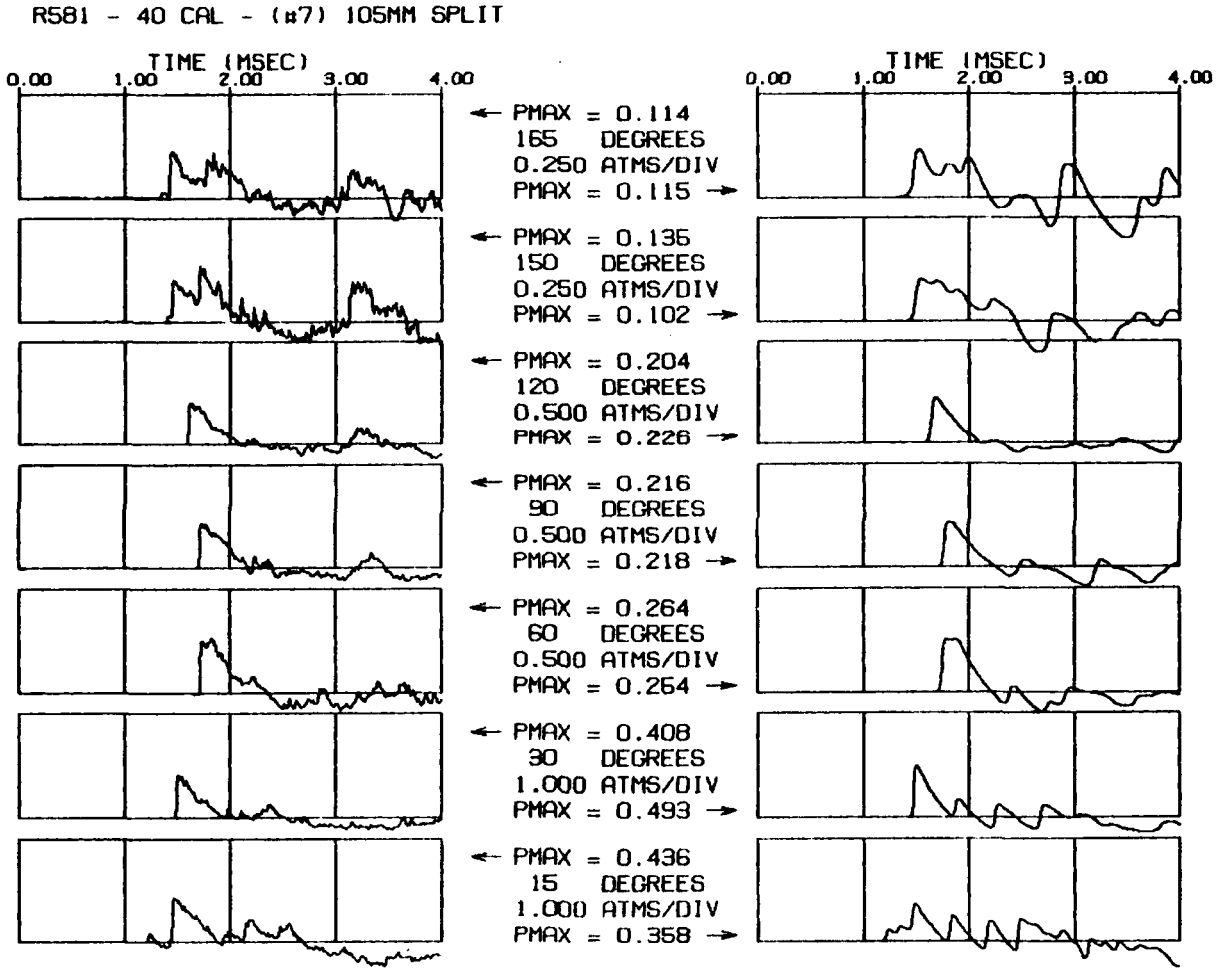

Figure 17. Pressure-time histories for the split brake at 40 calibers (round 19581, Appendix B).

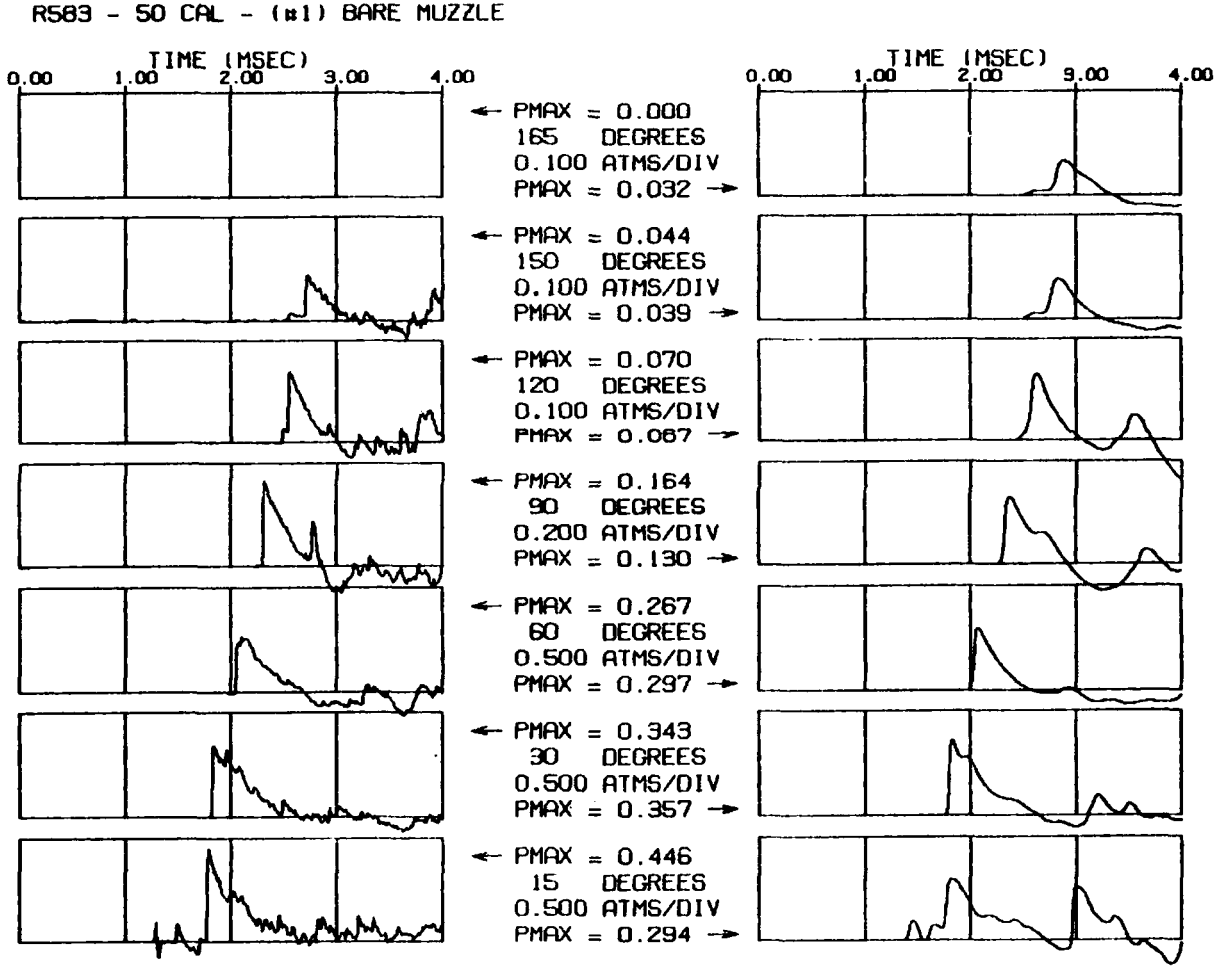

Figure 18. Pressure-time histories for the bare muzzle case at 50 calibers (round 19583, Appendix B).

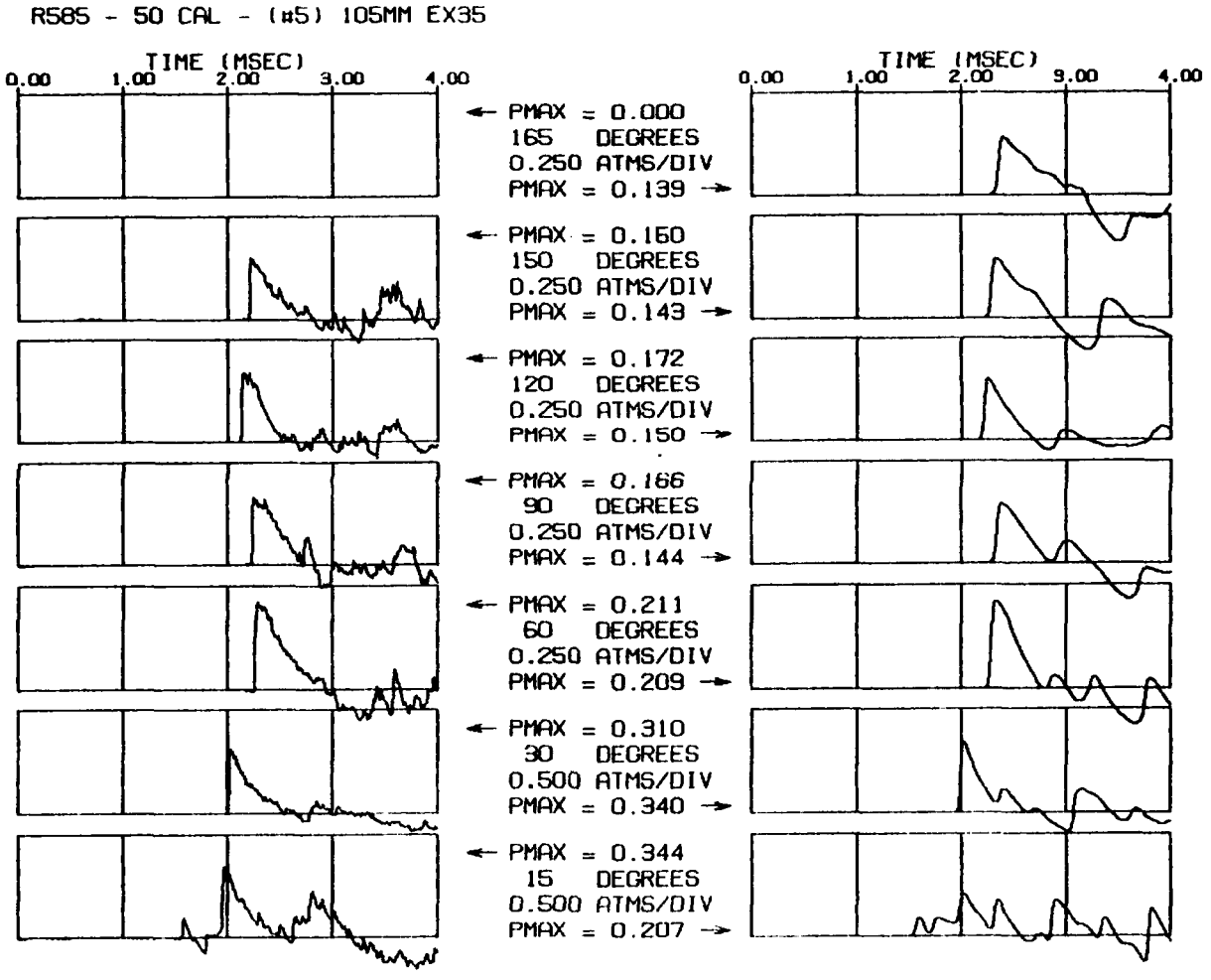

Figure 19. Pressure-time histories for the standard brake at 50 calibers (round 19585, Appendix B).

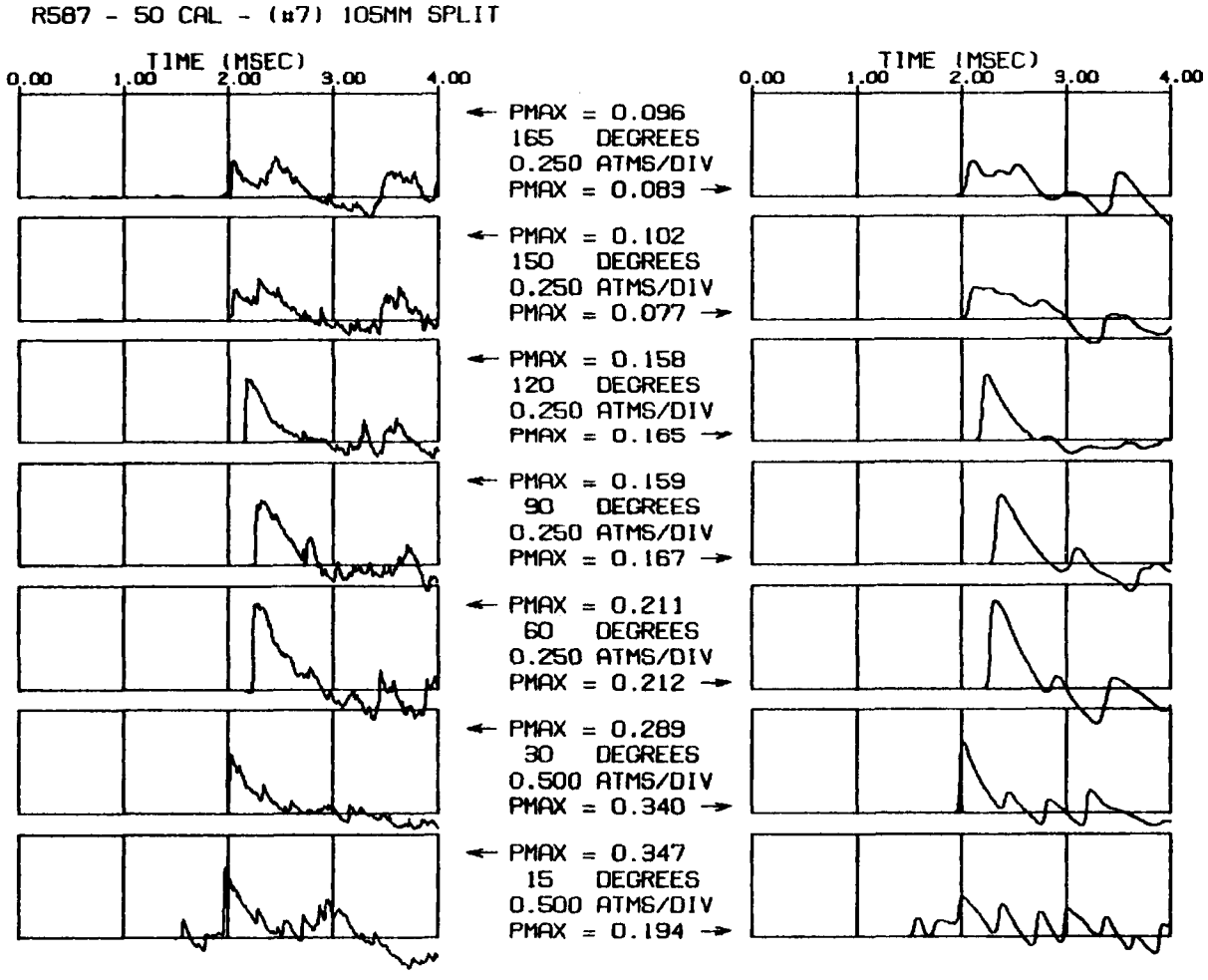

Figure 20. Pressure-time histories for the split brake at 50 calibers (round 19587, Appendix B).

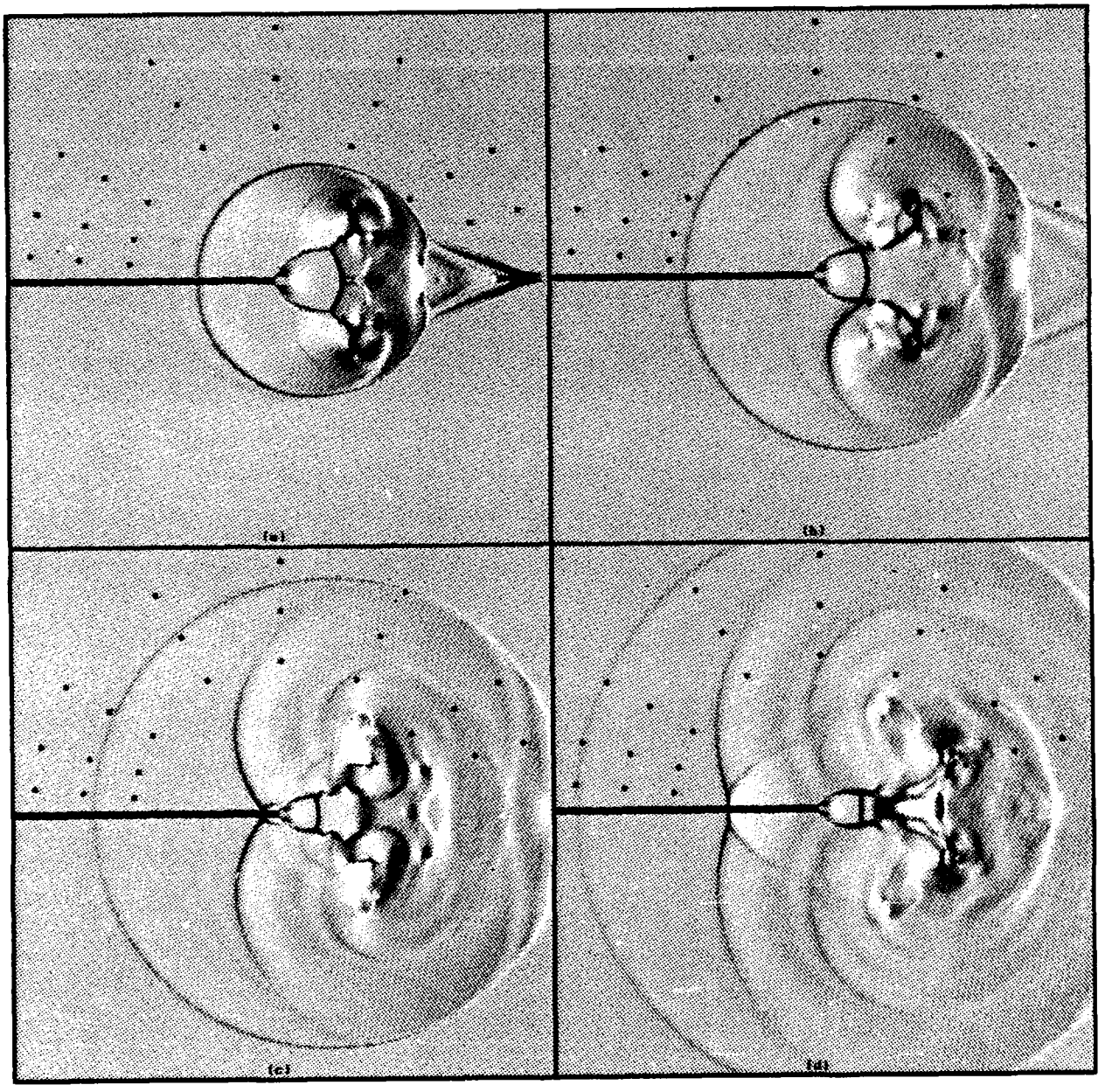

Figure 21. Set of surface plots for the bare muzzle case taken at (a) 0.906 msec, (b) 1.501 msec, (c) 2.132 msec, and (d) 2.791 msec.

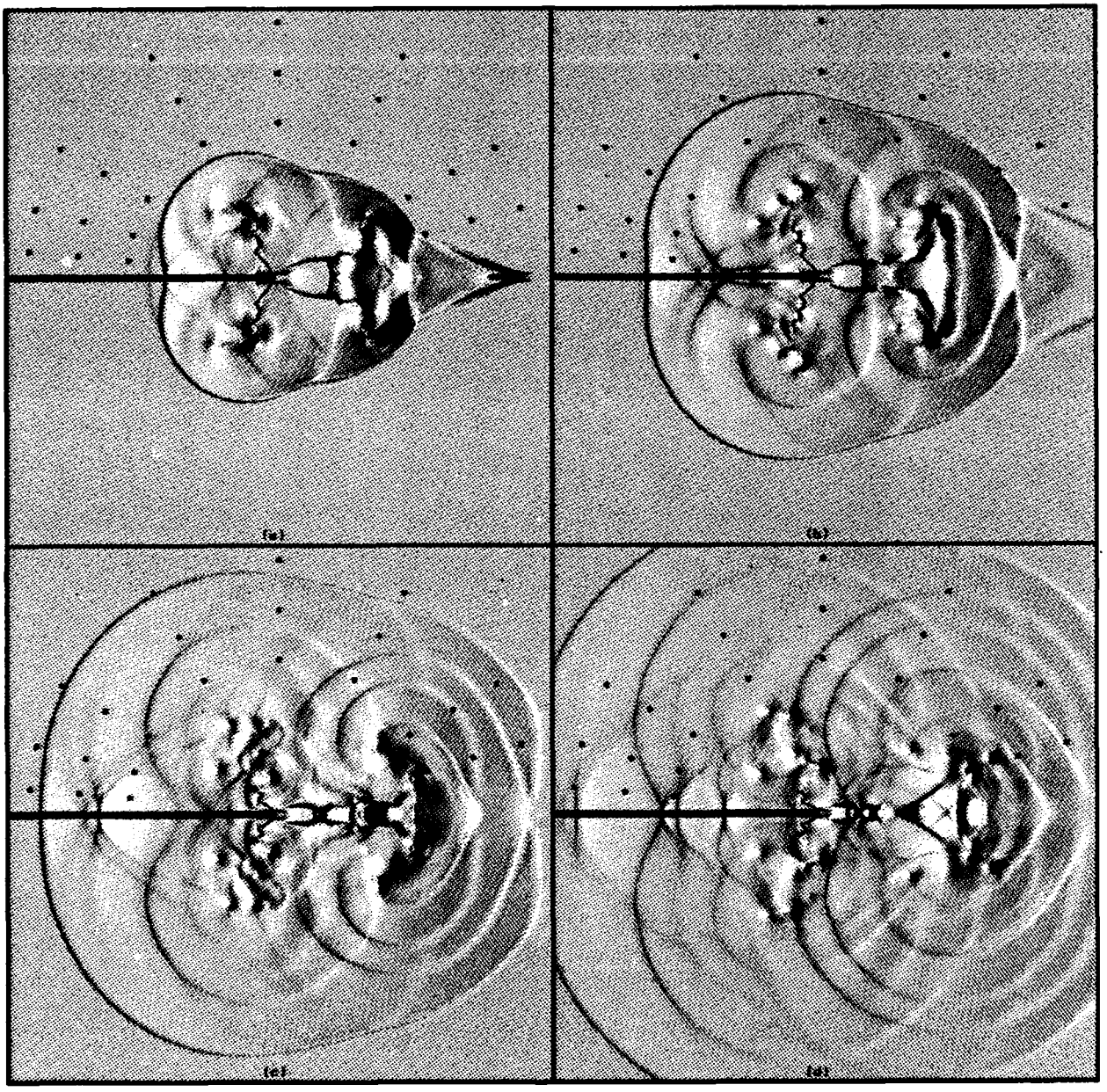

Figure 22. Set of surface plots for the standard brake case taken at (a) 0.972 msec, (b) 1.569 msec, (c) 2.203 msec, and (d) 2.866 msec.

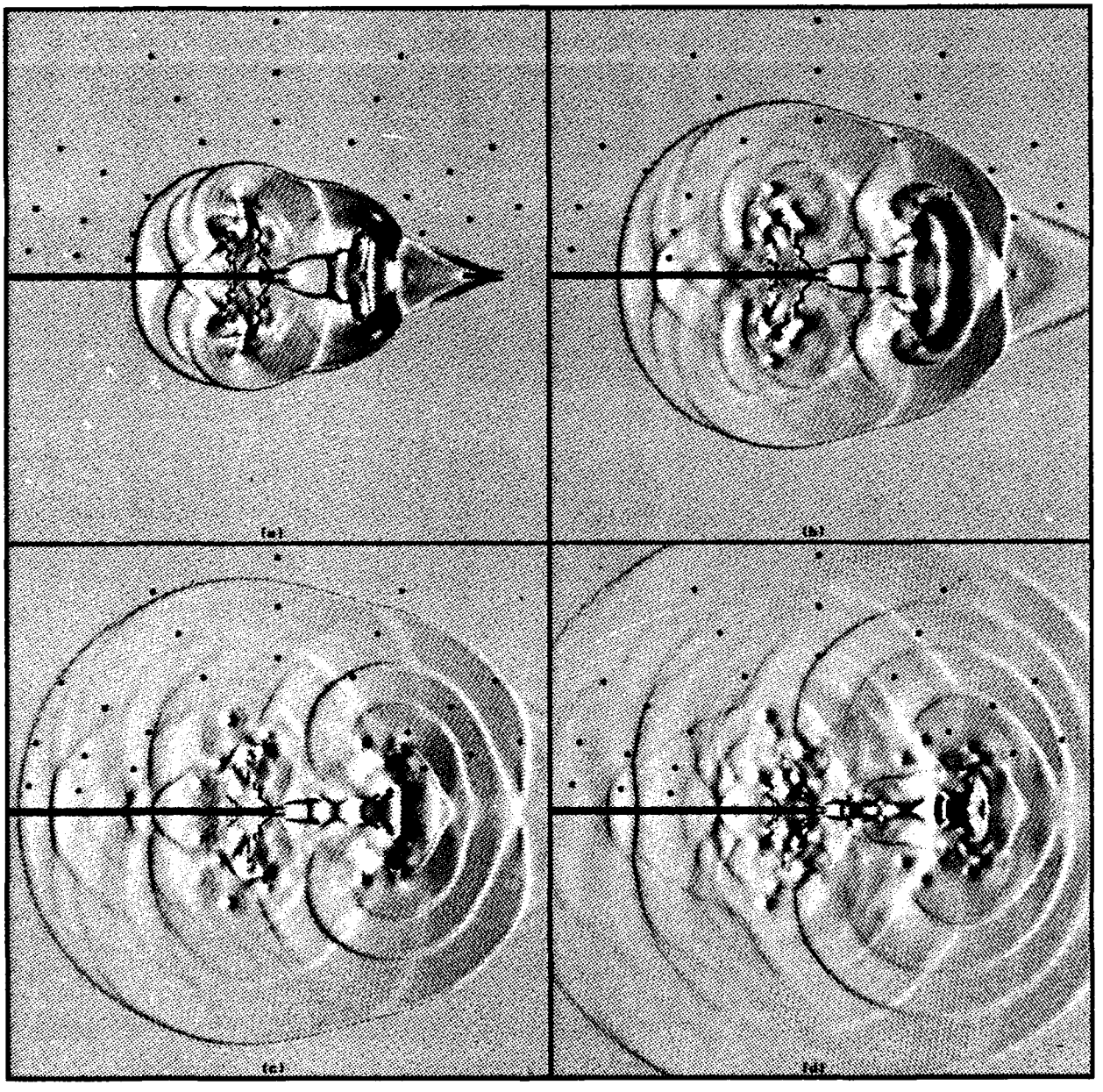

Figure 23. Set of surface plots for the split brake case taken at (a) 0.867 msec, (b) 1.462 msec, (c) 2.096 msec, and (d) 2.758 msec.

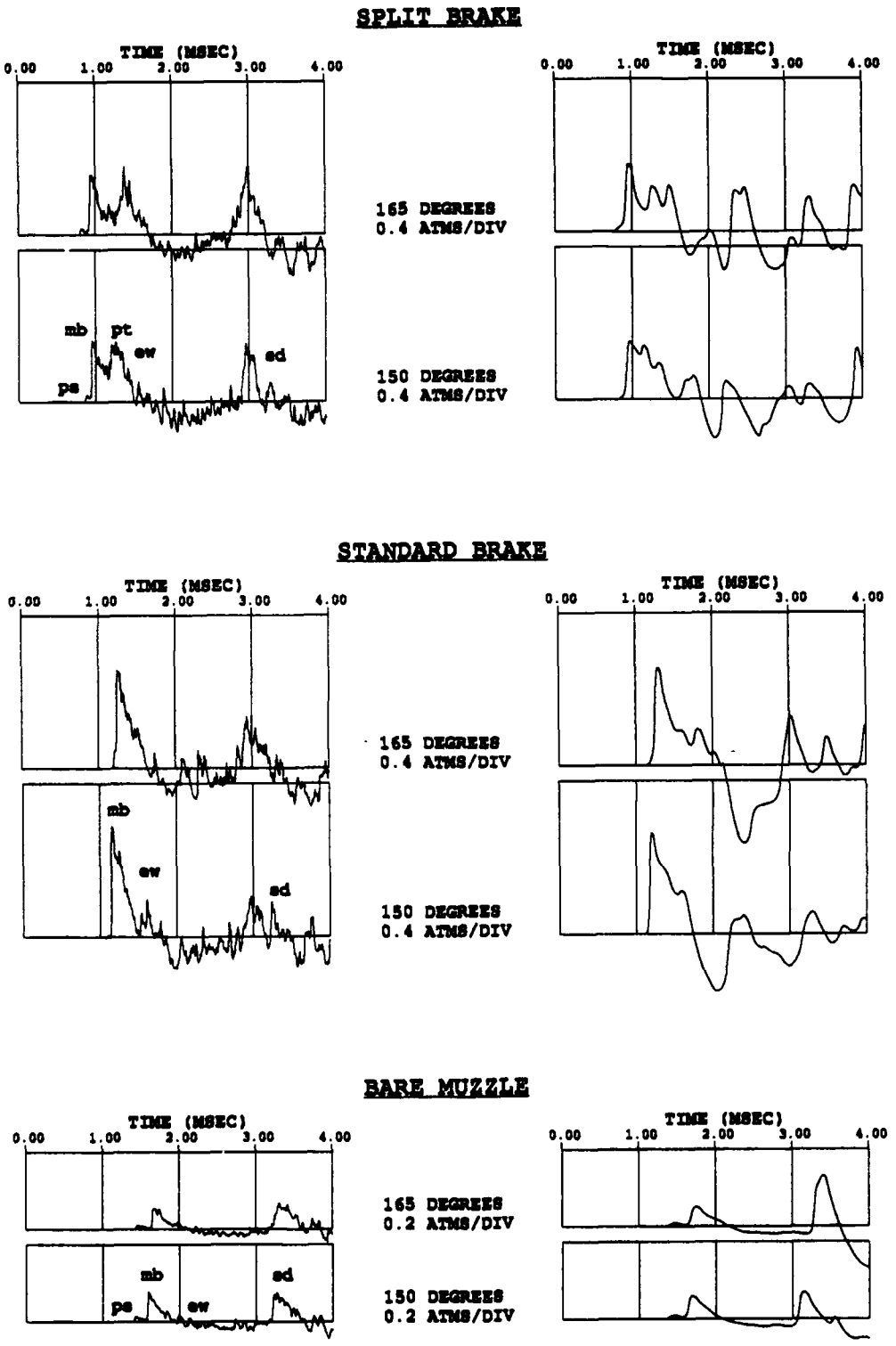

Figure 24. The pressure histories at the upstream transducer locations at 30 calibers for the three extensions.

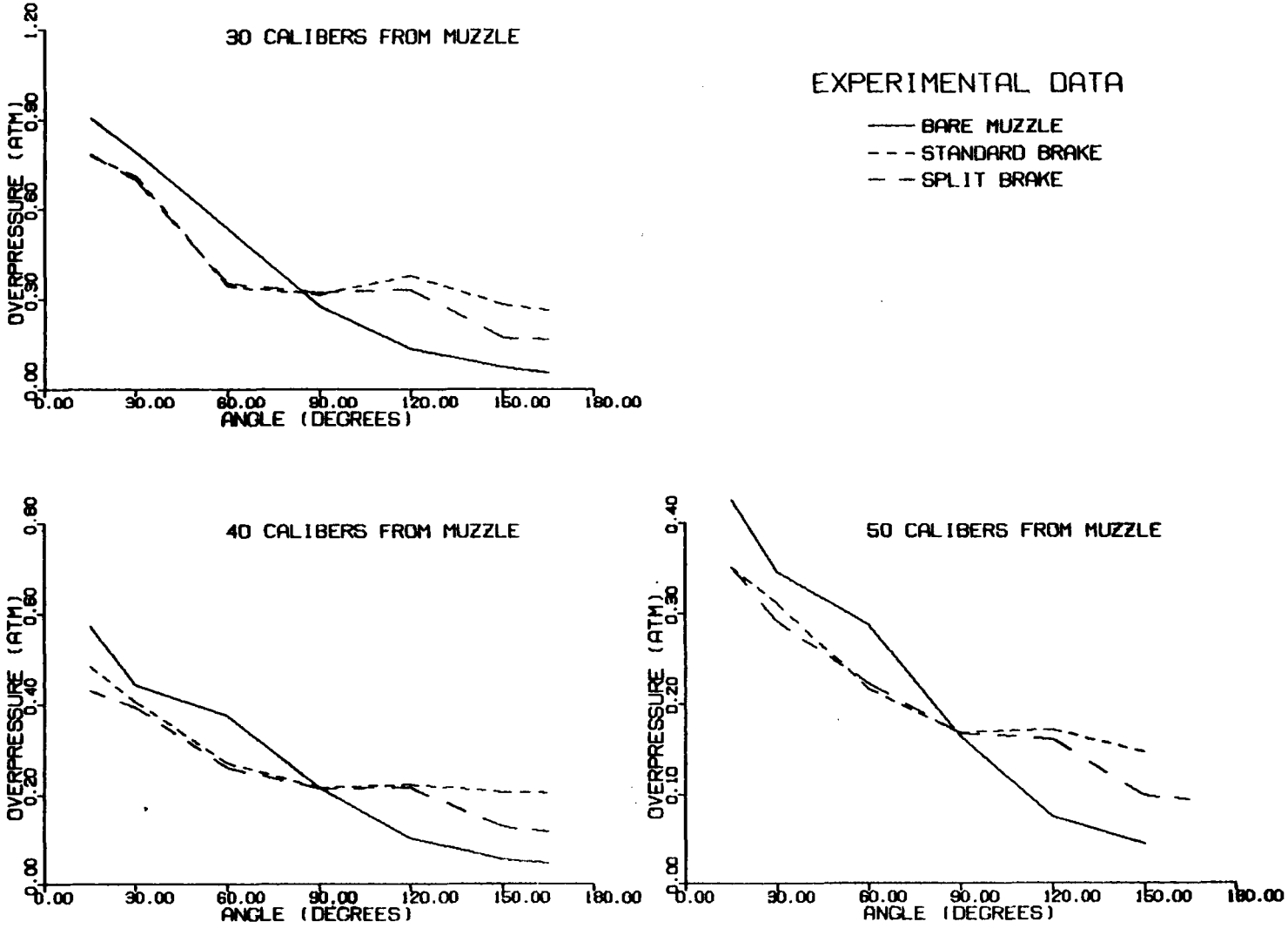

Figure 25. Summary of experimental overpressure data for the three extensions.

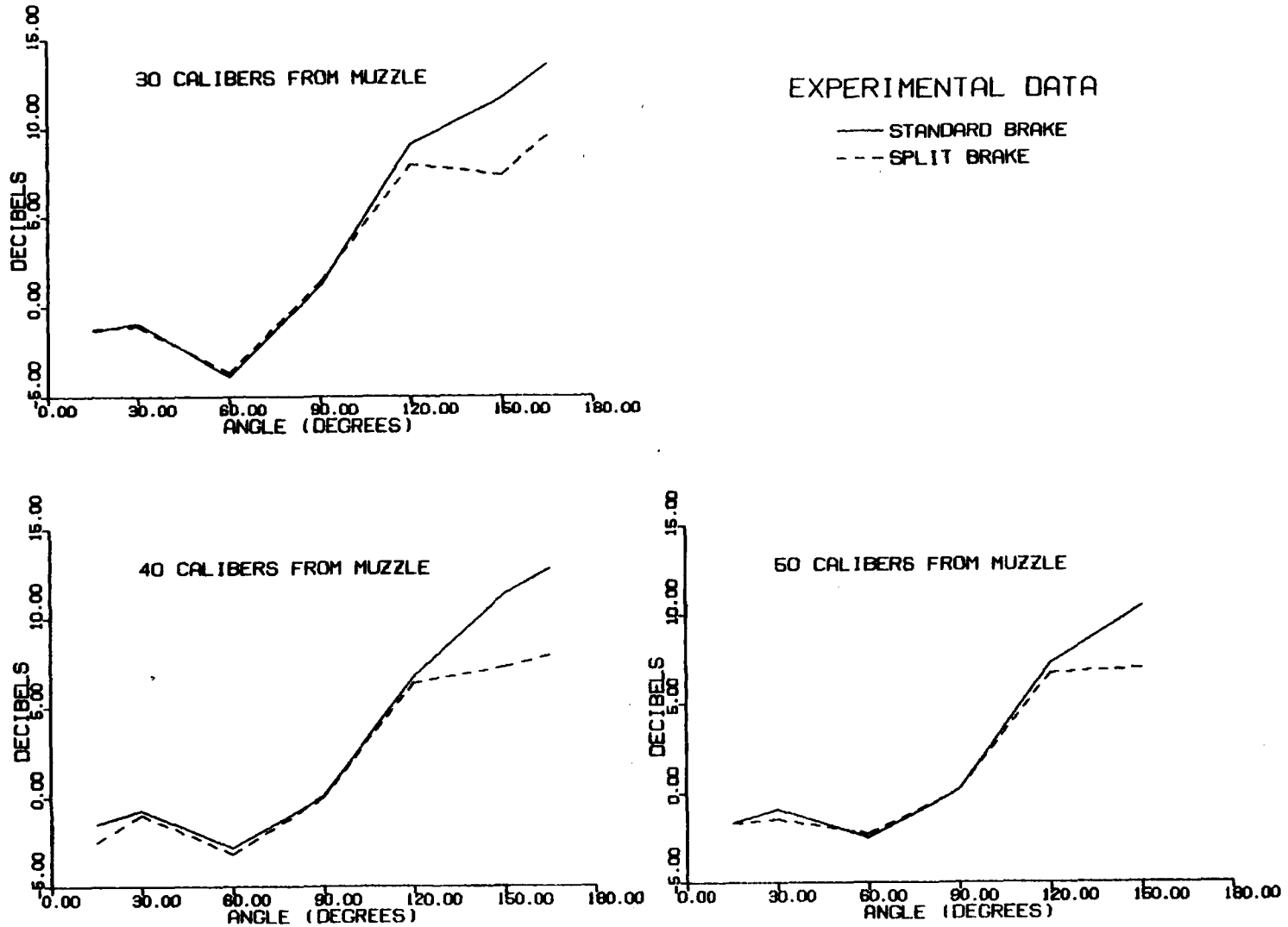

Figure 26. Comparison of experimental overpressure data, measured in decibels, for the two brake extensions.

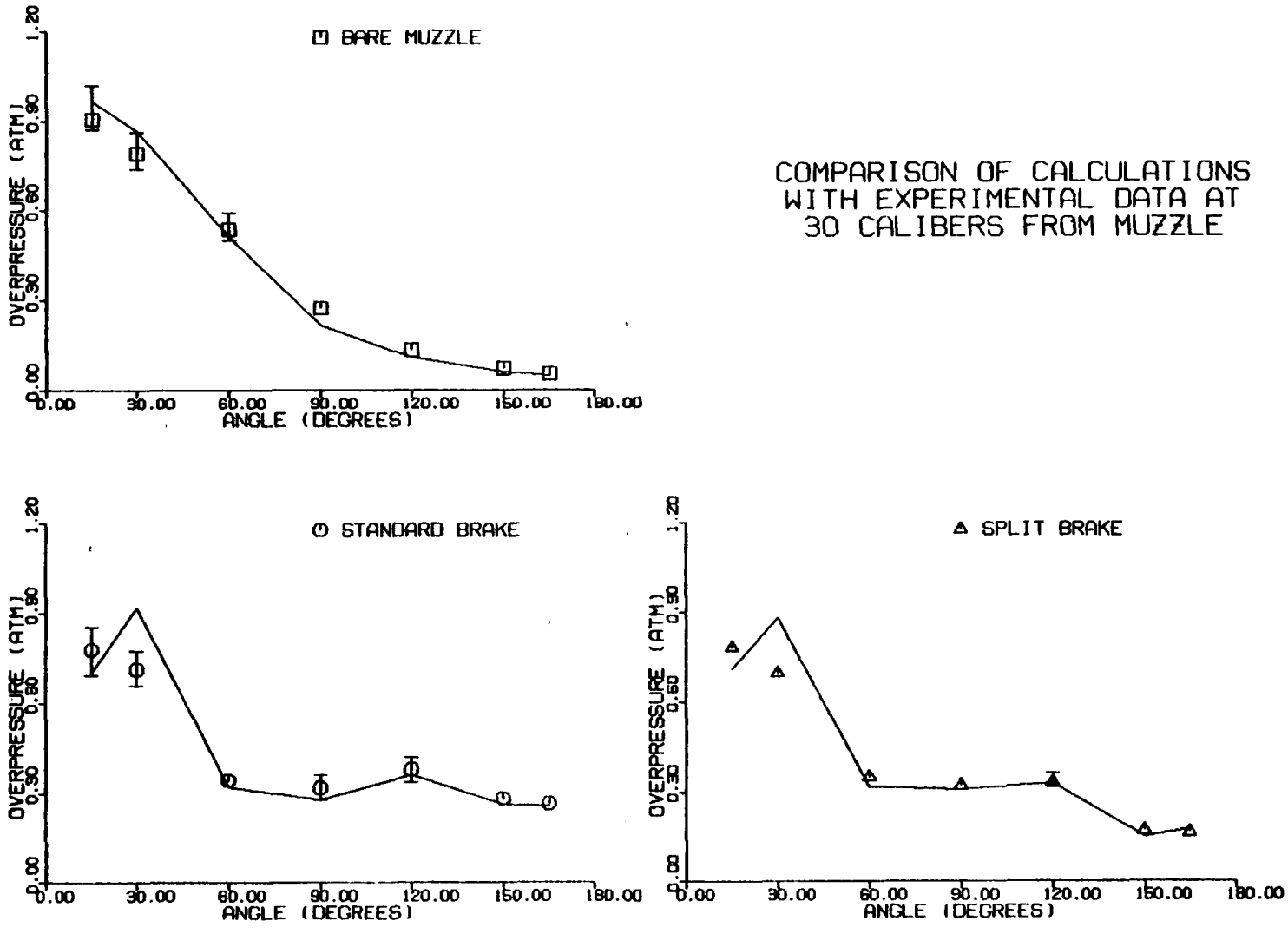

Figure 27. Comparison of model predictions (solid lines) with experimental free-field overpressure data at a 30-caliber radius.

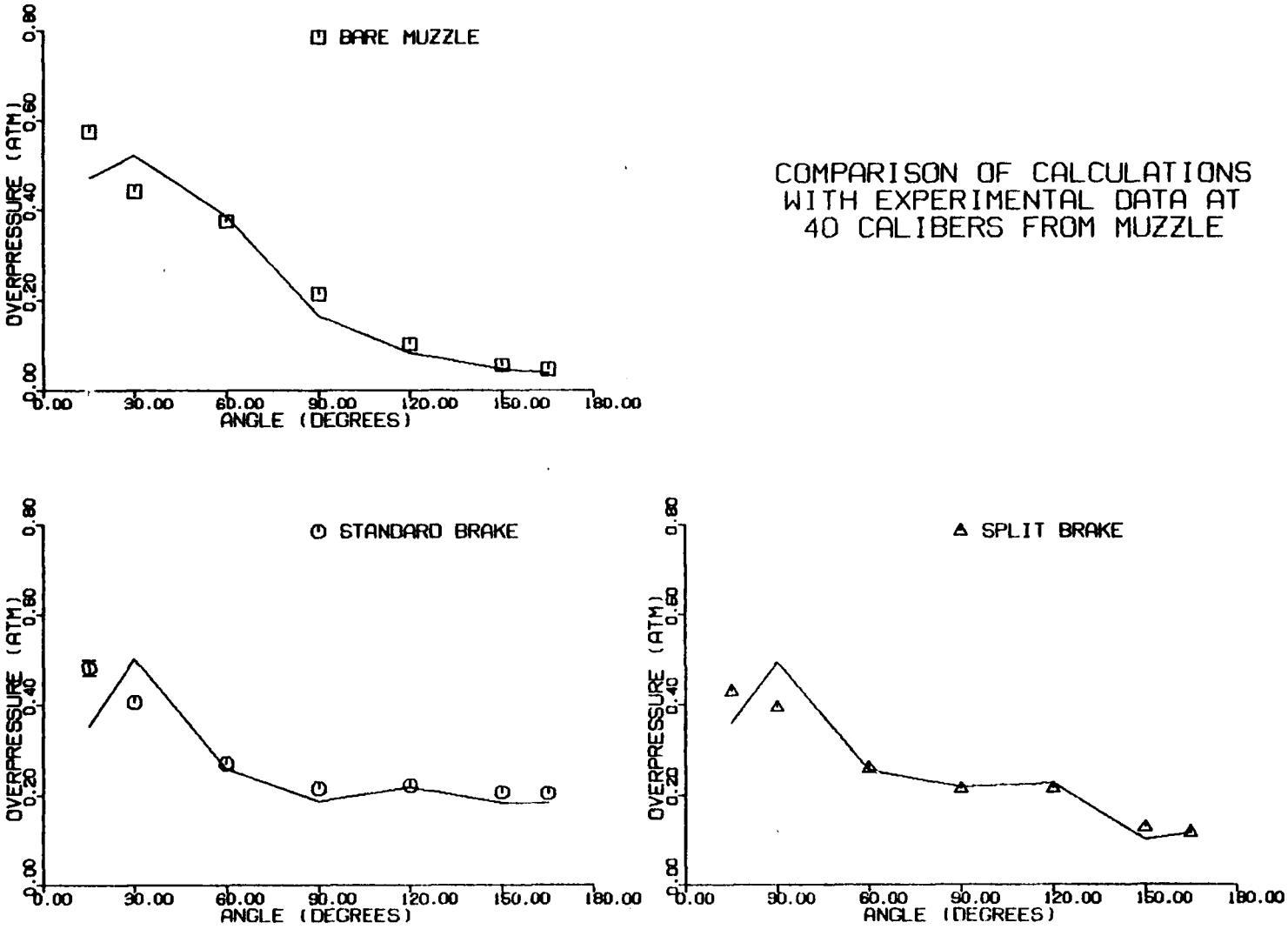

Figure 28. Comparison of model predictions (solid lines) with experimental free-field overpressure data at a 40-caliber radius.

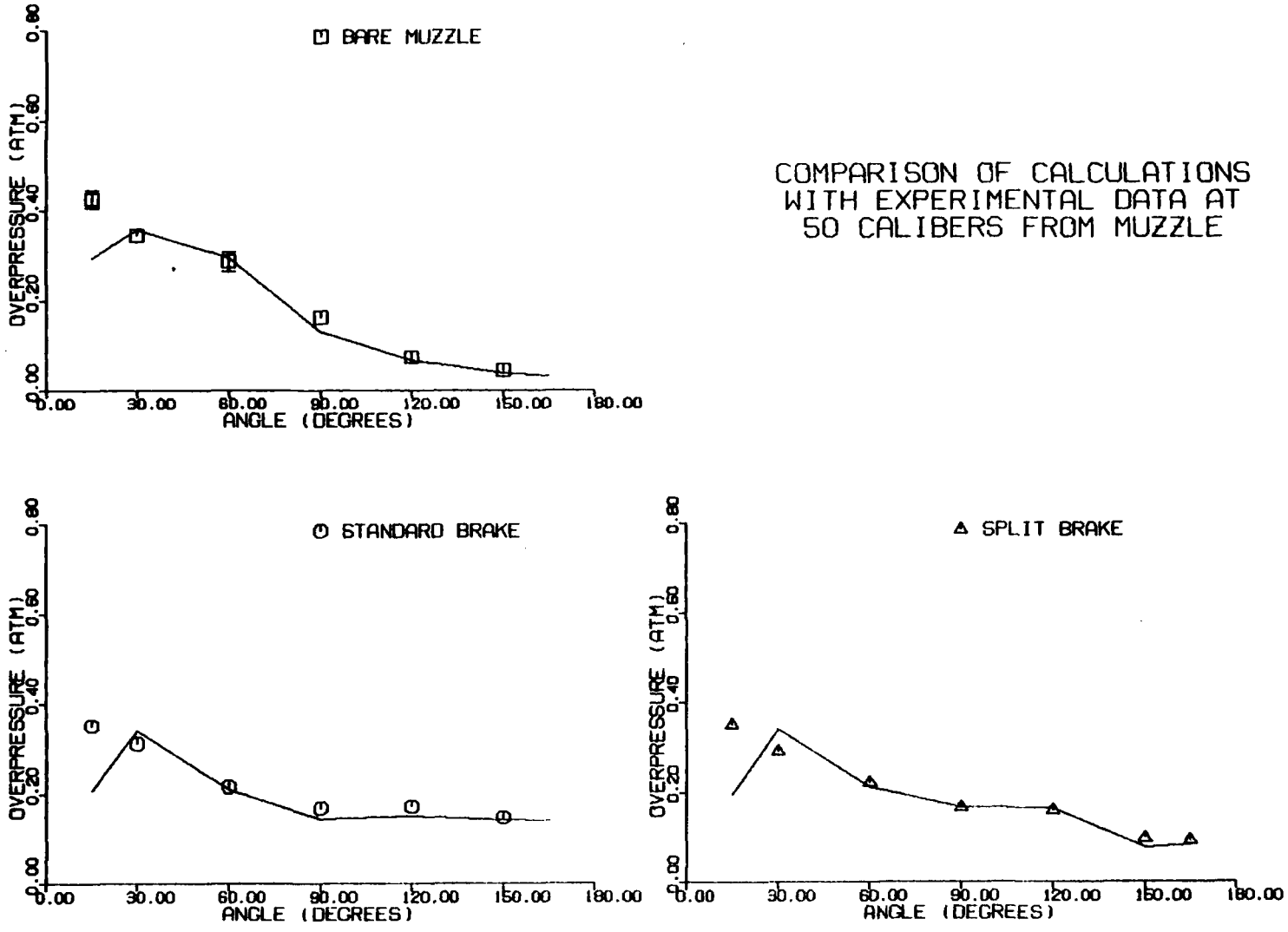

Figure 29. Comparison of model predictions (solid lines) with experimental free-field overpessure data at a 50-caliber radius.

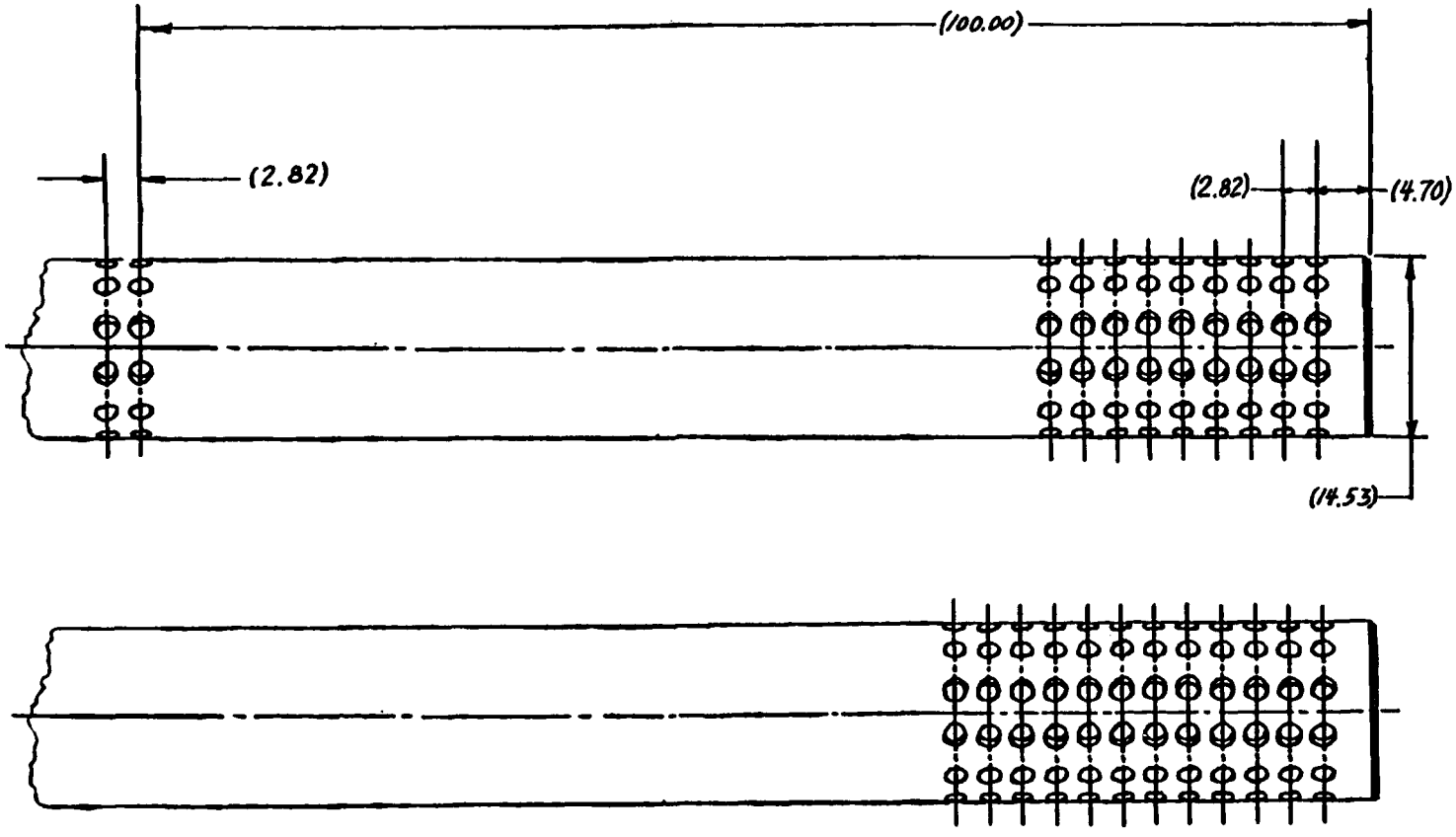

Figure 30. Drawing of the 105-mm brakes used in the field experiments. The standard brake used only the twelve rows of vents near the muzzle. For the split brake, the three rows of vents nearest the breech were covered and two rows of vents were added upstream. Dimensions are in centimeters.

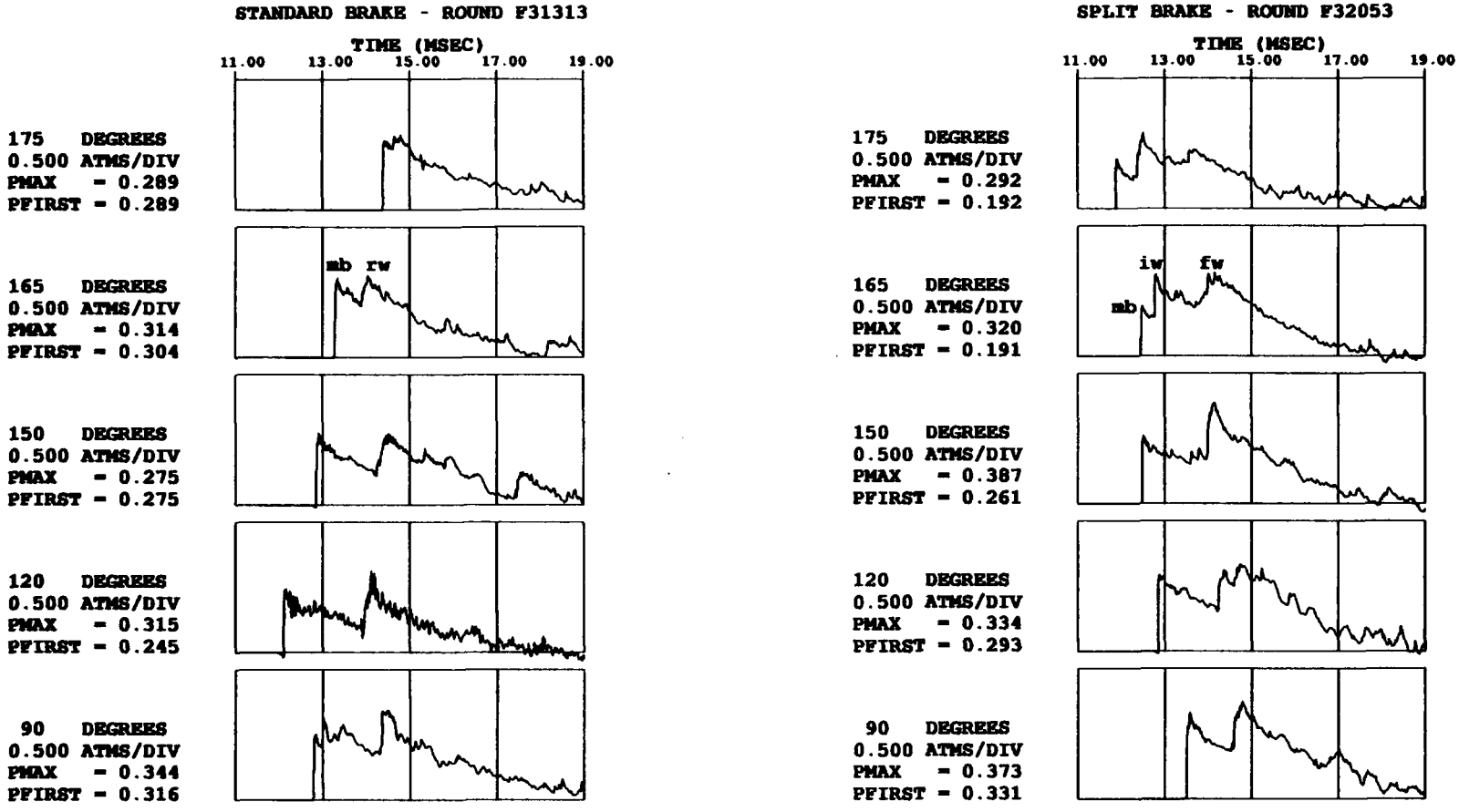

Figure 31. Comparison of experimental overpressure data at 60 calibers for the two 105-mm brakes. M490 ammunition was used in the tests. PMAX is the maximum pressure for the trace. PFIRST is the magnitude of the first wave to arrive in the trace.

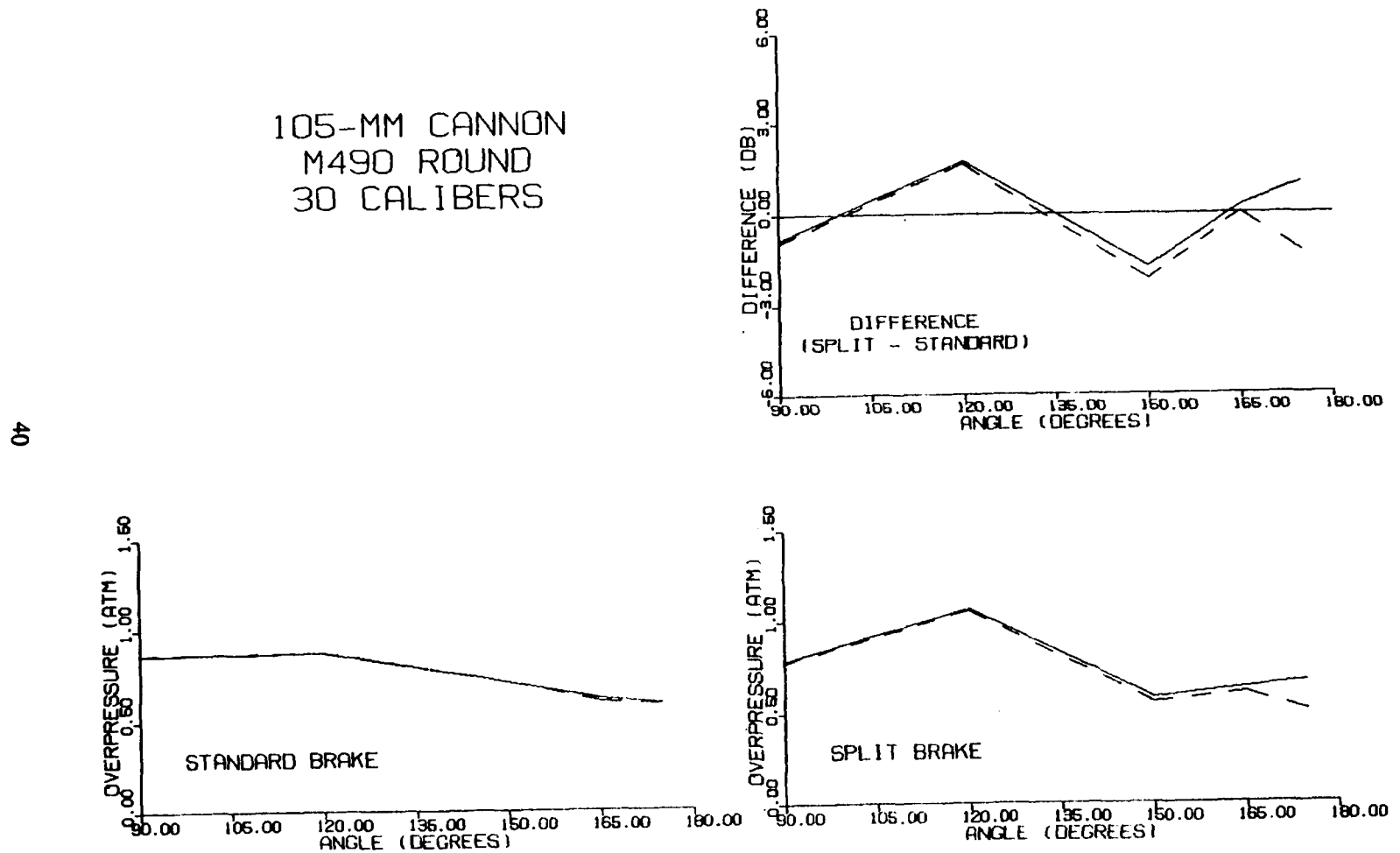

Figure 32. Summary of peak overpressure data for the two 105-mm brakes at 30 calibers using M490 ammunition. The solid line is the maximum pressure for the trace. The dashed line represents the magnitude of the first wave to arrive in the trace.

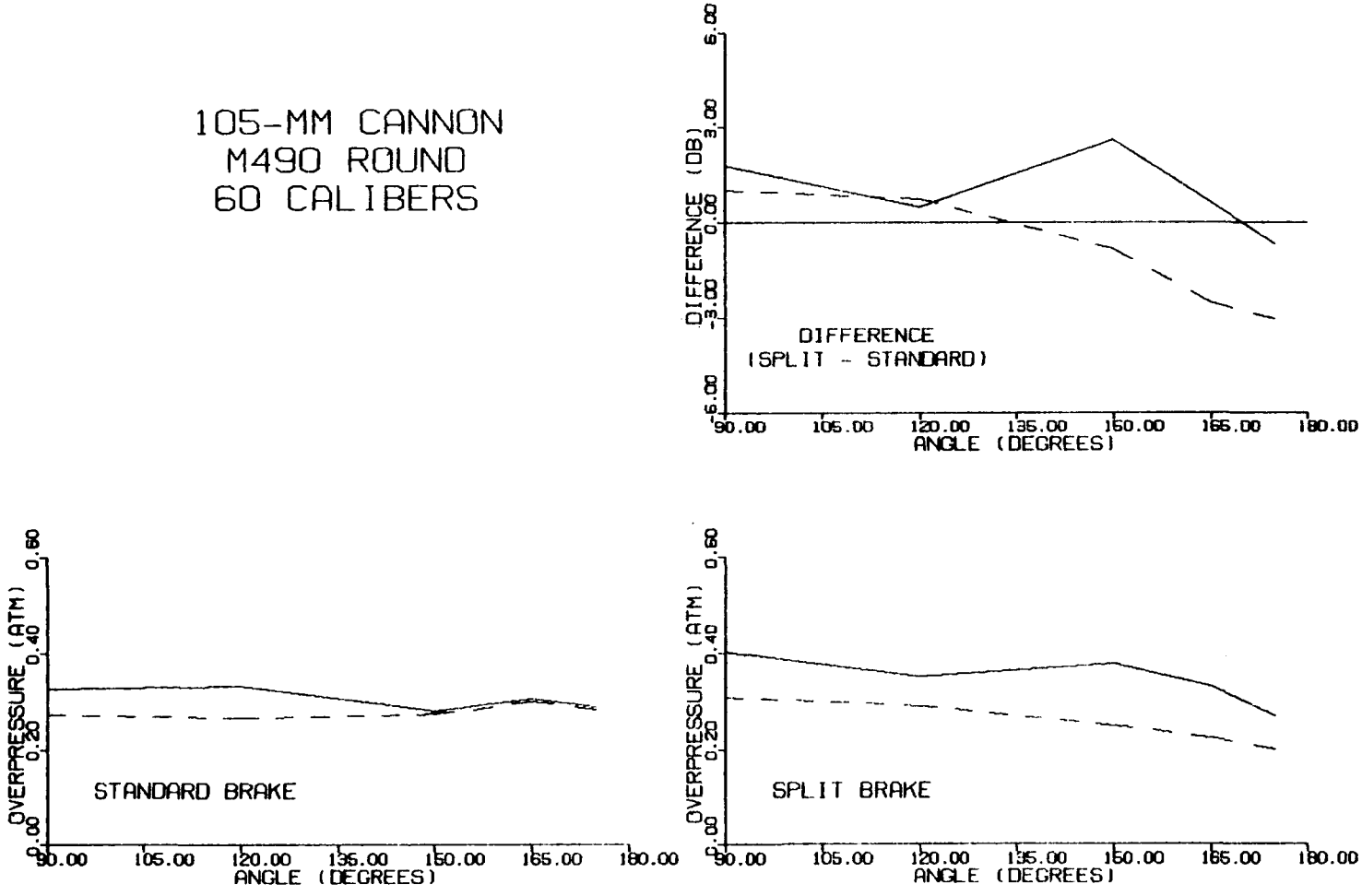

Figure 33. Summary of peak overpressure data for the two 105-mm brakes at 60 calibers using M490 ammunition. The solid line is the maximum pressure for the trace. The dashed line represents the magnitude of the first wave to arrive in the trace.

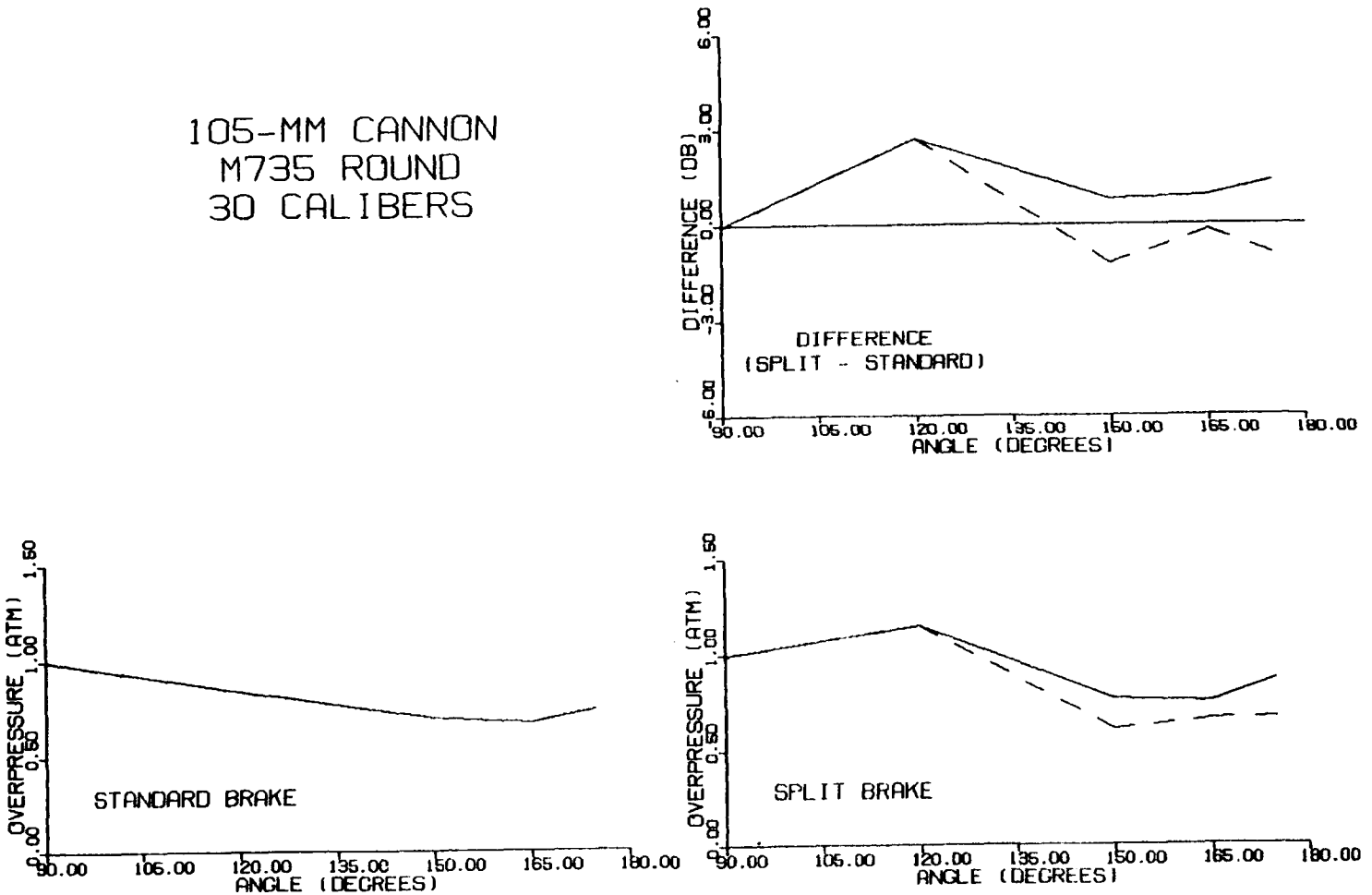

Figure 34. Summary of peak overpressure data for the two 105-mm brakes at 30 calibers using M735 ammunition. The solid line is the maximum pressure for the trace. The dashed line represents the magnitude of the first wave to arrive in the trace.

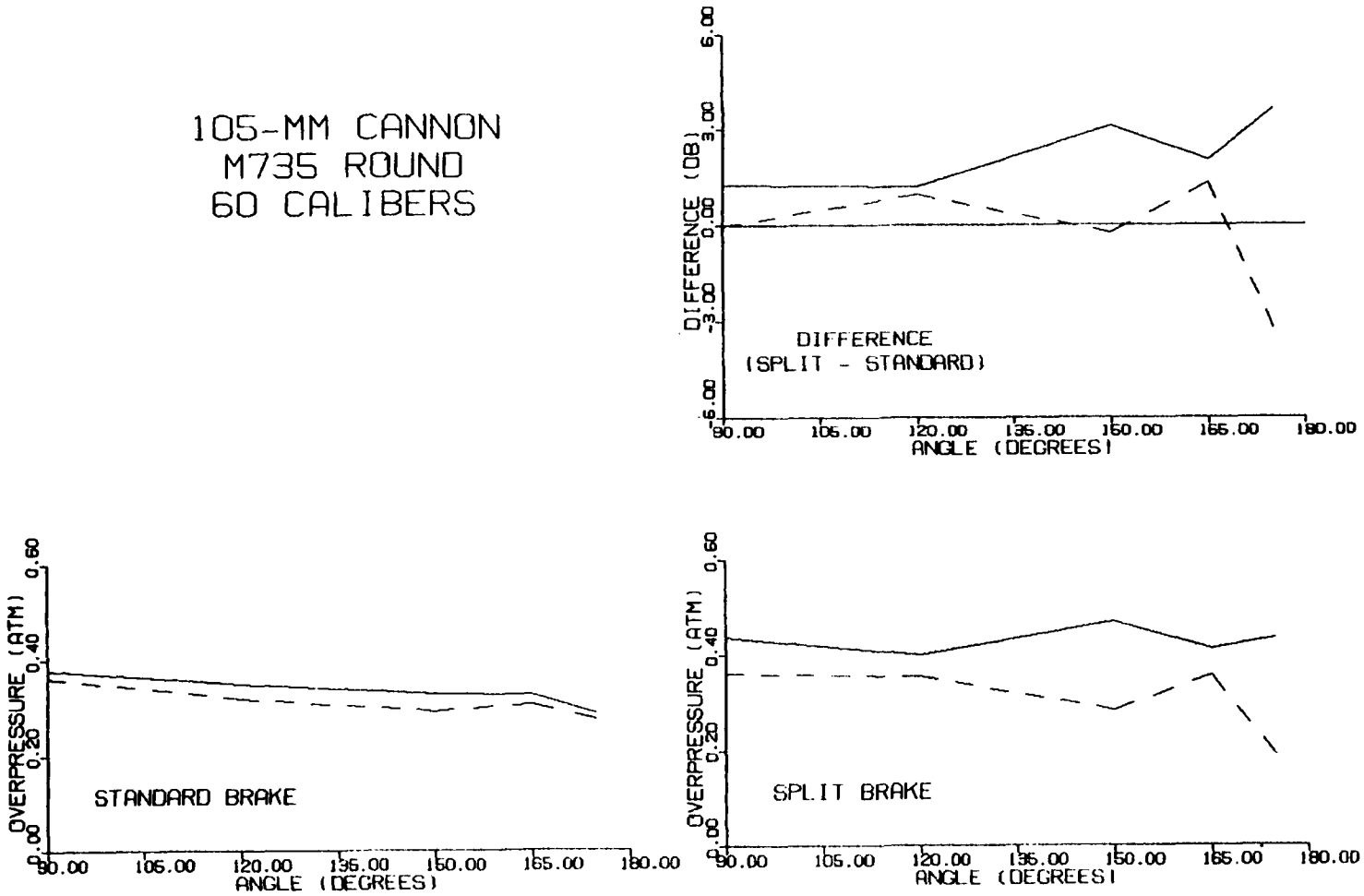

Figure 35. Summary of peak overpressure data for the two 105-mm brakes at 60 calibers using M735 ammunition. The solid line is the maximum pressure for the trace. The dashed line represents the magnitude of the first wave to arrive in the trace.

APPENDIX A

This appendix contains scaled drawings of the three extensions used in the experiments. Note that the dimensions are in English units, not metric units as used elsewhere in this report. Each extension was the same length.

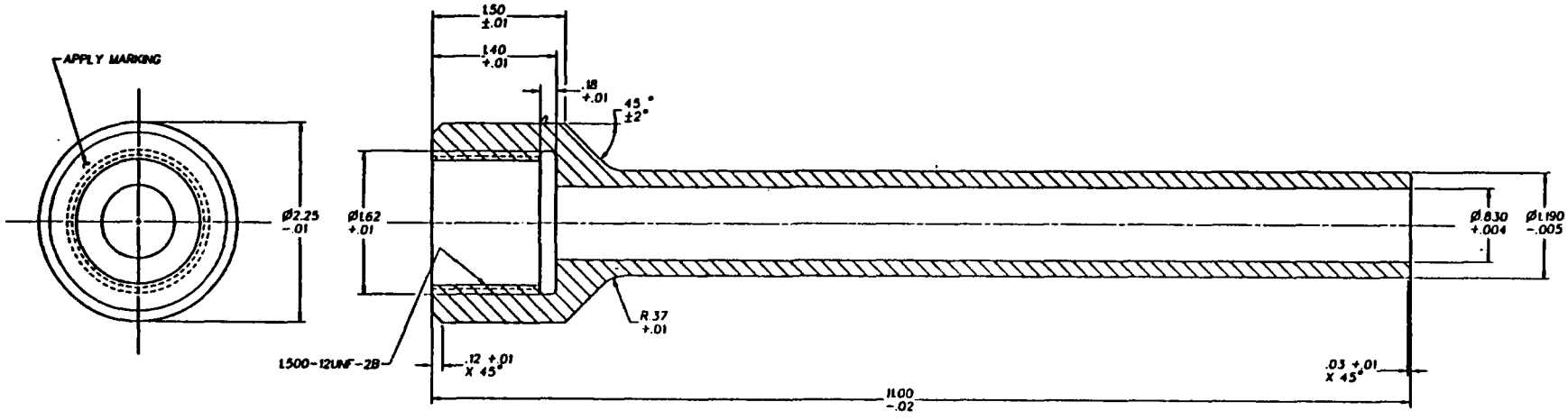

Figure A1. Scaled drawing of the bare muzzle extension.

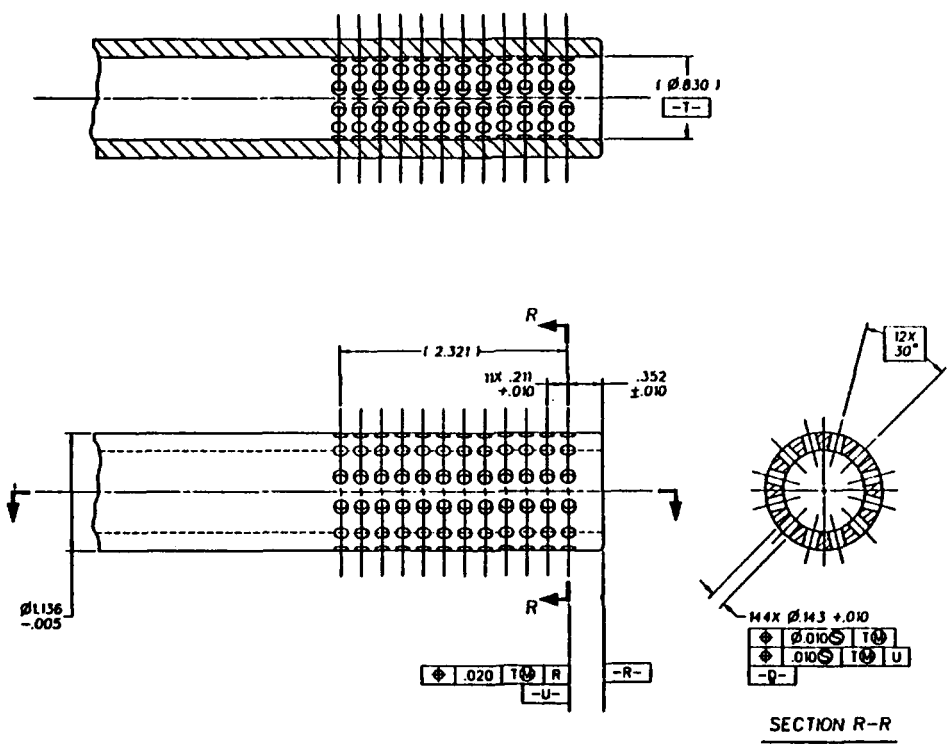

Figure A2. Scaled drawing of the standard brake extension.

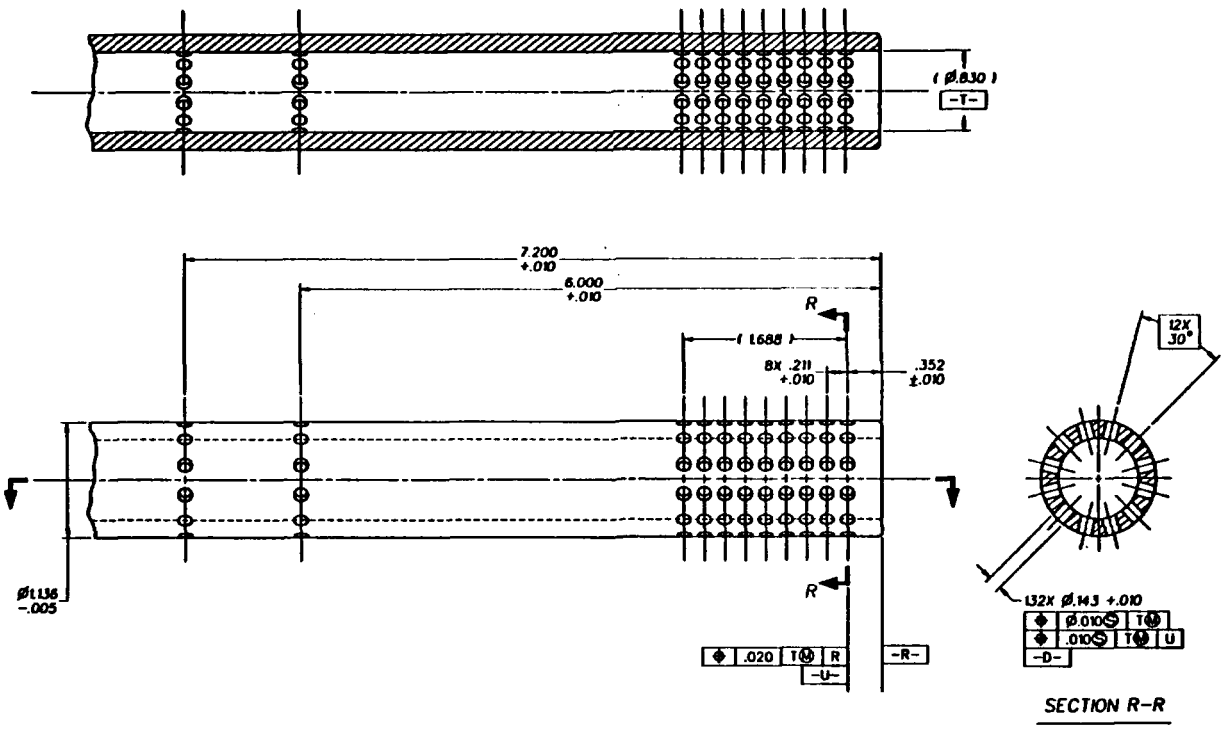

Figure A3. Scaled drawing of the split brake extension.

APPENDIX B

The data presented in this appendix were obtained as part of a brake efficiency study to be reported elsewhere (ref 10). Fifty-nine rounds were fired in that program, thirty-five of which pertain to this study. For consistency, the round number identifier used in the efficiency study is retained here, therefore some gaps appear in the figures below.

For each round, a set of pressure histories is given on the left-hand page and the corresponding shadowgraph is given on the right-hand page. In some cases, data at one or more of the transducer locations is missing, in others, the shadowgraph is missing. When constructing the overpressure plots in Figures 24 through 28 of the report, only those rounds for which data were available at every transducer location were used. An exception was made for rounds 19583 through 19586 where the trace at the 165-degree position is missing. Because these were the only data sets available at 50 calibers, the information had to be used. To avoid confusion, the data used in the report is specified in the figure captions.

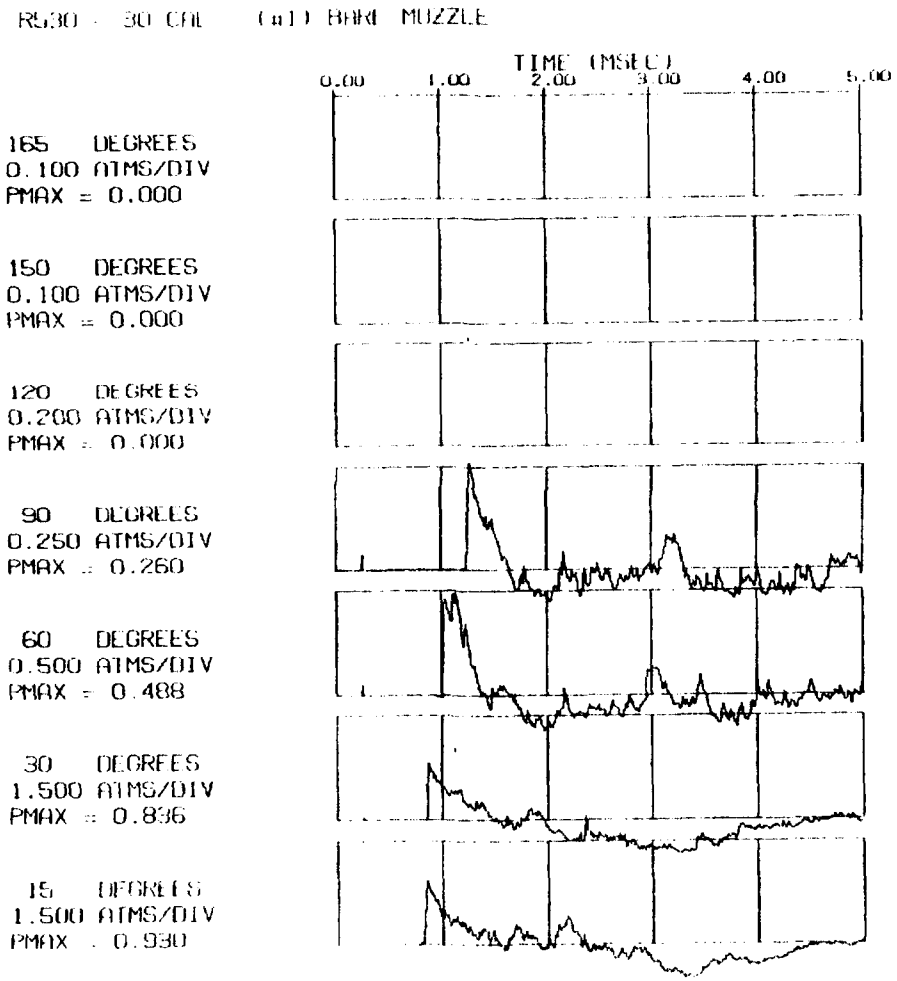

Figure B1a. Pressure histories for round 19530, bare muzzle, at 30 calibers. Data not used in report figures.

Figure B1b. Shadowgraph for round 19530, bare muzzle, taken with a 15-microsecond time delay.

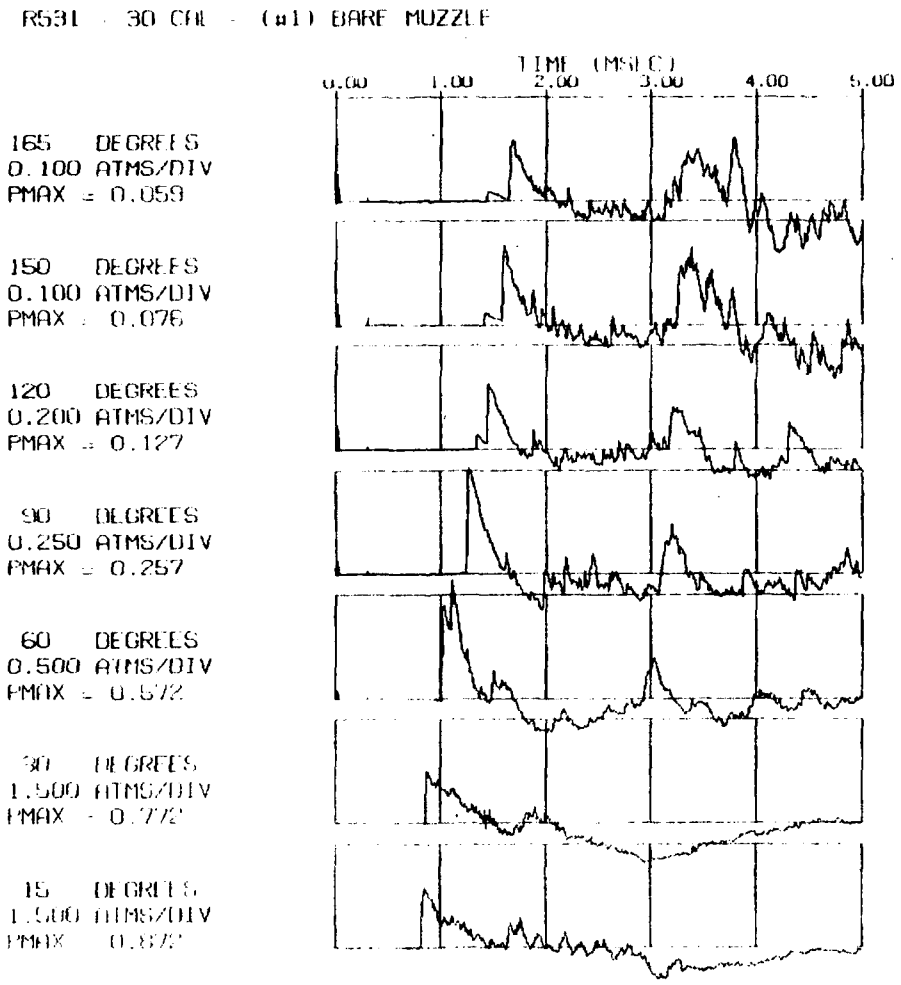

Figure B2a. Pressure histories for round 19531, bare muzzle, at 30 calibers. Data used in report figures.

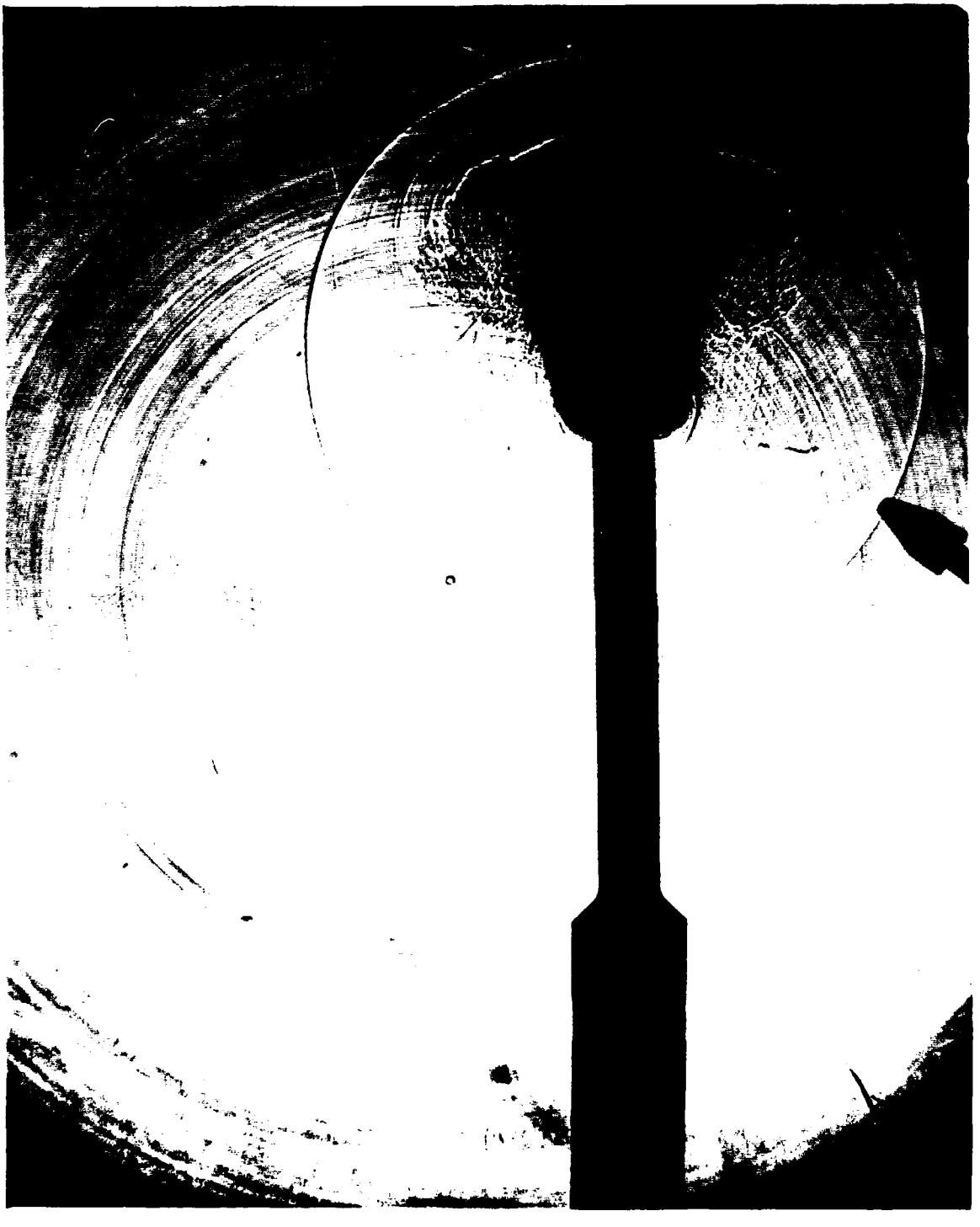

Figure B2b. Shadowgraph for round 19531, bare muzzle, with no time delay.

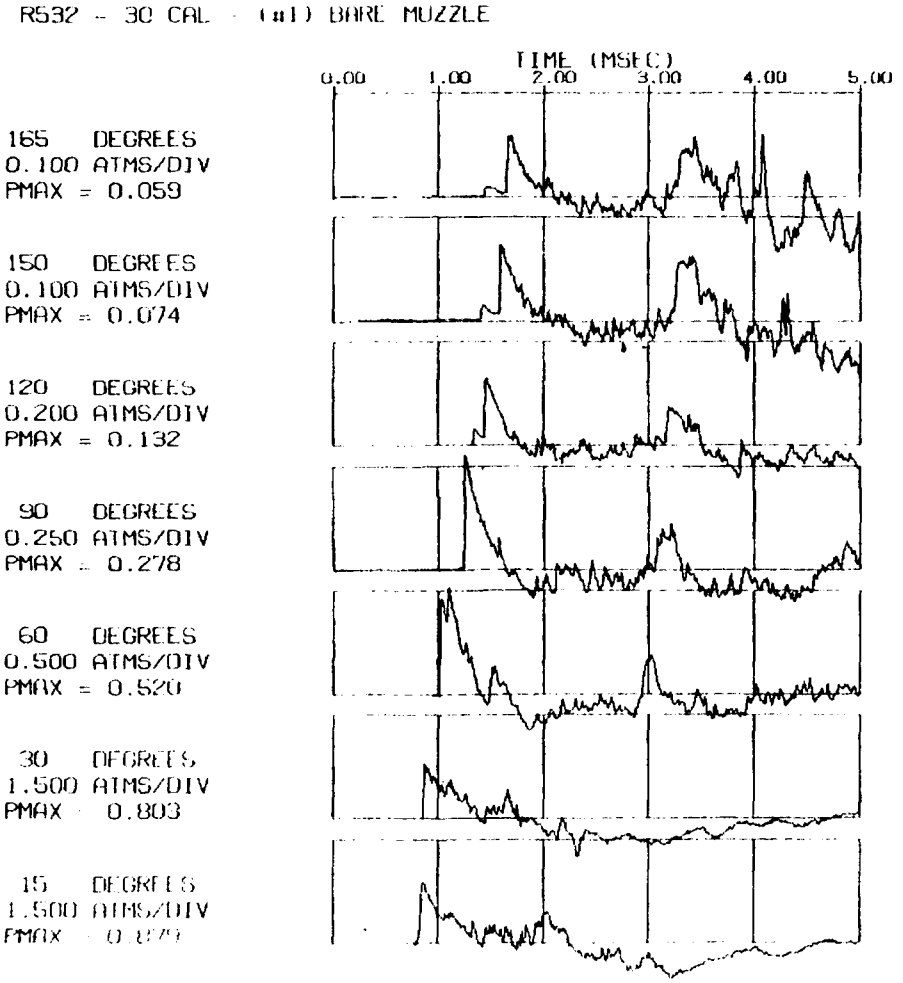

Figure B3a. Pressure histories for round 19532, bare muzzle, at 30 calibers. Data used in report figures.

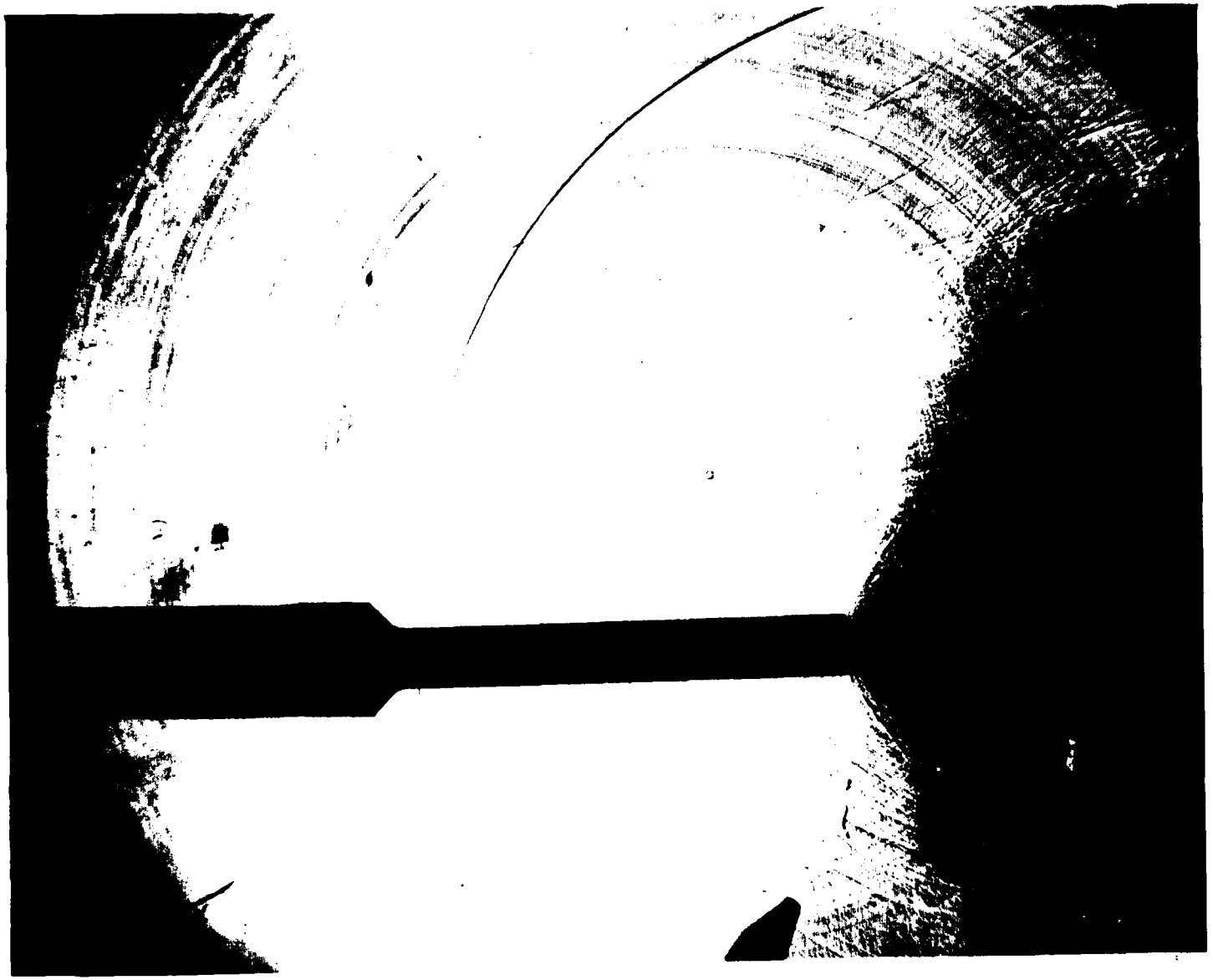

Figure B3b. Shadowgraph for round 19532, bare muzzle, taken with a 575-microsecond time delay.

Figure B4a. Pressure histories for round 19533, bare muzzle, at 30 calibers. Data not taken.

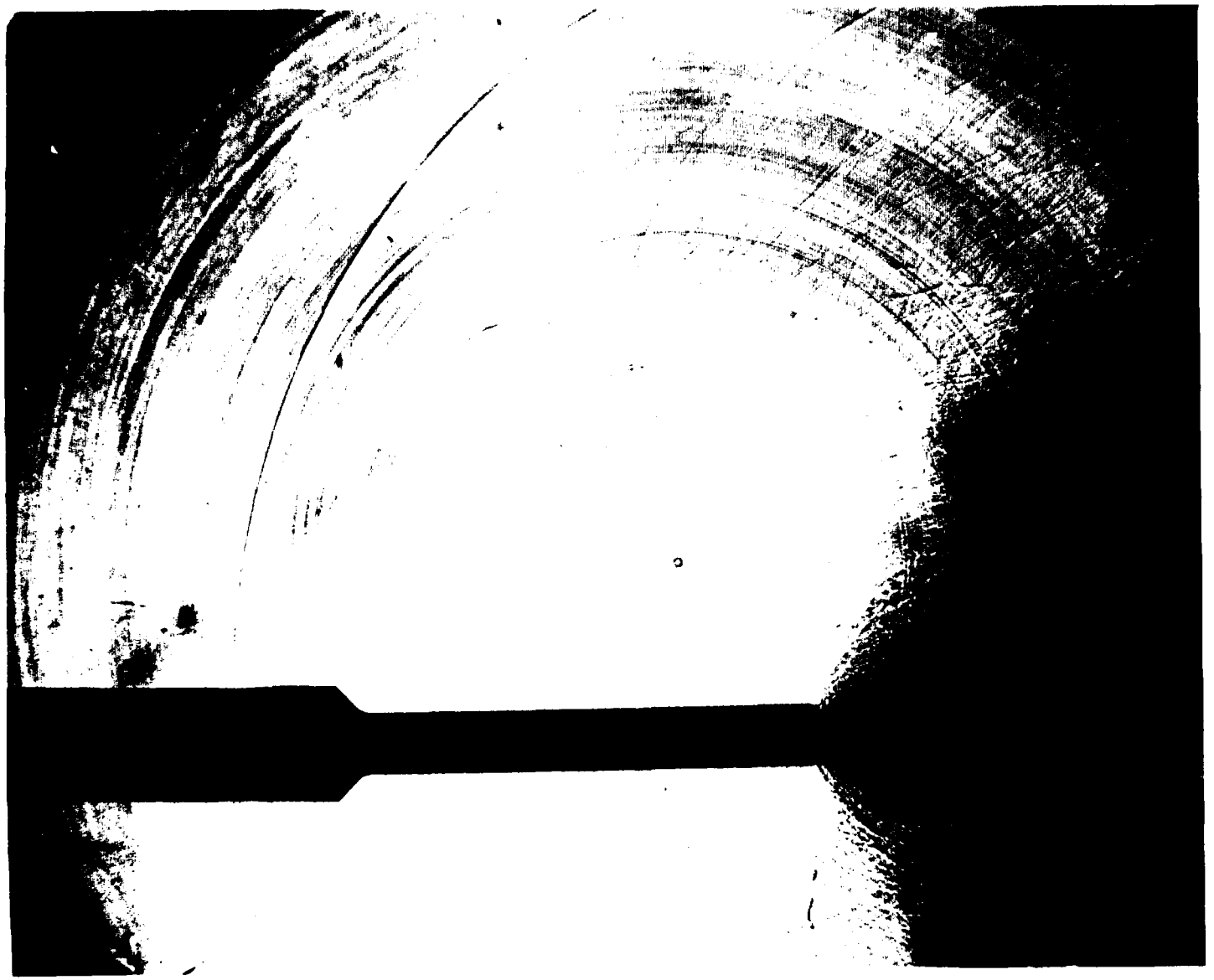

Figure B4b. Shadowgraph for round 19533, bare muzzle, taken with an 800-microsecond time delay.

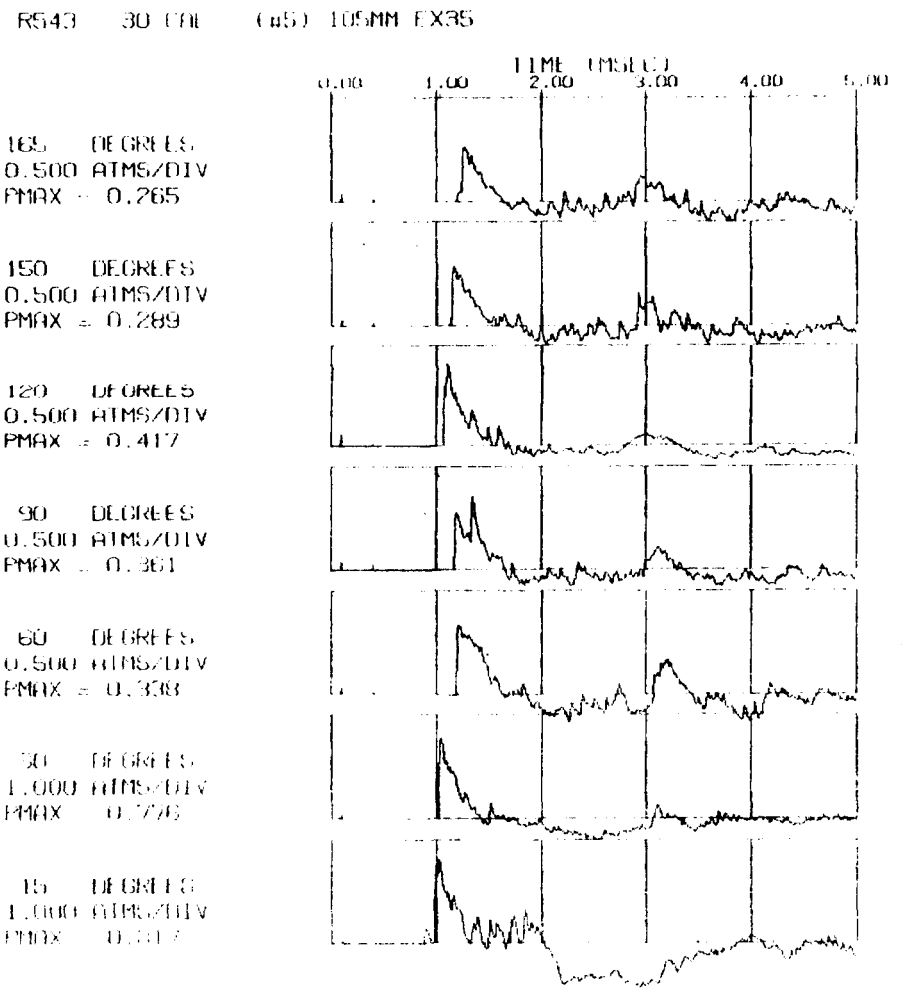

Figure B5a. Pressure histories for round 19543, standard brake, at 30 calibers. Data used in report figures.

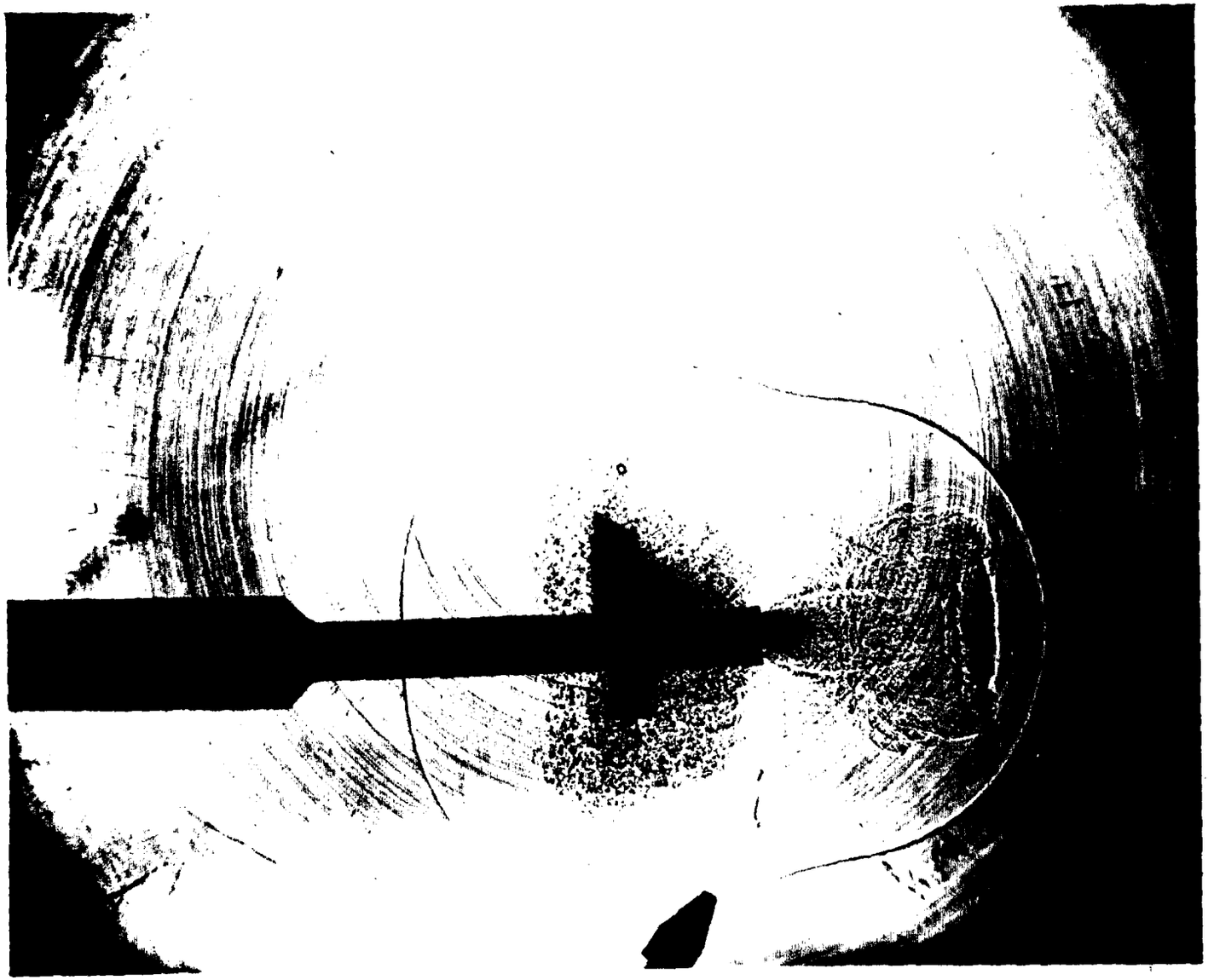

Figure B5b. Shadowgraph for round 19543, standard brake, taken with no time delay.

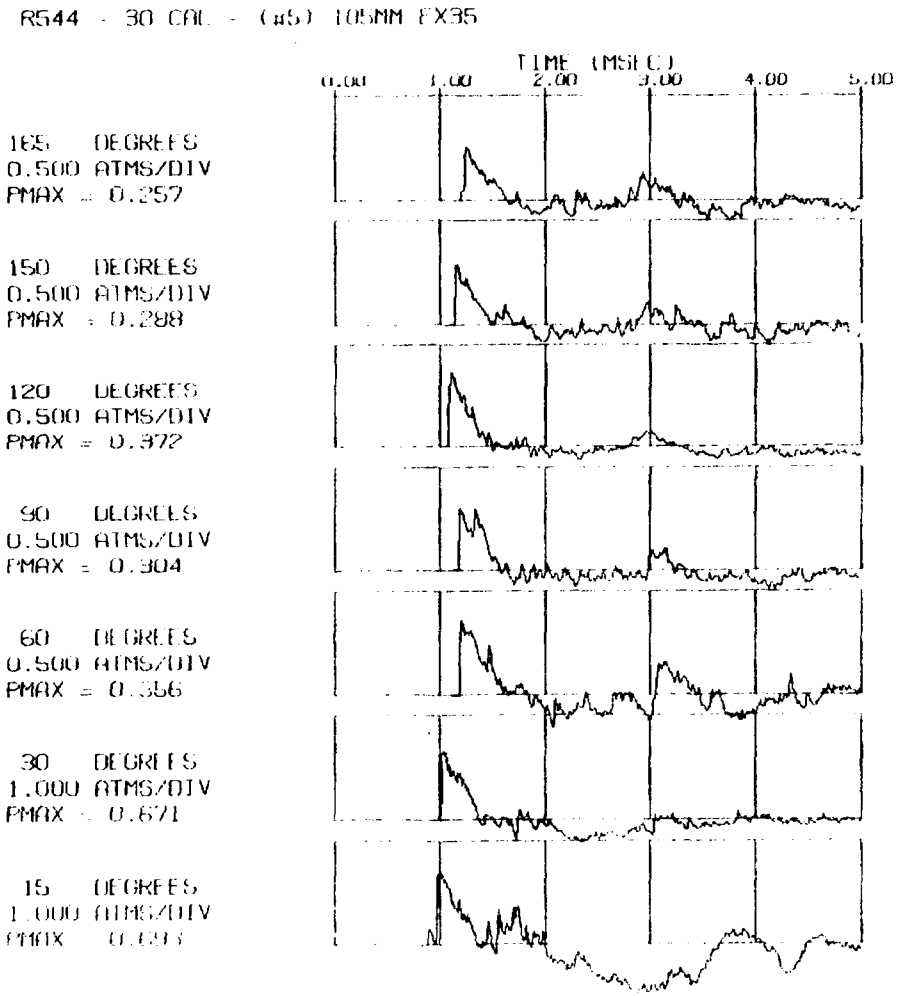

Figure B6a. Pressure histories for round 19544, standard brake, at 30 calibers. Data used in report figures.

Figure B6b. Shadowgraph for round 19544, standard brake, taken with a 150-microsecond time delay.

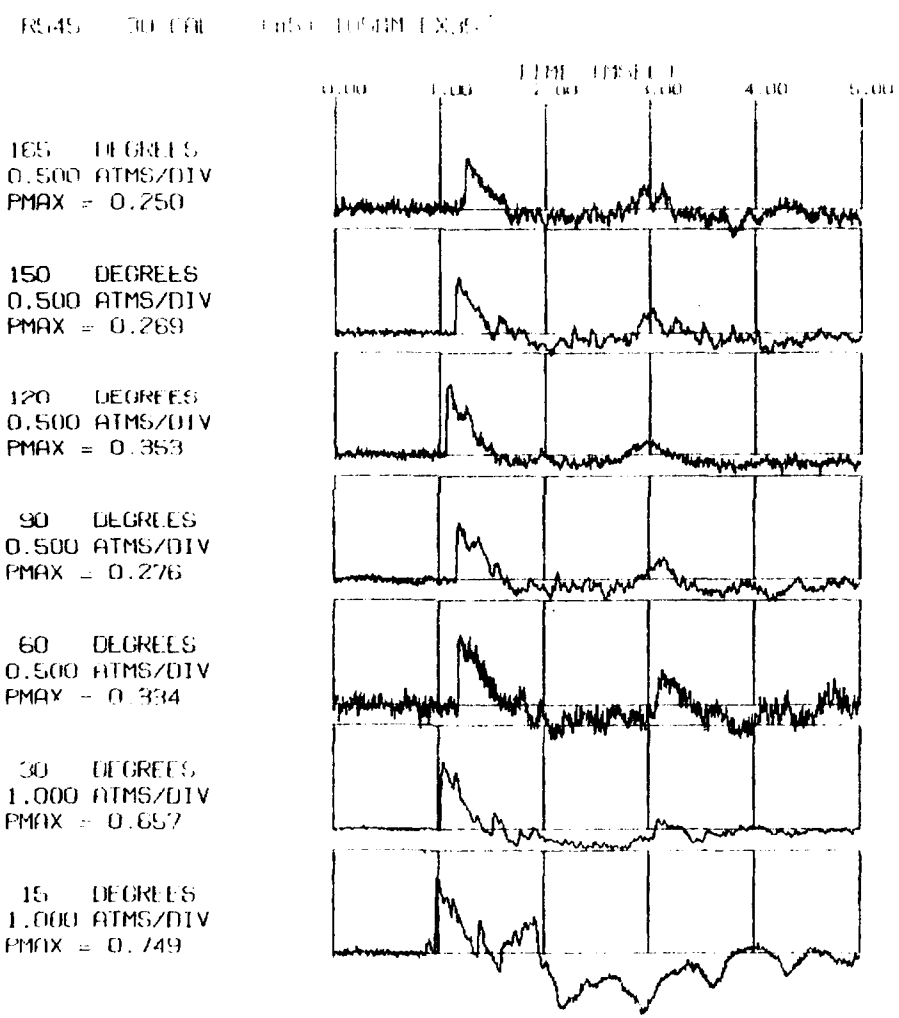

Figure B7a. Pressure histories for round 19545, standard brake, at 30 calibers. Data used in report figures.

Figure B7b. Shadowgraph for round 19545, standard brake, taken with a 300-microsecond time delay.

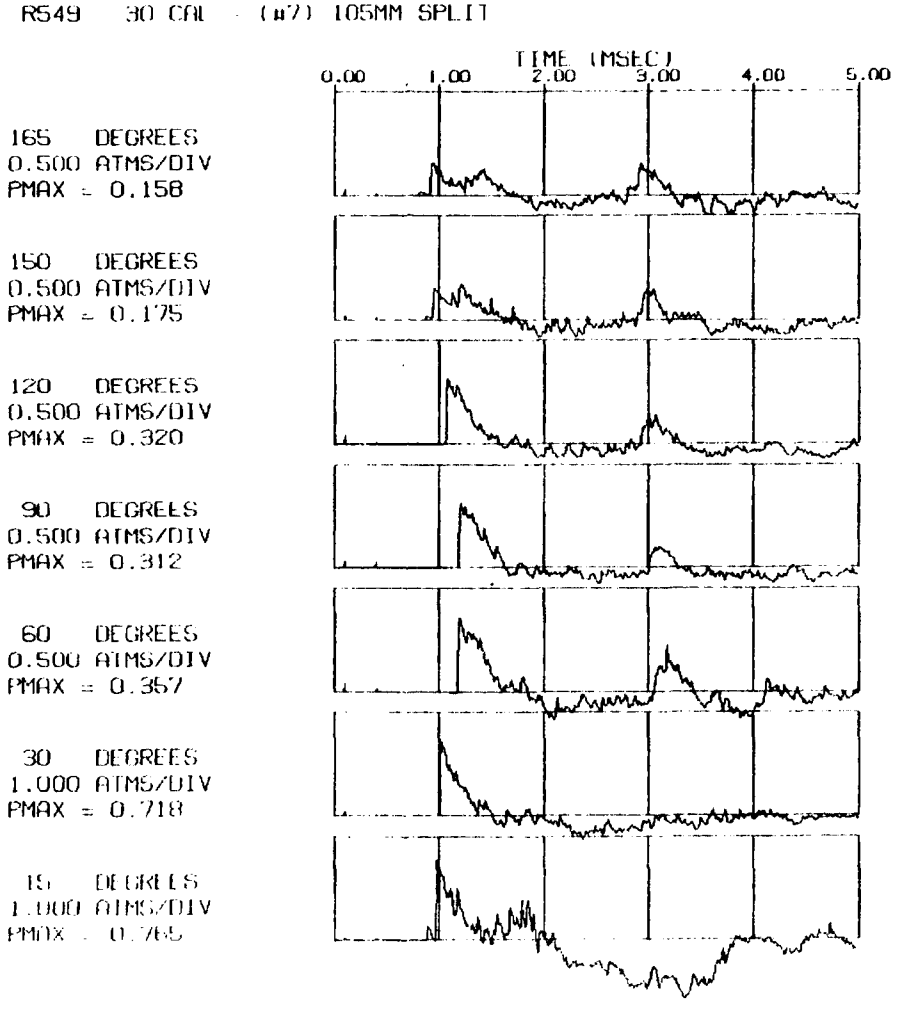

Figure B8a. Pressure histories for round 19549, split brake, at 30 calibers. Data used in report figures.

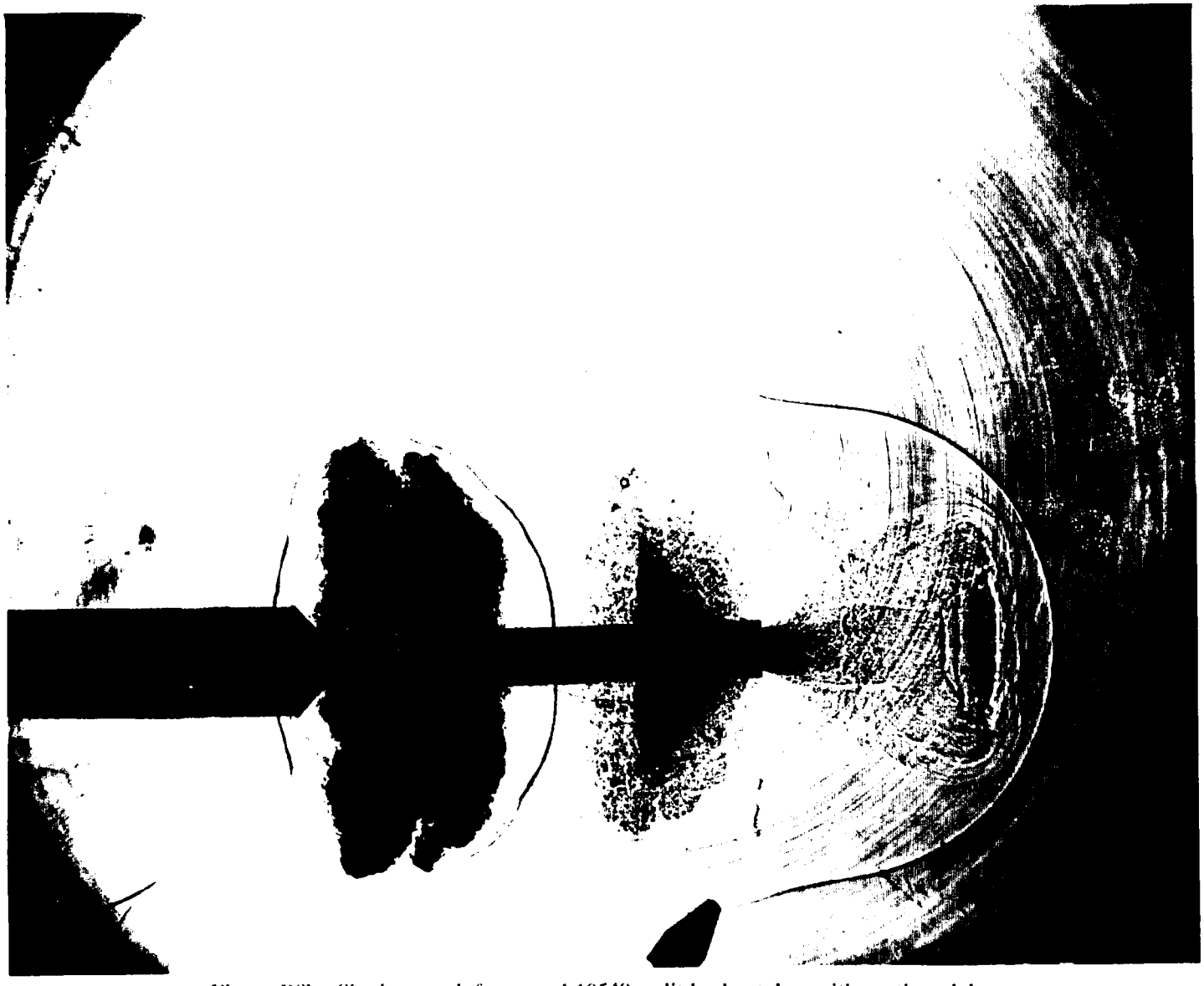

Figure B8b. Shadowgraph for round 19549, split brake, taken with no time delay.

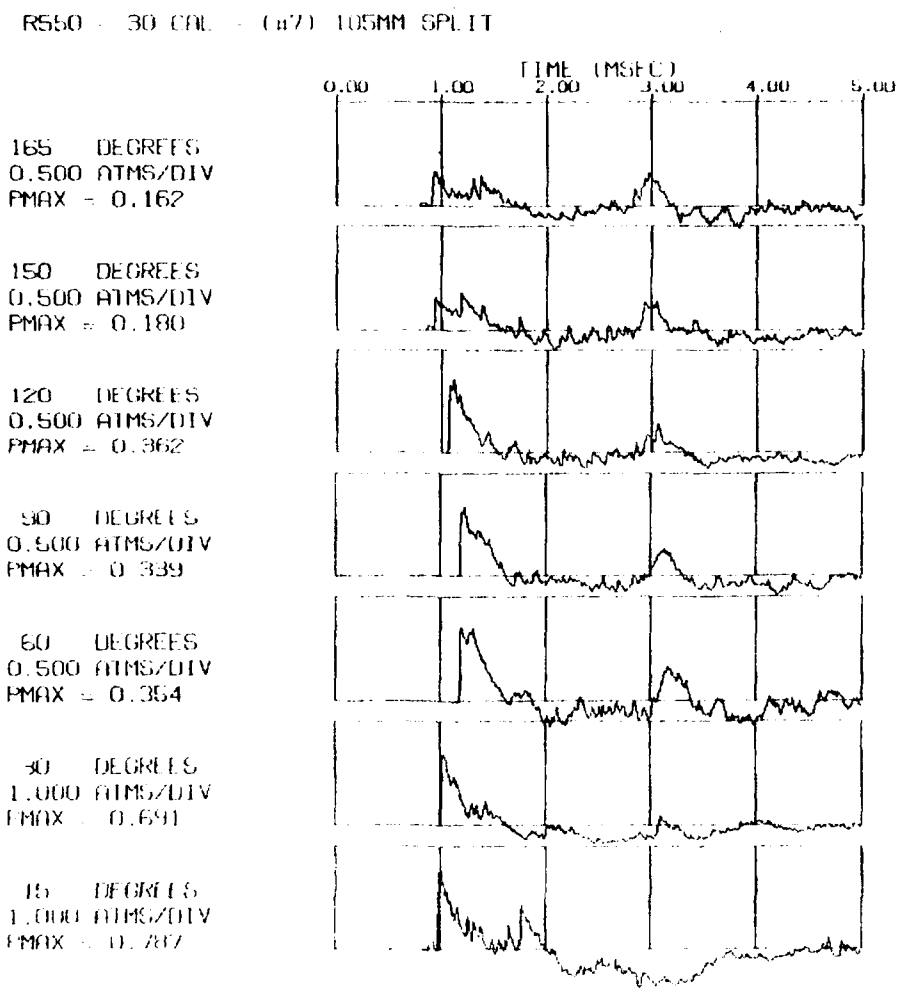

Figure B9a. Pressure histories for round 19550, split brake, at 30 calibers. Data used in report figures.

Figure B9b. Shadowgraph for round 19550, split brake, taken with a 150-microsecond time delay.

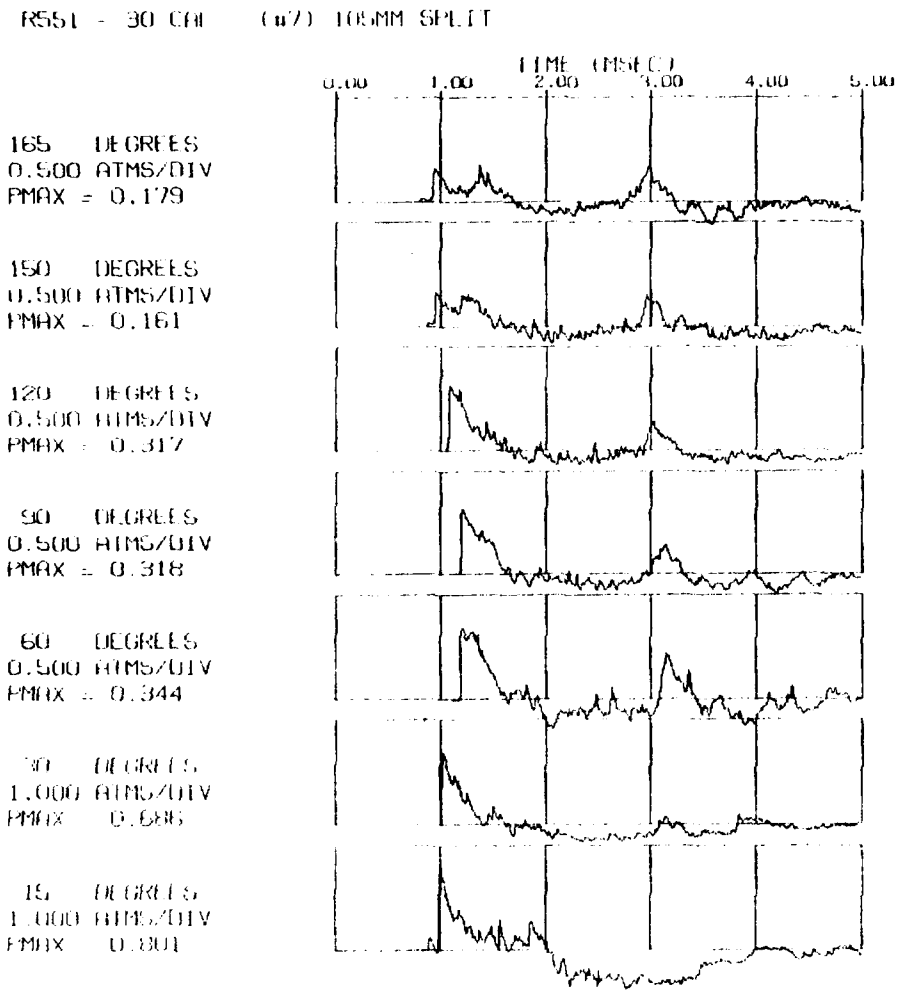

Figure B10a. Pressure histories for round 19551, split brake, at 30 calibers. Data used in report figures.

Figure B10b. Shadowgraph for round 19551, split brake, taken with a 300-microsecond time delay.

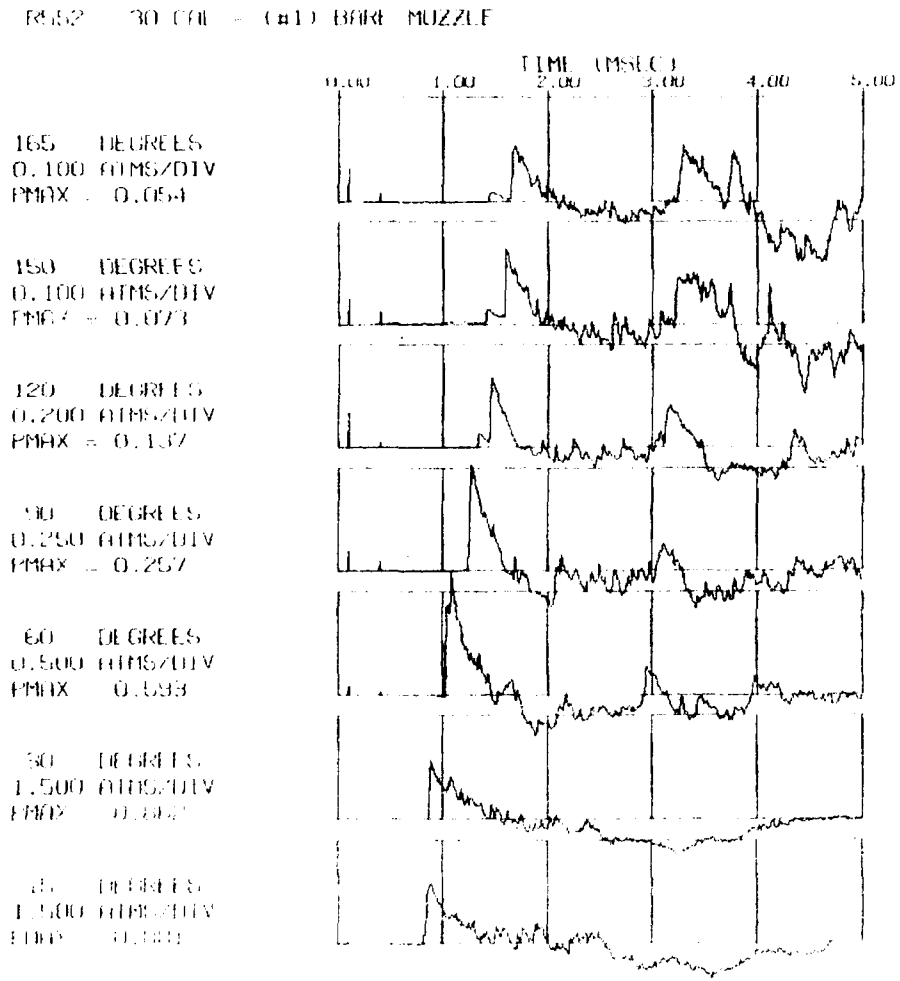

Figure B11a. Pressure histories for round 19552, bare muzzle, at 30 calibers. Data used in report figures.

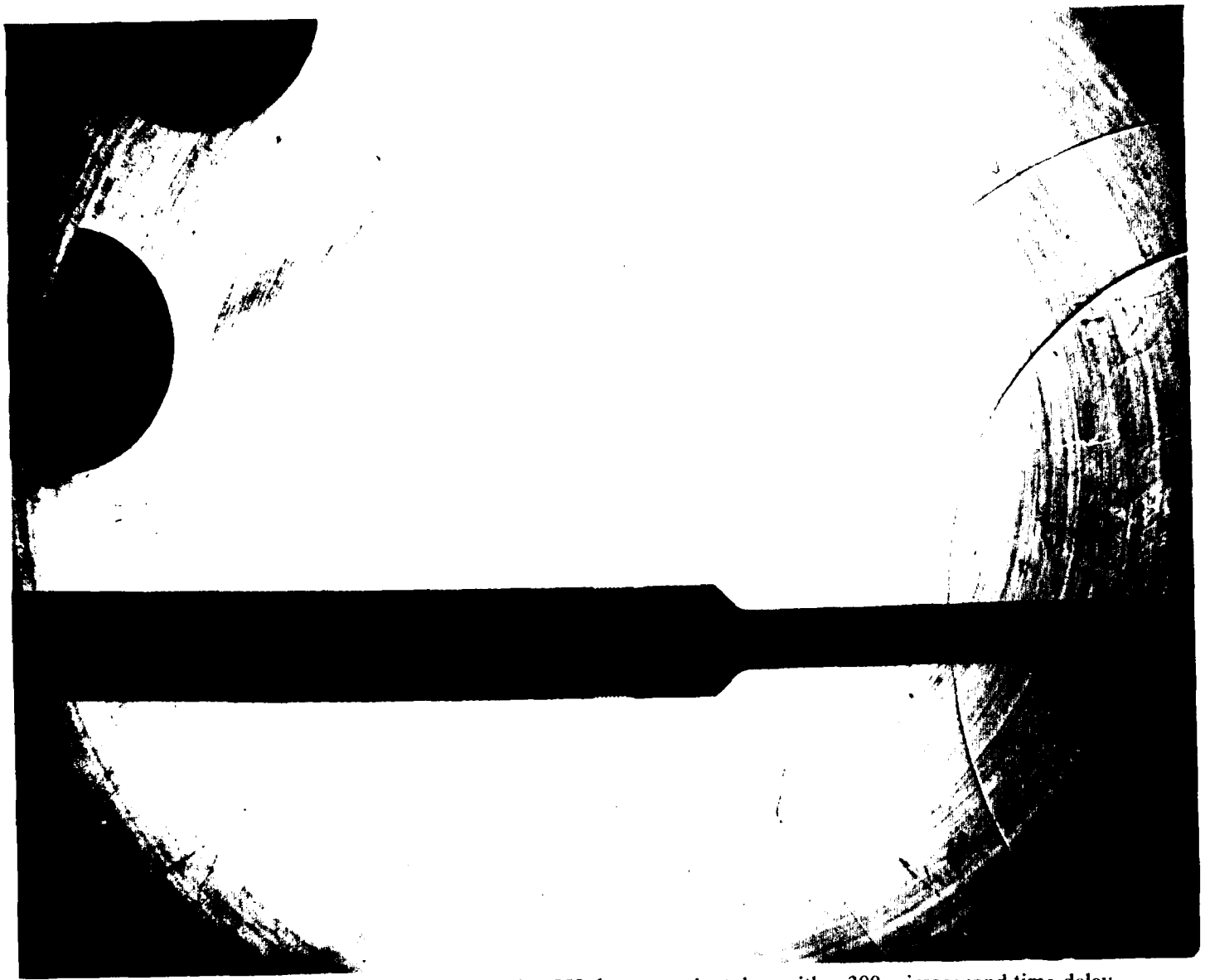

Figure B11b. Shadowgraph for round 19552, bare muzzle, taken with a 300-microsecond time delay.

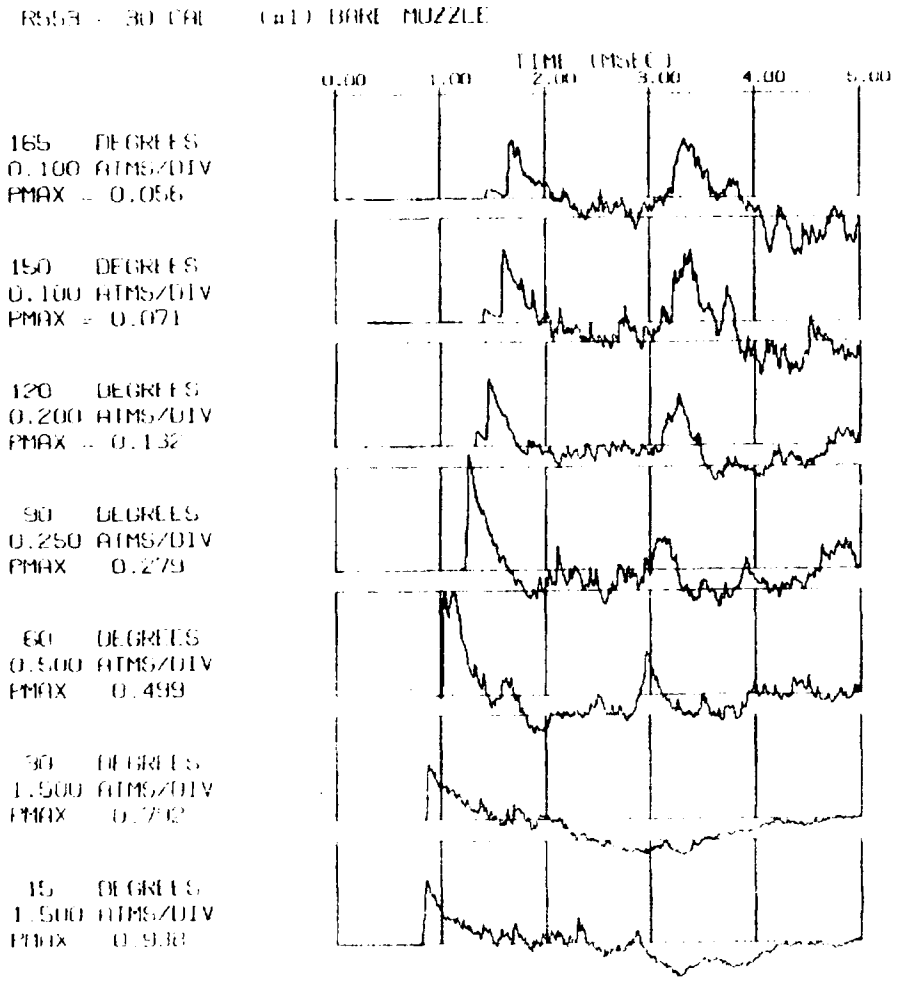

Figure B12a. Pressure histories for round 19553, bare muzzle, at 30 calibers. Data used in report figures.

Figure B12b. Shadowgraph for round 19553, bare muzzle, taken with a 150-microsecond time delay.

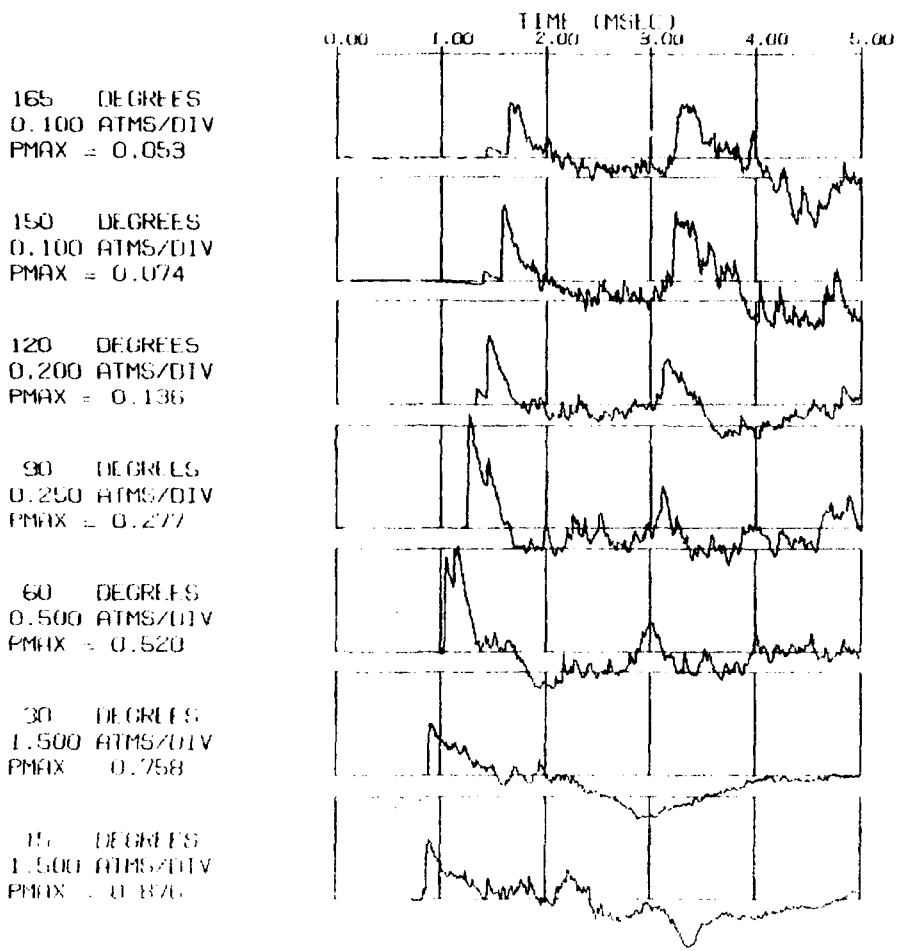

Figure B13a. Pressure histories for round 19554, bare muzzle, at 30 calibers. Data used in report figures.

Figure B13b. Shadowgraph for round 19554, bare muzzle, taken with a 450-microsecond time delay.

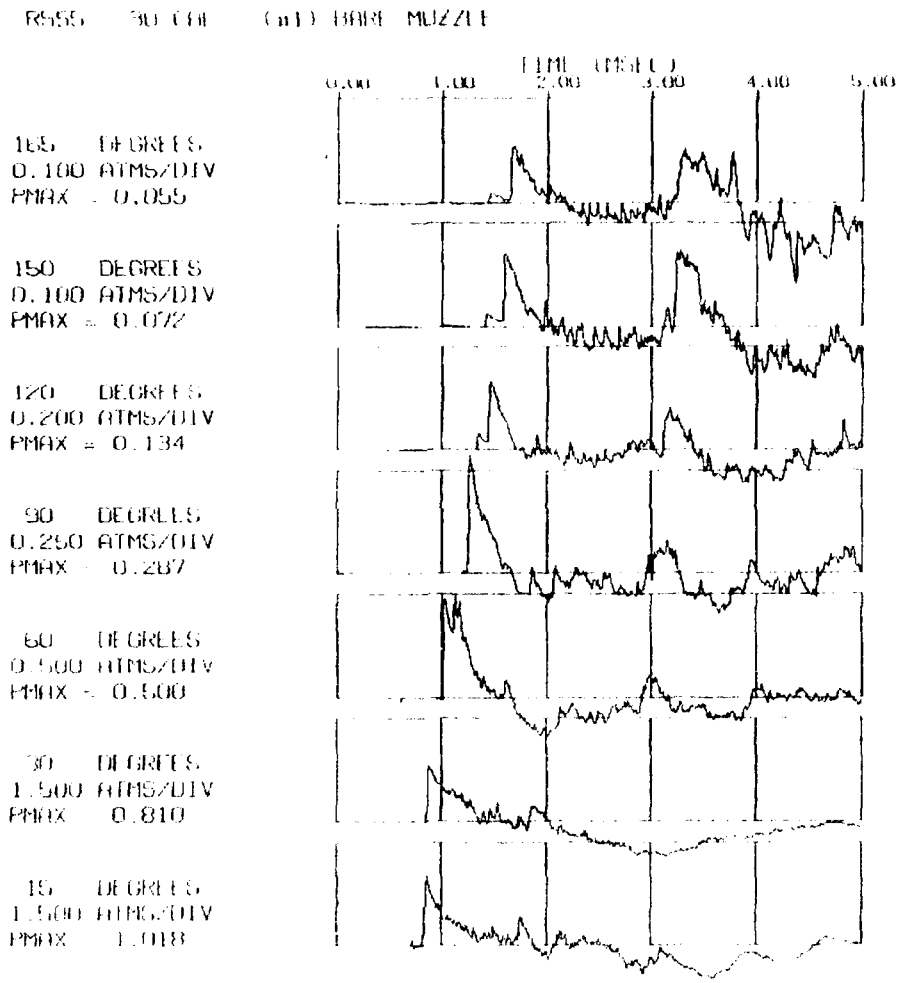

Figure B14a. Pressure histories for round 19555, bare muzzle, at 30 calibers. Data used in report figures.

Figure B14b. Shadowgraph for round 19555, bare muzzle, taken with a 600-microsecond time delay.

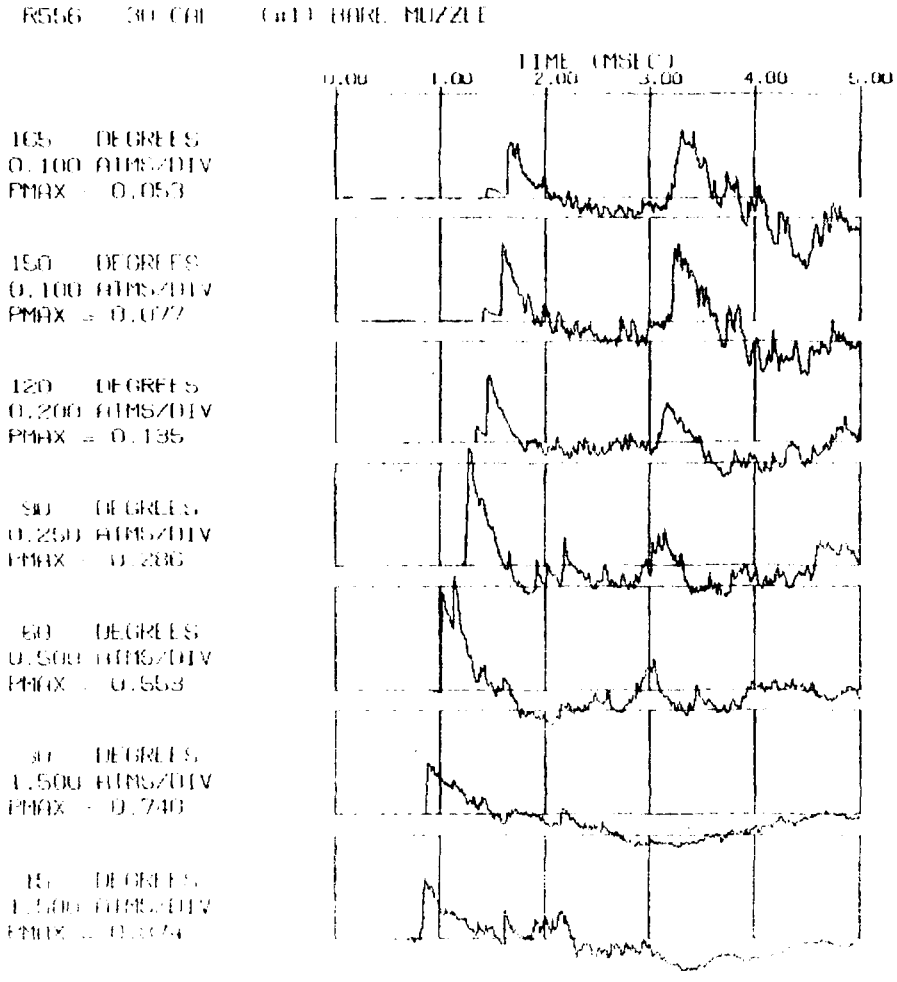

Figure B15a. Pressure histories for round 19556, bare muzzle, at 30 calibers. Data used in report figures.

Figure B15b. Shadowgraph for round 19556, bare muzzle, taken with a 750-microsecond time delay.

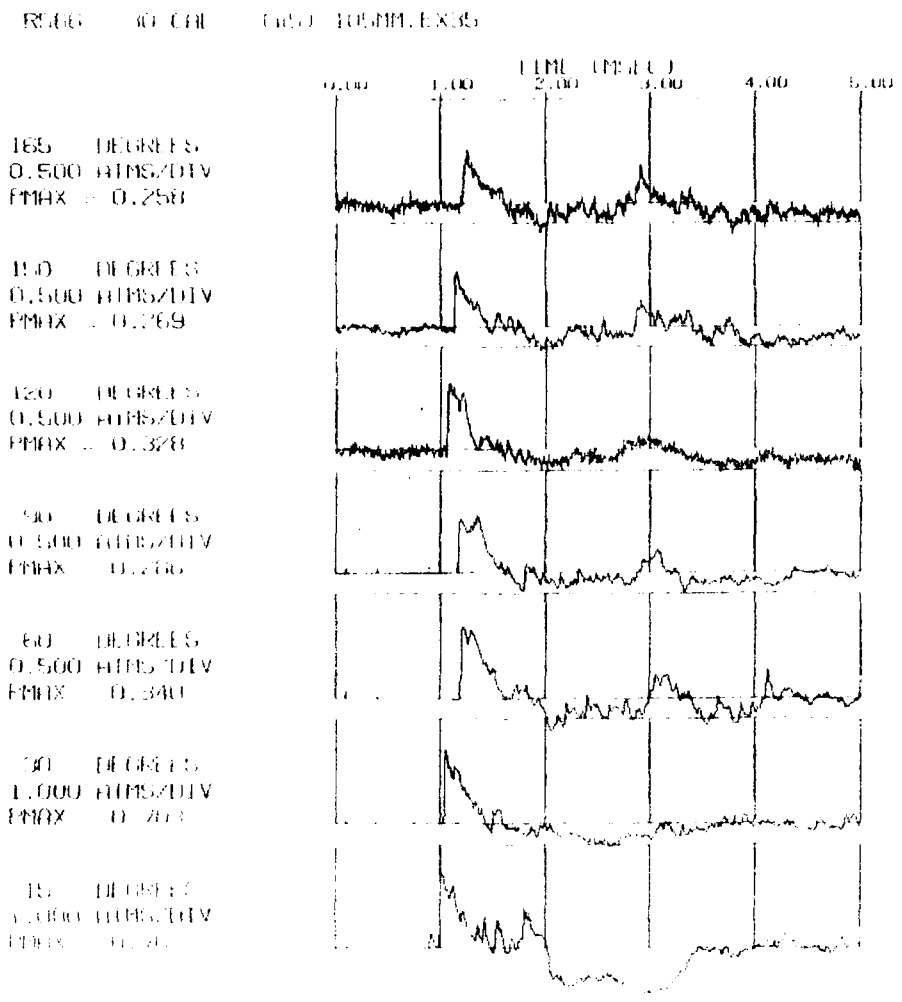

Figure B16a. Pressure histories for round 19566, standard brake, at 30 calibers. Data used in report figures.

Figure B16b. Shadowgraph for round 19566, standard brake, taken with a 450-microsecond time delay.

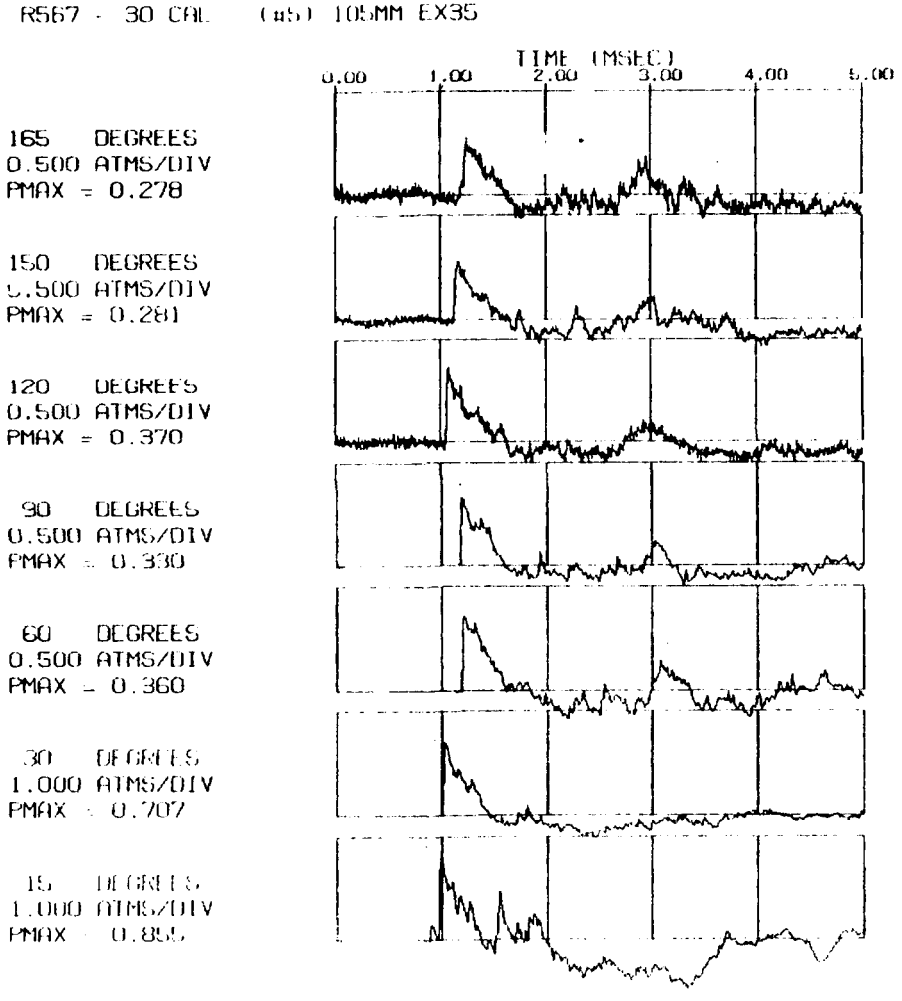

Figure B17a. Pressure histories for round 19567, standard brake, at 30 calibers. Data used in report figures.

Figure B17b. Shadowgraph for round 19567, standard brake, taken with a 600-microsecond time delay.

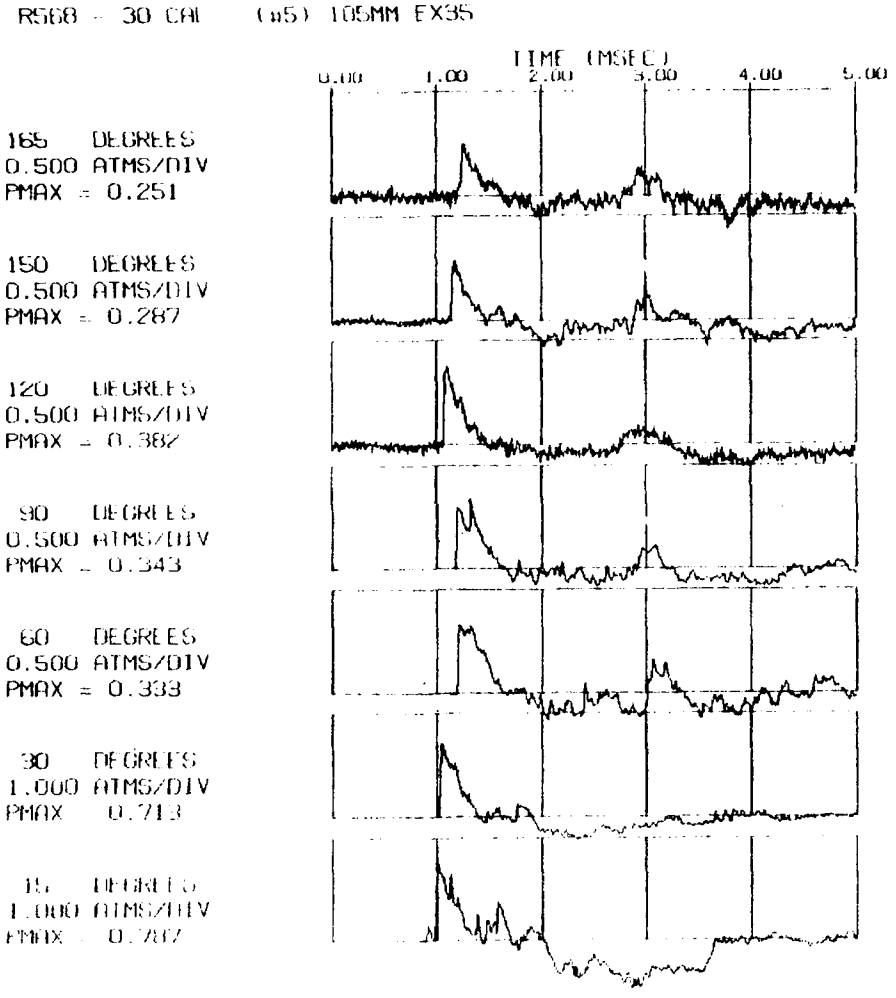

Figure B18a. Pressure histories for round 19568, standard brake, at 30 calibers. Data used in report figures.

Figure B18b. Shadowgraph for round 19568, standard brake, not taken.

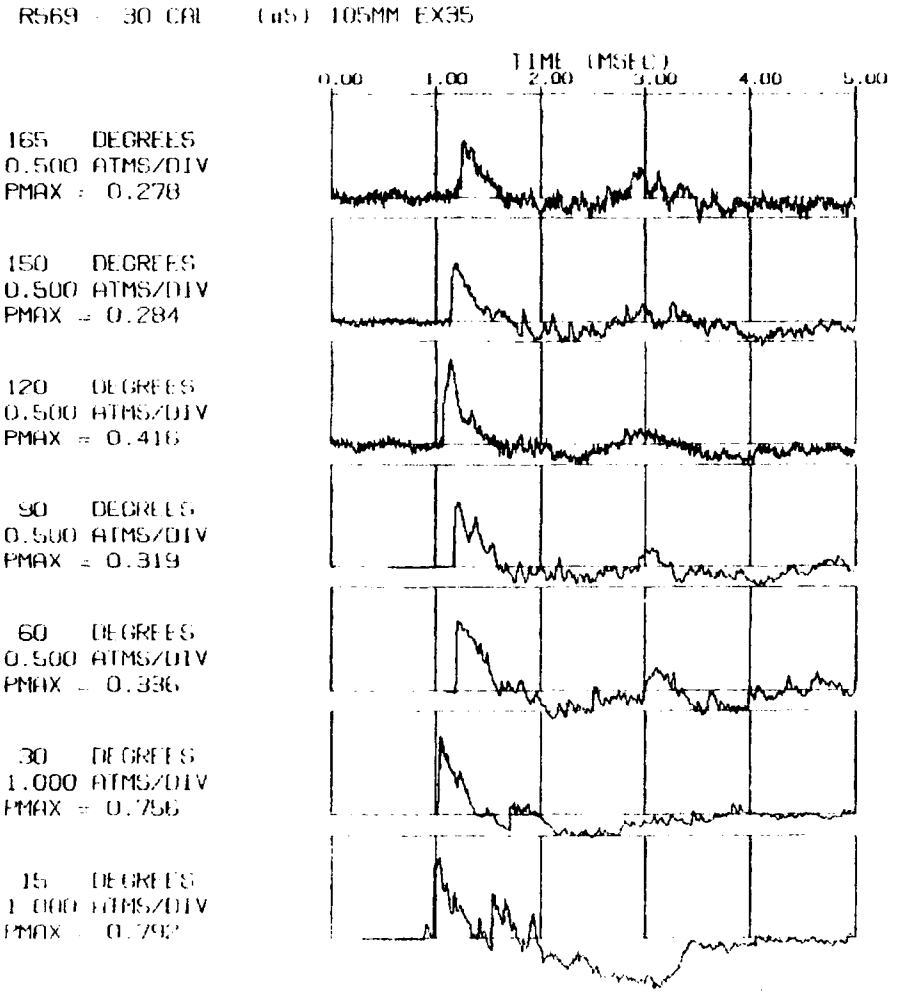

Figure B19a. Pressure histories for round 19569, standard brake, at 30 calibers. Data used in report figures.

Figure B19b. Shadowgraph for round 19569, standard brake, taken with a 750-microsecond time delay.

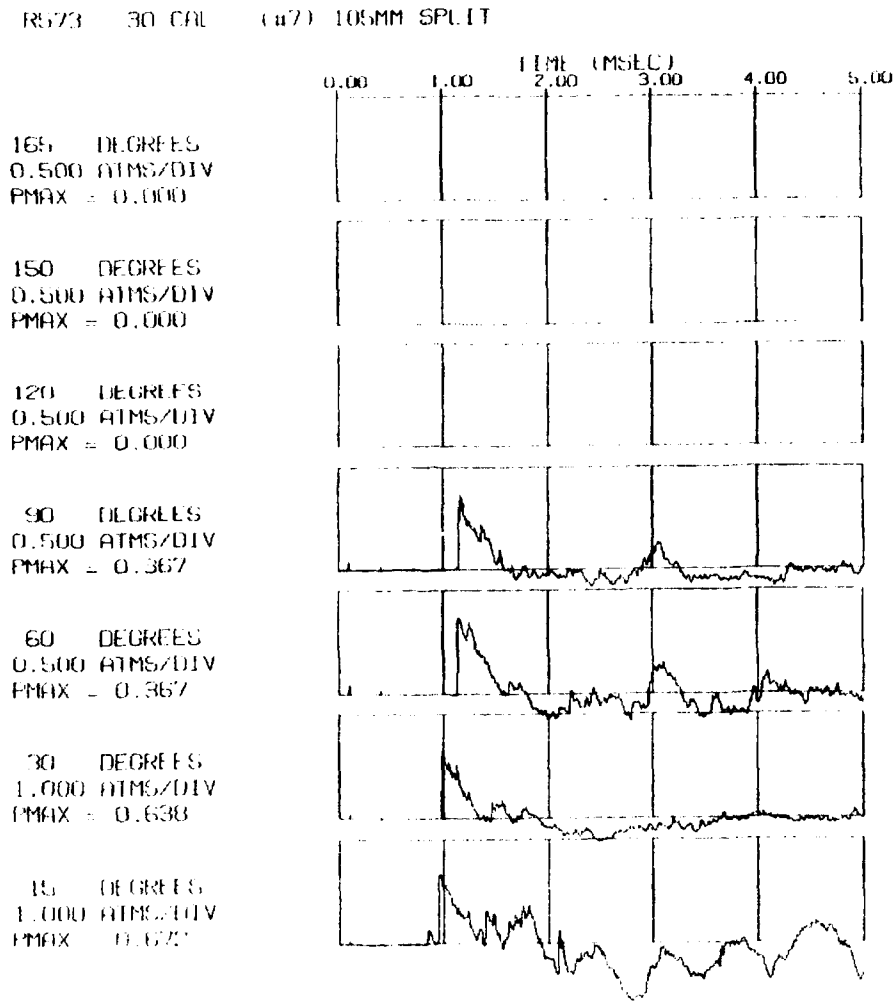

Figure B20a. Pressure histories for round 19573, split brake, at 30 calibers. Data not used in report figures.

Figure B20b. Shadowgraph for round 19573, split brake, taken with a 450-microsecond time delay.

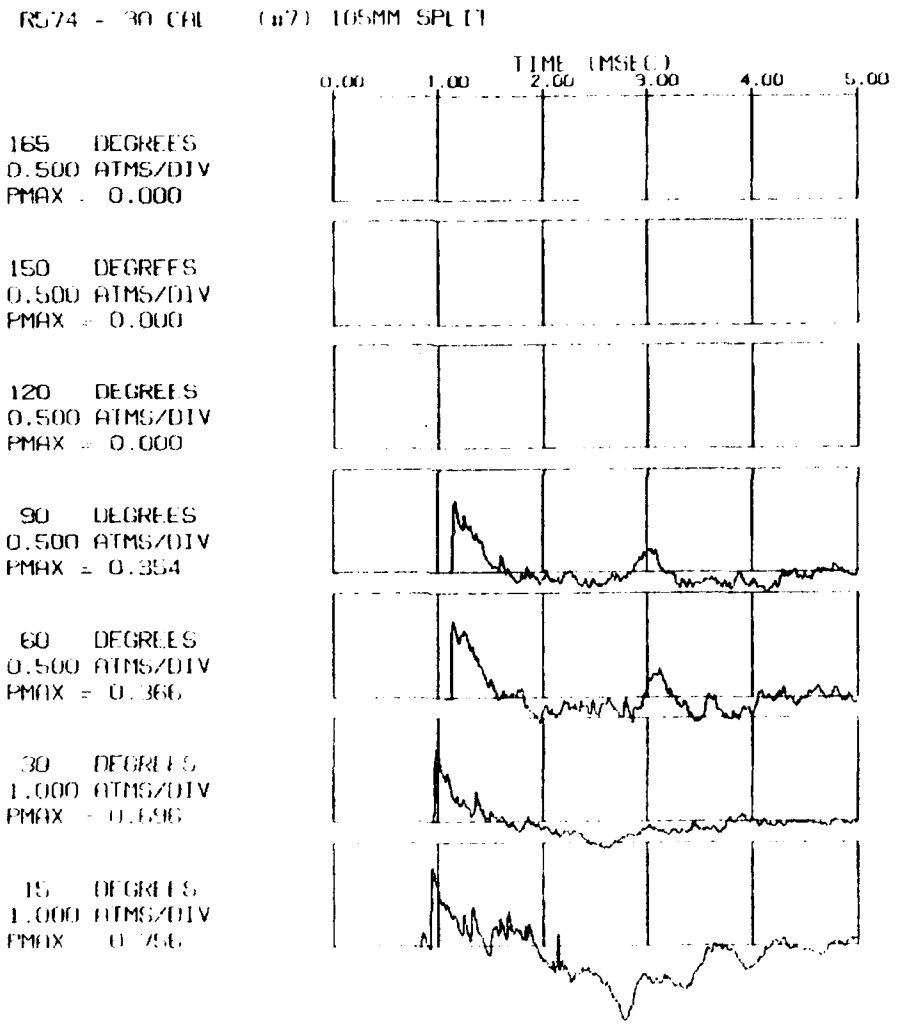

Figure B21a. Pressure histories for round 19574, split brake, at 30 calibers. Data not used in report figures.

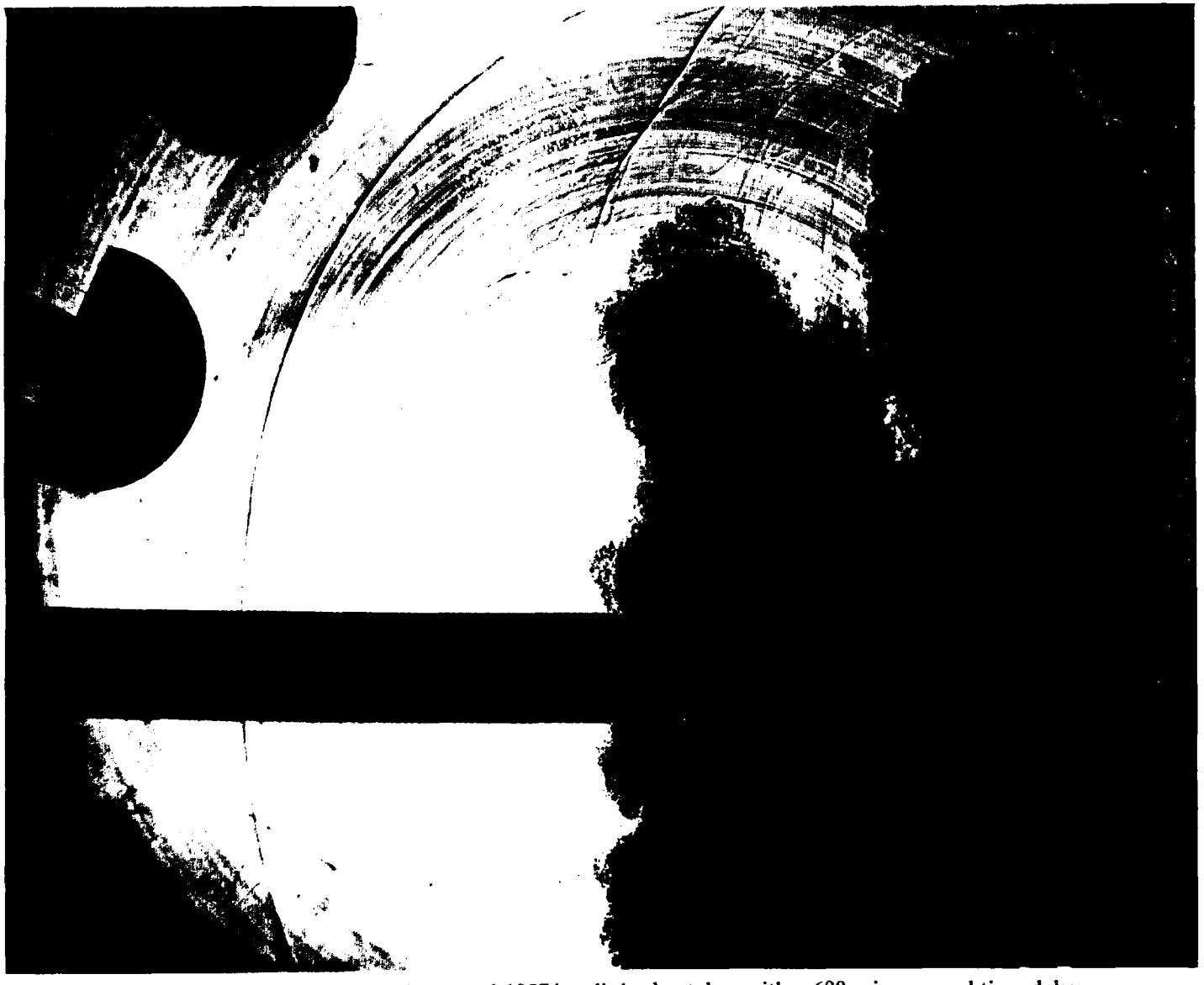

Figure B21b. Shadowgraph for round 19574, split brake, taken with a 600-microsecond time delay.

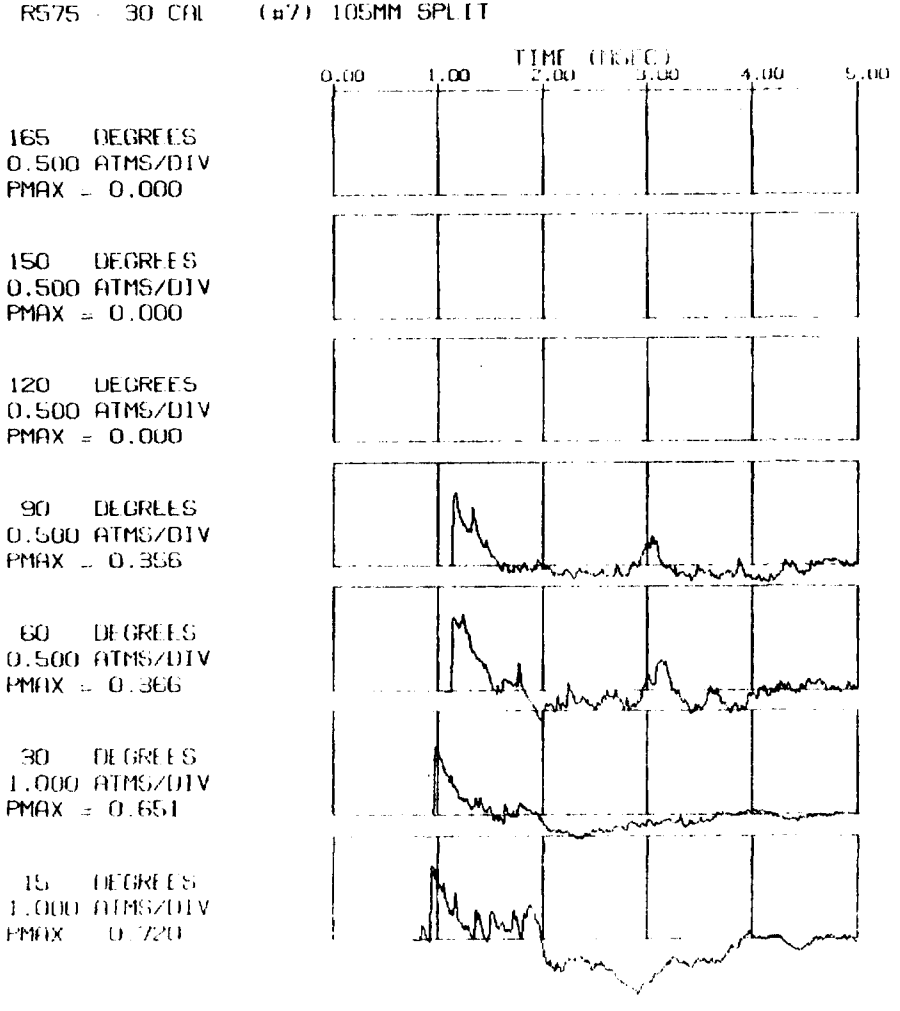

Figure B22a. Pressure histories for round 19575, split brake, at 30 calibers. Data not used in report figures.

Figure B22b. Shadowgraph for round 19575, split brake, taken with a 750-microsecond time delay.

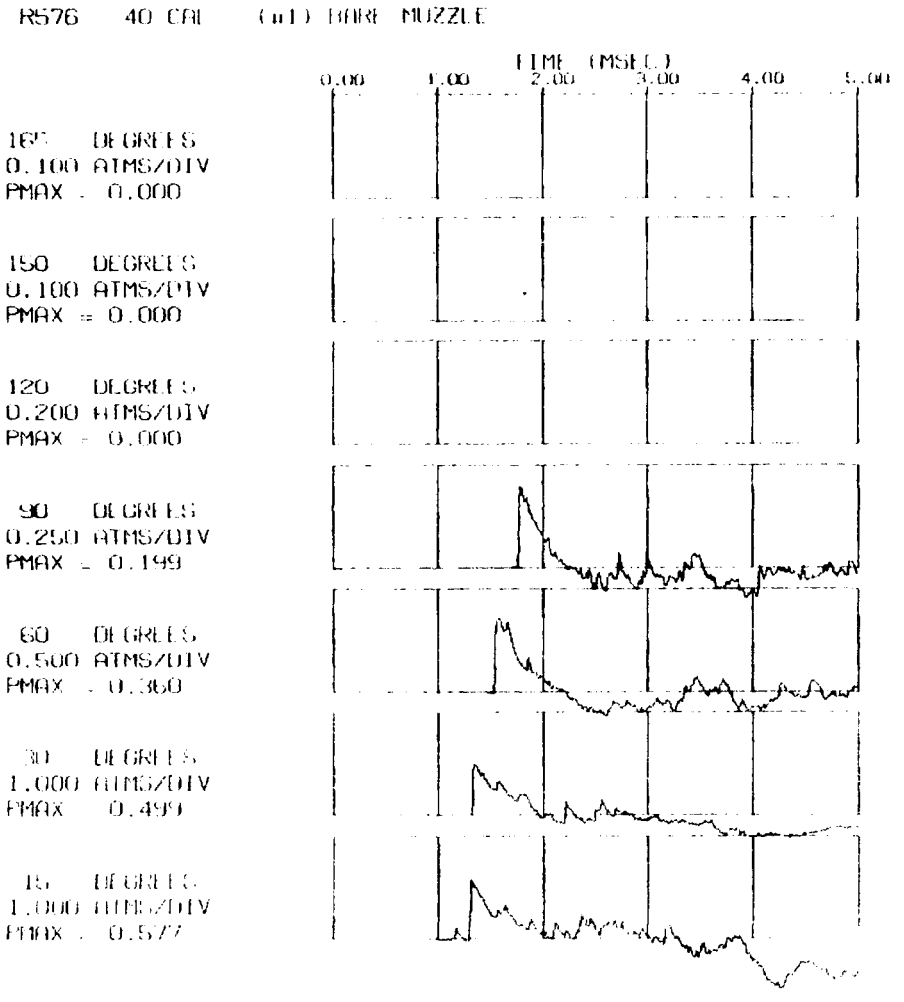

Figure B23a. Pressure histories for round 19576, bare muzzle, at 40 calibers. Data not used in report figures.

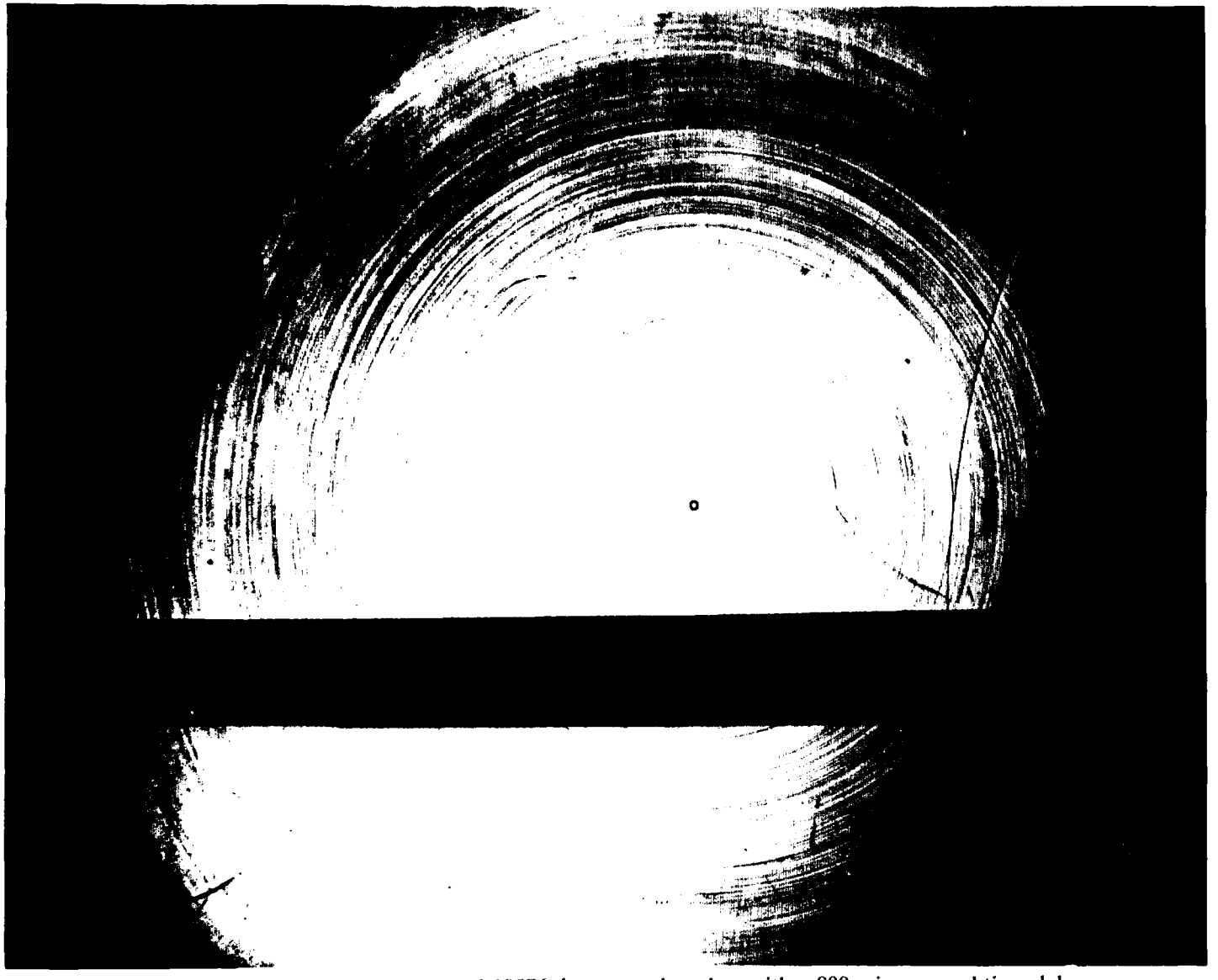

Figure B23b. Shadowgraph for round 19576, bare muzzle, taken with a 900-microsecond time delay.

Figure B24a. Pressure histories for round 19577, bare muzzle, at 40 calibers. Data not taken.

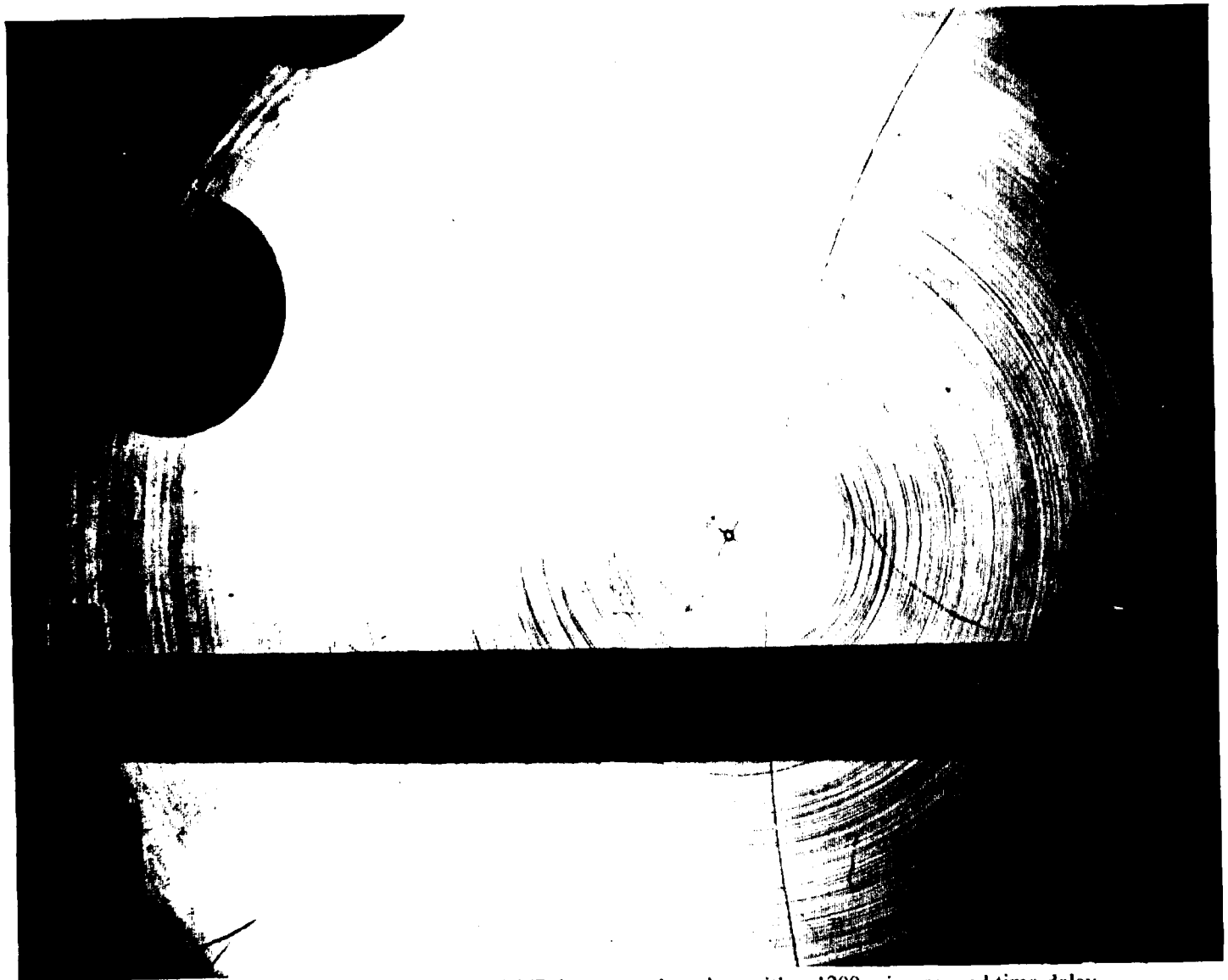

Figure B24b. Shadowgraph for round 19577, bare muzzle, taken with a 1200-microsecond time delay.

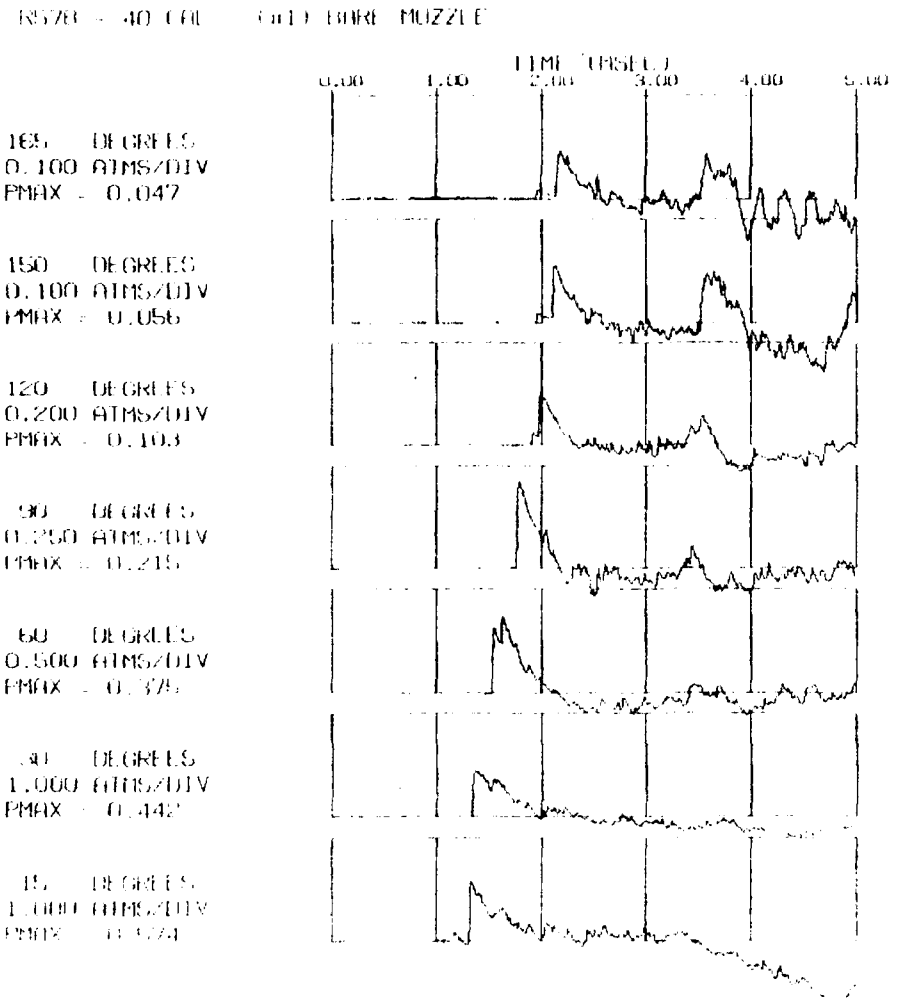

Figure B25a. Pressure histories for round 19578, bare muzzle, at 40 calibers. Data used in report figures.

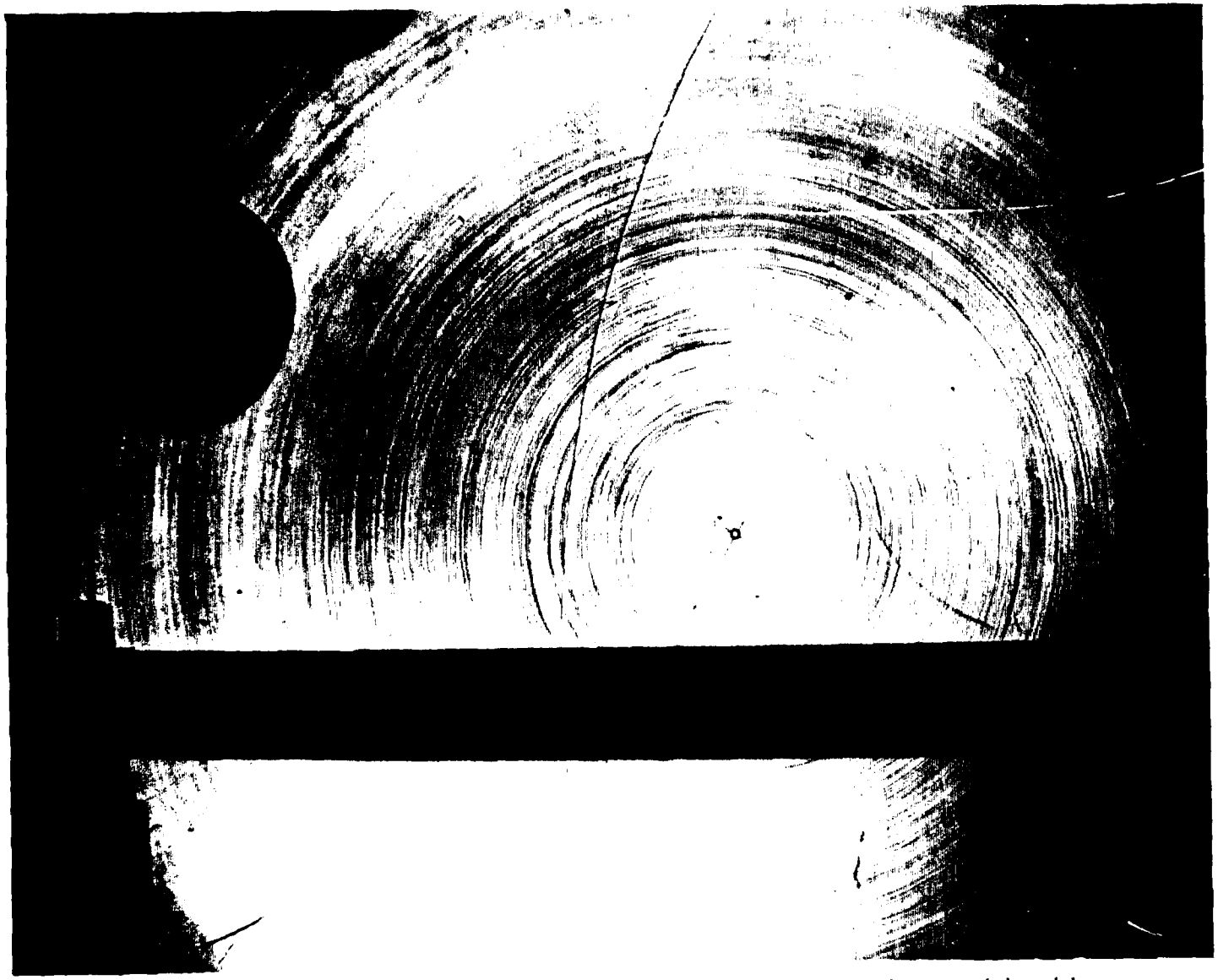

Figure B25b. Shadowgraph for round 19578, bare muzzle, taken with a 1500-microsecond time delay.

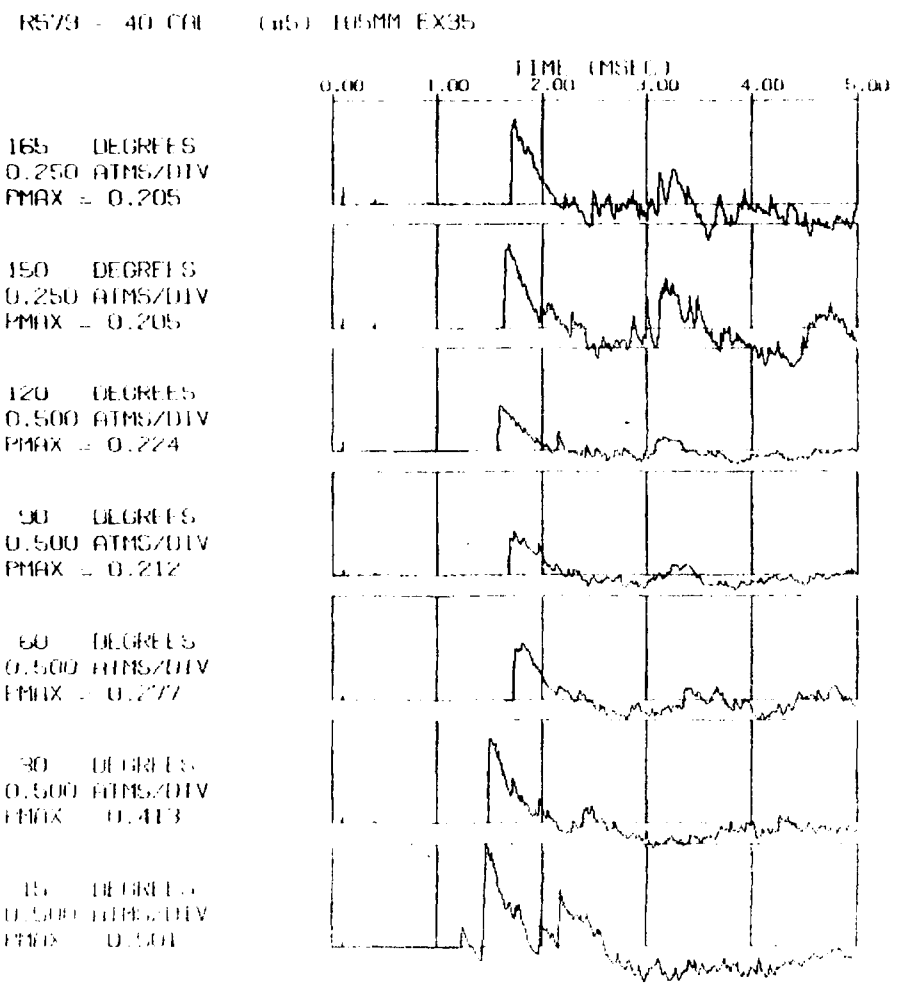

Figure B26a. Pressure histories for round 19579, standard brake, at 40 calibers. Data used in report figures.

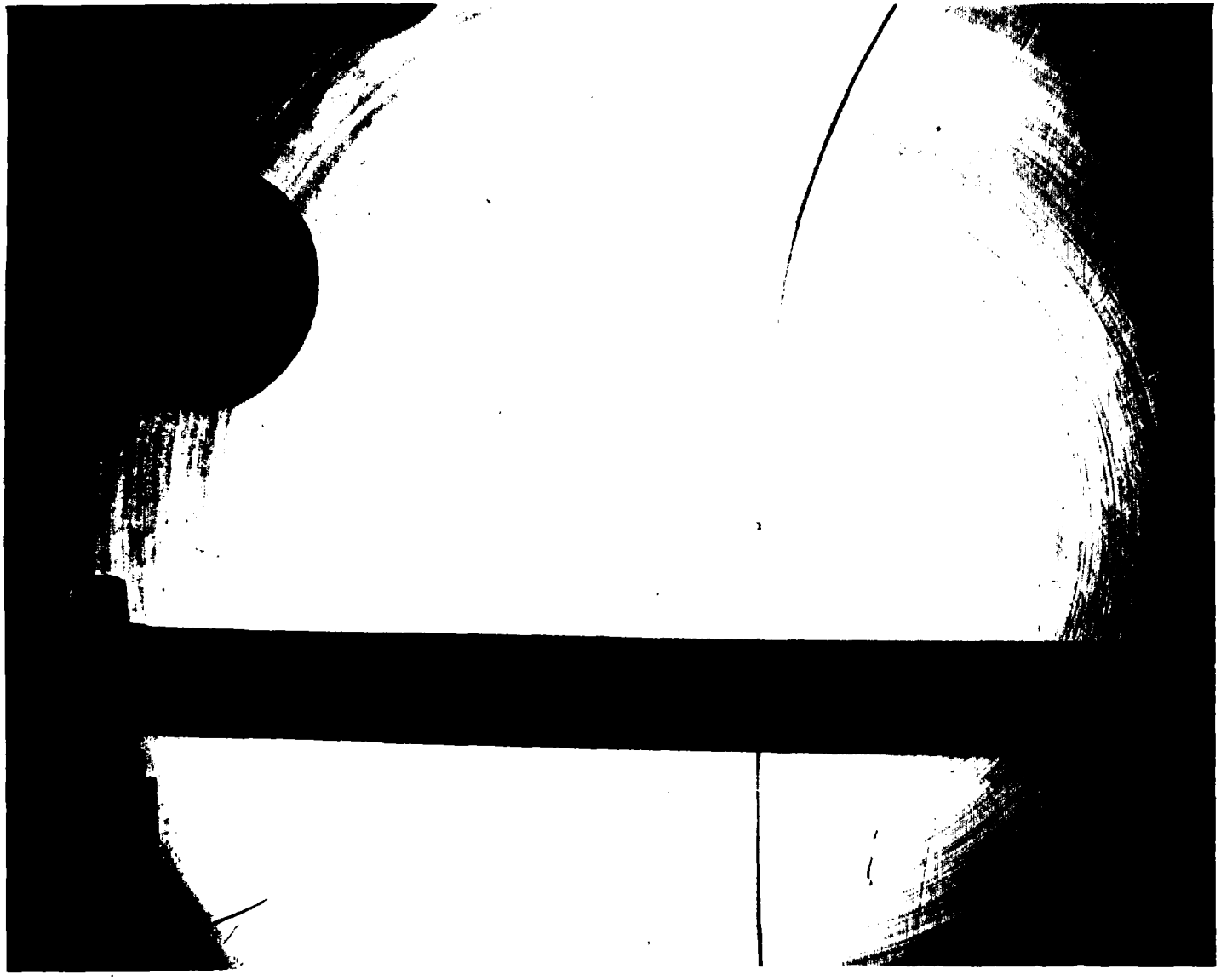

Figure B26b. Shadowgraph for round 19579, standard brake, taken with a 900-microsecond time delay.

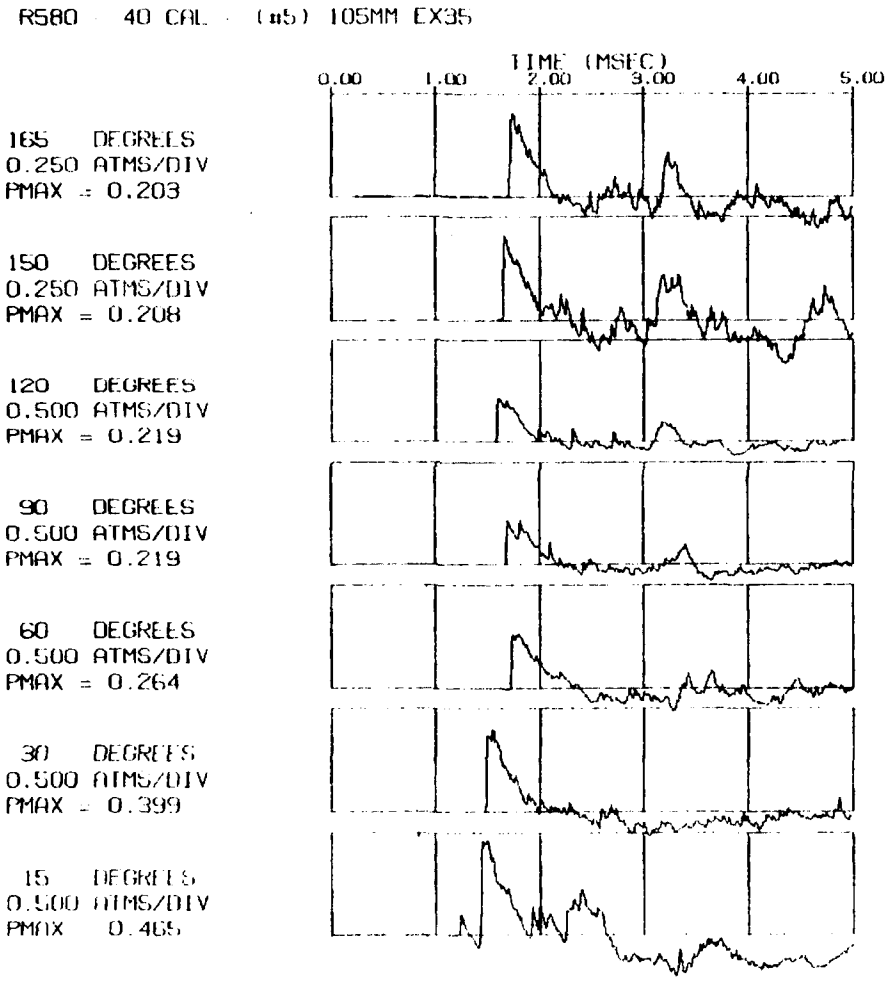

Figure B27a. Pressure histories for round 19580, standard brake, at 40 calibers. Data used in report figures.

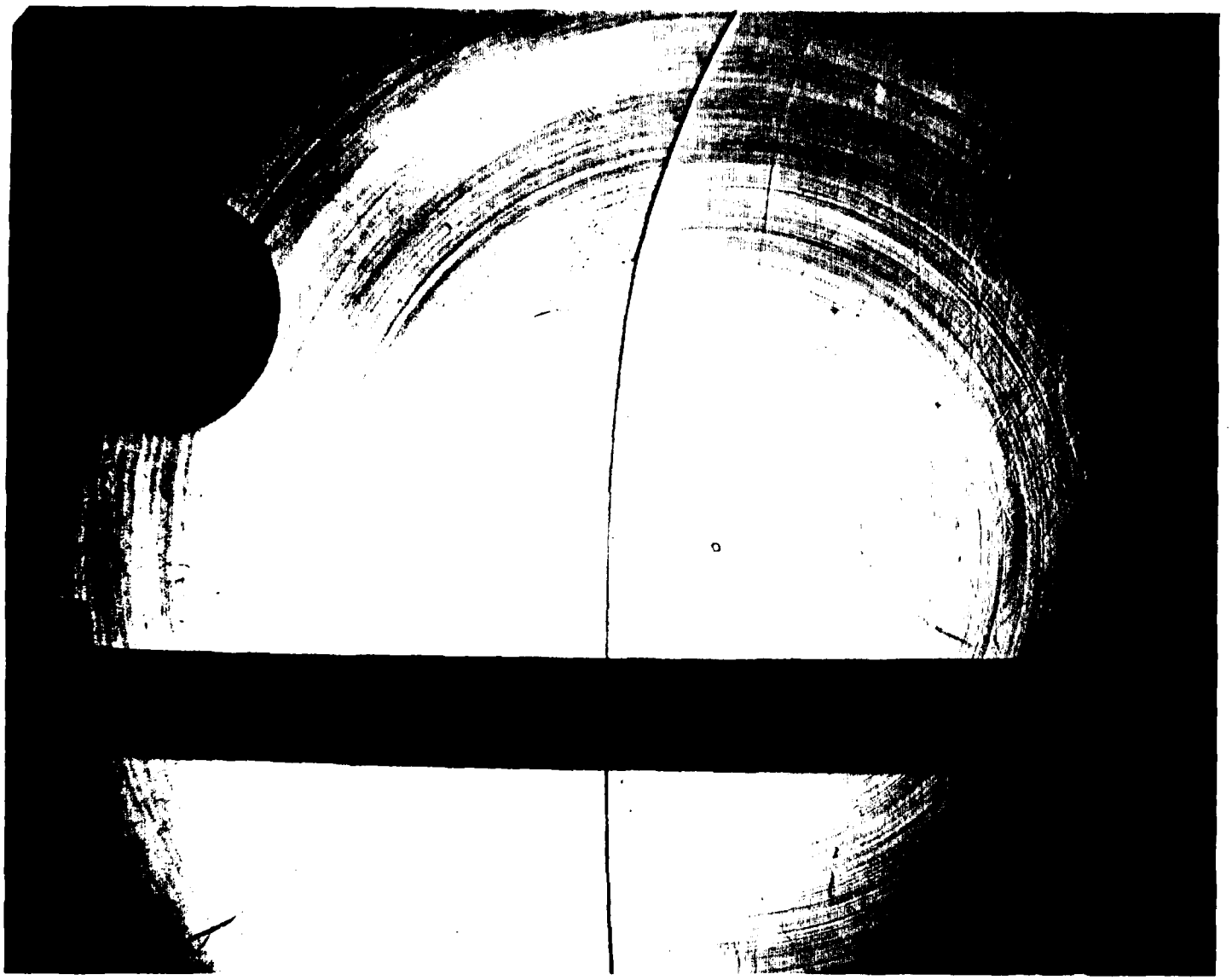

Figure B27b. Shadowgraph for round 19580, standard brake, taken with a 1050-microsecond time delay.

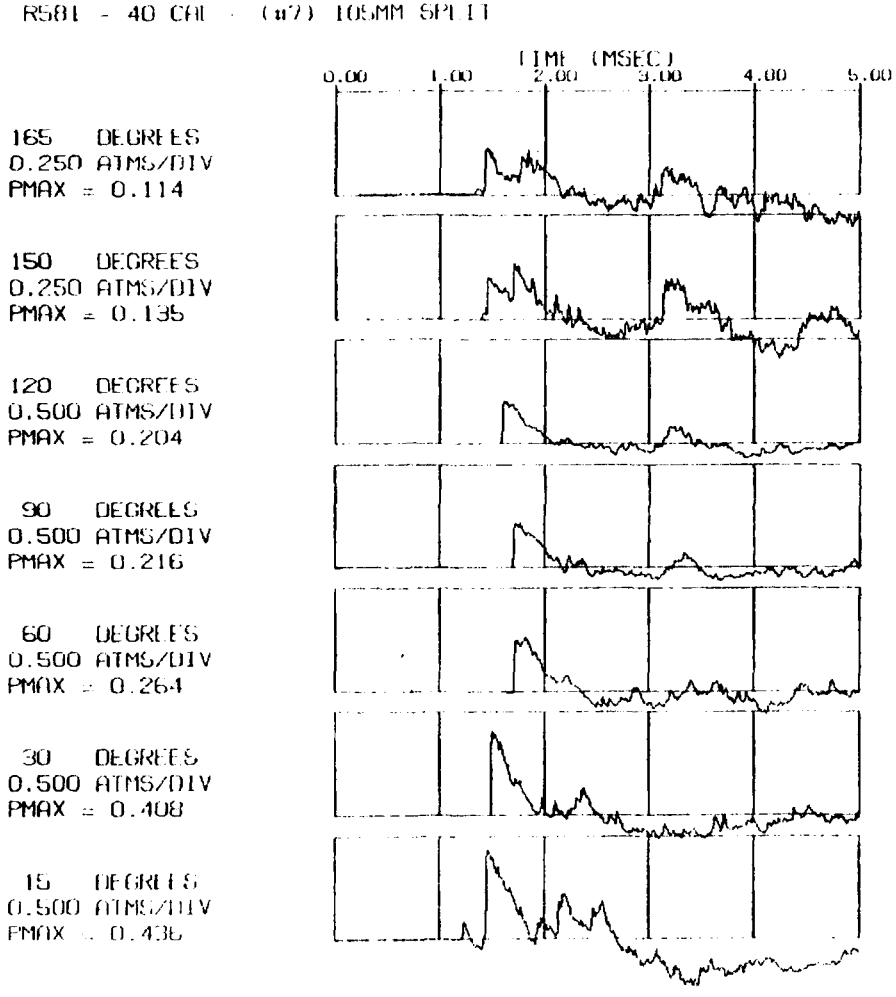

Figure B28a. Pressure histories for round 19581, split brake, at 40 calibers. Data used in report figures.

Figure B28b. Shadowgraph for round 19581, split brake, taken with a 900-microsecond time delay.

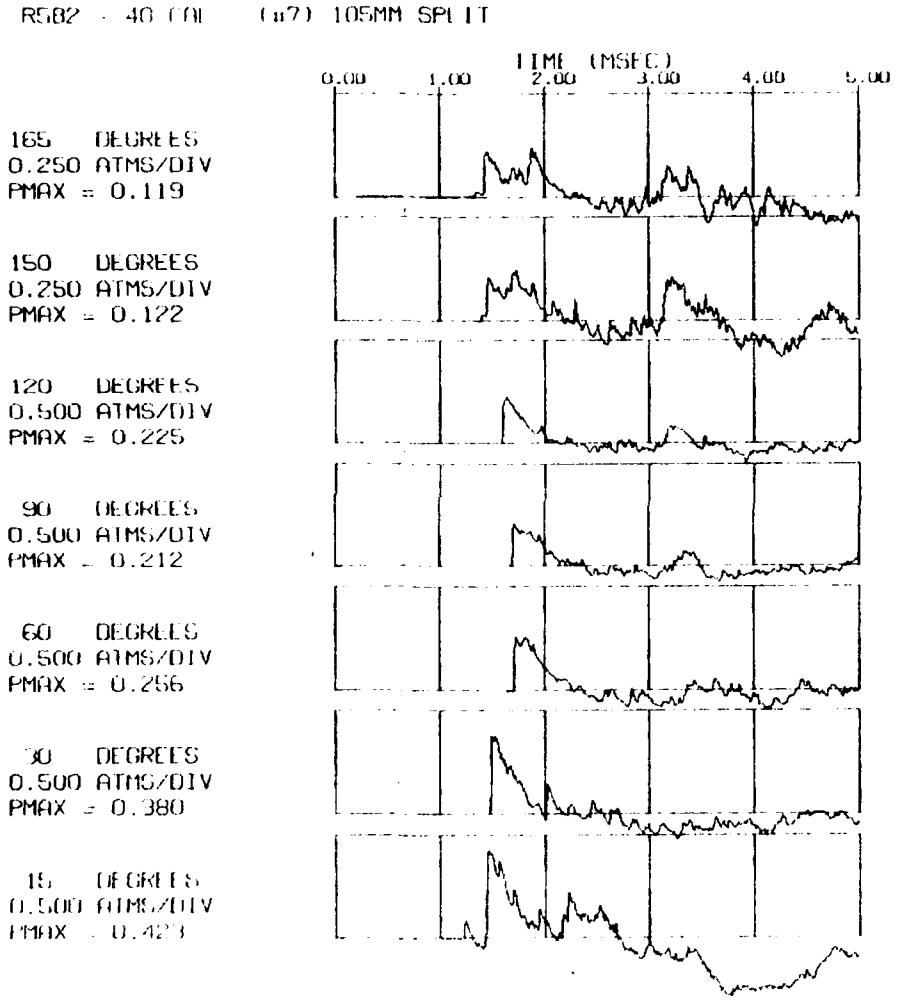

Figure B29a. Pressure histories for round 19582, split brake, at 40 calibers. Data used in report figures.

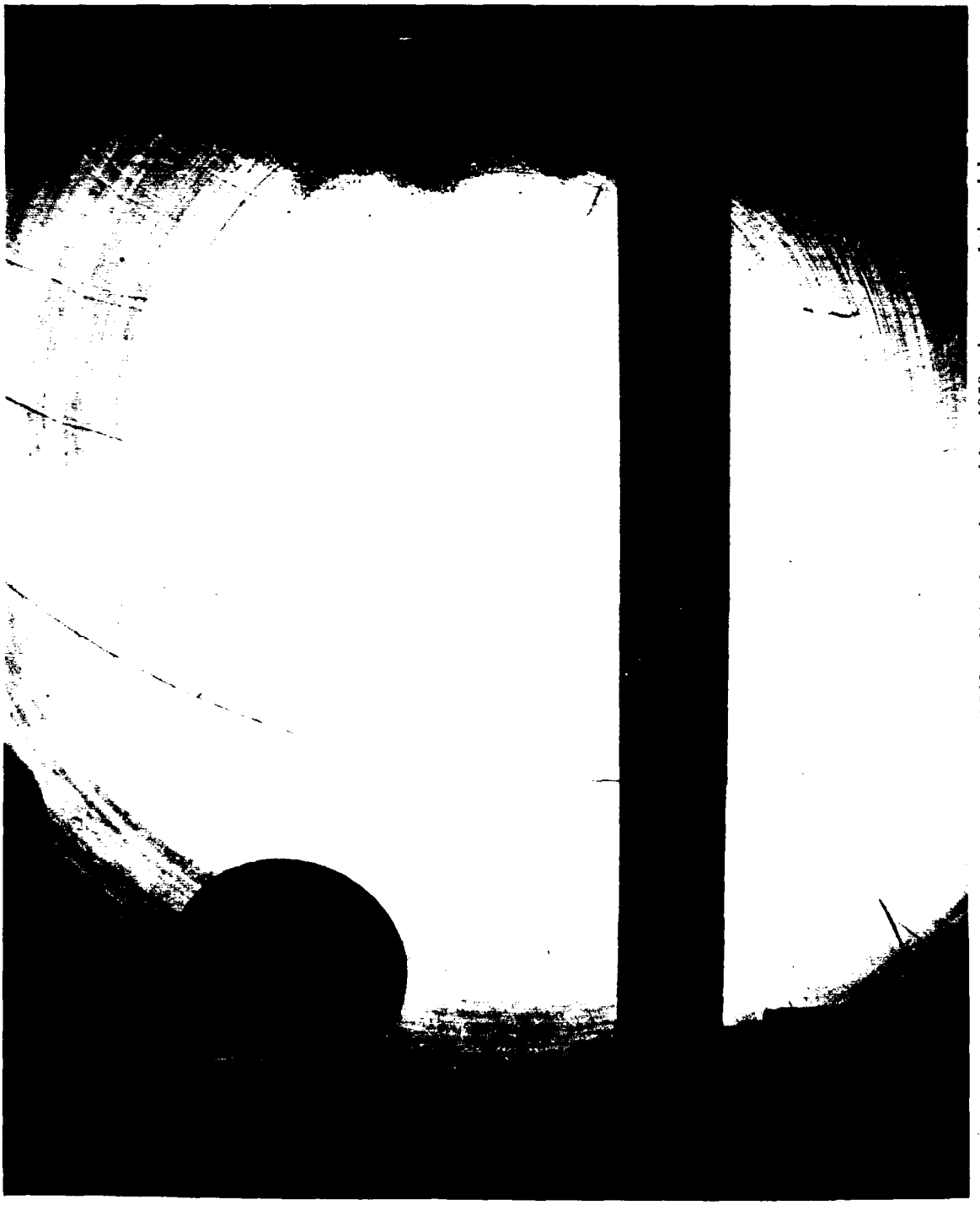

Figure B29b. Shadowgraph for round 19582, split brake, taken with a 1050-microsecond time delay.

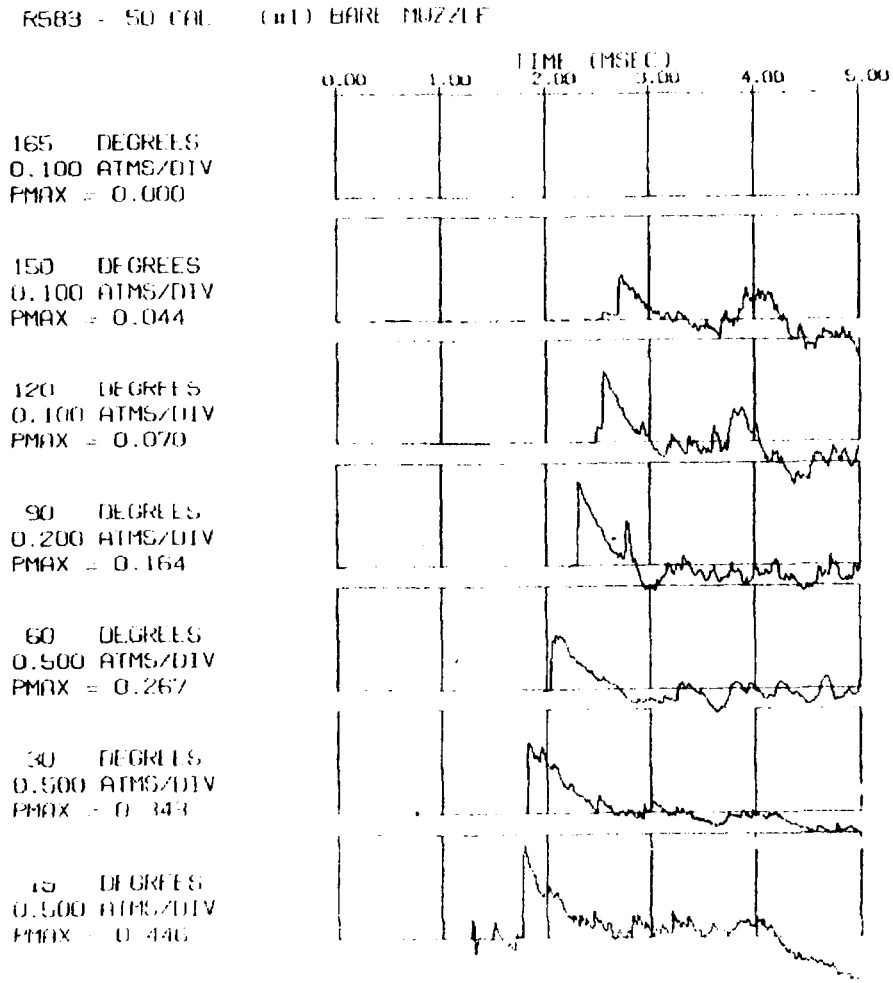

Figure B30a. Pressure histories for round 19583, bare muzzle, at 50 calibers. Data used in report figures.

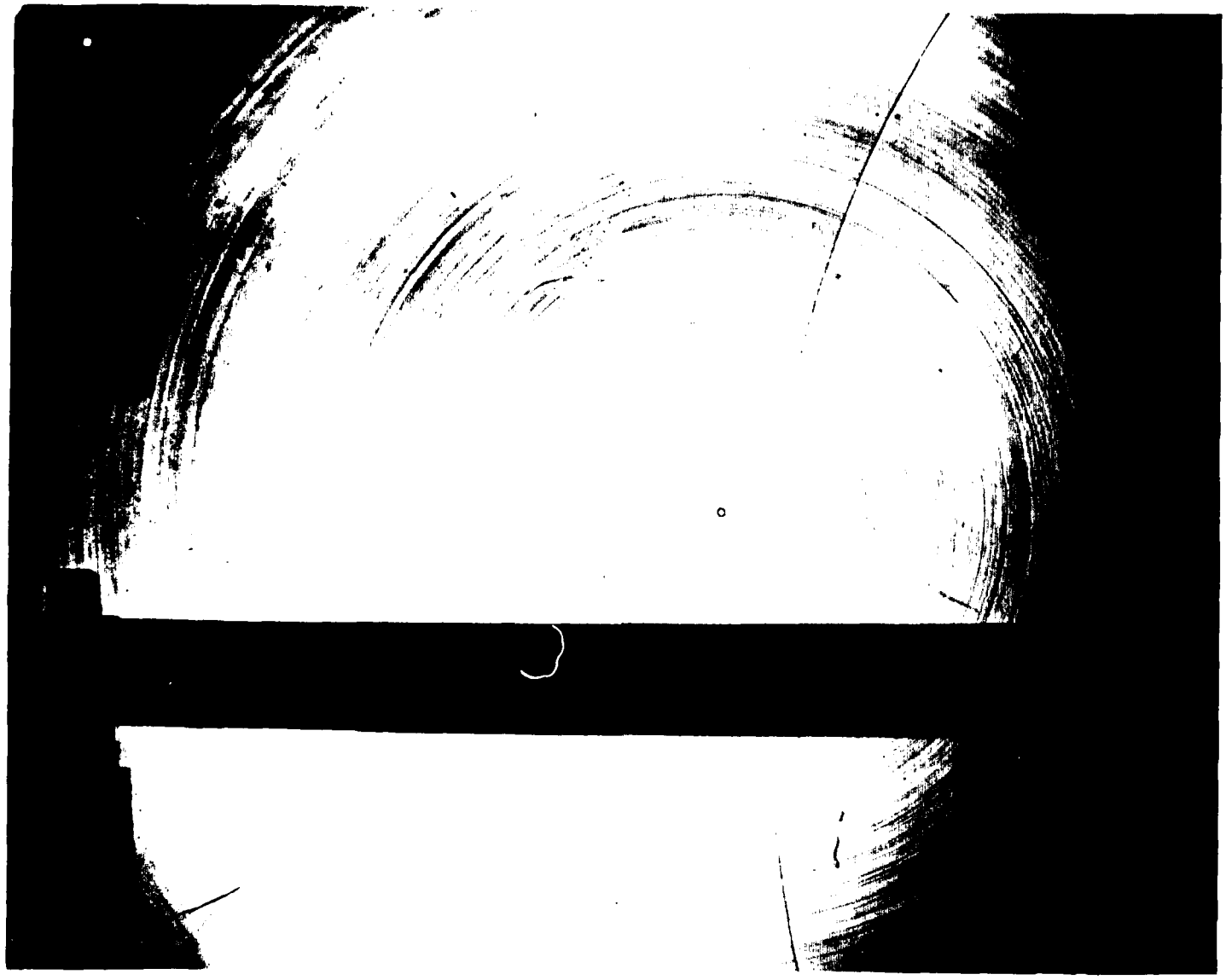

Figure B30b. Shadowgraph for round 19583, bare muzzle, taken with a 1200-microsecond time delay.

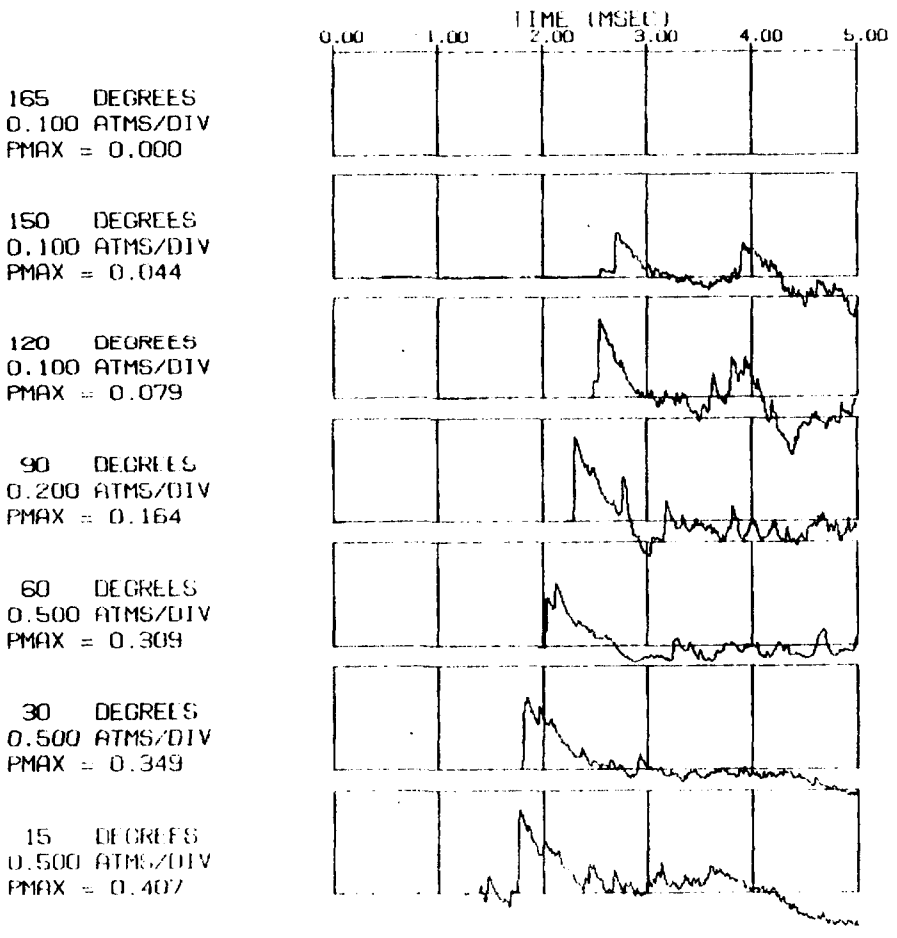

Figure B31a. Pressure histories for round 19584, bare muzzle, at 50 calibers. Data used in report figures.

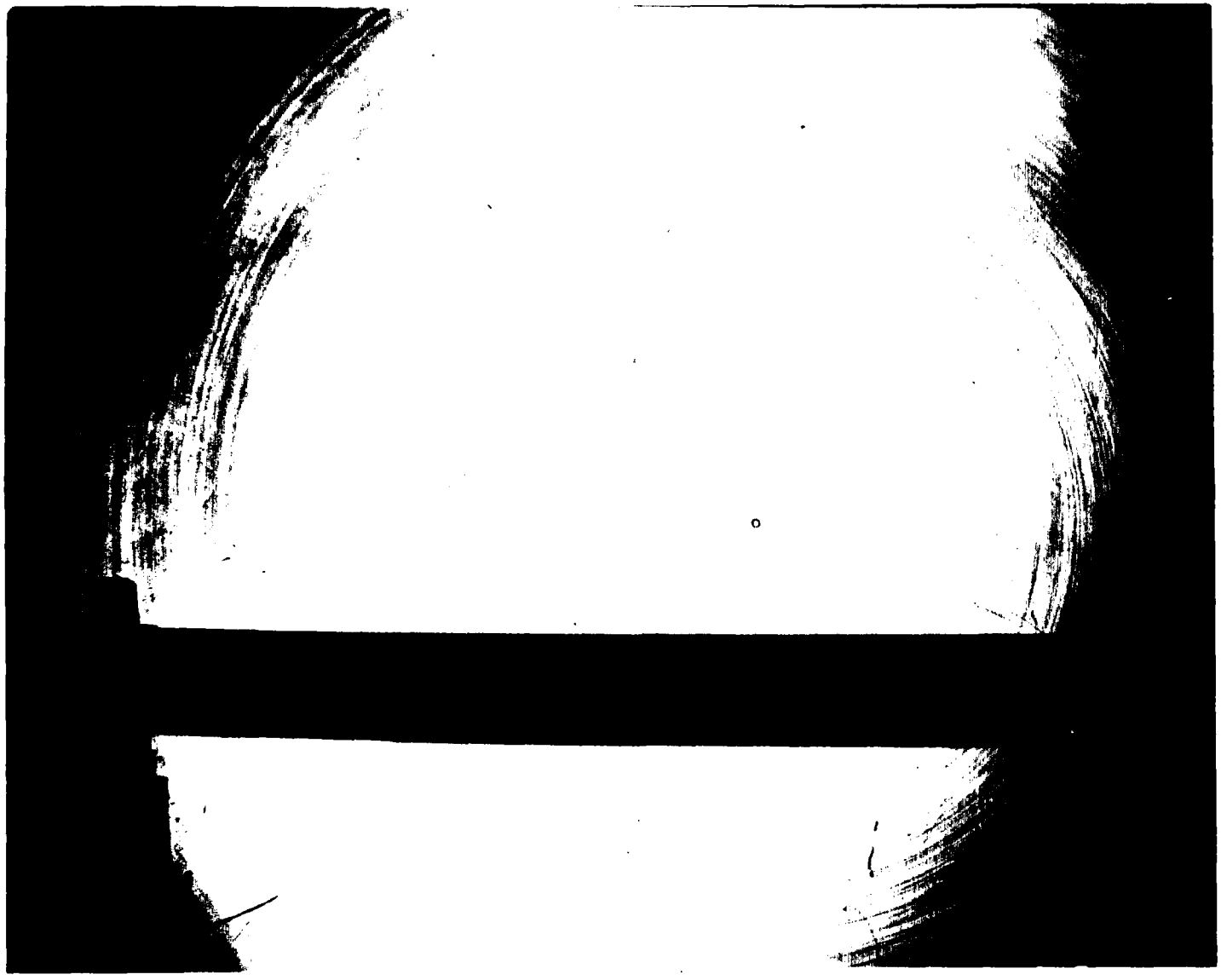

Figure B31b. Shadowgraph for round 19584, bare muzzle, taken with a 1350-microsecond time delay.

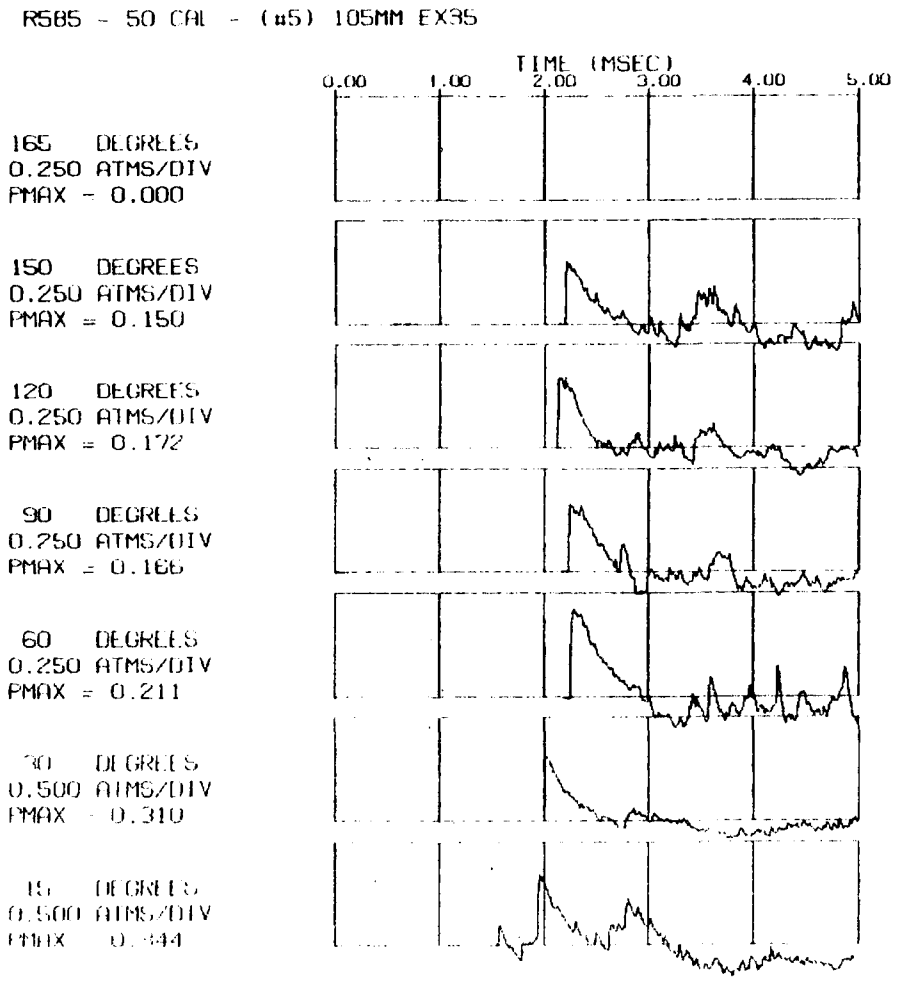

Figure B32a. Pressure histories for round 19585, standard brake, at 50 calibers. Data used in report figures.

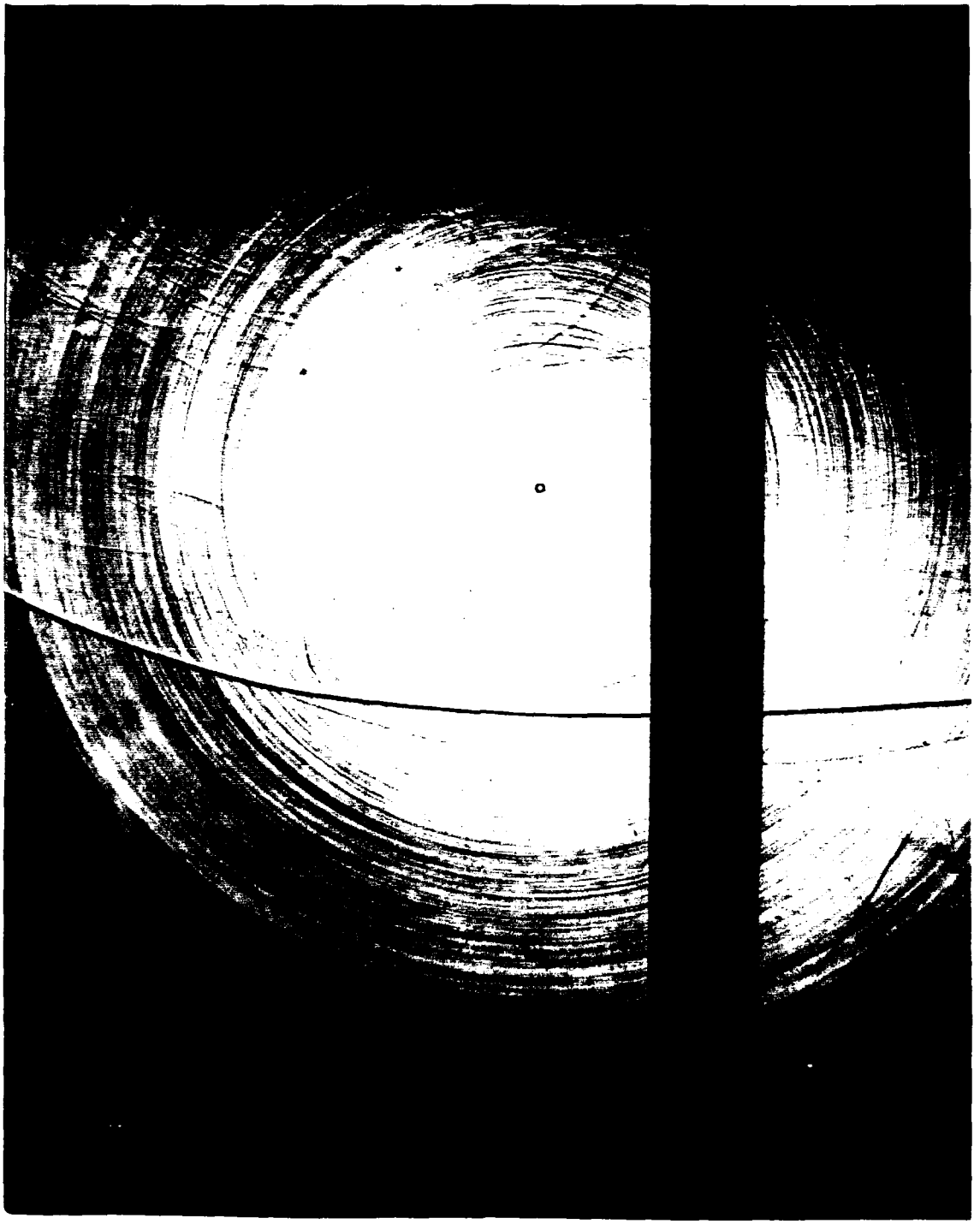

Figure B32b. Shadowgraph for round 19585, standard brake, taken with a 1200-microsecond time delay.

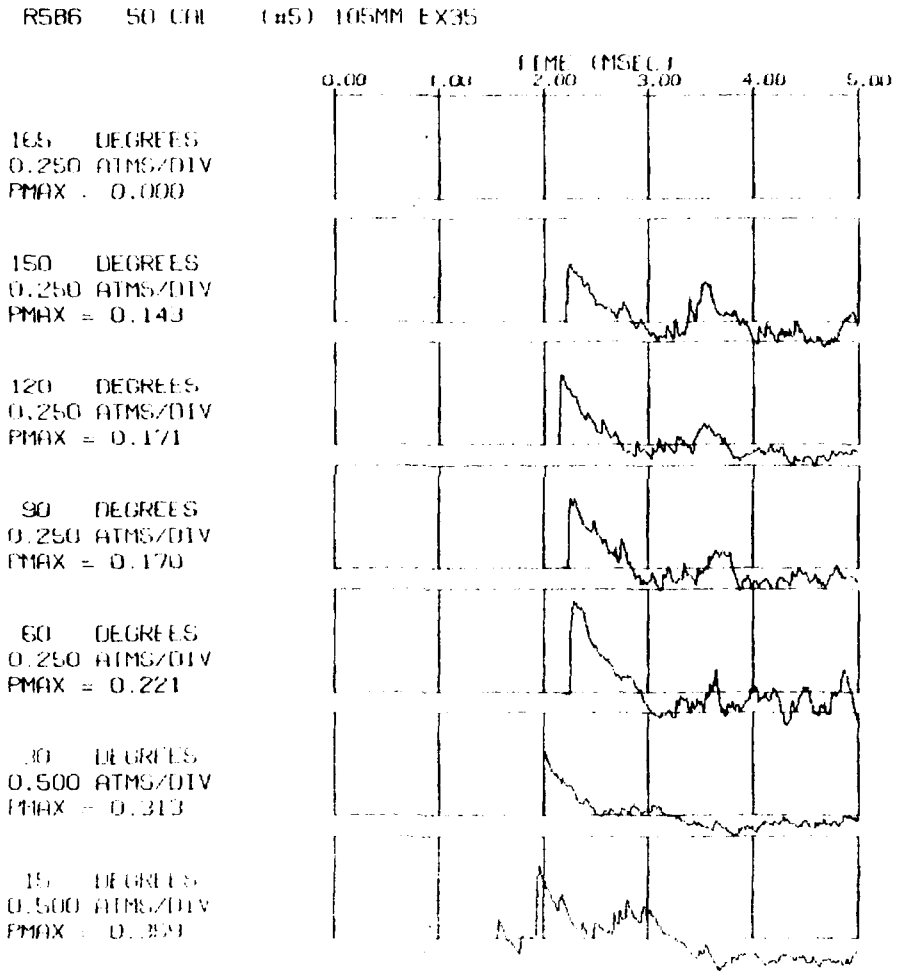

Figure B33a. Pressure histories for round 19586, standard brake, at 50 calibers. Data used in report figures.

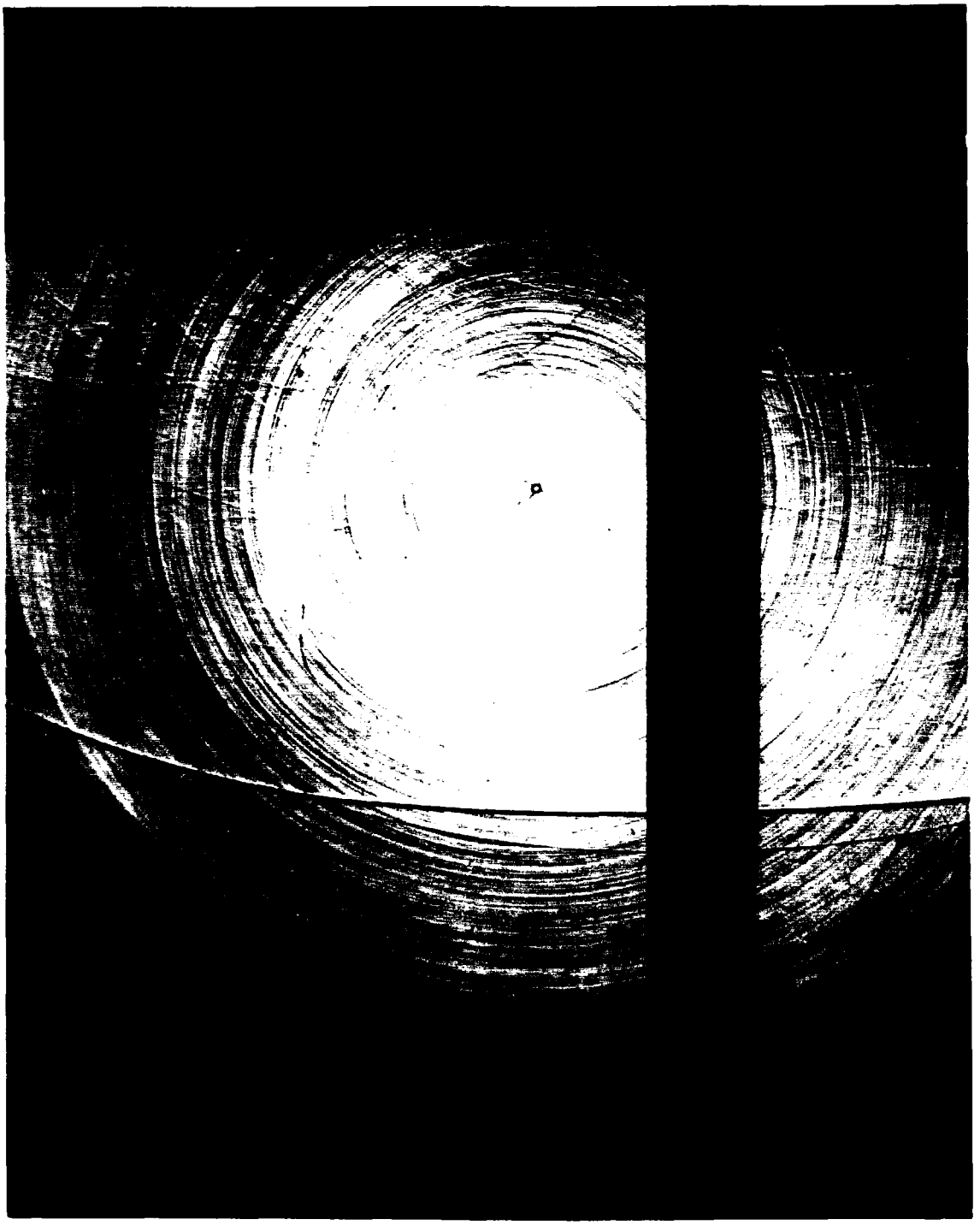

Figure B33b. Shadowgraph for round 19586, standard brake, taken with a 1350-microsecond time delay.

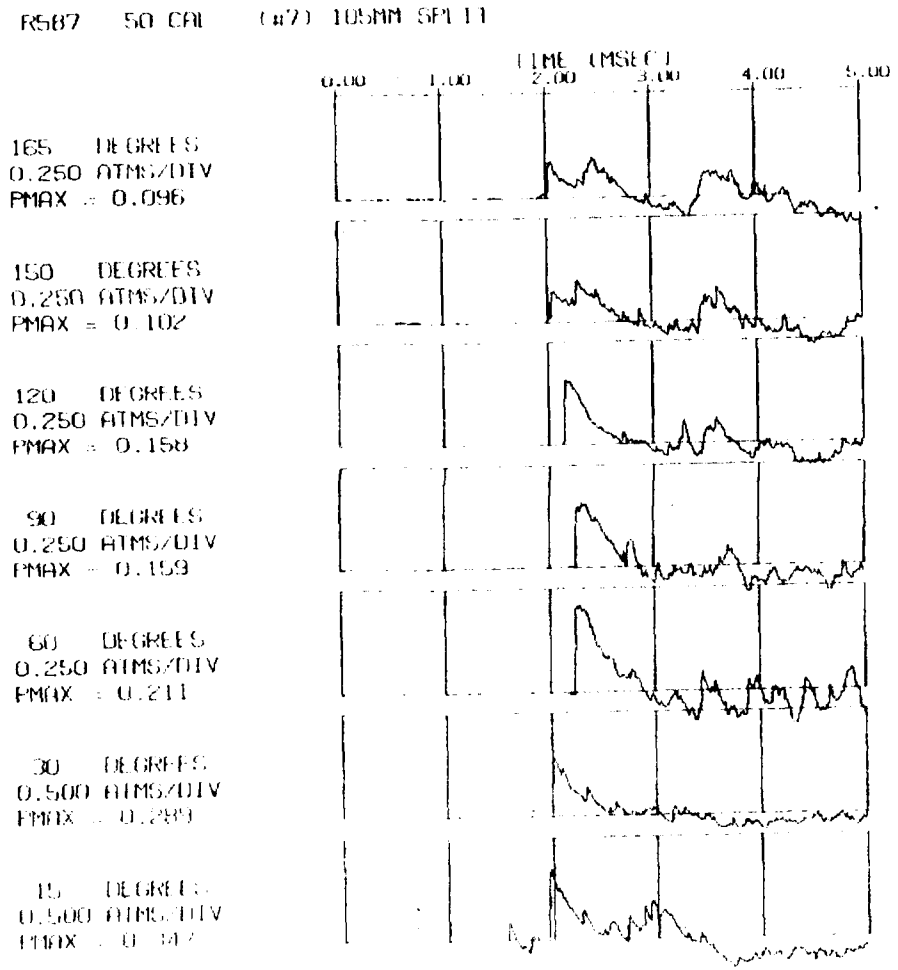

Figure B34a. Pressure histories for round 19587, split brake, at 50 calibers. Data used in report figures.

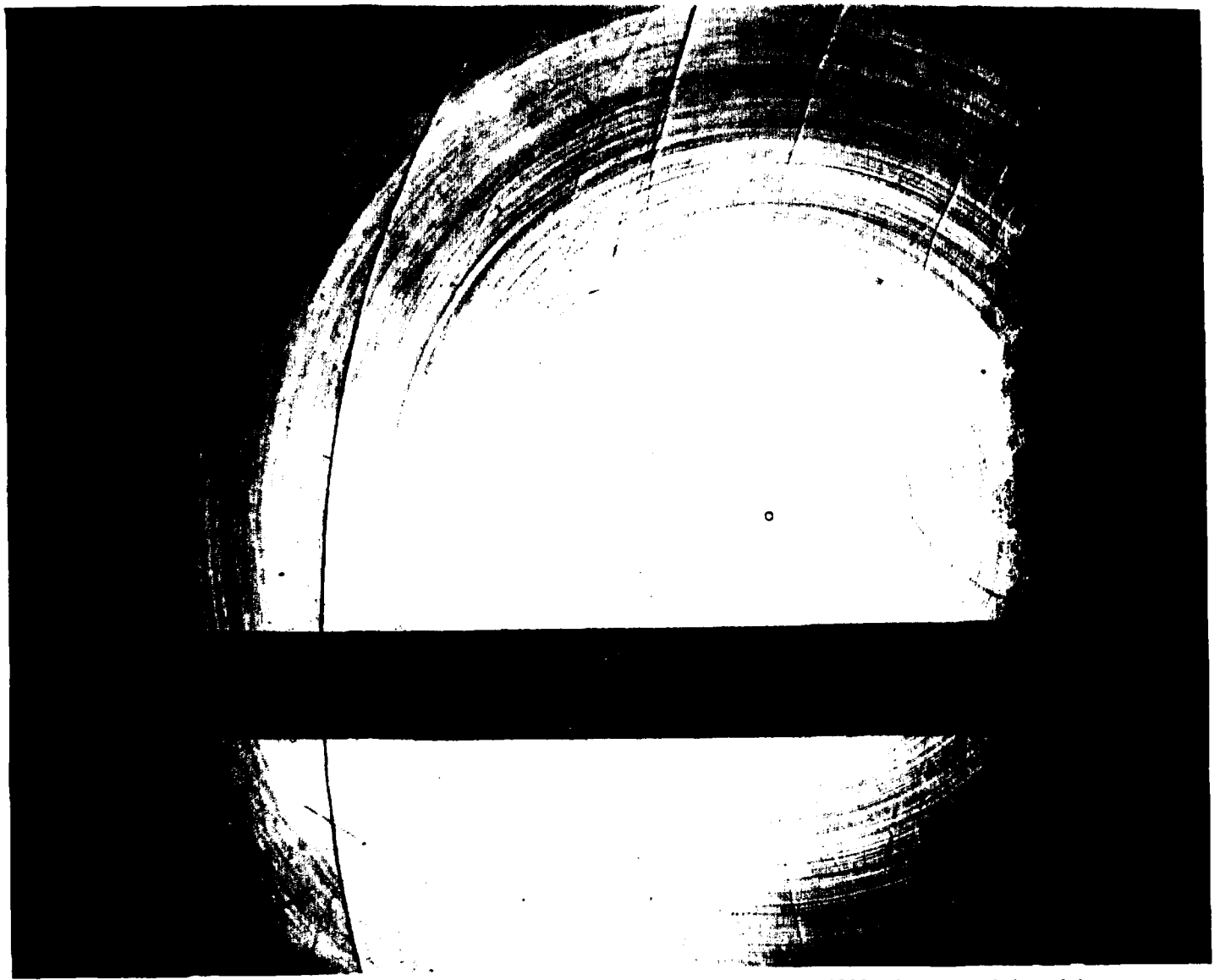

Figure B34b. Shadowgraph for round 19587, split brake, taken with a 1200-microsecond time delay.

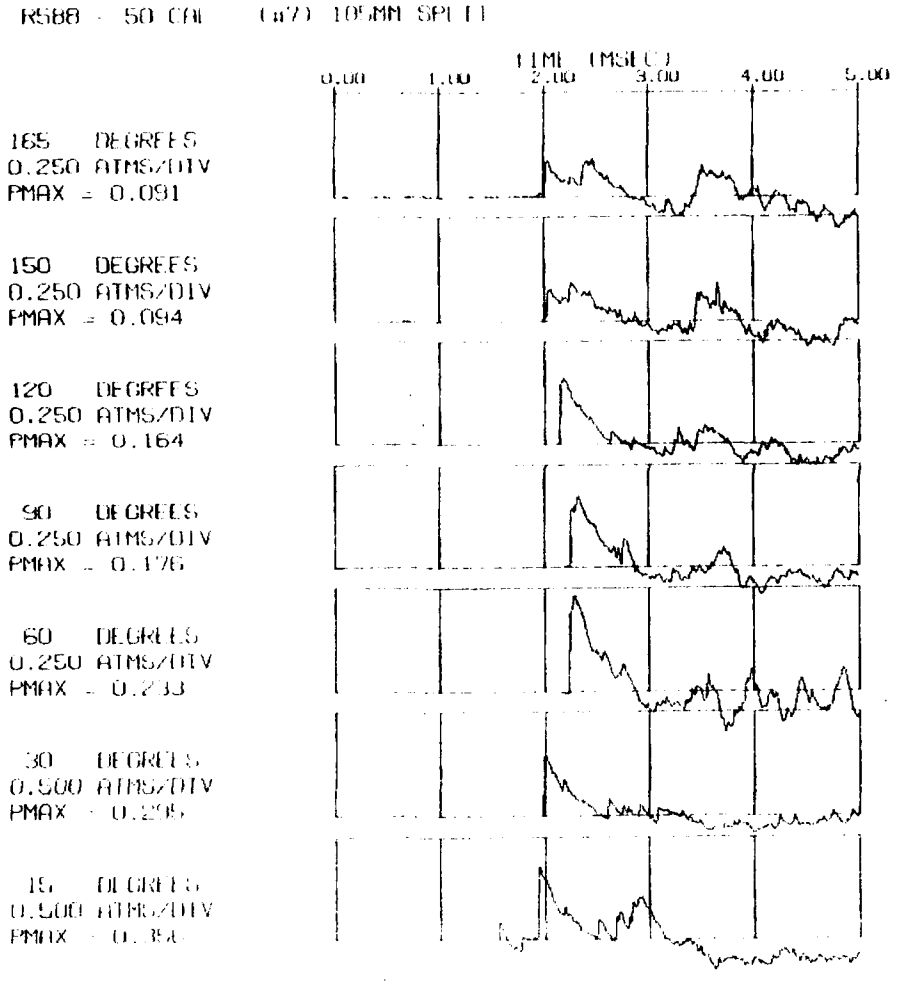

Figure B35a. Pressure histories for round 19588, split brake, at 50 calibers. Data used in report figures.

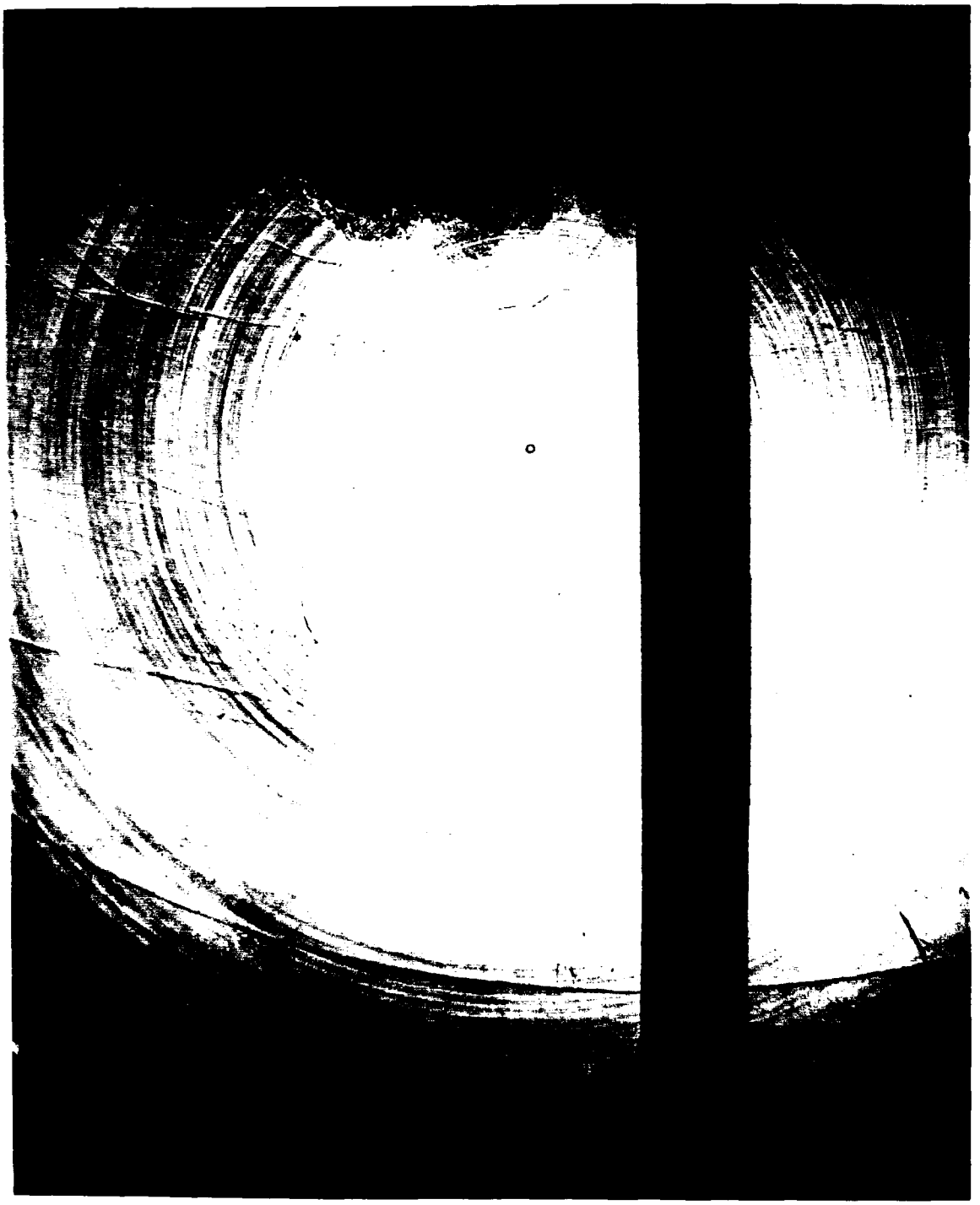

Figure B35b. Shadowgraph for round 19588, split brake, taken with a 1350-microsecond time delay.

APPENDIX C

The data presented in this appendix were obtained as part of a brake efficiency study reported elsewhere (ref 10). Fifty-nine rounds were fired in the program, thirty-five of which pertain to this study. For consistency, the round number identifier used in the efficiency study is retained here, therefore some gaps appear in Table C1 below.

The projectile velocity was measured by a pair of light stations placed downstream which produced an average value 4.6 m from the muzzle. The cannon recoiled freely in the experiment, and the impulse was determined from its mass and terminal velocity.

Table C1. Measured Velocity and Impulse Data

Round	Extension	Velocity (m/sec)	Impulse (nt-sec)
19530	bare muzzle	1060.1	150.1
19531	bare muzzle	1055.5	151.5
19532	bare muzzle	1065.3	153.8
19533	bare muzzle	1051.0	-
19543	standard brake	1060.7	122.1
19544	standard brake	1060.7	127.0
19545	standard brake	1061.0	123.0
19549	split brake	1058.6	123.2
19550	split brake	1048.2	122.1
19551	split brake	1050.6	122.8
19552	bare muzzle	1058.3	149.9
19553	bare muzzle	1058.0	150.3
19554	bare muzle	1054.9	150.9
19555	bare muzzle	1058.9	151.1
19556	bare muzzle	1056.1	149.9
19566	standard brake	1060.4	121.1
19567	standard brake	1066.2	119.0
19568	standard brake	1056.1	-
19569	standard brake	1061.6	120.3
19573	split brake	1060.1	122.8

Table C1. Continued

Round	Extension	Velocity (m/sec)	Impulse (nt-sec)
19574	split brake	1060.1	118.2
19575	split brake	1061.0	122.1
19576	bare muzzle	1055.5	148.8
19577	bare muzzle	1065.0	149.7
19578	bare muzzle	1061.6	149.1
19579	standard brake	1057.0	121.1
19580	standard brake	1061.0	121.8
19581	split brake	1060.7	121.3
19582	split brake	1061.9	121.1
19583	bare muzzle	1062.2	149.9
19584	bare muzzle	1065.3	150.1
19585	standard brake	1055.5	121.3
19586	standard brake	1056.4	120.7
19587	split brake	1059.8	121.8
19588	split brake	1058.0	120.7

The data in Table C1 were numerically averaged to give the results in Tables C2 and C3 along with the maximum and minimum deviations from the averages. The impulses were not reported for rounds 19533 (bare muzzle) and 19568 (standard brake), which accounts for the smaller number of rounds in Table C3.

Table C2. Averaged Velocity Data

Extension	Number of Rounds	Velocity (m/sec)	+ Dev (m/sec)	- Dev (m/sec)
bare muzzle	14	1059.1	6.2	-8.2
standard brake	11	1059.7	6.5	-4.2
split brake	10	1057.9	4.0	-9.7

Table C3. Averaged Impulse Data

Extension	Number of Rounds	Impulse (nt-sec)	+ Dev (nt-sec)	- Dev (nt-sec)
bare muzzle	13	150.4	3.4	-1.6
standard brake	10	121.4	2.2	-2.4
split brake	10	121.6	1.6	-3.4

APPENDIX D

This appendix contains the pressure histories obtained in the 105-mm field experiment for the standard brake and the split brake. At the left of each trace the maximum overpressure, PMAX, and the magnitude of the first wave to arrive in the trace, PFIRST, are given, both in atmospheres. The gage location in degrees is also shown. The magnitude of the ordinate for every trace is one atmosphere per division.

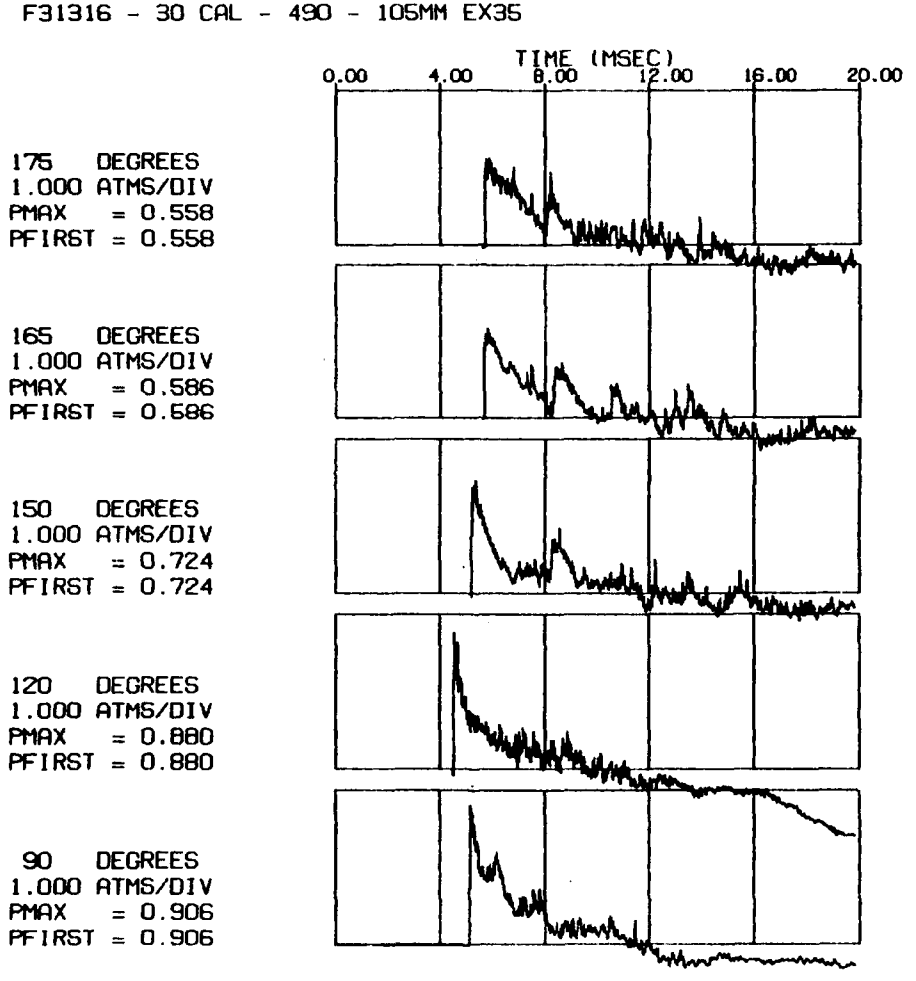

Figure D1. Pressure histories at 30 calibers for round 31316 using the 105-mm standard brake and M490 ammunition.

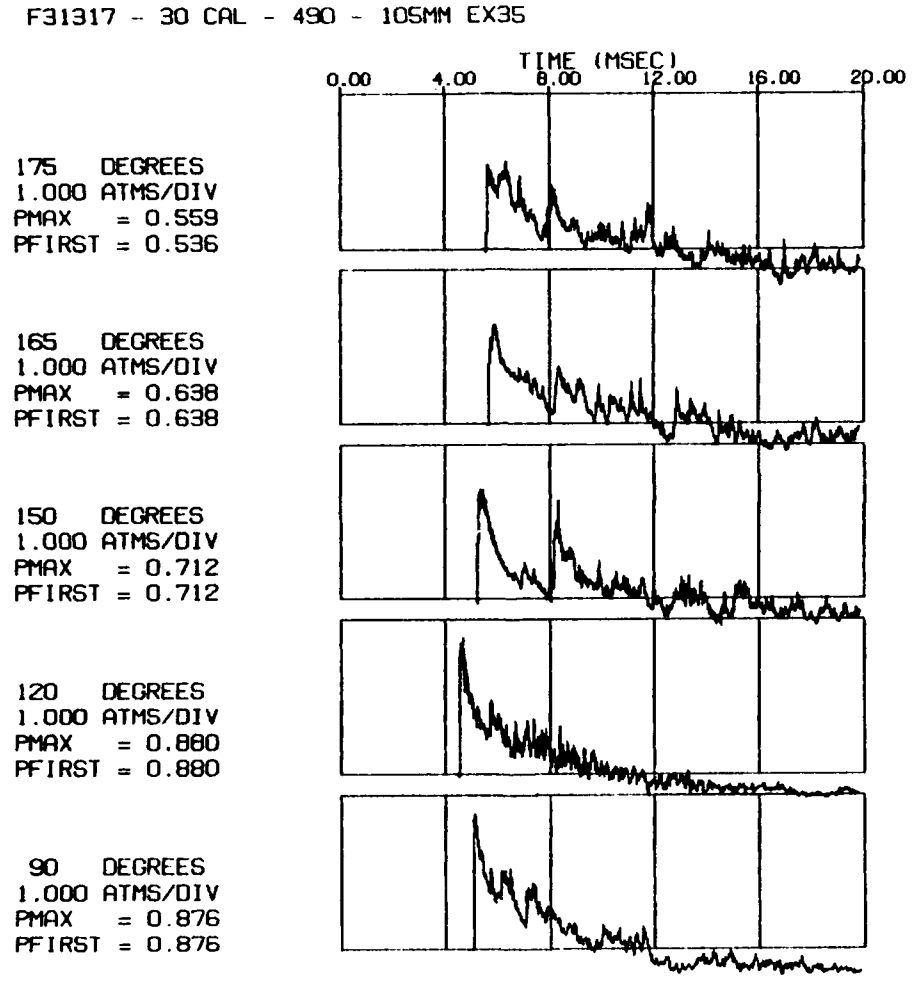

Figure D2. Pressure histories at 30 calibers for round 31317 using the 105-mm standard brake and M490 ammunition.

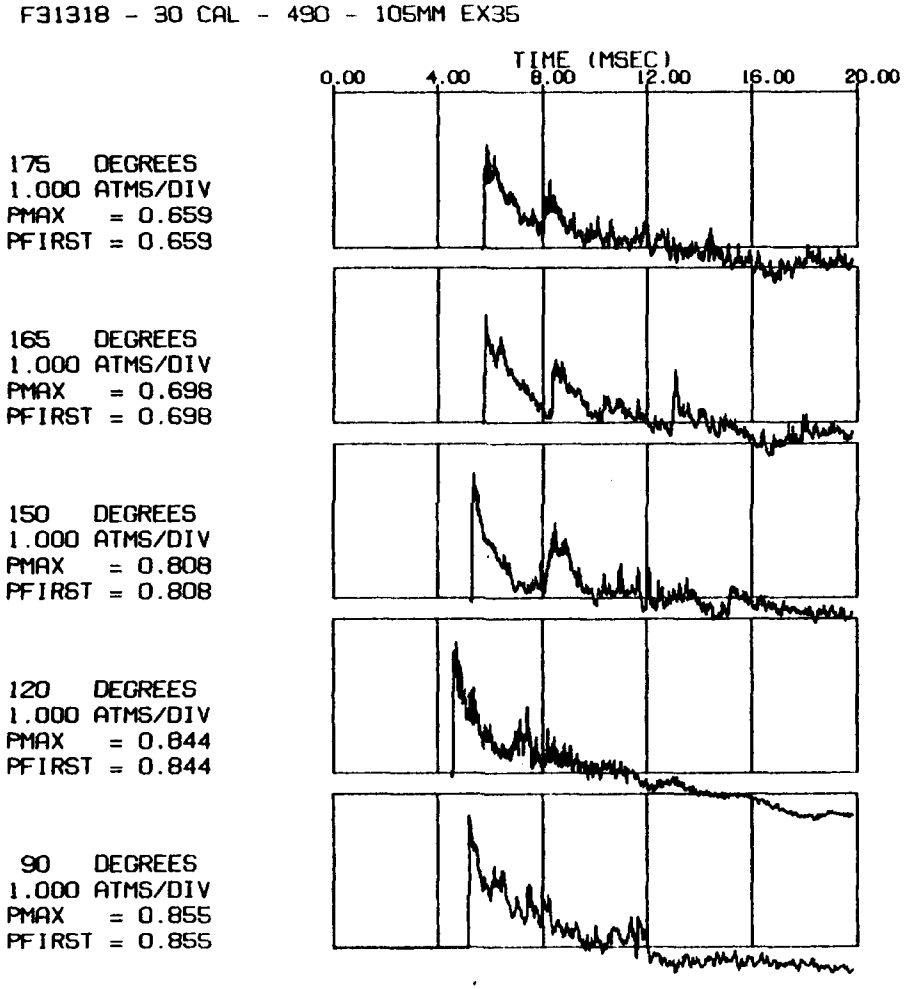

Figure D3. Pressure histories at 30 calibers for round 31318 using the 105-mm standard brake and M490 ammunition.

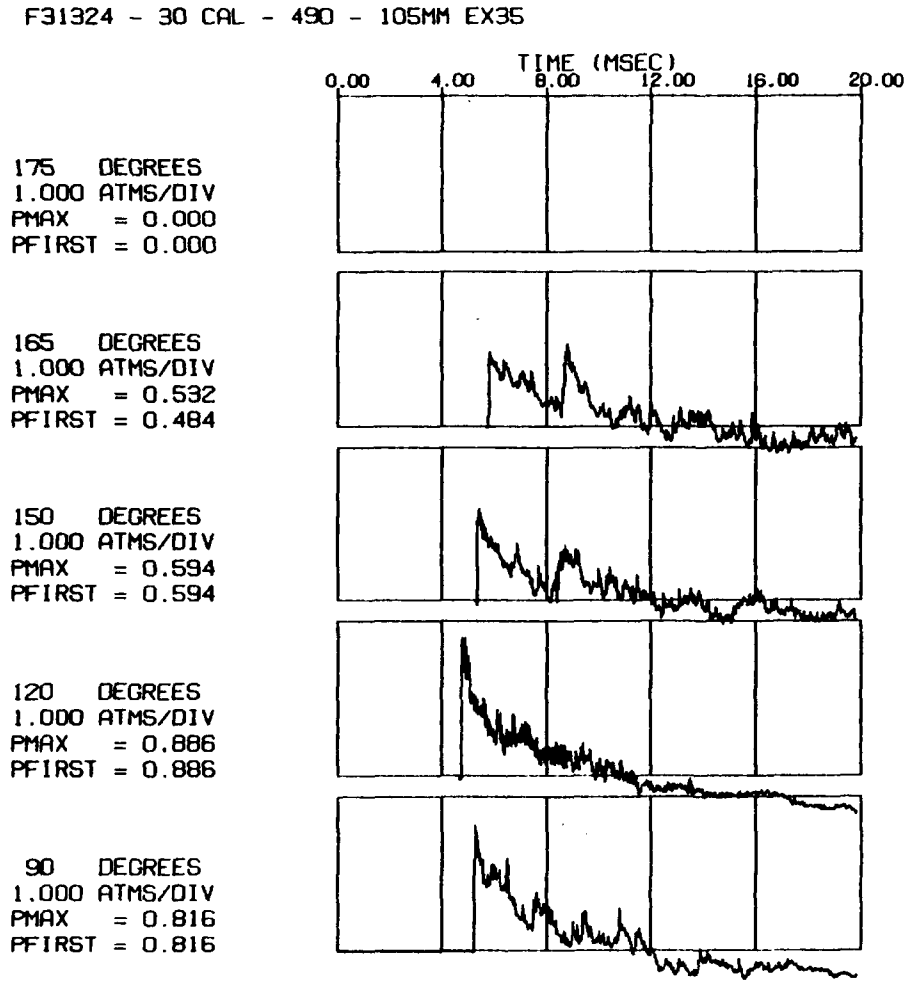

Figure D4. Pressure histories at 30 calibers for round 31324 using the 105-mm standard brake and M490 ammunition.

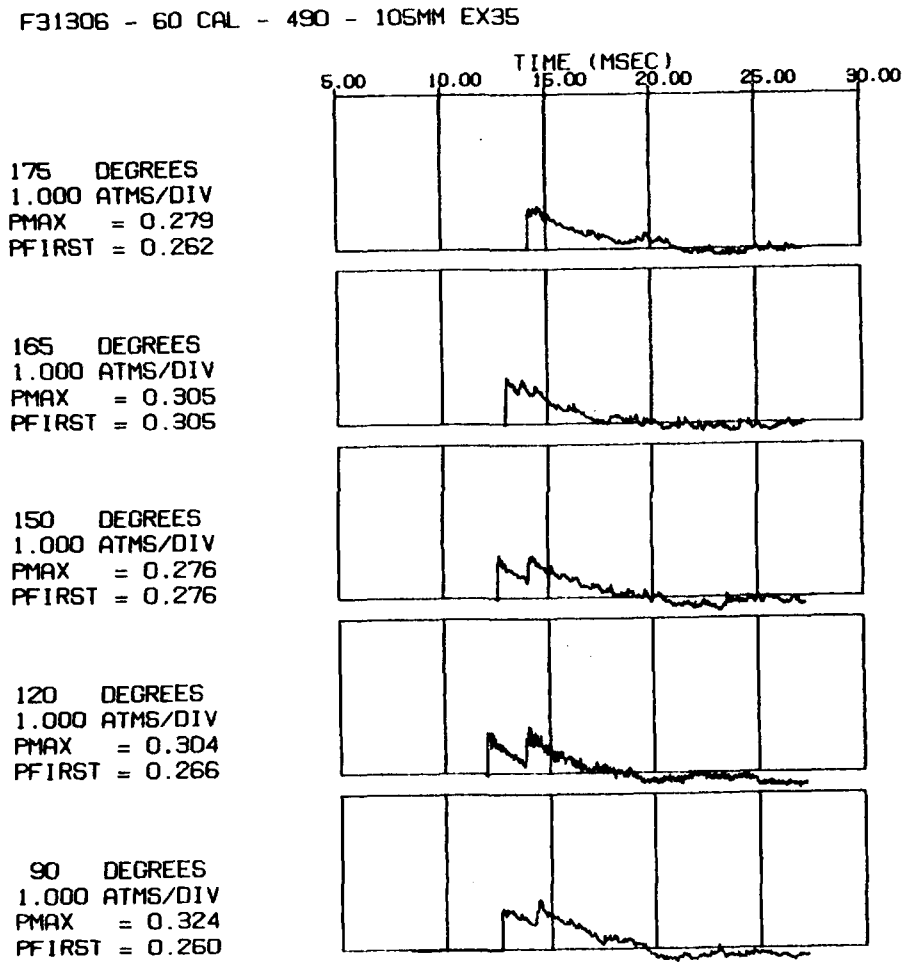

Figure D5. Pressure histories at 60 calibers for round 31306 using the 105-mm standard brake and M490 ammunition.

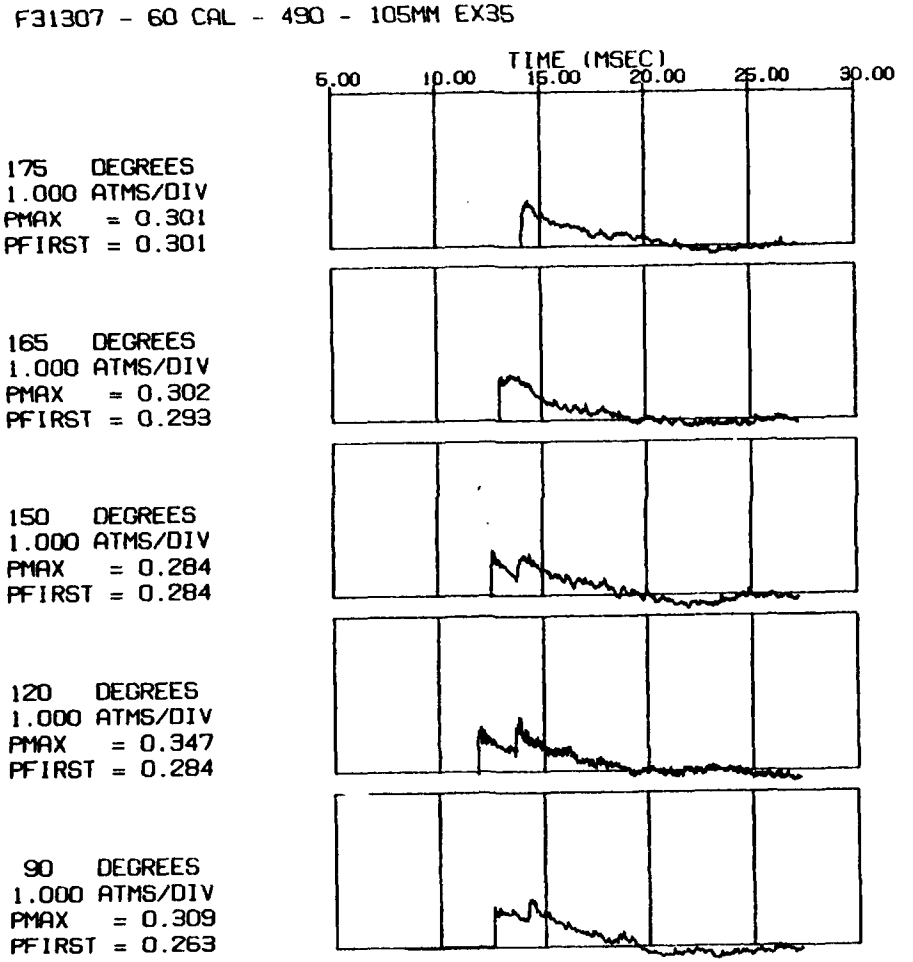

Figure D6. Pressure histories at 60 calibers for round 31307 using the 105-mm standard brake and M490 ammunition.

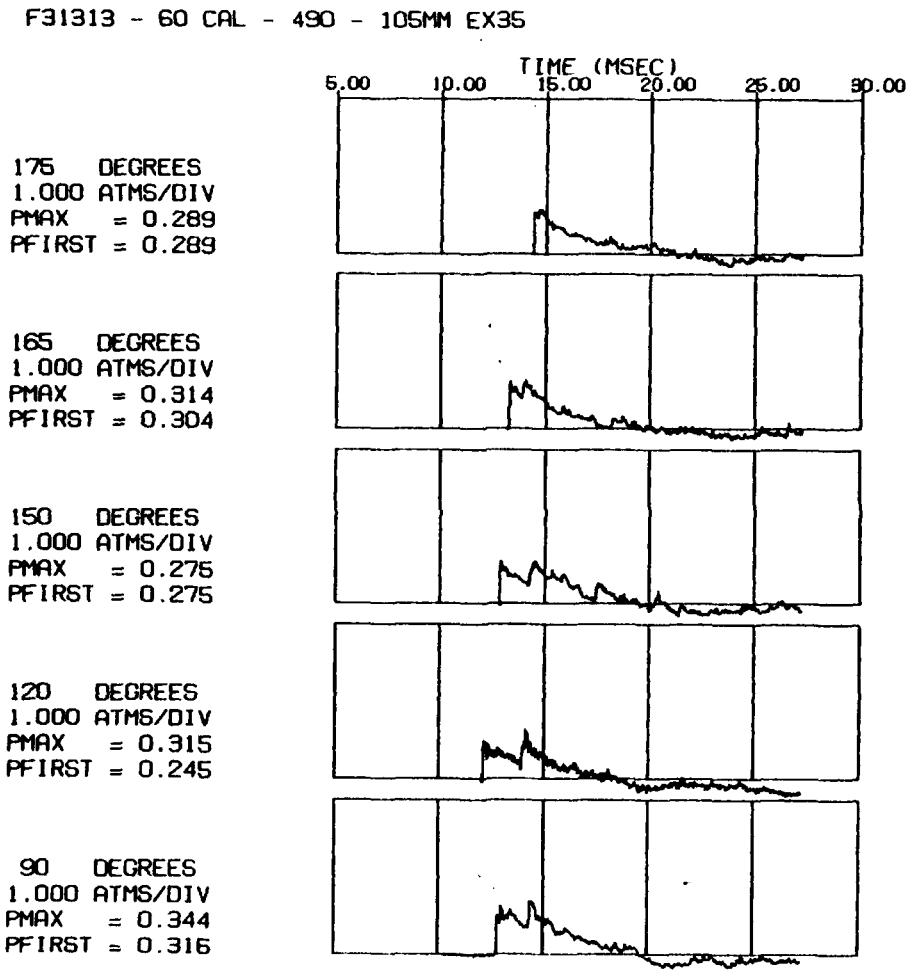

Figure D7. Pressure histories at 60 calibers for round 31313 using the 105-mm standard brake and M490 ammunition.

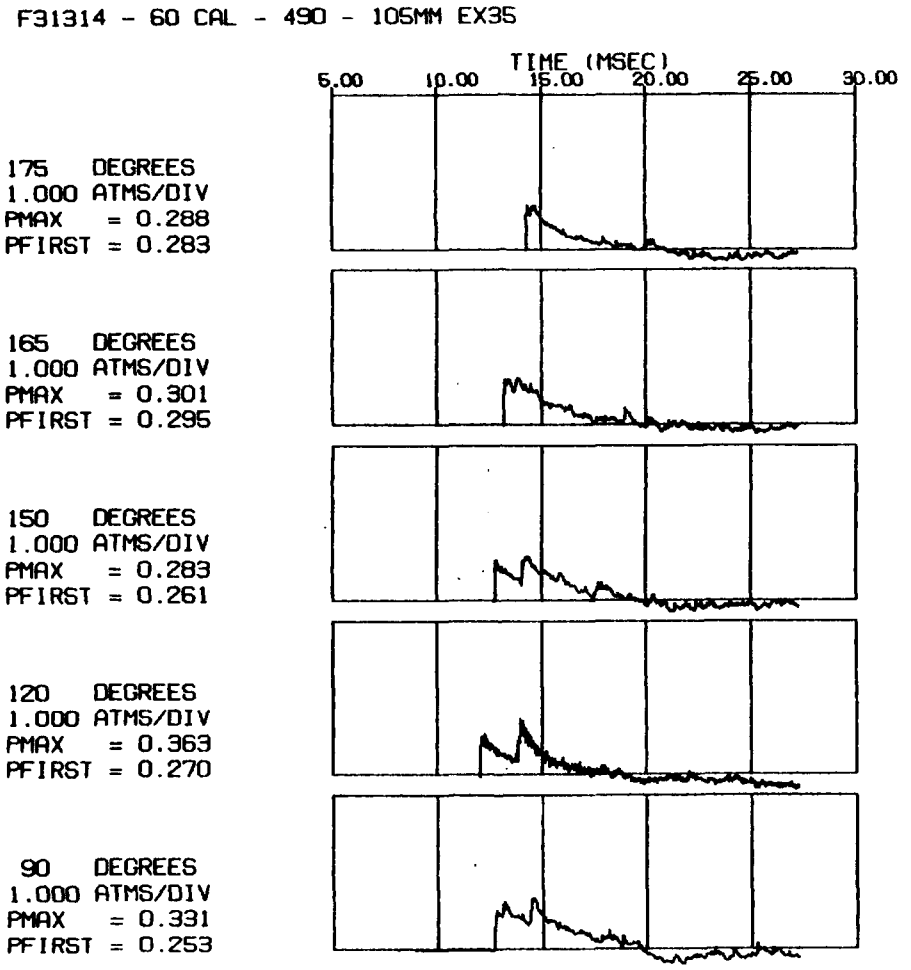

Figure D8. Pressure histories at 60 calibers for round 31314 using the 105-mm standard brake and M490 ammunition.

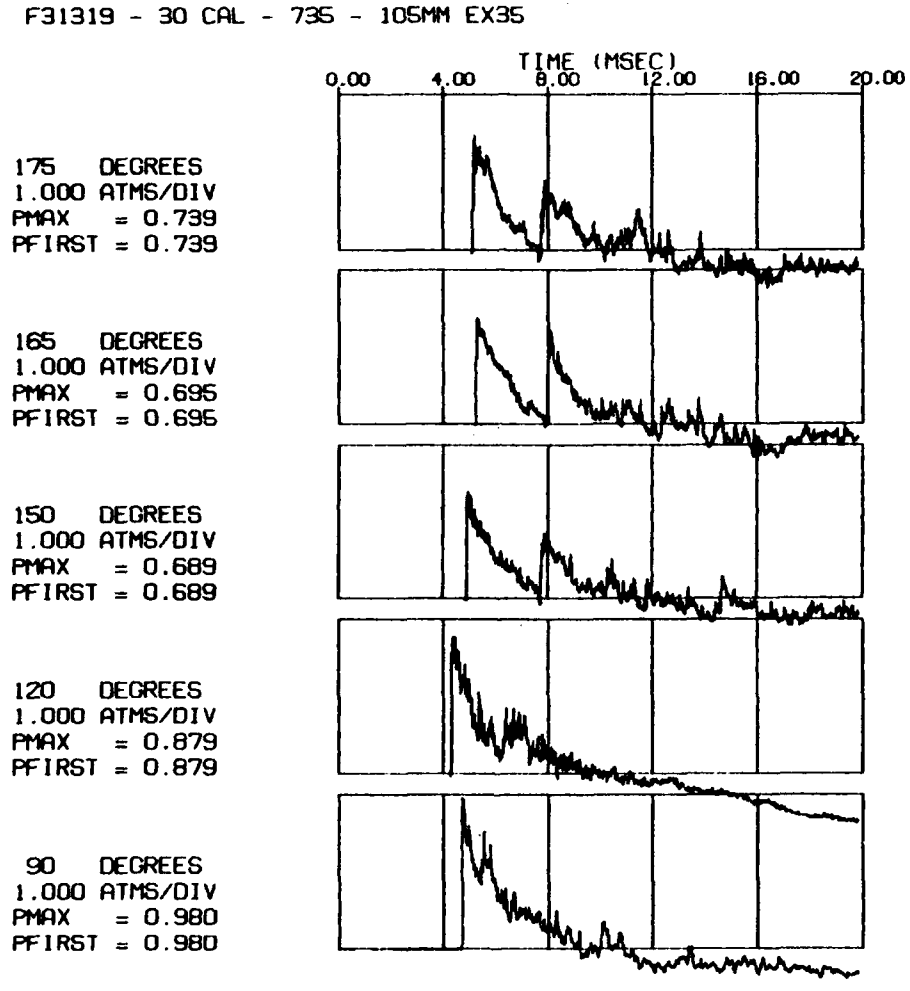

Figure D9. Pressure histories at 30 calibers for round 31319 using the 105-mm standard brake and M735 ammunition.

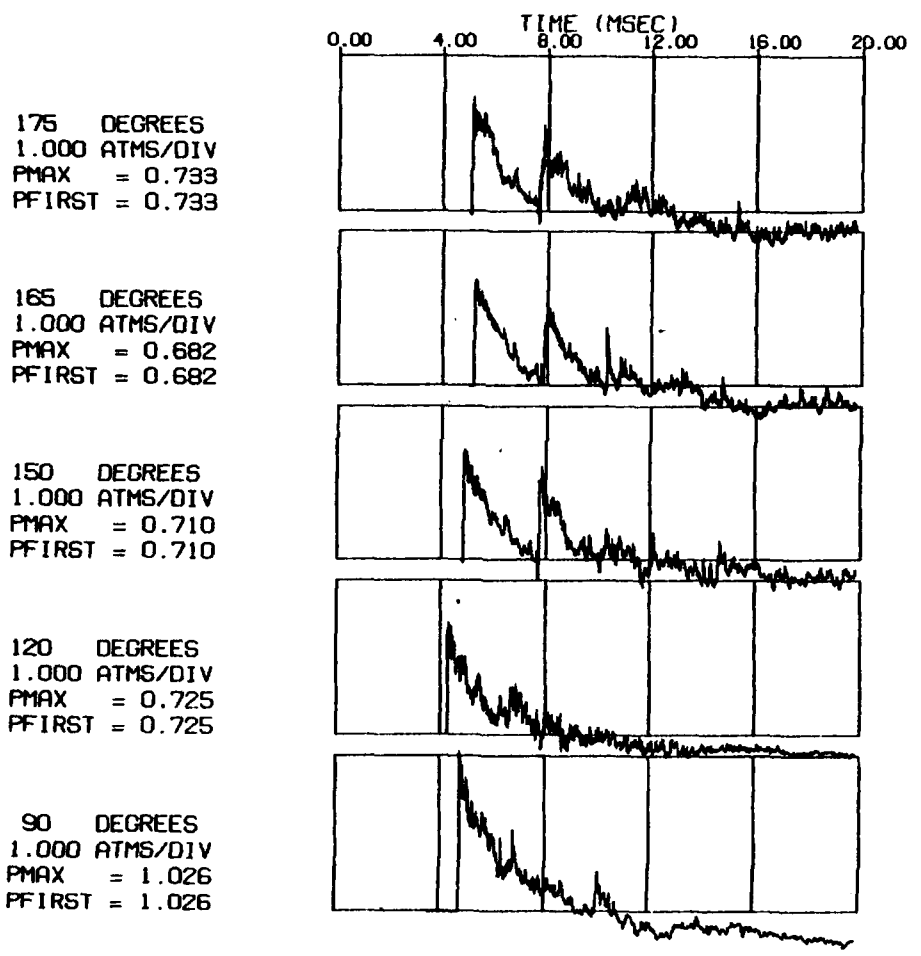

Figure D10. Pressure histories at 30 calibers for round 31320 using the 105-mm standard brake and M735 ammunition.

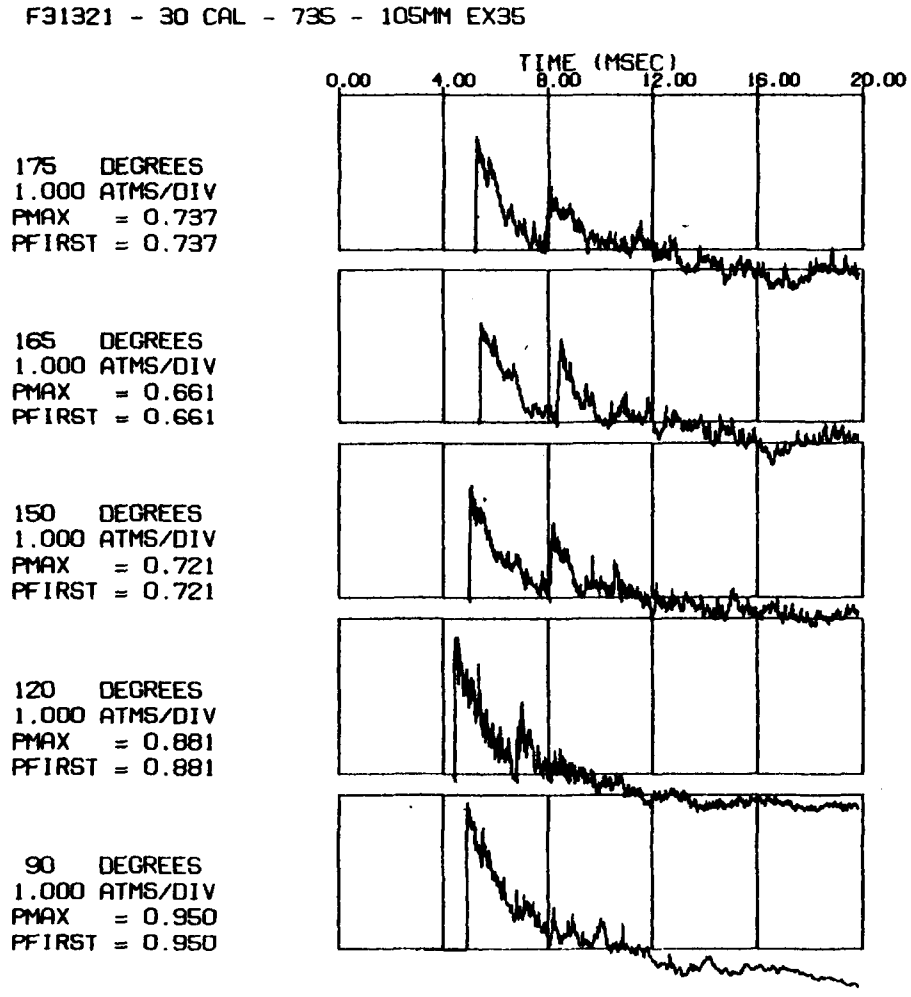

Figure D11. Pressure histories at 30 calibers for round 31321 using the 105-mm standard brake and M735 ammunition.

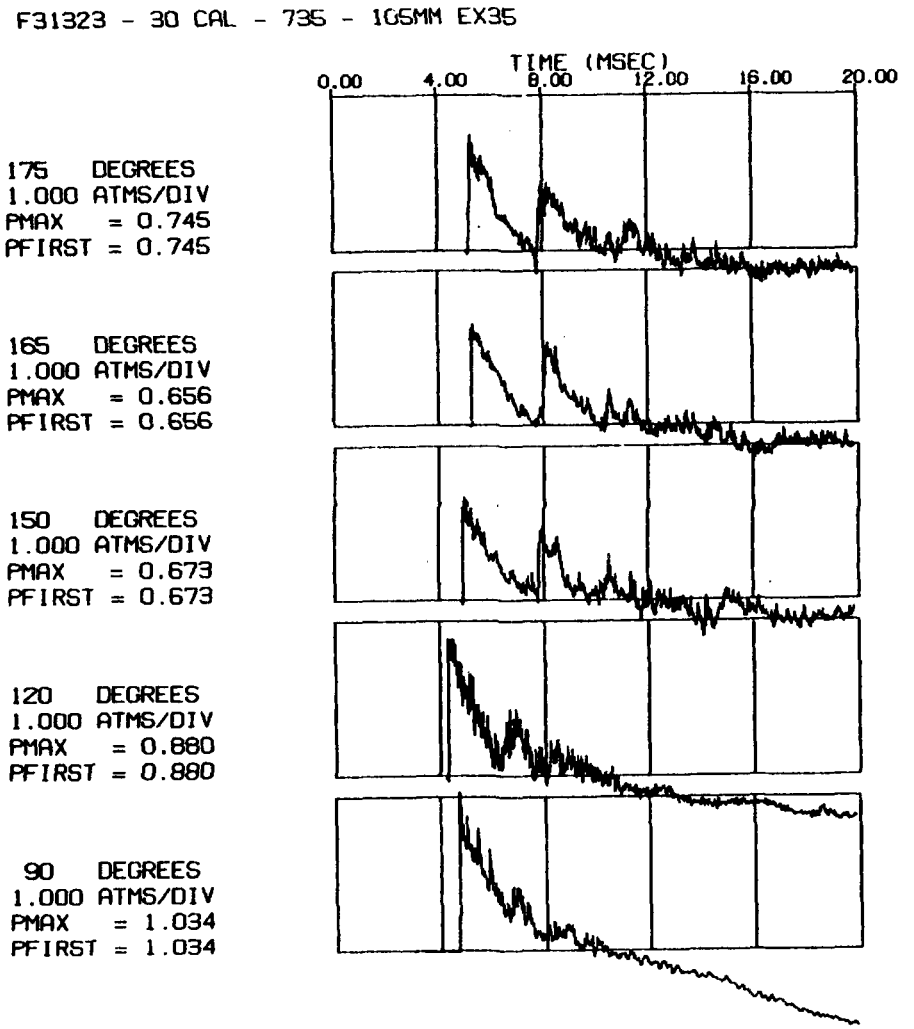

Figure D12. Pressure histories at 30 calibers for round 31322 using the 105-mm standard brake and M735 ammunition.

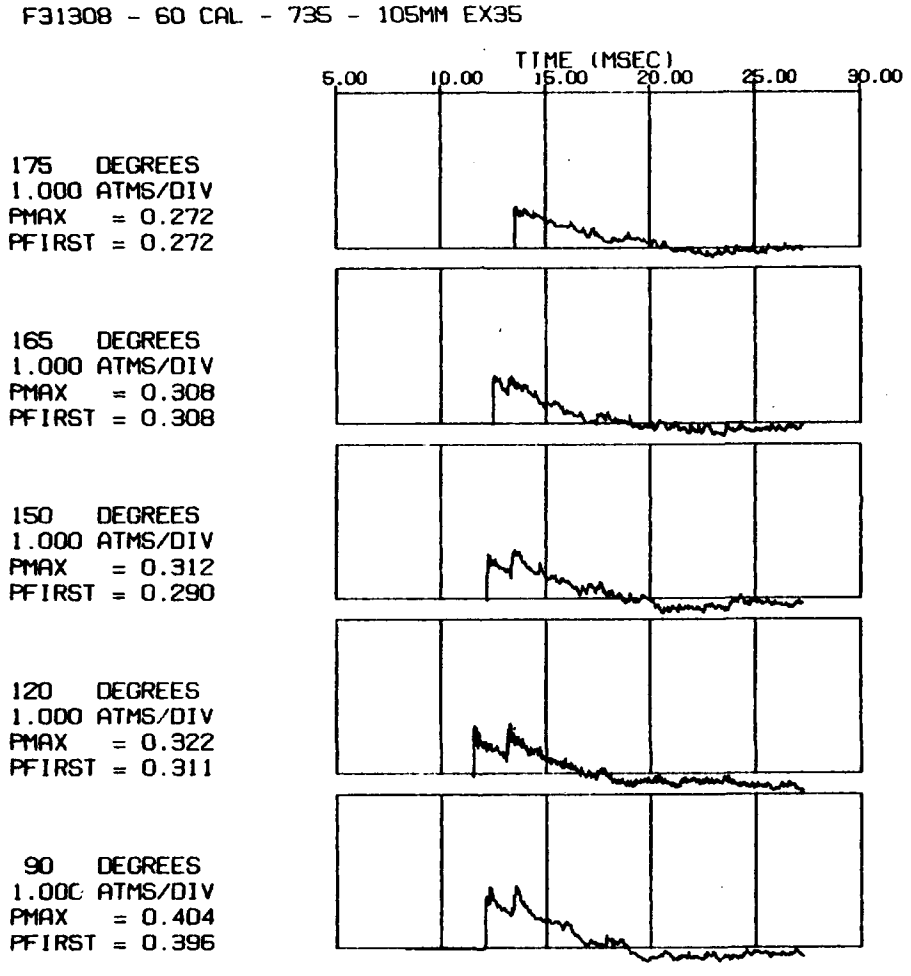

Figure D13. Pressure histories at 60 calibers for round 31308 using the 105-mm standard brake and M735 ammunition.

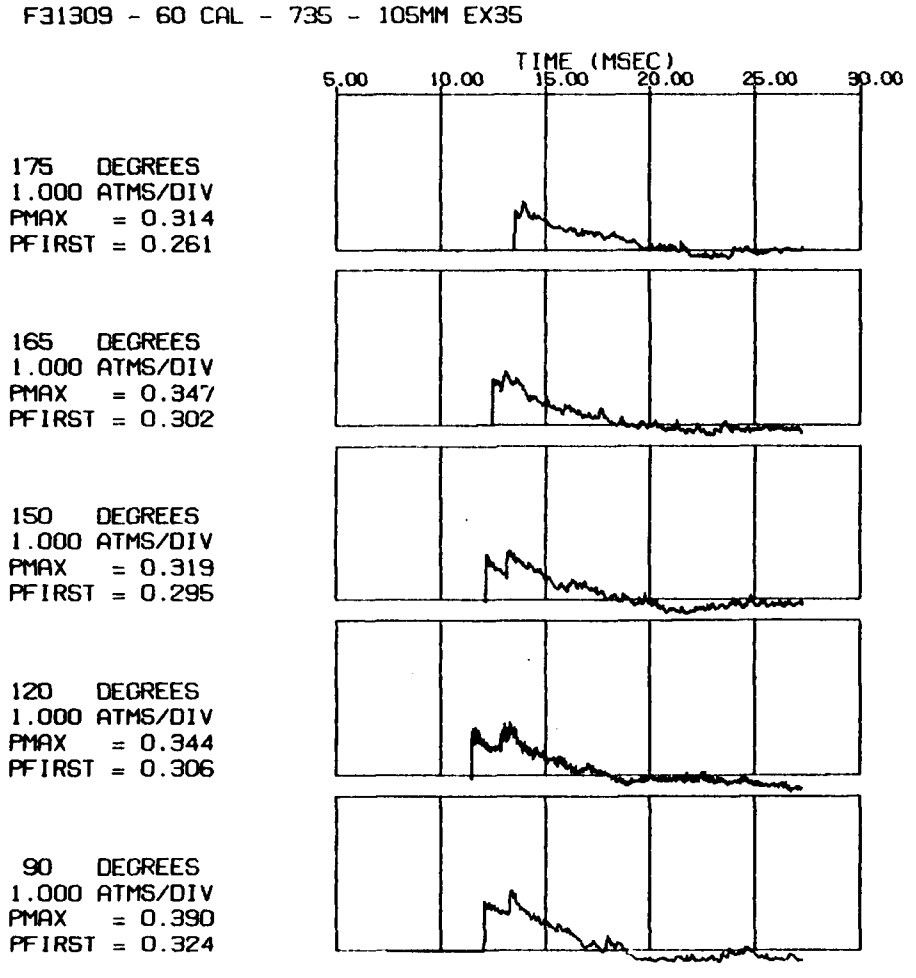

Figure D14. Pressure histories at 60 calibers for round 31309 using the 105-mm standard brake and M735 ammunition.

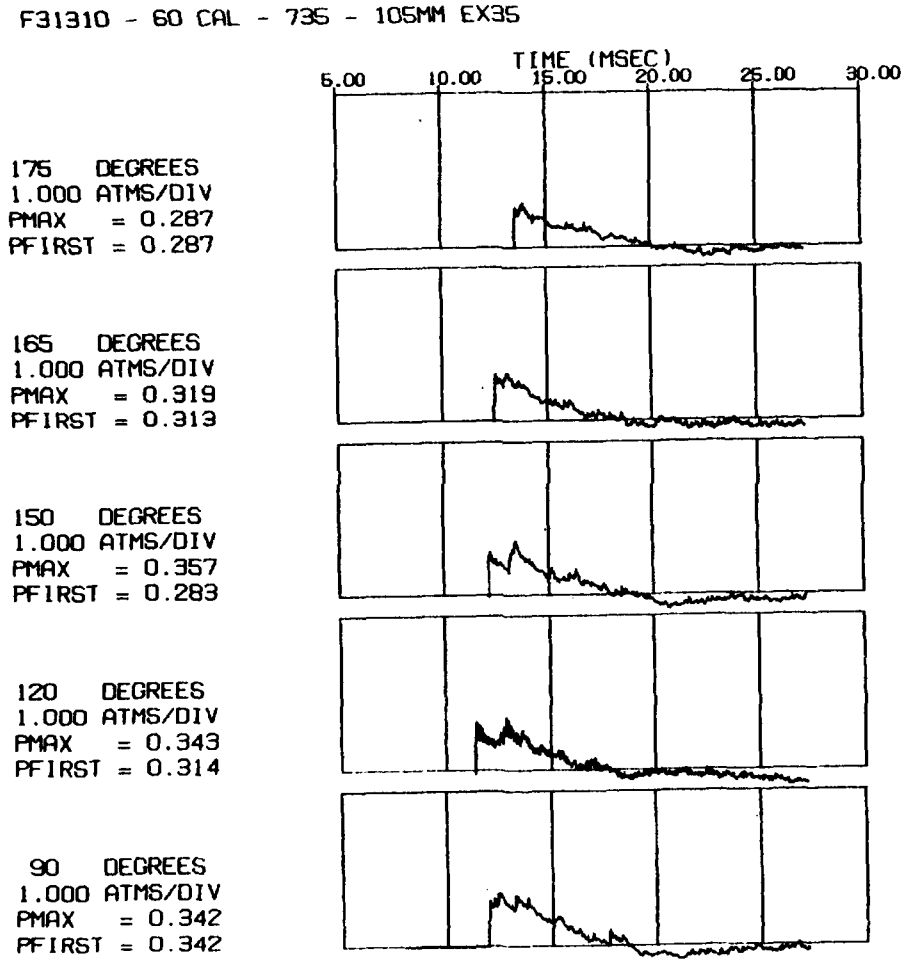

Figure D15. Pressure histories at 60 calibers for round 31310 using the 105-mm standard brake and M735 ammunition.

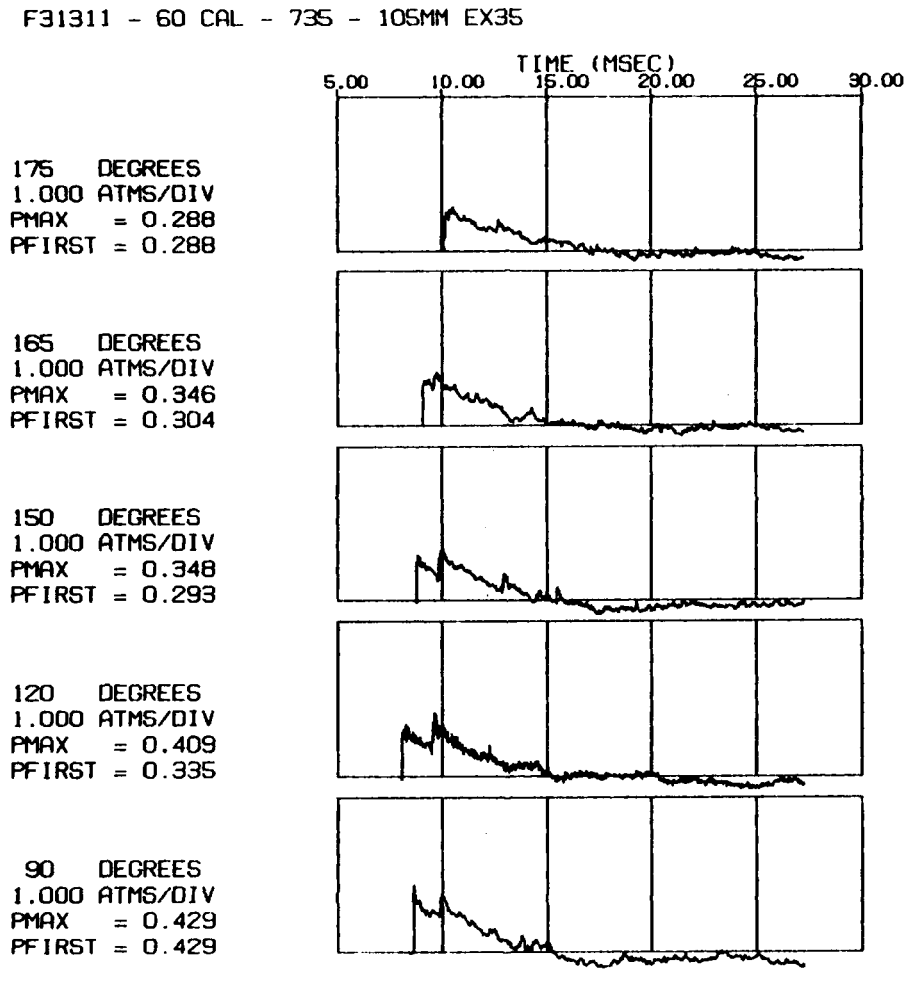

Figure D16. Pressure histories at 60 calibers for round 31311 using the 105-mm standard brake and M735 ammunition.

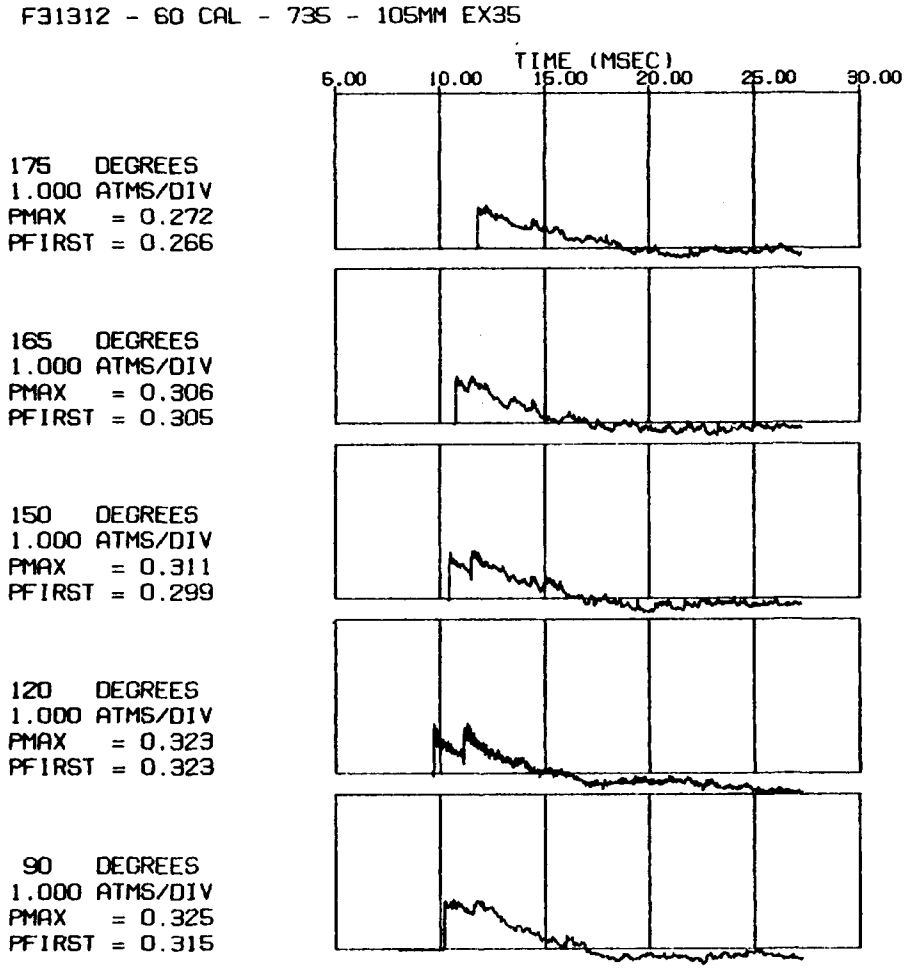

Figure D17. Pressure histories at 60 calibers for round 31312 using the 105-mm standard brake and M735 ammunition.

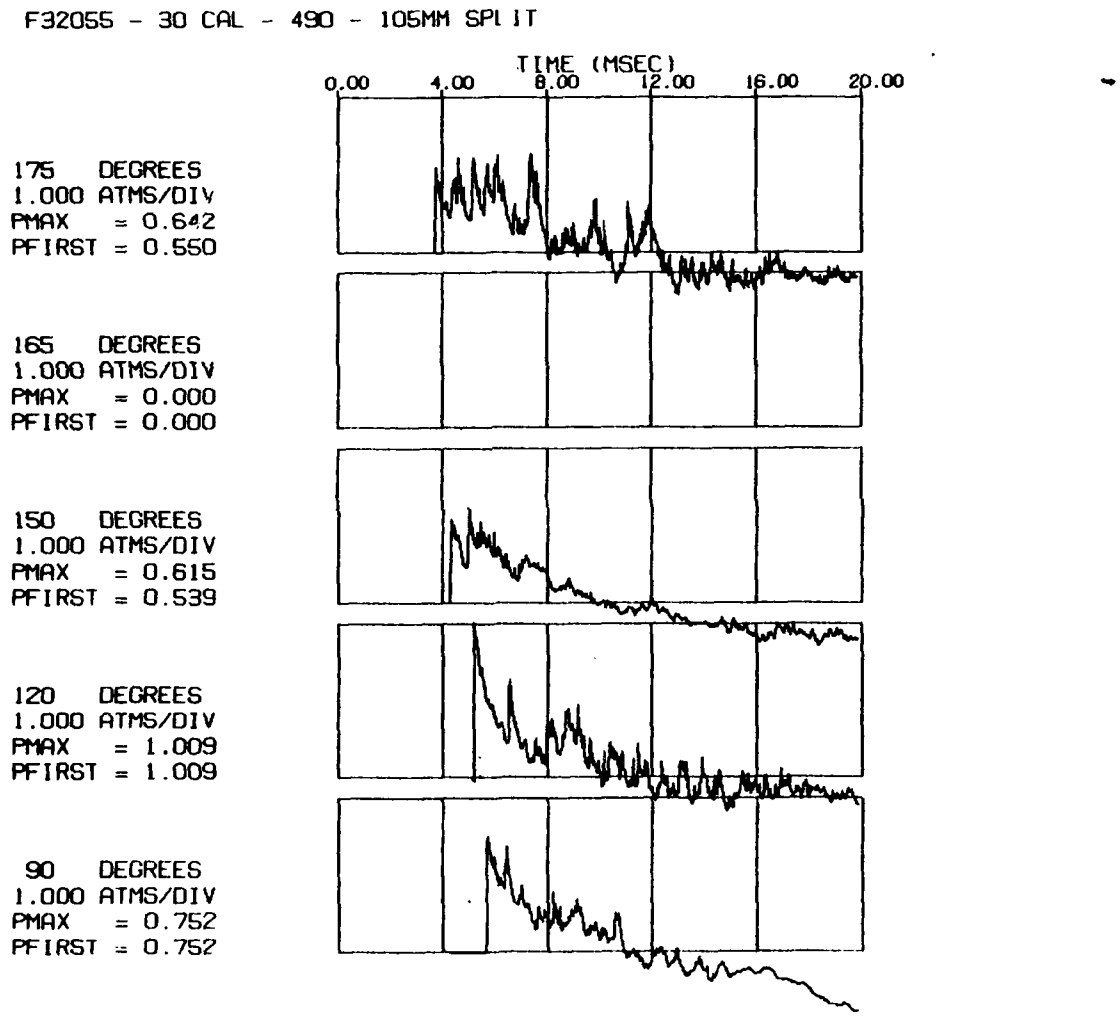

Figure D18. Pressure histories at 30 calibers for round 32055 using the 105-mm split brake and M490 ammunition.

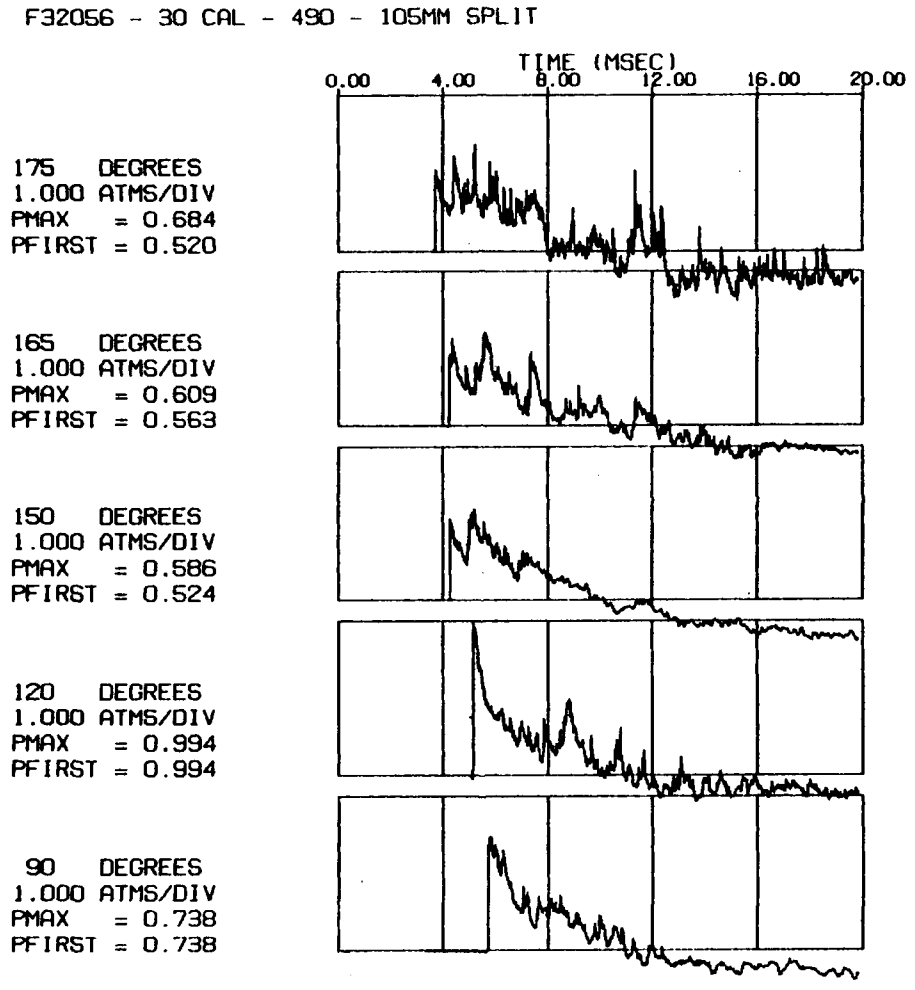

Figure D19. Pressure histories at 30 calibers for round 32056 using the 105-mm split brake and M490 ammunition.

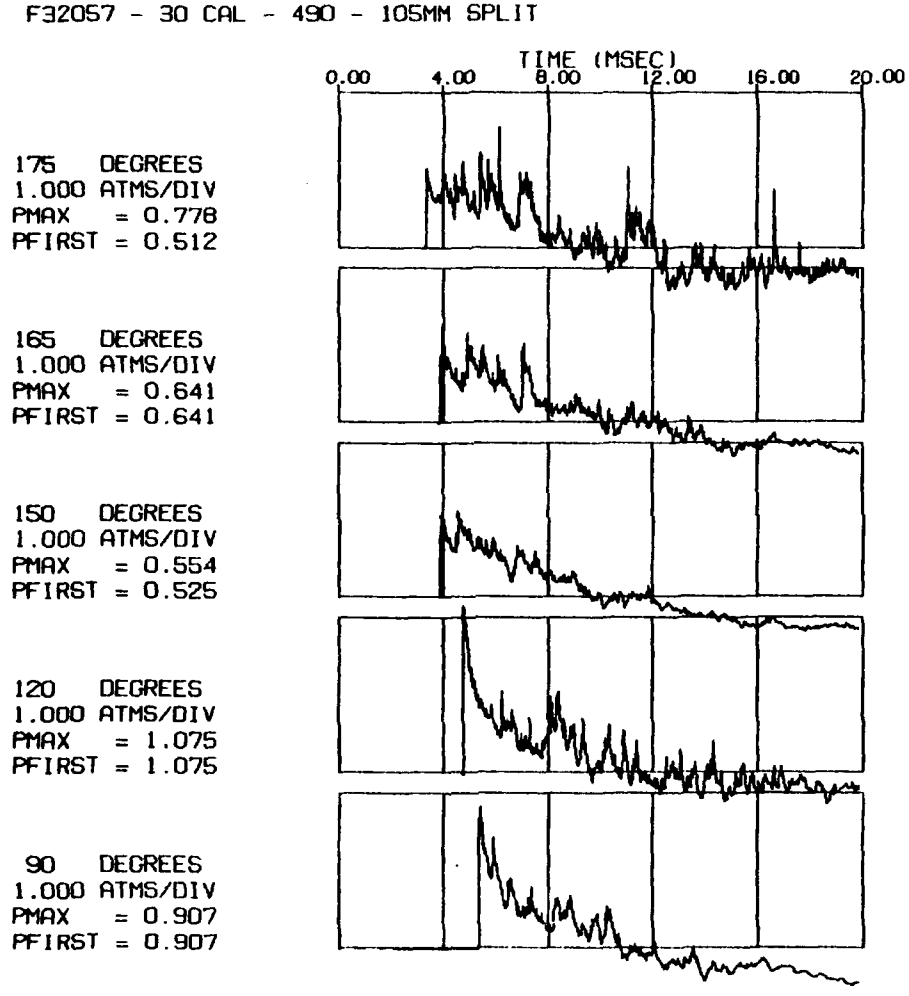

Figure D20. Pressure histories at 30 calibers for round 32057 using the 105-mm split brake and M490 ammunition.

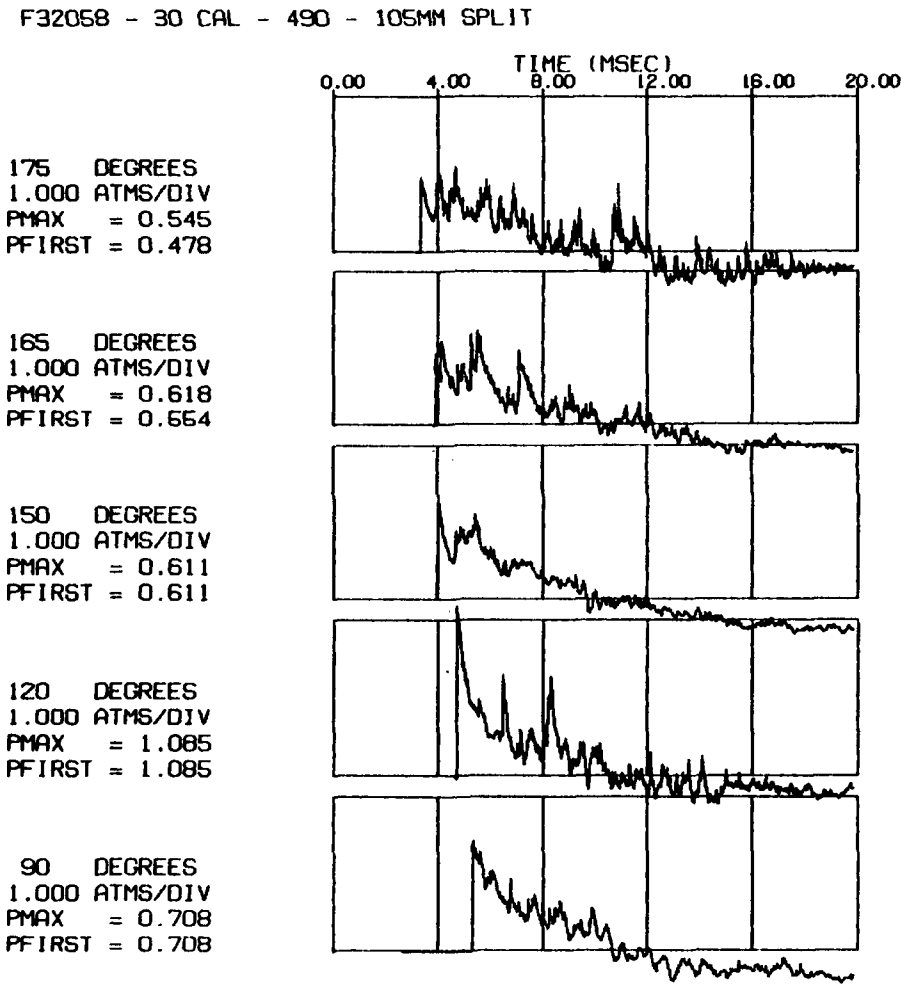

Figure D21. Pressure histories at 30 calibers for round 32058 using the 105-mm split brake and M490 ammunition.

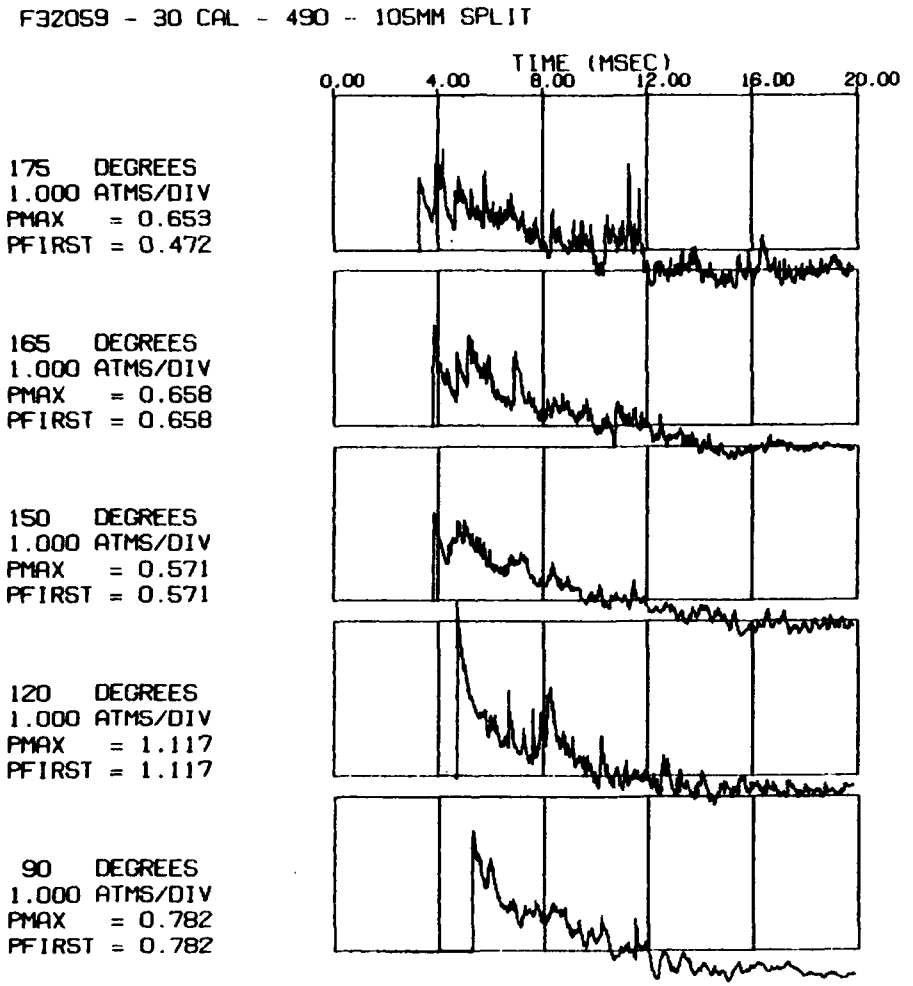

Figure D22. Pressure histories at 30 calibers for round 32059 using the 105-mm split brake and M490 ammunition.

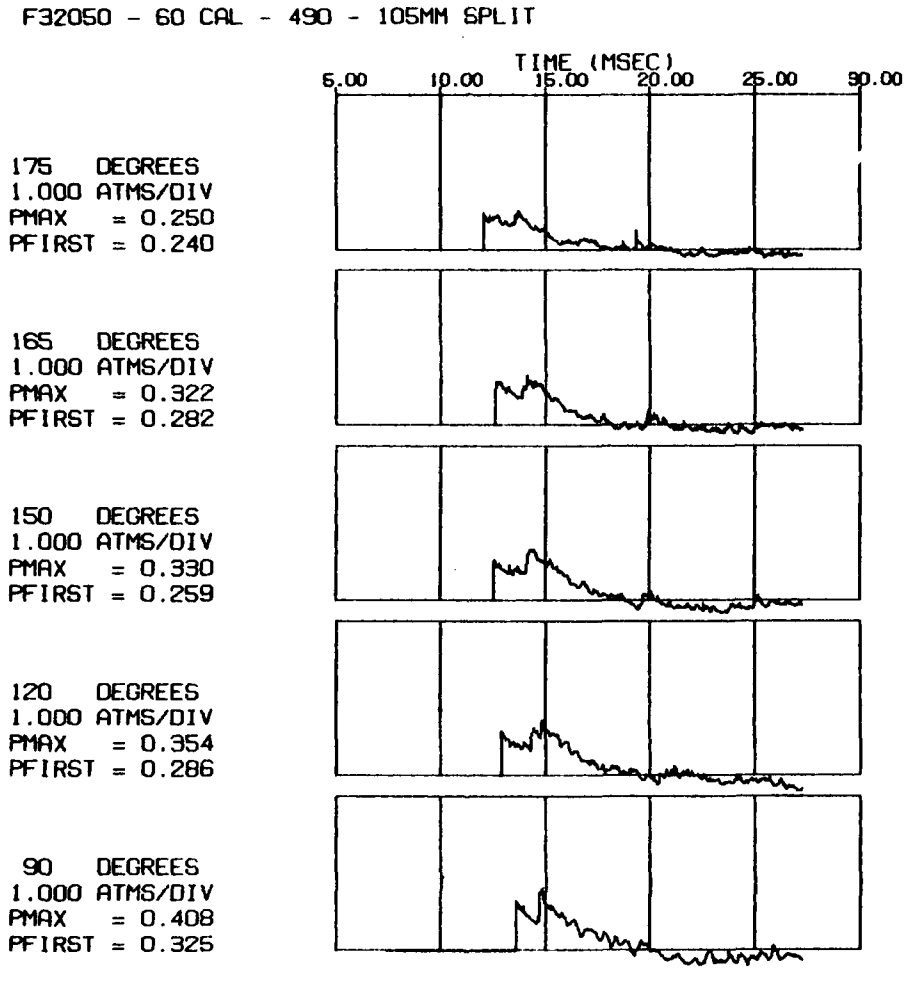

Figure D23. Pressure histories at 60 calibers for round 32050 using the 105-mm split brake and M490 ammunition.

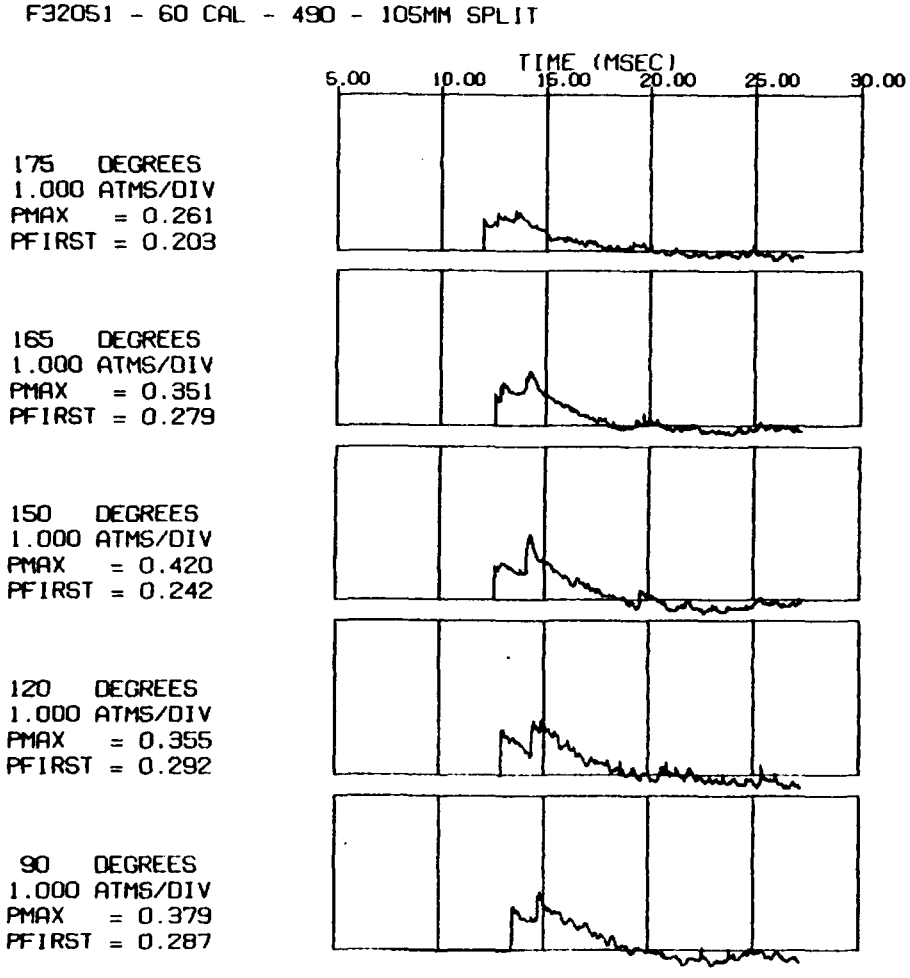

Figure D24. Pressure histories at 60 calibers for round 32051 using the 105-mm split brake and M490 ammunition.

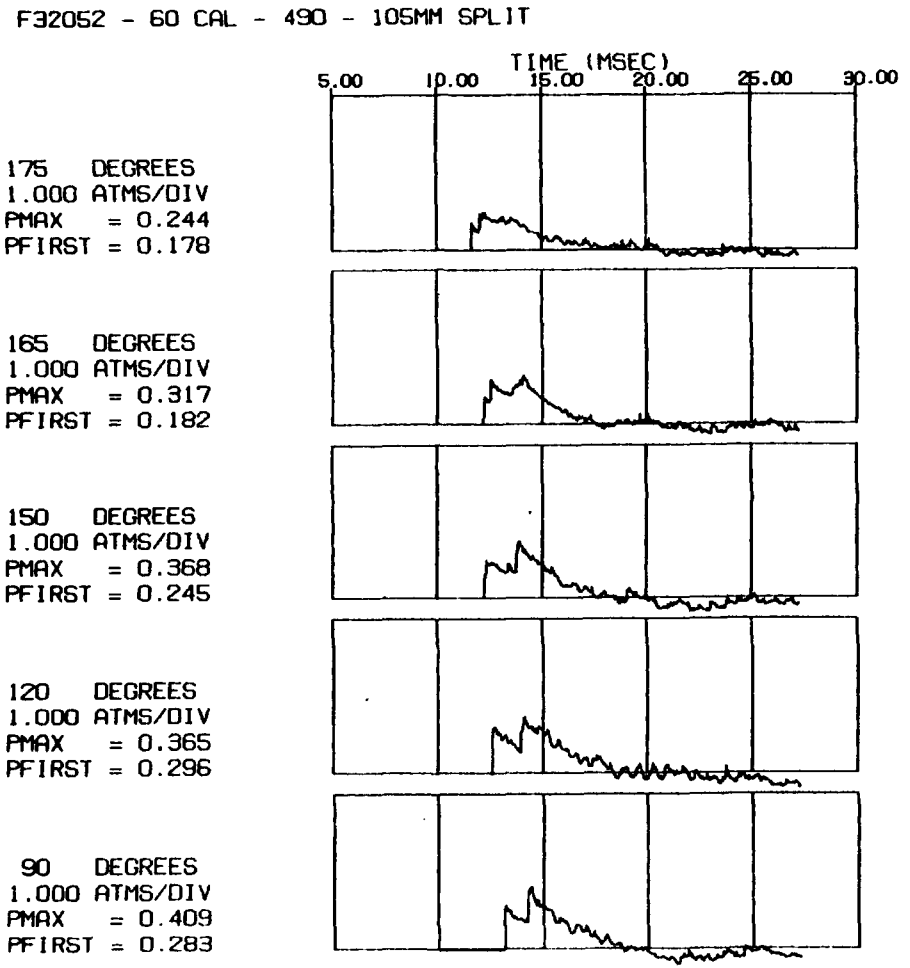

Figure D25. Pressure histories at 60 calibers for round 32052 using the 105-mm split brake and M490 ammunition.

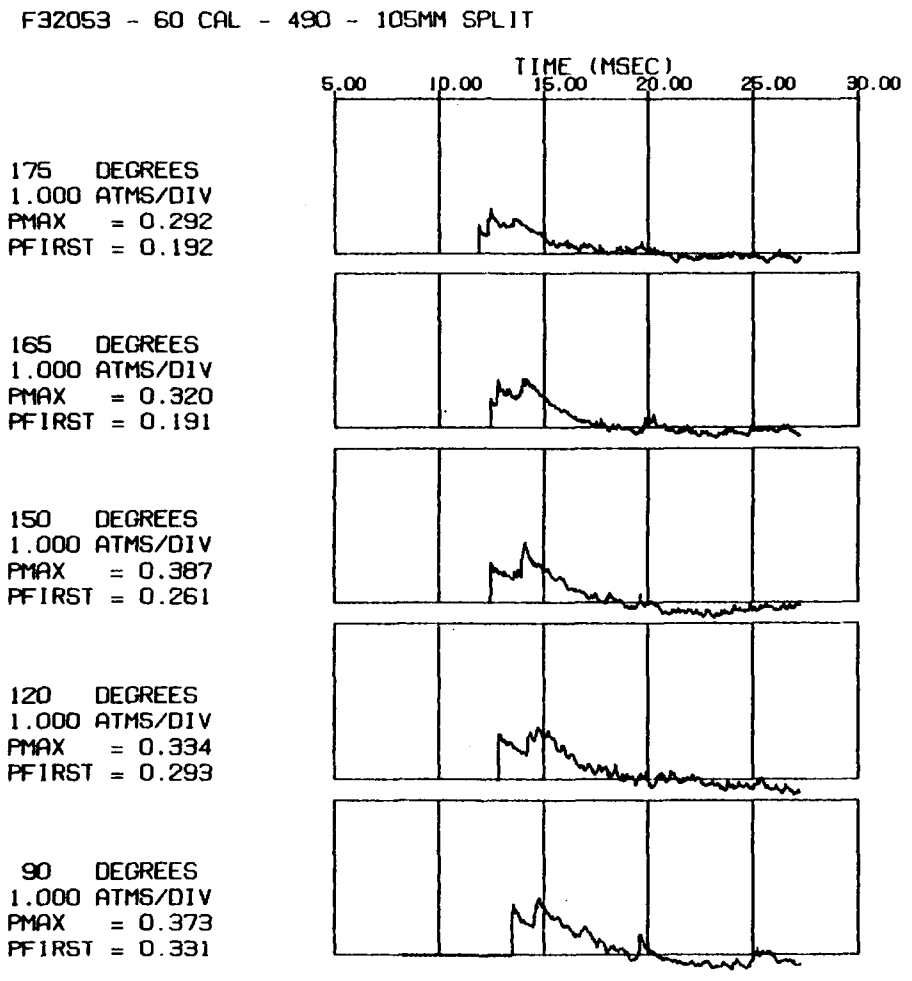

Figure D26. Pressure histories at 60 calibers for round 32053 using the 105-mm split brake and M490 ammunition.

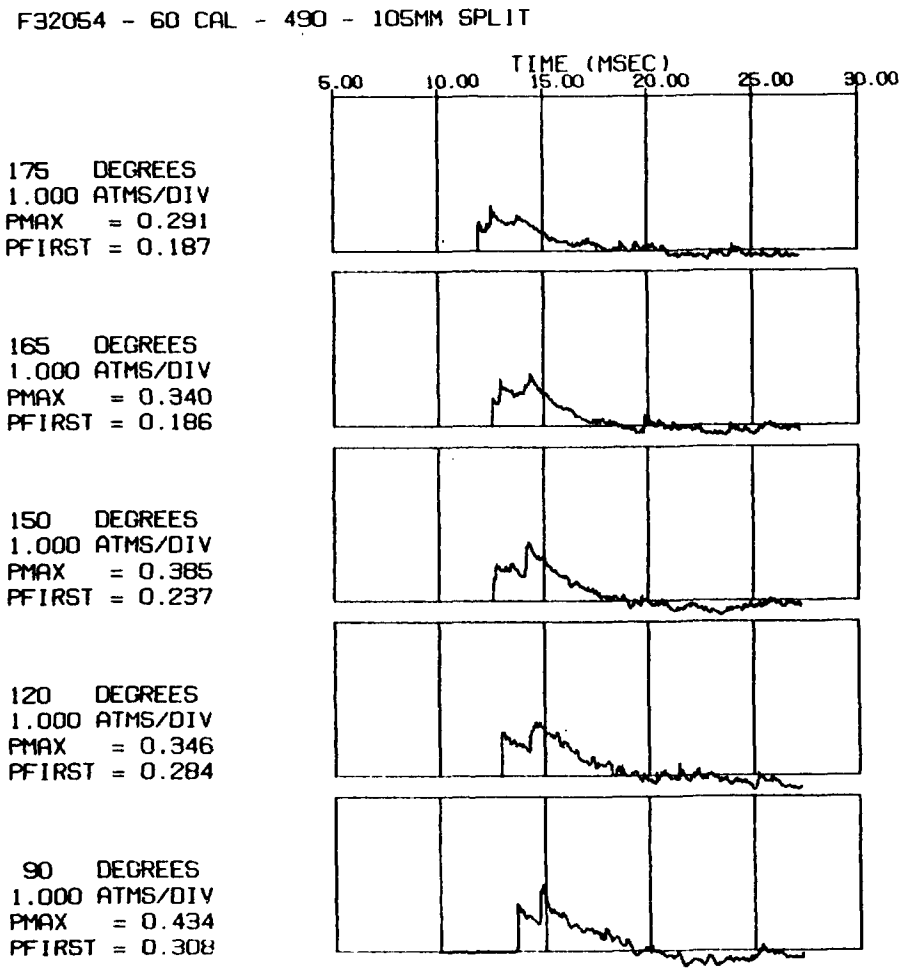

Figure D27. Pressure histories at 60 calibers for round 32054 using the 105-mm split brake and M490 ammunition.

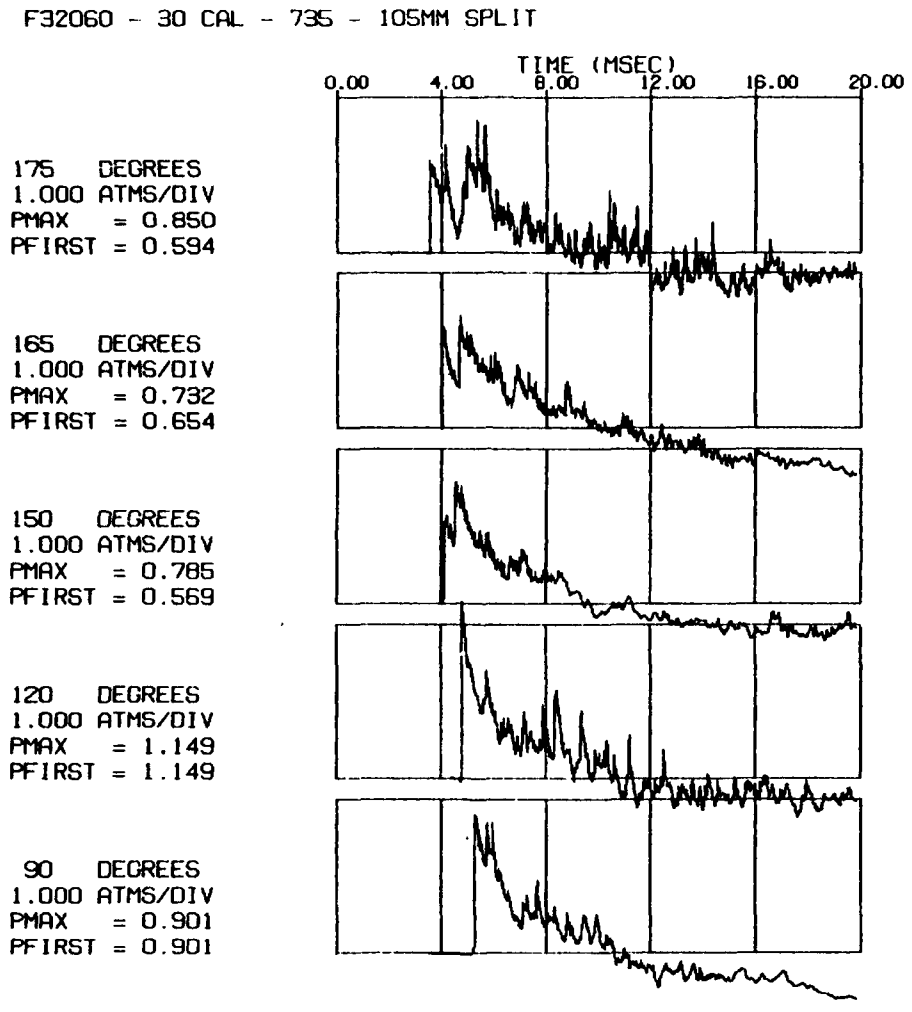

Figure D28. Pressure histories at 30 calibers for round 32060 using the 105-mm split brake and M735 ammunition.

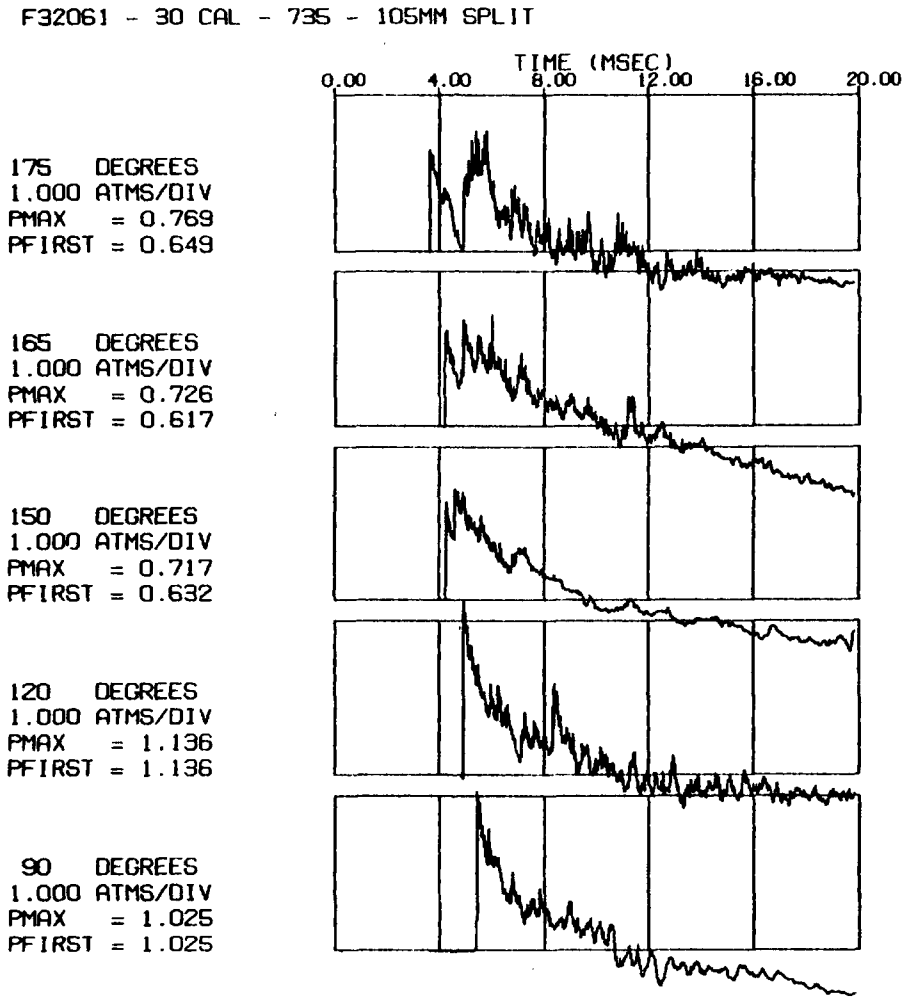

Figure D29. Pressure histories at 30 calibers for round 32061 using the 105-mm split brake and M735 ammunition.

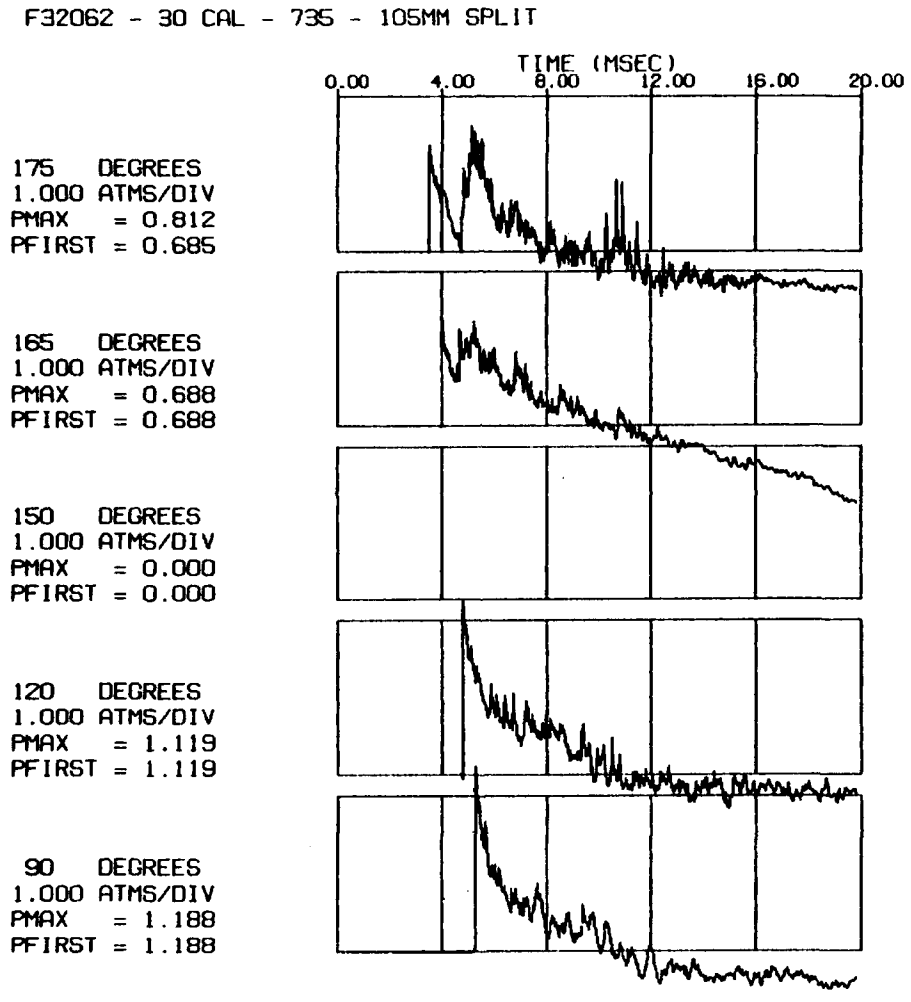

Figure D30. Pressure histories at 30 calibers for round 32062 using the 105-mm split brake and M735 ammunition.

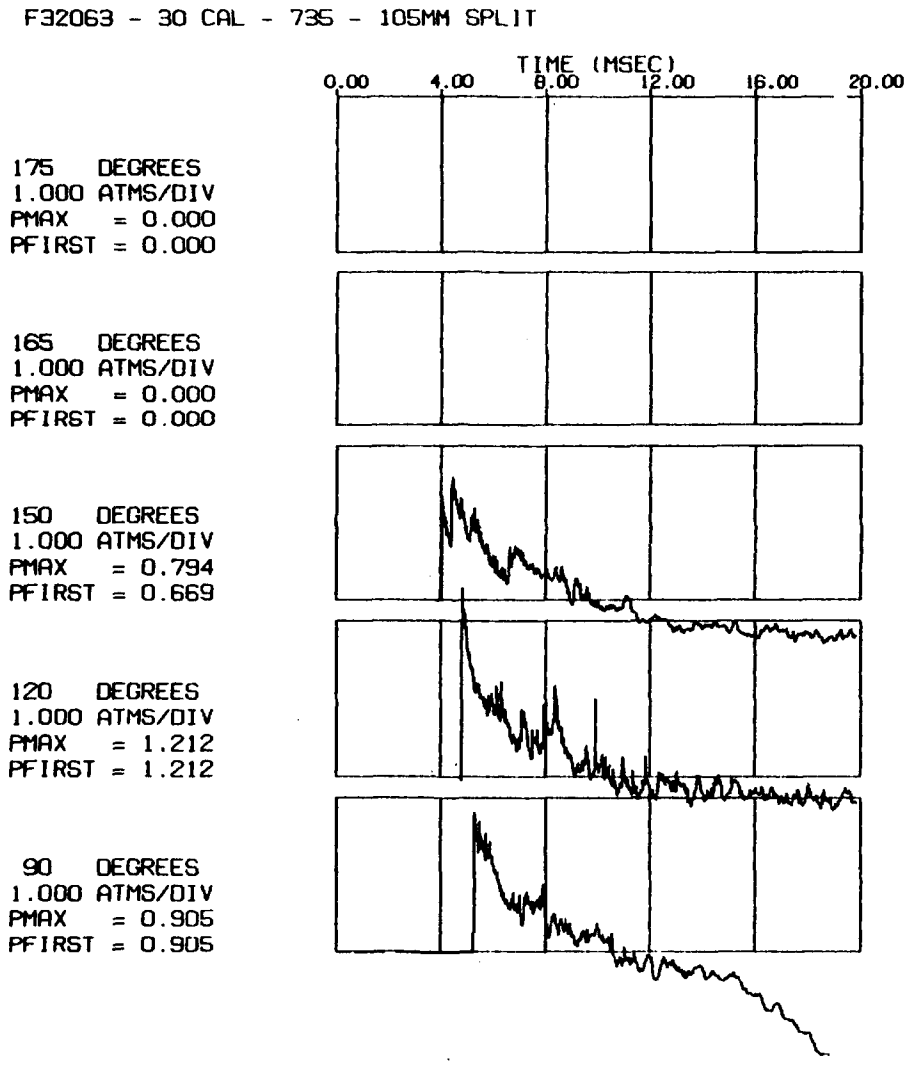

Figure D31. Pressure histories at 30 calibers for round 32063 using the 105-mm split brake and M735 ammunition.

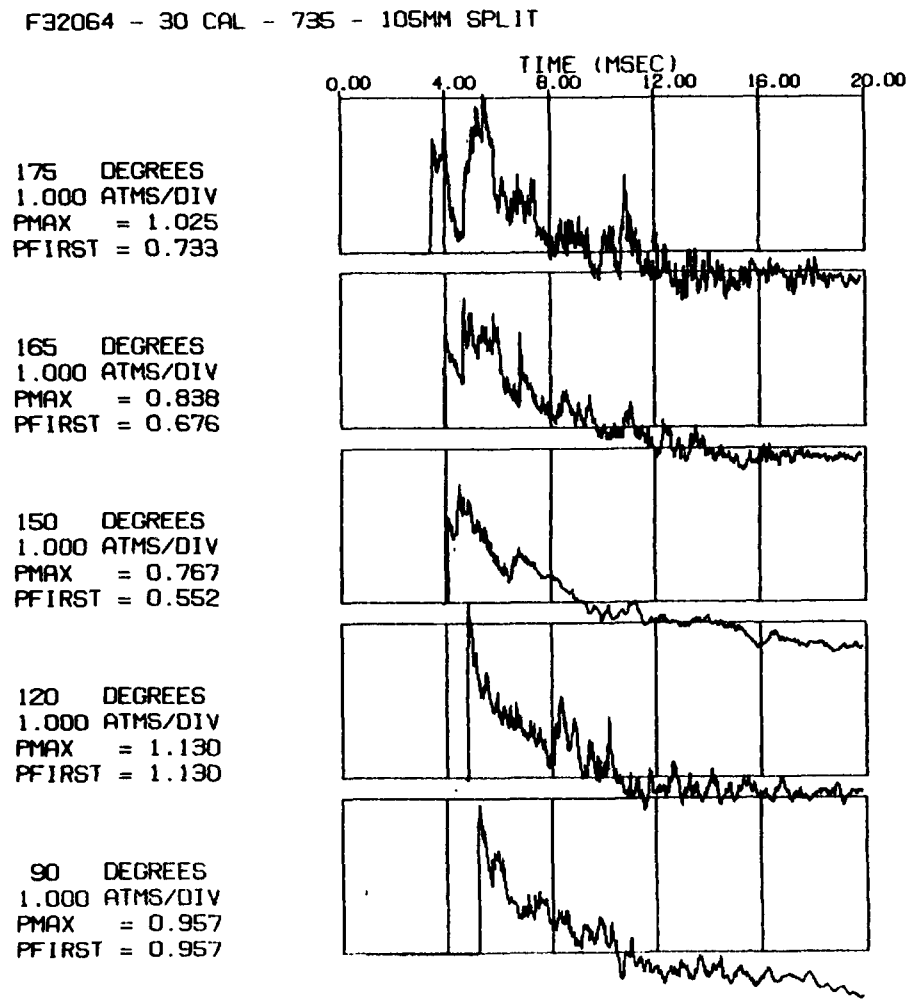

Figure D32. Pressure histories at 30 calibers for round 32064 using the 105-mm split brake and M735 ammunition.

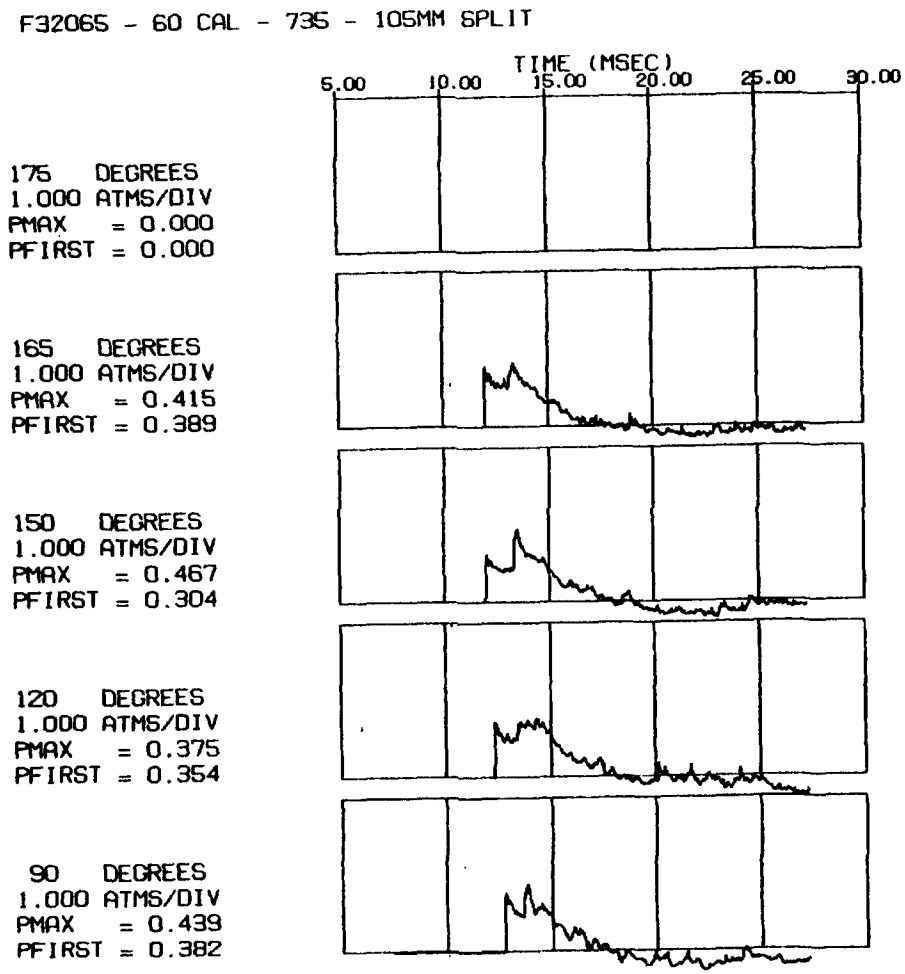

Figure D33. Pressure histories at 60 calibers for round 32065 using the 105-mm split brake and M735 ammunition.

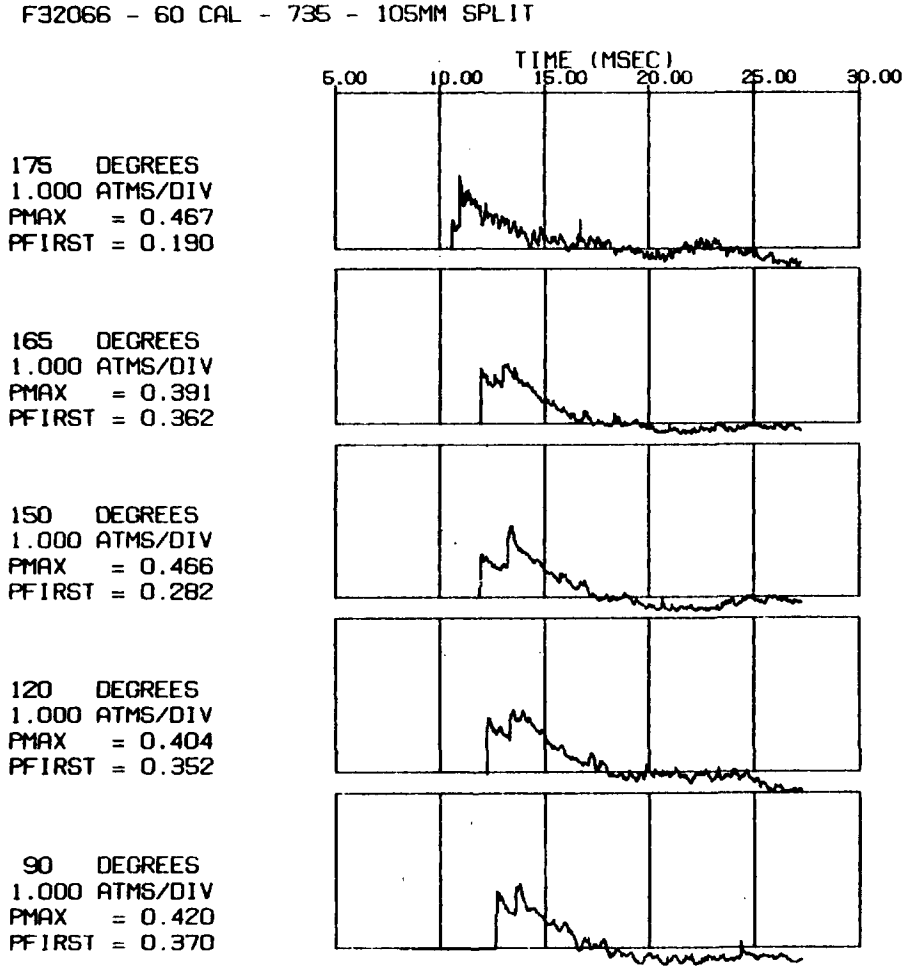

Figure D34. Pressure histories at 60 calibers for round 32066 using the 105-mm split brake and M735 ammunition.

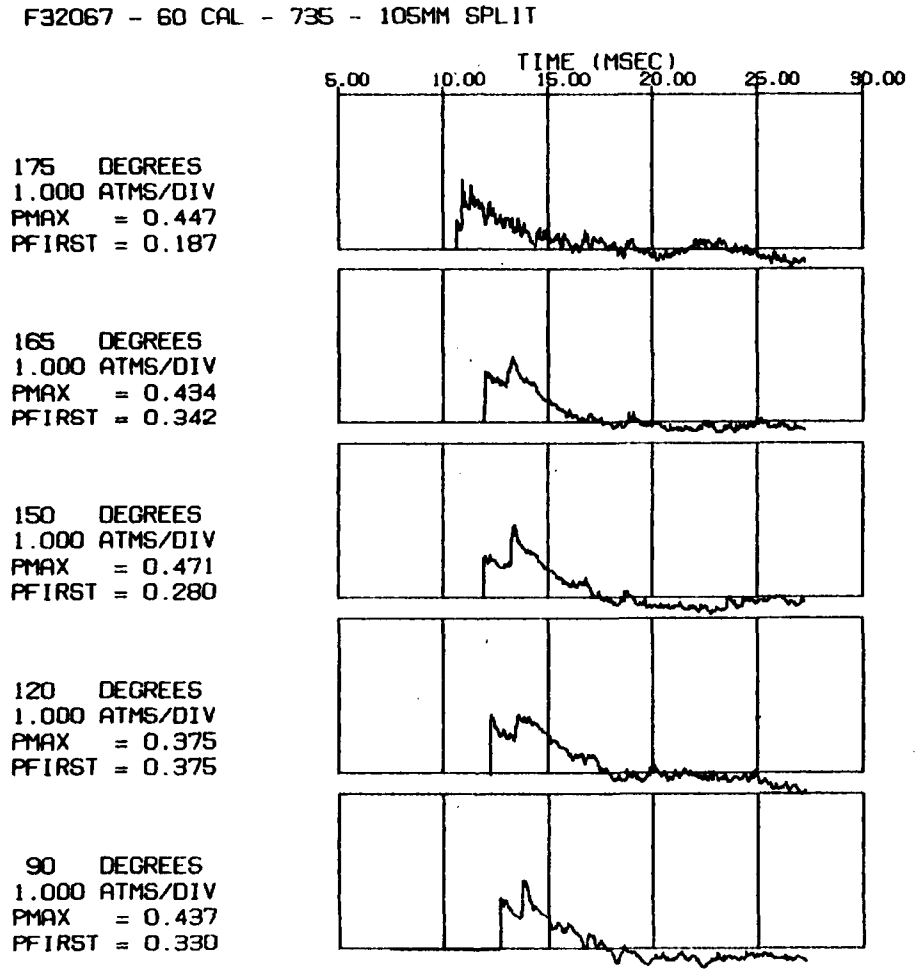

Figure D35. Pressure histories at 60 calibers for round 32067 using the 105-mm split brake and M735 ammunition.

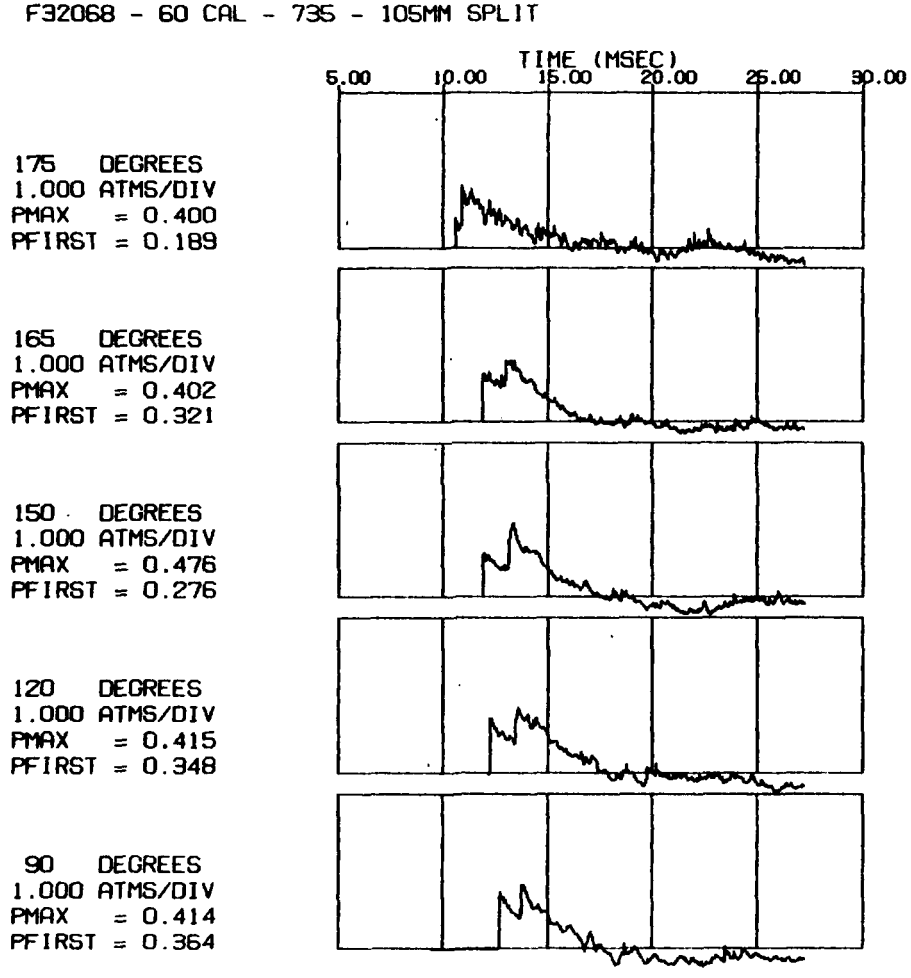

Figure D36. Pressure histories at 60 calibers for round 32068 using the 105-mm split brake and M735 ammunition.

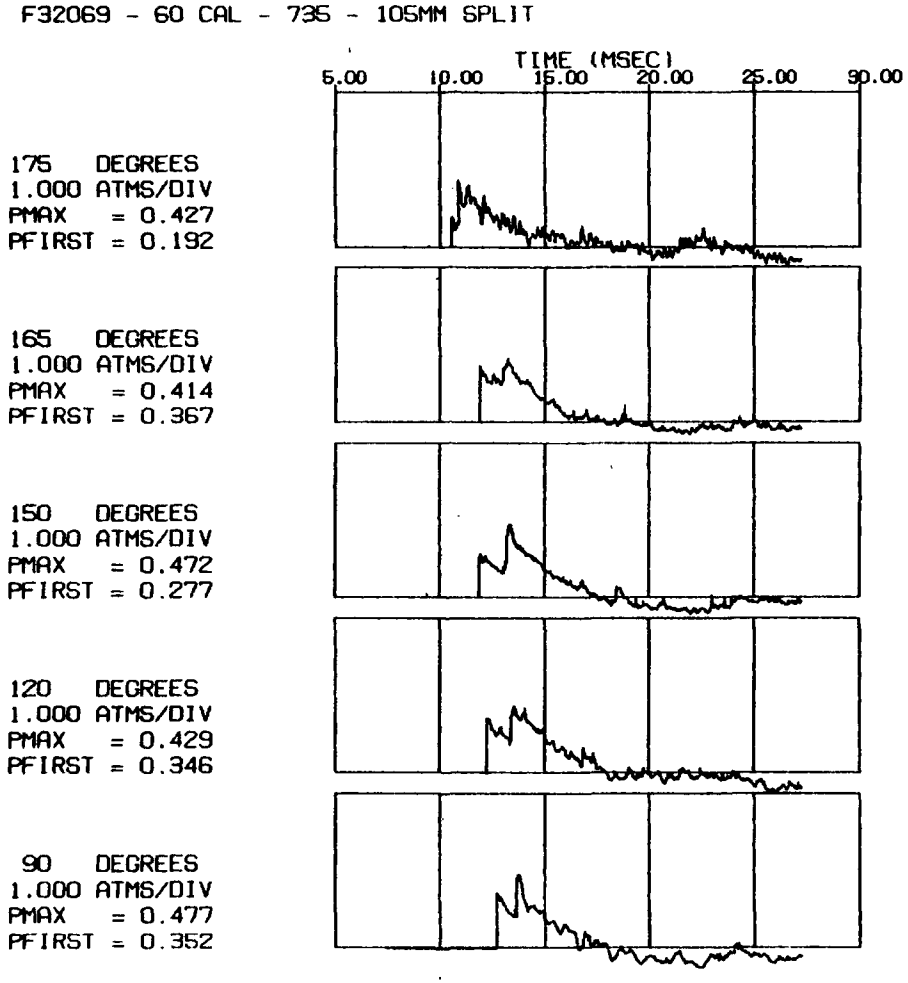

Figure D37. Pressure histories at 60 calibers for round 32069 using the 105-mm split brake and M735 ammunition.

TECHNICAL REPORT INTERNAL DISTRIBUTION LIST

	NO. OF COPIES
CHIEF, DEVELOPMENT ENGINEERING DIVISION	
ATTN: SMCAR-CCB-DA	1
-DC	1
-DI	1
-DR	1
-DS (SYSTEMS)	1
CHIEF, ENGINEERING SUPPORT DIVISION	
ATTN: SMCAR-CCB-S	1
-SD	1
-SE	1
CHIEF, RESEARCH DIVISION	
ATTN: SMCAR-CCB-R	2
-RA	1
-RE	1
-RM	1
-RP	1
-RT	1
TECHNICAL LIBRARY	5
ATTN: SMCAR-CCB-TL	
TECHNICAL PUBLICATIONS & EDITING SECTION	3
ATTN: SMCAR-CCB-TL	
OPERATIONS DIRECTORATE	1
ATTN: SMCWV-ODP-P	
DIRECTOR, PROCUREMENT DIRECTORATE	1
ATTN: SMCWV-PP	
DIRECTOR, PRODUCT ASSURANCE DIRECTORATE	1
ATTN: SMCWV-QA	

NOTE: PLEASE NOTIFY DIRECTOR, BENET LABORATORIES, ATTN: SMCAR-CCB-TL, OF ANY ADDRESS CHANGES.

TECHNICAL REPORT EXTERNAL DISTRIBUTION LIST

	NO. OF COPIES
ASST SEC OF THE ARMY RESEARCH AND DEVELOPMENT ATTN: DEPT FOR SCI AND TECH THE PENTAGON WASHINGTON, D.C. 20310-0103	1
ADMINISTRATOR DEFENSE TECHNICAL INFO CENTER ATTN: DTIC-FDAC CAMERON STATION ALEXANDRIA, VA 22304-6145	12
COMMANDER US ARMY ARDEC	
ATTN: SMCAR-AEE	1
SMCAR-AES, BLDG. 321	1
SMCAR-AET-O, BLDG. 351N	1
SMCAR-CC	1
SMCAR-CCP-A	1
SMCAR-FSA	1
SMCAR-FSM-E	1
SMCAR-FSS-D, BLDG. 94	1
SMCAR-IMI-I (STINFO) BLDG. 59	2
PICATINNY ARSENAL, NJ 07806-5000	
DIRECTOR US ARMY BALLISTIC RESEARCH LABORATORY ATTN: SLCBR-DD-T, BLDG. 305 ABERDEEN PROVING GROUND, MD 21005-5066	1
DIRECTOR US ARMY MATERIEL SYSTEMS ANALYSIS ACTV ATTN: AMXSY-MP ABERDEEN PROVING GROUND, MD 21005-5071	1
COMMANDER HQ, AMCCOM ATTN: AMSMC-IMP-L ROCK ISLAND, IL 61299-6000	1
COMMANDER ROCK ISLAND ARSENAL ATTN: SMCRI-ENM ROCK ISLAND, IL 61299-5000	1
MIAC/CINDAS PURDUE UNIVERSITY P.O. BOX 2634 WEST LAFAYETTE, IN 47906	1
COMMANDER US ARMY TANK-AUTMV R&D COMMAND ATTN: AMSTA-DDL (TECH LIB) WARREN, MI 48397-5000	1
COMMANDER US MILITARY ACADEMY ATTN: DEPARTMENT OF MECHANICS WEST POINT, NY 10996-1792	1
US ARMY MISSILE COMMAND REDSTONE SCIENTIFIC INFO CTR ATTN: DOCUMENTS SECT, BLDG. 4484 REDSTONE ARSENAL, AL 35898-5241	2
COMMANDER US ARMY FGN SCIENCE AND TECH CTR ATTN: DRXST-SD 220 7TH STREET, N.E. CHARLOTTESVILLE, VA 22901	1
COMMANDER US ARMY LABCOM MATERIALS TECHNOLOGY LAB ATTN: SLCMT-IML (TECH LIB) WATERTOWN, MA 02172-0001	2

NOTE: PLEASE NOTIFY COMMANDER, ARMAMENT RESEARCH, DEVELOPMENT, AND ENGINEERING CENTER, US ARMY AMCCOM, ATTN: BENET LABORATORIES, SMCAR-CCB-TL, WATERVLIET, NY 12189-4050, OF ANY ADDRESS CHANGES.

TECHNICAL REPORT EXTERNAL DISTRIBUTION LIST (CONT'D)

	NO. OF COPIES
COMMANDER US ARMY LABCOM, ISA ATTN: SLCIS-IM-TL 2800 POWDER MILL ROAD ADELPHI, MD 20783-1145	1
COMMANDER US ARMY RESEARCH OFFICE ATTN: CHIEF, IPO P.O. BOX 12211 RESEARCH TRIANGLE PARK, NC 27709-2211	1
DIRECTOR US NAVAL RESEARCH LAB ATTN: MATERIALS SCI & TECH DIVISION CODE 26-27 (DOC LIB) WASHINGTON, D.C. 20375	1 1
COMMANDER AIR FORCE ARMAMENT LABORATORY ATTN: AFATL/MN EGLIN AFB, FL 32542-5434	1
COMMANDER AIR FORCE ARMAMENT LABORATORY ATTN: AFATL/MNF EGLIN AFB, FL 32542-5434	1
DIRECTOR US ARMY BALLISTIC RESEARCH LABORATORY ATTN: SLCBR-IB-M (DR. BRUCE BURNS) ABERDEEN PROVING GROUND, MD 21005-5066	1

NOTE: PLEASE NOTIFY COMMANDER, ARMAMENT RESEARCH, DEVELOPMENT, AND ENGINEERING CENTER, US ARMY AMCCOM, ATTN: BENET LABORATORIES, SMCAR-CCB-TL, WATERVLIET, NY 12189-4050, OF ANY ADDRESS CHANGES.